Università degli Studi di Torino
Doctoral School of the University of Torino
PhD Programme in Chemical and Materials Sciences XXXIV cycle

Synthesis, characterization and catalysis of unconventional zeolites: from hierarchical structures to MAPOs.

Candidate: **Alessia Airi**

Supervisor: Prof. **Silvia Bordiga**

Co-Supervisor: Dr. **Valentina Crocellà**

Jury Members: Prof. **Svetlana Mintova**
Normandie Université, Caen, France
Laboratoire Catalyse et Spectrochimie

Prof. **Massimo Migliori**
Università della Calabria
Dipartimento di Ingegneria dell'ambiente

Dr. **Lorenzo Mino**
Università di Torino
Dipartimento di Chimica

Head of the Doctoral School: Prof. Alberto Rizzuti
PhD Programme Coordinator: Prof. Bartolomeo Civalleri

Torino, March 2022

Index

APPENDIX I: RELATED PUBLICATIONS

APPENDIX II: OFF TOPIC PUBLICATION

Preface

Zeolites are the archetype of the porous catalyst. Although the genesis of other porous materials such as MOF and porous silicas has been inspired from zeolites, their effective application is still unmatched. In heterogeneous catalysis, no other material better reflects the profile of the ideal catalyst in such a vast number of processes than zeolites, due to the combination of high activity and selectivity ensured by the zeolitic structure. The latter involves the interplay between highly specialised actives sites, dispersed in a vast surface area and the geometric confinement determined by the micropore channel systems.

The research on these materials is constantly growing, both for industrial and purely academic interest, as they represent an extraordinary example of chemical complexity, and their study is articulated on many levels of specific expertise. The term zeolites defines a class of materials whose composition and structure have a very wide range of expressions, resulting in unparalleled variability and versatility. If historically they were defined as microporous aluminosilicates, referring to natural zeolitic minerals, nowadays, considering the enormous progress in the synthetic field, this description is no longer adequate to fully describe the zeolites. More modern synthetic approaches have led to an expansion of the definition limits of zeolite, encompassing materials with structures and compositions that go beyond the traditional boundaries. From a structural point of view, the concept of expansion can be taken literally. In fact, the demand for catalysts with improved inner transport capacities and lower propensity for deactivation has led to the development of zeolites no longer confined to the microporosity level. These are the so-called hierarchical zeolites, that present multi-level porous systems in which microporosity and mesoporosity are combined to reduce the steric limitations typical of the traditional materials and to expand the application possibilities to bulky substrates, offering new reactive pathways while maintaining high selectivity. From a compositional point of view, the possibilities offered by the accurate isomorphic insertion of heteroatoms pushes the description of zeolites beyond the definition of aluminosilicate, allowing to observe such a variety of chemical behaviours and catalytic applications. The zeolites with aluminophosphate composition (AlPOs) are a great example of this, moreover if synthetized in presence of further heteroatoms, as SAPOs (Si containing AlPOs) and MAPOs (metal containing AlPOs).

The huge structural and chemical variety that derives from the considerations above, implies the necessity to have a deep and individual knowledge of each zeolitic system that requires a specific synthesis and characterization protocol. This also implies a highly specific catalytic evaluation that cannot disregard a profound intrinsic knowledge of the material. This doctoral work, articulated in three years, had as objective the achievement of that kind of knowledge on different "unconventional" zeolitic systems. This thesis is structured to underline this concept, through the exposure of the theoretical knowledge acquired during the three years and then presenting six different case studies, in which synthesis, characterisation and catalytic evaluation are combined.

An overview on the nine chapters, constituting this thesis, is presented hereafter.

Chapter 1. This chapter exposes the theoretical knowledges acquired on zeolitic materials, providing a definition of zeolitic structure, with reference to specific catalytic application based on the active site nature and composition, ranging from aluminosilicate to aluminophosphates. An important part of this chapter has been dedicated to reviewing the vast literature regarding hierarchical zeolites. This is quite a "popular topic" in the recent literature, that often involves misinterpretations and incorrect applications of the term. The chapter wants to outline the characteristics necessary for defining hierarchical zeolites and try to classify the materials by their catalytic behaviour, achievable by applying different synthetic strategies.

Chapter 2. This chapter collects the experimental procedures employed along this thesis work and the technical knowledges acquired. These mainly deal with the practice in the zeolites synthesis and with the deepening of spectroscopic techniques for the characterization of materials, among which *in situ* FT-IR spectroscopy has been the main tool adopted during the studies. The experimental instrumentation, set-ups and specific sample treatments are exposed. Moreover, the most relevant theoretical information is provided for justify the selection of the adopted technique or experimental strategy that led to the results exposed in the following chapters.

Chapter 3. It is dedicated to the hierarchical zeolites mM-Z, which were the subject of the first PhD year. This research dealt with the synthesis of the gemini type surfactant C_{18}-N_3-C_{18},[1] in collaboration with the organic chemistry group of Chemistry department (University of Turin) then employed as templating agent in the optimisation of synthesis of the hierarchical MFI structures denoted mM-Z. The produced material has been fully characterised by applying volumetric and spectroscopic techniques for understanding the structural displacement of the multilevel porous system and the nature and abundance of the active sites. The work has been completed by performing catalytic tests of n-decane hydroconversion at the University of Leuven (Belgium). The catalytic results were analysed, according to the guidance of prof. Martens, to reconstruct a sort of internal map of the material. This was possible by identifying the dislocation of the active sites based on the products obtained, as result of the unique shape selectivity induced by this particular hierarchical zeolitic structure.

Chapter 4. The synthetic knowledges acquired during the period spent at KU Leuven University (particularly focused on the employing of "clear solution" for the precipitation of silicate zeolites nuclei then assembled to form hierarchical structures) have been applied in the synthesis of mesoporous silicates templated by commercial surfactants. This chapter presents the results obtained by applying the surfactant Triton-X100, solubilised in cinnamic acid solution, for obtaining road-like micelles as mesoporogen. The reported characterisation results show how the variation of the process parameters in the synthetic conditions influence the final materials. Finally, the synthesis procedure able to produce a material with high surface area and monodisperse distribution of mesopores, has been identified.

Chapter 5. Following similar approaches to ones of Chapter 4, the research reported in this chapter aimed to develop the synthesis of Ti(IV) containing hierarchical zeolites. The synthetic level of difficulty in this case was raised, aiming to achieve a hierarchical structural organisation while ensuring the proper tetrahedral coordination of Ti(IV), which represents the active site of Titanium Silicalite-1 like reactivity. The chapter reports the most relevant results leading to the formation of Ti(IV) containing mesoporous materials. Of these, the proper Ti(IV) insertion was evaluated by FT-IR, UV-vis, and Raman spectroscopies. Finally, the most promising material was tested in the hydrogen peroxide epoxidation reaction (followed by FT-IR spectroscopy), proving to be catalytically active.

Chapter 6. Thanks to the knowledge acquired regarding hierarchical zeolites (in particular in the work described in chapter 3) it has been possible to carry out a complete advanced characterization of a substantially unknown material. This zeolite was synthetised by the University of Cambridge, as result of a new synthetic strategy capable of obtaining zeolitic monoliths (without the use of binders), particularly promising in MTO conversion. In order to understand the structural organization and the active species present in this peculiar material, N_2 physisorption at low T and various *in situ* FT-IR spectroscopy experiments coupled with the use of different probe molecules have been performed. The results obtained will be used in the development of a computational model of the structure operated by the University of Gent.

Chapter 7. The skills acquired in the advanced characterization of zeolites (mainly dealing with spectroscopies) in the first years of the PhD, were put to use in the third year to describe a series of SAPO-18 and MAPO-18 synthesized at the University of Oslo, particularly promising in MTO conversion. All these materials presented a discrepancy between the concentration of heteroatoms and that of acidic sites, which should have coincided. For understanding the origin of this peculiarity, targeted *in situ* FT-IR spectroscopy experiments have been designed. The results reported in Chapter 7 have been finally able to explain the phenomenon, which depends on intrinsic features of each material.

Chapter 8. During the study described in Chapter 7, it was found that among the MAPO-18 studied, one had surprising characteristics. It was the cobalt (II) containing AlPO-18, named CoAPO-18. In this material, Co (II) is found in isomorphic substitution of Al(III), leading to a charge imbalance and to acidic properties (H-CoAPO-18). The peculiarity of this material is that Co (II) can be oxidized to Co(III), without leaving the framework, giving rise to a neutral structure. Preliminary studies have shown that the amount of acidic sites, which depend on the concentration of tetrahedral Co(II), is very sensitive to the catalyst activation conditions. These observations, obtained by FT-IR and optical spectroscopies, contrast with the results generally reported in the literature. For this reason, Chapter 8 reports a short review of the literature in which some bias due to outdated techniques have been found. The obtained results that give a novel view of the nature of the active sites of CoAPO-18 are therefore presented in details.

Chapter 9. H-CoAPO-18 has been tested in the conversion of methanol at 400°C during continuous acquisition of in situ IR spectra and compared with a H-SAPO-18 in the same conditions. This study was performed with a custom set-up combining a mass-flow controller for the gas dosage toward the catalyst and a high temperature measurements IR system. Chapter 9 reports all the phases of this *ad hoc* designed experiment and the most relevant results. It revealed that the population of strong acidic catalyst sites profoundly affects the methanol conversion in the very early stages of the process. Indeed, spectroscopic evidence was obtained of the production of CO *in situ* from the decomposition of methanol itself. When the concentration and availability of BAS sites was optimized a consumption of CO has been spectroscopically proved, achieving some observations helpful in understand the acid catalysed MTO conversion.

These chapters are followed by the list of the bibliographic references and by Appendix I that collects the publications deriving from the experimental work above summarised. Appendix II presents a further publication, collecting the work developed during the master thesis. Even this is off the thesis topic, the work of synthesis and characterisation of a novel MOF, provided useful tools applied during the PhD.

Chapter 1: Zeolites for catalysis

The relevance of zeolites as catalysts has gained over the years increasingly importance in industry, becoming the key of both traditional and modern processes in various fields, from petrol chemistry to fine chemicals production.[2] Moreover, the growing urgent need to develop sustainable practices finds important solutions in the use of zeolites. These heterogeneous catalysts are able to completely replace the classic industrial catalysts based on environmental dangerous reactives as concentrated acids or strong oxidants. Moreover, the extremely wide possibility of engineering zeolites enables developing processes-target materials, turning them suitable catalysts for the conversion of renewable resources such as natural gas, biomass and waste convoy.

The so wide application possibilities of zeolites are traced in the unique variability and tunability of their bulk properties achievable operating a fine control of the structure at atomic level which allows their employing in numerous different catalytic processes. The rigidity and the precise shape of the inner space of zeolites, organized in a microporous channels system, combined with the distribution of the active sites, determine their application as extremely selective catalyst and the definition as molecular sieves. These characteristics, indeed, allow the control and prediction of the access of reactants to the active sites and drive the formation of selected products through the imposition of the shape of intermediates and transition states. At the same time, the zeolites active sites confinement in a narrowed space with a defined shape (the microporous framework) represents the major drawback of these materials. Indeed, the zeolites microchannels (diameter < 1 nm) implies strong limitations in accessibility and diffusion rate of the reacting species and forces the molecular transport, bringing easily to the deactivation of the catalyst by obstruction of the micropores. This can be overcome again by the engineering of the structure, that, following the most modern synthesis techniques, allow the introduction of multiple level of porosity for increasing the catalyst mass transport while retaining selectivity and reactivity. These enhanced materials are called hierarchical zeolites.

1.1. The zeolitic structure: framework and extra-framework

Due to the great variety and complexity of these materials, to find a univocal definition of zeolites, sufficient to gather all the aspects that characterize them, is still matter of ongoing debate. The ATLAS of Zeolites framework types provides the definition of "corner-sharing network of tetrahedrally coordinated atoms" defining the crystal organization of zeolites.[3] The definition of aluminosilicate is generally applied by mineralogists, referring to the natural mineral forms, but is at the same time very reductive. First of all, the possible compositions of zeolites are not limited to the formula of aluminosilicate, but above all this definition does not highlight the essential characteristics that differentiate them from other oxides with similar composition. Starting from the natural occurrence, zeolites are crystalline silica polymorphs constituted by SiO_4 tetrahedra as primary building units, which are distinguished above the tectosilicates by the low-density framework, with $\rho_T < 21$ n_T/nm^3 (where n_T is the number of the tetrahedra per unit cell). The isomorphous substitution of Si^{4+} by other cations retaining the same coordination is easily admitted.[4] For natural zeolites, Al^{3+} partially replace framework Si^{4+} in a wide range of concentration, it follows the definition of aluminosilicates widely adopted for zeolites in general, which for the greatest part present that composition. In general, however, any definition based on composition is limiting, considering the fact that currently a broad variety of zeolite-like microporous materials with T-atoms other than silicon and aluminium are known. The structural organization of zeolitic type is in fact allowed even in the total absence of silicon. Often, materials of this type are referred with the term *zeotypes* to emphasize this aspect. The most relevant example are the microporous aluminophosphates with generic formula $AlPO_4$ (AlPOs), silicon free structures in which the tetrahedral cations Al^{3+} and P^{5+} assembly sharing corner oxygens in an open tridimentional low density framework. Therefore, currently, defining zeolites, including the so-called zeotypes, as *microporous solids* and *molecular sieves* is the most appropriate way, because it directly indicates the intrinsic properties of this type of structural organization.[4]

The zeolitic structure is composed of two essential components, the framework, i.e. the crystallographic lattice composed of tetrahedral atoms covalently bonded, and the extra-framework species that occupy the voids generated within the lattice. This confers to zeolites a double nature of covalent framework, ionically bounded to extra-framework species, which are fundamental part of the overall structure. This will be better explained describing the composition of zeolites. Therefore, structure and composition are closely related and mutually dependent on each other, giving rise to the enormous variety of different materials. A general description of zeolitic frameworks can be given by considering as constituent units, the tetrahedra formed by a central cation (generally defined as T, if the chemistry of the element is not considered) to which 4 oxygen atoms are coordinated, whose repetition in space generates the periodic lattice. The rigidity of the tetrahedral units, in which the angle enclosed in the OTO units is closed to 109.4° (tetrahedral angle) is counterbalanced by the variability of the possible angle enclosed between neighbours tetrahedra which ranges from 145° to 180°.[5] All the possible configurations in which the tetrahedra are connected each other sharing the corner oxygen atoms, generate an extremely wide range of different frameworks, determining an unpacked framework in which channel and cavities of molecular dimensions are formed. The free space that is generated can accommodate atoms and molecules from 0.2 up to 1 nm in diameter and represents the *porosity* which characterize all the zeolitic materials. Thus, the primary zeolite properties depend on the crystallographic structure, always characterized by periodic voids. In general, zeolites are classified as microporous materials, following the pores classification proposed by IUPAC:[6,7]

-**micropores** have diameter smaller than 2 nm. It can be subdivided in ultramicropores (below 1 nm diameter) and supermicropores (between 1 nm and 2 nm in diameter)

-**mesopores** have diameter between 2 nm and 50 nm

-**macropores** have diameter larger than 50 nm

Among the zeolite variety, a further classification of the pore size, which all rely in the ultramicropores definition, can be done by the number of T atoms involved in the pore openings, which are defined as Member Ring (MR) atoms. The subdivision is the following:

-**small pores zeolites**: constituted by 8MR, with a diameter about 0.4 nm;

-**medium pores zeolites**: 10MR, with a diameter of 0.45-0.65 nm;

-**large pores zeolites**: 12MR, with a diameter of 0.7-0.8 nm;

-**extra-large pores zeolites**: exceptional cases of more than 12MR, with diameters reaching 1 nm.[8]

The architecture of the zeolitic lattice is more complex and a common way to describe it is to use progressively more structured elements starting with what is defined Secondary Building Units (SBUs). The SBU is a bidimensional symmetry unit generated by the simplest assembly of the T atoms (PBU) to form polihedra and is the first element that defines the zeolite framework. The shape of the SBU depends on the number of the T cations involved forming the polihedra, considering that the entire framework is built up by only one kind of SBU and one unit cell contains an integral number of them. The SBU assembly form higher symmetry elements containing structures denoted as Composite Building Units (CNU) that corresponds to cages or other composite structures. Another way of assembly for SBU is to form chains, growing in one crystallographic direction. The CBU can be common to different frameworks, which differ instead for the way in which CBUs are connected for spatial symmetry. A common example is the case of sodalite cage, which is shared by both FAU and zeolite A.[5]

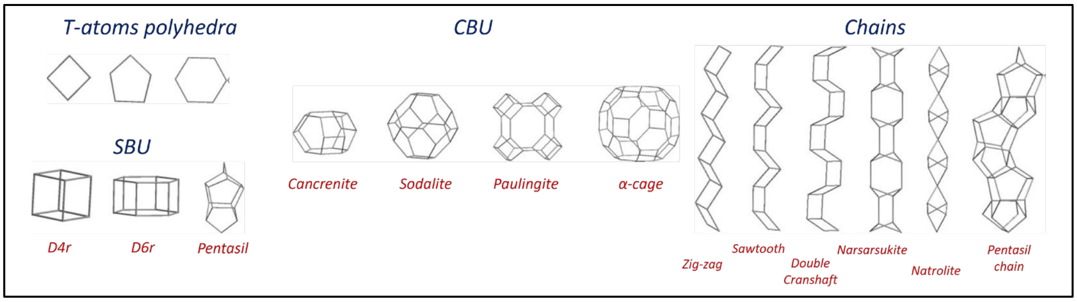

Figure 1. 1. Graphical schematization of the conventionally adopted zeolites constituting elements.

The lattice results from the periodic repetitions of these simpler units in tridimentional symmetry, considering that the combination of the tetrahedra within all the possible space groups is ideally infinite. Taking into account these structural elements and all the possible spatial symmetry operations it is possible to predict new zeolitic frameworks. Due to the crystallographic complexity, to identify if a new material corresponds to a new structure or a variation of a pre-existent one is not straightforward. Therefore, the official discovery of a new zeolitic structure is sanctioned by an international group of experts composed of 16 crystallographers, who make up the Structure Commission of the International Zeolites Association (IZA). Once the structure has been approved by the Commission, it is assigned to a univocal three-letters code and included in the “Atlas of Zeolite Framework types”.[9] The latest version of the ATLAS, published in 2017, contained 255 framework types, to which other 16 codes approved by IZA in the following years until now, must be added. Moreover, it is necessary to consider the enormous number of frameworks only theorized, that with the modern development of modelling software, are assuming an increasing importance to push forward the zeolites synthesis. The stability of a framework is strictly dependent on the composition considering a silicon content ranging from 0 to infinity. Some frameworks contained in ATLAS are reported only for AlPO composition, while others have stability both in the presence or in the absence of silicon, generating a correspondent aluminosilicate and aluminophosphate of the same framework. A good example is the case of the framework CHA, which is encountered in the natural mineral aluminosilicate chabazite as far as in the synthetic aluminophosphate AlPO-34.[10]

For a complete overview on the structure of the zeolites and how the framework is built up, the framework MFI will be focused and explained as example, because an important part of the present work will be dedicated to it. At the same manner, the framework AEI will be presented as example of preferentially stable AlPO form, to which the remaining part of the further chapters will be devoted.

The most relevant characteristics that distinguish a zeolitic framework are in the pores displacement. The two main distinction relay in CBU-based zeolites, that present cages often interconnected by a small pore window and chain-based zeolites that more easily form channels. The channel direction and dimensionality (1D, 2D, 3D), the number of T atoms forming the ring, which control the diffusion within the channel (or cage) and the diameter of the inner free space are the parameter expressing the shape selectivity of a zeolite, that can regard different moments in the interaction with a substrate. Namely:

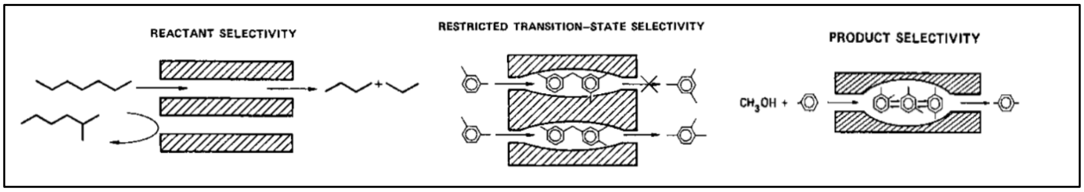

Figure 1. 2. Schematization of the different type of selectivity induced by the zeolitic pore geometry.

Reactant selectivity: the access of reactants is determined by the spatial constrictions of the pore openings.

Transition-state selectivity: the stabilization of a specific TS is determined the by shape/size of the inner space of the pores and the location of the active site.

Products selectivity: the products release is determined by the inner diffusion and pore diameters.

As already mentioned, the catalytic behaviour of zeolites arises from a combination of size/shape selectivity originates from the geometry of the porous array and the chemical activity depending on the composition, with a close interdependence between framework and extra-framework species. From a compositional point of view zeolites (in the extended sense, including zeotypes) are oxides of tetrahedral cations. With reference to the IZA database, two major families of composition are distinguishable, aluminosilicates and aluminophosphates.

Aluminosilicates are based on tetrahedra of SiO_4 and AlO_4, sharing corner oxygen atoms. Due to the charge imbalance between Si (4+) and Al (3+) the structural formula is better described as SiO_2 and AlO_2^- resulting in a net negative charge for each Al tetrahedron, from which a great part of the zeolites reactivity derives. Therefore, the generic formula for aluminosilicate zeolites is:[4]

$$A^{m+}_{y/m} \cdot [(SiO_2)_x \cdot (AlO_2)^-_y] \cdot z\, H_2O \qquad \text{Eq. 1}$$

where *A* is a cation of *m+* charge needed for compensating the negative charge induced by *y* Al(III), *(x + y)* is the total number of tetrahedra per unit cell, while a *z* content of H_2O is need for pore filling, considering that *z* varies with the dimensions of the free space. The exact stoichiometry depends on the Al(III) content and by the degree of incorporation of Al(III) allowed by the zeolitic frameworks *(x/y).* The concentration of Al(III) is expressed in relation with the Si(IV) as *(x/y) = Si/Al* ratio, which is the most important parameter for expressing the reactivity of the aluminosilicate, related with the nature of the cation *A,* which will be described later in details. The incorporation of the Al(III) is governed by the Löwenstein's rule, for which pairing vicinal Al(III) in Al-O-Al is forbidden in a zeolitic structure, because of the unfavourable interaction of adjacent negative charges.[5] Si/Al approaching 1, where there is strict alternation between Si and Al, is not tolerate from all the zeolitic framework, but only by ones that allow the right distance between the negative species, as zeolite A. Zeolites can crystallizes also in in absence of Al, with only Si tetrahedra (Si/Al = ∞) resulting in a neutral charged framework of SiO_2. The isomorphous substitution of Si with other cations (besides Al) is highly tolerated, if size (ionic radius) and charge criteria are satisfied, avoiding distortions in the tetrahedral coordination. Different properties arise if the substitution regards isovalent (charge 4+) as Ti(IV), Ge (IV) which guarantee the charge neutrality or aliovalent cations (with charge 2+ or 3+) as Zn (II), Be (II) and Ga (III) that provide a charge imbalance. Generally, the incorporation of different tetrahedral cations give rise to different structure, following the impositions due to the variations in the ionic radii and charge repulsion. Moreover, the presence of a heterometal in zeolites provides specific reactivity.

The same rules are valid for **aluminophosphates,** generally defined zeotypes. These materials have been firstly hypothesized at the beginning of 70s, following the same principle of charge balancing that drives the tetrahedral net formation of zeolites.[11] The structure built up of AlO_2^- and PO_2^+ in this case ensures the charge neutrality, reaching properties closer to pure SiO_2 based zeolites, became a recognized family of microporous molecular sieves in 1982.[12] AlPOs show a great variety of structures and find different application, even the structural possibilities are limited compared with aluminosilicate. It must be noted that the Löwenstein's rule in AlPOs is valid for both Al-O-Al and P-O-P bonds, limiting the possible combination, as the formation of 5 T rings (for this reason, for example the AlPO analogous of MFI is forbidden). Several elements can be incorporated in the AlPO frameworks selectively substituting Al or P or both the tetrahedral centres. In comparison with aluminosilicate zeolites, the incorporation possibilities offered by zeotypes are also expanded to elements that usually do not admit tetrahedral coordination, however this limits the number of possible structures among all the known zeolitic frameworks. The reason for this higher tolerability for isomorphous substitution is traced in the larger spatial accommodation offered by T-O-T linkage in AlPOs and in the more ionic character of the network-bonding (better described as Al^{3+} and PO_4^{3-}) in comparison with aluminosilicates, allowing tetrahedral inclusion of otherwise forbidden elements.[13,14]

The possible substitutions are differentiated in:

Substitution type I: when Al^{3+} is replaced by isovalent cations (3+) inducing charge neutrality or divalent cations (2+) that bring a negative charge.

Substitution type II: P^{5+} can be substituted by isovalent cations (5+) or by tetravalent cations (4+), which again confers to the framework negative charge.

The insertion of silicon cation (Si^{4+}) in AlPOs framework induces a charge imbalance, resulting in net negative charge, which needs to be compensated by extra-framework cations for reaching the neutrality. This case represents a very important materials family, denoted as silicoaluminophospates or SAPOs, which properties are closer to aluminosilicates. The other family of great importance is the one represented by bivalent metal substituted AlPOs, often defined MAPOs that combines framework charge imbalance with the metal properties of the heteroatom, particularly enhanced when M^{2+} is a transition metal. It must be added also the combination of the two cases, to form the so called MAPSOs (metal-aluminosilicophosphates).[15]

Coming back to Eq. 1, it is of extreme importance defining the nature of the A^{m+} cation. When a negative framework is formed for the reasons described above, an extra-framework positive species is needed for reaching the charge neutrality. This cooperation between framework and extra-framework is the second distinctive aspect of the zeolite structure, after shape selectivity, which allows zeotypes to be fully included in the large class of zeolites. The reactivity of zeolites is linked to the extra-framework species, since the ionic pair formed between negative and positive charge represents the active site. The only case in which the active site is different from this, is when a neutral structure contains a transition metal in isomorphic substitution, for which the reactivity depends on that of the metal itself. The cases are mainly distinguished into:

- *A* is **hydrogen**, the extraframework species is H^+ and the zeolite assumes an acidic character (protonic zeolites).
- *A* is an **alkaline or alkaline earth metal** (M^+ or M^{2+}), in this case the zeolite assumes basic character.
- A is a **transition metal** (M^{n+}), generally presenting redox properties.

The extra-framework cations are easily exchangeable. Apart of the specific reactivity deriving from the nature of cation A, which will be discussed in detail, the zeolites can act also as ion exchangers, thanks to the high ionic character of the couple framework- extra-framework species.

1.1.1. Materials related to this work

1.1.1.1. The MFI framework

The MFI framework entered the zeolite world with the synthesis of the ZSM-5 in 1965 (Zeolite Socony Mobil – five), patented in 1972 by the Mobyl Oil company.[16] The ZSM-5 is an aluminosilicate, stable in a wide range of Si/Al ratios, from about 15 to infinite. This zeolite immediately aroused enormous interest because it presented exceptional properties in hydrocarbons conversion. It is one of the first synthetic productions and it revolutionized the zeolites synthesis providing a new method based on the use of ammonium organic salts as structure directing agents (tetrapropyl ammonium TPA^+), that successively multiplied the number of feasible structures. In the following years, many other applications of ZSM-5 have been identified, which is already finding industrial use since the 1980s. Notable among these is the process of producing olefins from methanol (MTO), which continues to be attractive as it offers a clean resource for the production of high valuable chemicals. The reasons why ZSM-5 has always been prominent in the world of zeolites are many. This material has very high chemical and thermal stability, it is synthesized easily and with low-cost precursors, it can present a Si/Al ranging over a wide and in its protonic form it presents an acid strength comparable to that of concentrated inorganic acids. Furthermore, it has a shape selectivity that makes it a versatile catalyst towards the obtainment of many useful products. In order to better understand these last aspects, it is necessary to describe in detail the framework of ZSM-5, which also unites other zeolites with a different composition from their progenitor. This family of zeolites has been assigned the code MFI within the IZA structure database already in 1978.[9] In the course of its history other particularly noteworthy examples have been added, such as Silicalite-1, the purely siliceous neutral polymorph of ZSM-5, discovered in 1978,[17] and Titanium

Silicalite-1 in 1983,[18] which has a percentage of Ti(IV) cations in the totally siliceous framework.

The MFI framework model can be built by connecting five T atoms, forming a pentagon. Eight pentagons sharing corners in D_{2d} symmetry, form the so-called *pentasil units,* which correspond to the CBU that MFI shares with other frameworks as MEL and MOR. In the MFI, the units are assembled by edges to form pentasil chains that grows along the c-axis. The linkage of neighbor chains form sheets on the b-c plane. The assembly of sheets by mirror planes creates 4 and 6 membered rings and give rise to the tridimensional framework creating a system of two dimensional 10-member-rings (10-MR) channels: one sinusoidal along the *a*-axis that is interconnected with the one 10-MR straight channel that runs along the *b*-axis. The pore opening of the MFI results in 0.55 nm of diameter in both directions, enclosed by 5 pentasil units.[19]

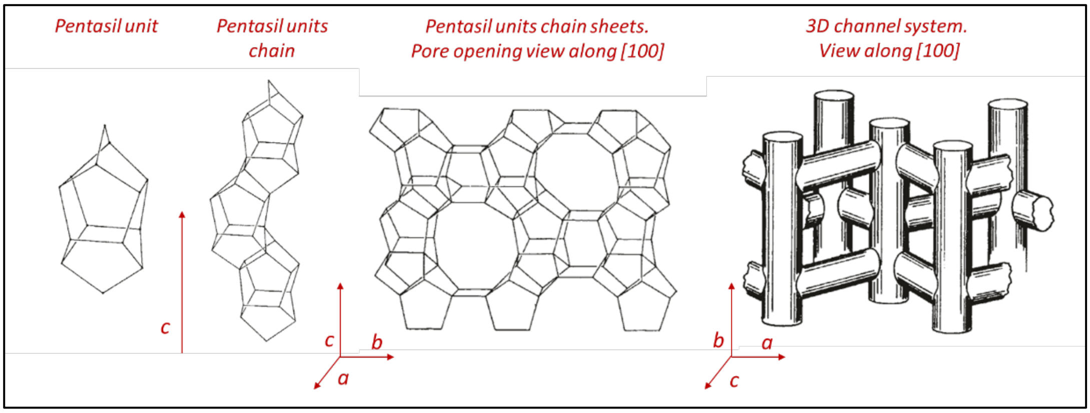

Figure 1. 3. Structural elements and channel system of MFI framework.

The MFI framework crystallizes around the structure directing agent TPA^+ in orthorhombic symmetry with space group Pnma. After calcination is common to observe a phase transition of the empty framework towards the monoclinic symmetry with space group $P2_1/n11$.[20]

1.1.1.2. The AEI framework

The reference material for the AEI framework is the aluminiumphosphate AlPO-18, synthetized for the first time in 1982, while the structure has been determined in 1991, accepted in the IZA database in 1992.[21] The AEI materials are synthetized by hydrothermal synthesis starting from Al_2O_3 and H_3PO_4 in presence of N,N diisopropylethylamine at 150°-180°C in 3-10 days. The structure of AlPO-18 is particularly prone to the isomorphous substitution of framework Al^{3+} by various heteroatoms. SAPO-18,[22] the silicon containing analogous has been synthetized in 1994 suddenly followed by a series of divalent metal containing AlPO-18 denoted as MAPO-18 in which M = Mg^{2+}, Zn^{2+}, Co^{2+}.[23] These materials will be the object of Chapters 7,8 and 9. The isomorphous aluminosilicate has been obtained later, in 2000 and denominated SSZ-39.[24] SAPO-18 and MAPO-18 present strong Brønsted acidity that allow their successfully employing in the catalysed reaction of methanol conversion to light olefins (MTO). The arrangement of AlPO-18 is structurally related with the one of SAPO-34 (Si containing AlPO-34, CHA framework), one of the most diffuse materials for the industrial application of the MTO. The two structures present the same CBU defined *d6r* connected by a 4atoms ring SBU (s4r) to form the frameworks. While in AlPO-34 d6r are all aligned (in a sequence AAA) in AlPO-18 the d6r layers are tilted (ABA) forming a cage containing six 8 MR and twelve 4MR. The d6r are connected forming chains growing along the *c*-axis, a tridimentional pore system is formed with diameter 0.38 nm in all direction, the 8 MR openings of slight elliptical section running along the b-axis are highlighted in Figure 1.4.

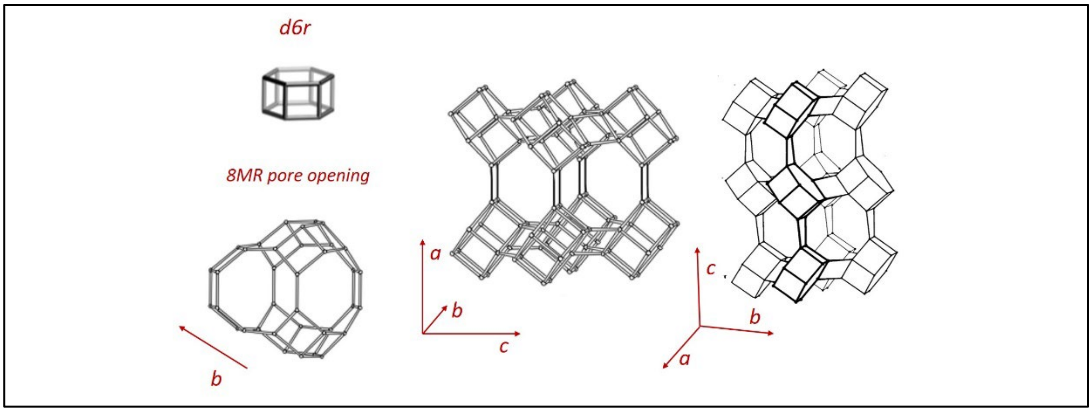

Figure 1. 4. Structural elements and schematized channel system of AEI framework.

Due to the pore dimension, AEI is classified as small pore zeolite. The lattice is formed by strictly alternation of AlO_4 and PO_4 tetrahedra and belong to the spatial group Cmcm, with orthorhombic cell.

Among all the members of the AEI family, particularly interesting is the case of Cobalt containing AlPO-18, because it represents a peculiar case in the zeolitic world, since the transition metal can be oxidized from Co(II) to Co(III). This induce the presence of different possible active sites. The isomorphous substitution of Al(III) by little percentage of Co(II), bringing to a charge imbalance, compensated by the presence of exchangeable protons, confers to the material a strong Brønsted acidic site. This is ensured as long as the heterometal presents the same tetrahedral coordination of the aluminophosphate structural units. When Co is oxidized to Co(III), the charge neutrality is stabilised, and the material does not present any Brønsted acidic character. Compared to other AlPO frameworks, CoAPO-18 is particularly prone to easily change oxidation state while maintaining a stable porous structure.[25]

The different oxidation state of the cobalt can confer completely different chemical behaviour to the zeotype. Upon calcination (removal of the templating agent by combustion), the acidic form of the catalyst is generated through strongly reducing treatments (high temperature in presence of pure H_2) that would induce the stabilization of the framework Co(II) state responsible for the presence of the Brønsted site. The catalyst in this form, is generally applicated in acid-catalysed reactions, such as the production of light hydrocarbons from methanol.[26] In the absence of a subsequent reductive treatment, the oxidative conditions of the calcination can favour the presence of Co(III). In this case the zeotype finds application as an oxidation catalyst in reactions such as oxyfunctionalization of alkanes, epoxidation of alkenes or Baeyer-Villiger oxidations of ketones.[27,28]

The spectroscopical characterization of this material, with particular attention to the changes in the metal oxidation state, will be the object of Chapter 8, while its application in the MTO reaction will be discussed in Chapter 9.

1.2. The zeolitic active sites

The active site of heterogeneous (solid) catalyst is generally represented by structural defects, which represent point of higher entropy, maximizing the free energy when involved in a reaction. Zeolites do not subtract of this. For neutral zeolitic forms as Silicalite-1 or AlPOs the difectivity and therefore the active species, is represented by OH^- groups that constitute chain breakers. The covalent framework can be seen as a polymer constituted by the ideally infinite repetition of SiO_2 (or $AlPO_4$), which is interrupted when the terminates with a OH^- group. These groups are exposed to the surface and are Si-OH, Al-OH, P-OH. They are mainly involved in weak interaction (as hydrogen bonding) with possible substrate and have an important role in adsorption, moreover they present a week acidity which is employed in some acid catalysed reaction (as Beckman rearrangement, for Silicalite-1).[29]

The isomorphous substitution is, strictly defining, a point defect. To it mainly derives the enormous variability of the zeolites reactivity. When the substitution induces a charge imbalance, the reactivity is mainly related with the nature of the counterbalancing species, as previously described. If the substitution brings to charge neutrality the reactivity depends on the nature of the heteroatom itself that can present Lewis acidity, extra coordination beyond tetrahedral or redox properties.

1.2.1. Protonic zeolites

When the framework negative charge of aluminosilicates (or SAPO and MAPOs) is compensated by a proton, the involved OH site constitutes a strong Brønsted acidic site, bridged between vicinal Al and Si atoms. The general structure is

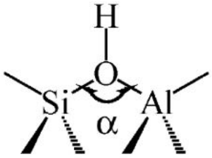

In zeolites, the Si–O and Al–O distances and the α angle are the most important structural parameters influencing the bridge structure of the Brønsted sites and therefore the acidity of the OH groups present in micropores.[30] The presence of the site can be guaranteed only by the perfect tetrahedral coordination of the framework atoms. Zeolites presenting Brønsted sites have acidic strength comparable to concentred inorganic acids and find several industrial applications.[31] One of the most relevant is the methanol to hydrocarbons (MTH) conversion, which is discussed below.

1.2.1.1. Catalytic application of protonic zeolites: the MTH conversion

The processes of methanol conversion into different valuable hydrocarbons (MTH, specifically: to olefins MTO, to gasoline MTG, to aromatics MTA) catalysed by zeolitic materials has been of high industrial relevance since the 1970s[32] and it is gaining even more importance in the context of sustainable processes no longer dependent on fossil fuels. Indeed, the reaction can exploit methanol of non-extractive carbon, generated by renewable sources (as from the CO_2 hydrogenation), and it is conducted at relatively mild pressure and temperature conditions (1,5-5 bar; 350°-500°C).[33] The catalyst in this process plays a key role,[34] since the topology of the zeolite affects the selectivity of the products and the catalyst lifetime, while its acidity determines the activity and the yield together with the operating conditions.[35–37] Although the engineering of zeolite catalysts for the MTO is in constant development, two frameworks are routinely used in industrial processes allowing to push the reaction to the two opposite extremes of the so-called dual-cycle mechanism driving the methanol conversion.[38] The H-ZSM-5 (MFI framework, 3D 10MR zeolite) operates at temperature around 500°C and promotes the formation of propylene from the alkene cycle, while H-SAPO-34 (CHA framework 3D 12-8MR zeotype) is selective for C2-C4 olefins at 350-400°C passing through the arene cycle. The dual cycle mechanism is schematised in Figure 1.5.

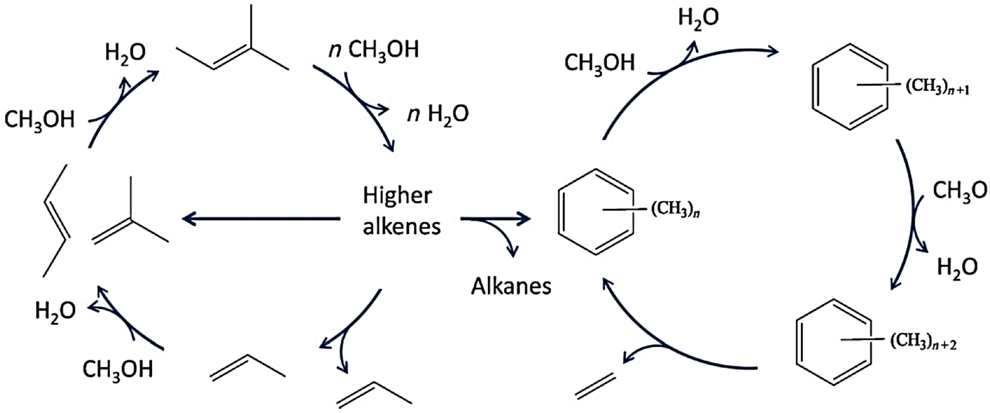

Figure 1. 5. Dual cycle mechanism of the HCP formation in the MTO conversion catalysed by acidic zeolites. Alkene cycle is on the left, while arene cycle is on the right.

Despite the long history of this industrial process, some aspects of the chemistry of MTH remain unresolved and continue to attract great interest in the academic world.[37] The nature and the evolution of the hydrocarbons within the catalyst pore system, the species and the mechanism involved in the first C-C bond formation, the role of zeolite Lewis acidity in catalysing the MTH reactions still generate a large debate.

The overall MTH process, summarized in Figure 1.6 , involves a complex interplay of different events that includes alkylation-dealkylation reactions within the zeolites cavities that act as H-transfers by their acidic functionalities.[33] In case of

MTO, light olefins can be finally released after intermediates methylations or cracking following the dual-cycle process. The steady state of the reaction is widely accepted and defined as “hydrocarbon pool” (HCP) mechanism, during which long hydrocarbons and coke like species are continuously forming.[39] It is attested that the reaction involves an induction period and then proceeds very quickly in an autocatalytic manner, as the forming intermediates themselves push to the proceeding of the reaction and the release of the products. This observation lends great support to the HCP theory according to which the intermediates are methylated cyclic carbocations that are constantly growing and being transformed by the zeolite catalyst (via protonations, alkylations and cracking) whose pore system determine their size and nature during the reaction steady state.[40] The autocatalytic growth of aromatic system representing the HCP species determines at the same time the deactivation of the catalyst by pore obstruction.[37] Therefore, knowing the species involved and their formation not only explains the chemistry of the reaction process but also that of catalyst deactivation, and is therefore of great importance in practical applications. Although these species are not completely listed, there is a wide range of experimental evidence that has outlined their nature.[41–43] However, the induction period is undoubtedly also linked to the formation of the first C-C bond, whose mechanism is the source of an intense debate.[44] The hypothesis of a direct coupling of C_1 species induced by impurities in the precursors, although long supported, is now strongly refused because energetically disadvantaged.[45,46] Nowadays more than 20 different mechanisms have been proposed, because of the lack of unambiguous experimental evidence due to the poor concentration of the intermediates and the velocity of the transformations. Only very recently the direct C-C bond formation has been outlined passing through a methoxide intermediate over the zeolite surface ($ZeOCH_3$), upon adsorption on the BAS.[33]

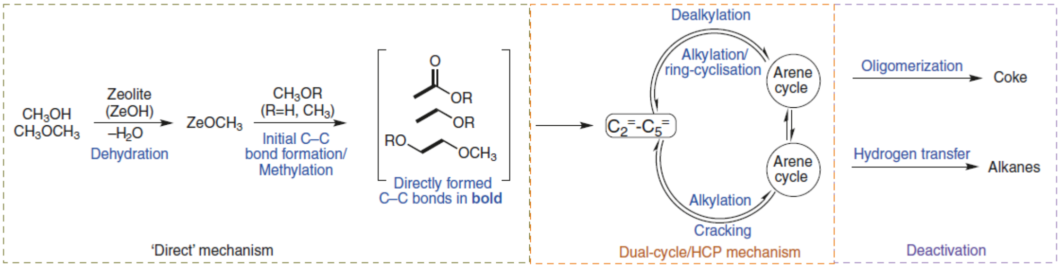

Figure 1. 6. General mechanisms of the overall MTH process as accepted by the most recent literature. Image taken from Ref.[33]*.*

It is well established that during any hydrocarbon conversion process at high temperatures, the methoxide groups on the zeolite surface are able to establish new C-C bonds. What is still debated is the exact nature of the coupling process, the intermediates involved and what the actual mechanism is. Among the most recent mechanisms proposed, with a certain experimental support, those based on carbene,[47] methyleneoxy intermediates,[48] direct coupling of methane-formaldehyde[49] and the catalysis by Lewis acid represented by extraframework species[50] must be counted, even if they are limited by calculated activation energy barriers. These mechanisms are excellently summarized by Li et al. in 2021.[44]

In 2016, the group of Lercher[51] proposed the initiation of C-C bond formation via **Koch carbonylation** of methoxide species ($ZeOCH_3$) by CO generated in situ from methanol degradation at process conditions, identifying the methyl acetate as first C-C containing molecule. The reaction, summarised in Scheme 1, involves the coupling of the electrophilic C atom of MeOH (or its derivates as -OCH3, DME and formaldehyde) with the nucleophilic C atom of CO molecule, giving at the same time a reasonable explanation of the C-C formation and for the autocatalytic pathway for the MTH proceeding. The group performed the reaction over a H-ZSM-5 at 450°C recording an increasing of olefins production cofeeding the methanol source with CO, which was previously detected among the methanol degradation product in the same conditions. Moreover, the hypothesis is supported by an extremely low calculated activation energy (80 kJ/mol) and by the spectroscopic observation of carbonyl intermediates at the very early stages of reaction also by other groups. In parallel, Weckhuysen and co-workers provided evidences of the Koch carbonylation occurring over the H-SAPO-34, individuating methanol and formaldehyde as subsequent carbonylating agents for the acetate species produced by CO and surface $ZeOC_3$.[52–54] This aspect will be deepened in Chapter 9.

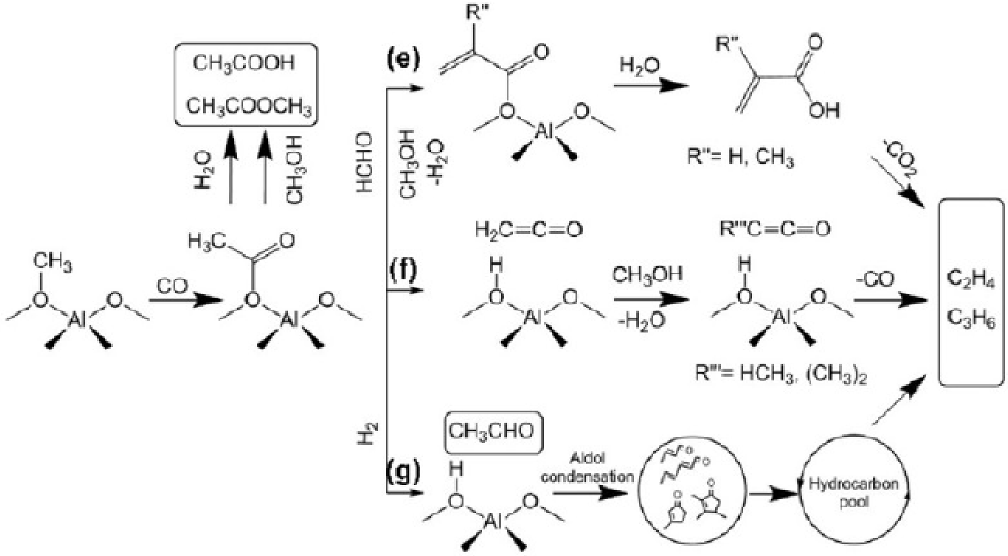

Scheme 1. 1. Koch carbonylation mechanism involving zeolites -OCH_3 groups and CO. The e, f, g options show different literature proposals of the subsequent steps of the reaction.

1.2.2. Heterometals containing zeolites: the TS-1 case

Among all the zeolites containing metals in isomorphic substitution, the Titanium Silicalite-1 (cited in Section 1.1.1.1) deserves a special description, due to its large application as partial oxidation reactions catalyst and to the complexity of its active sites. It is attested that the proper incorporation of Ti(IV) in the Silicalite-1 framework (MFI) tolerates a maximum Ti content of 2.5% expressed as TiO_2/SiO_2 ratio.[18] This is due to the tetrahedral coordination of the framework in which Ti(IV) is forced, which is energetically disfavored by the crystalline field compared to the octahedral one found in the stable TiO_2. For this reason, Ti(IV) can be easily found in TS-1 zeolites as partially extra framework species presenting expanded coordination toward the more stable octahedral geometry. When this is stabilized, segregated TiO_2 phase can form during the zeolite synthesis. Partially distorted species and TiO_2 extra-phase represent defective sites of TS-1 and are considered inactive in catalytic partial oxidation. Therefore the synthesis of perfect TS-1 involve particular attention to the correct insertion of tetrahedral Ti(IV). Long term debate about the nature of the TS-1 active sites and their behavior during the catalytic reaction, characterize the history of this zeolite.[55] It is now established that the activity of the tetrahedral sites resides in the tendence of framework Ti(IV) species to expand their coordination sphere upon interaction with adsorbates. When strong ligands, such as water or ammonia, interact with the dehydrated TS-1, they are able to affect the electronic transitions of Ti sites. Spectroscopic evidences explained this mechanism. When Ti is coordinated by strong ligands, TS-1 exhibits the LMCT electronic transition induced by six atoms coordination, as in the case of TiO_2 polymorphs. This absorption is found at higher wavelength with respect to the perfect tetrahedral Ti(IV) centres in an activated TS-1 (200 nm). The latter represent the most important feature for recognising a perfectly crystallised TS-1 with atomically isolated, proper active sites.[56]

1.2.2.1. Application of Titanium containing zeolites: Hydrogen Peroxide to Propylene Oxide (HPPO) reaction

TS-1 is an interesting selective catalyst in low temperature partial oxidation reactions, with aqueous H_2O_2 as the oxidant agent. Propylene oxide (PO) is an important raw material, which is extensively applied in chemical and petrochemical industries. It can be produced by direct epoxidation of propylene by action of H_2O_2 in the catalyzed process HPPO. The unique oxidation properties of TS-1 enabled the liquid-phase epoxidation of propylene and hydrogen peroxide to propylene oxide process (HPPO). Using TS-1 as a catalyst makes possible the reaction to be carried out under mild conditions (usually not exceeding 70°C) using low concentration aqueous H_2O_2 solution (10 % wt) as oxidant. The HPPO process follows a one-step reaction where propylene oxide is obtained directly from propylene, as in Scheme 1.1

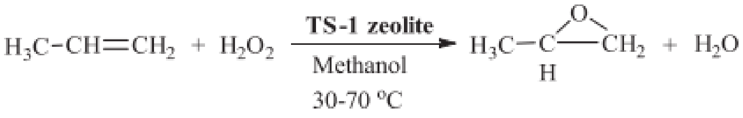

Scheme 1. 2. Reaction schematization of HPPO process catalysed by TS-1.

The catalytic mechanism involving the perfectly tetrahedral sites of TS-1 has long been debated. Spectroscopic evidence has finally demonstrated the equilibrium between the species reported in Scheme 1.2. that present a significant colour change.[57] Ti(VI) coordinates H_2O_2 in water solution forming a hexacoordinated peroxo-complex, after dehydration a hydroperoxo-complex is formed, which is the active oxygen donor species. The water content is the key factor in the TS-1 activity.[56]

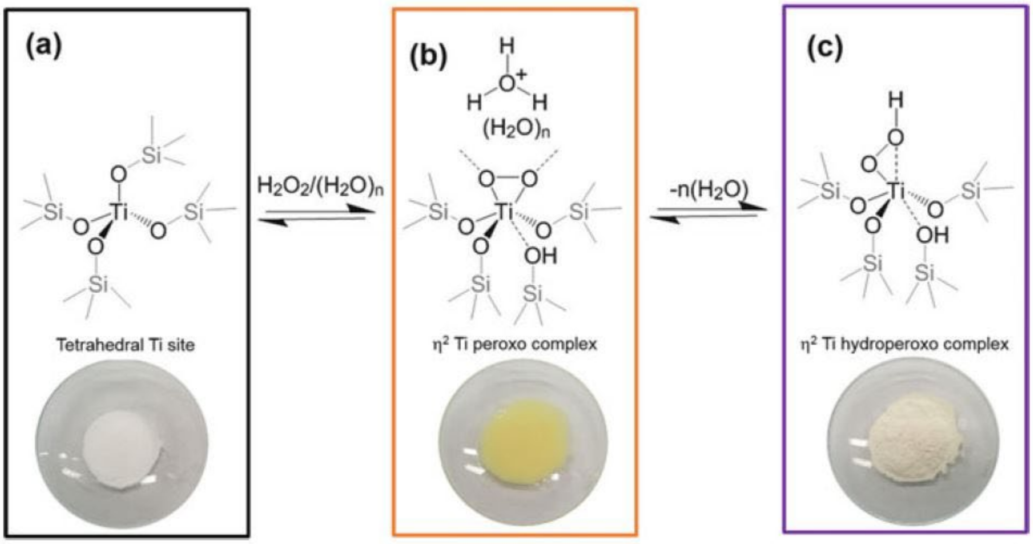

Scheme 2. 1. Images taken from reference [57]*. Schematic representation of Ti(I)V framework species (a), formation of "side-on" Ti-peroxo complexes in* H_2O_2/H_2O *solution (b) and "side-on" and "end-on" Ti-hydroperoxo complexes upon dehydration (c). The images in the bottom refer to the typical colour changings.*

1.3. The synthesis of zeolites

In general, the synthesis of zeolites results in a methodology that relies heavily on a trial-and-error approach. This is a consequence of the incomplete understanding of the formation processes and the great number of variables involved in the process. However, the fundamental principles can be outlined and the accuracy of synthetic methodologies continuously improves, as more knowledge of the process is gained.

The synthesis of zeolites is generally structured in two main steps, one of sol-gel formation during which the elemental precursors are combined and the first bond are formed and one of hydrothermal treatment under autogenous pressure (> 20bar) during which the crystal structure is stabilized. The chemistry behind the formation of aluminosilicates and aluminophosphates is very different, especially in the early steps, for which the first are formed mostly in alkaline medium, while low to neutral pH values are ideal for aluminophosphate synthesis.[13] In this dissertation, only the synthesis of aluminosilicate zeolites will be examined.

The starting requirement [58] for the preparation of the precursors gel is composed by:

- The sources of the tetrahedral atoms: for silicon, solid silica (fumed, precipitated or colloidal) or tetralkylorthosilicate (commonly TEOS, tetraethyorthosilicate) can be used. For aluminium generally sodium aluminate, aluminium solfate or akoxide as aluminium isopropoxide are selected, depending on the target material. In case of heteroatoms insertion, the choice of the precursor is very wide, for Titanium tetraethylorthotitanate, titanium tetrabutoxide or halides as $TiCl_4$ and TiF_4 are the most useful choices.
- The source of a mineralizing agent: in alkali media, the mineralizing agent is OH^-, deriving from alkali hydroxide (NaOH, KOH), sodium aluminate and

hydroxide salts of organic structure directing agents. In fluoride mediated synthesis the mineralizing agent is F^-.

- The structure directing agent: SDA are usually cationic species, with single or multiple charges, able to direct the assembly of the negatively charged framework toward a specific zeolitic structure. Moreover, often the source of the SDA is a hydroxide salt, that releases OH^- anions, rising the synthesis pH and helping the zeolite crystallization. SDA can be inorganic, as alkaline and alkaline earth metals cations, or organic, the most applied quaternary ammonium salts or quaternarized amines. The introduction of organic SDA historically, allowed the increasing of the number of zeolitic frameworks with different chemical compositions. Many of these topologies do not have a natural counterpart, as the significant example of the synthesis of the MFI by action of TPA^+. Organic SDA molecules can act in different ways for influencing the structural properties of the forming zeolite. Some molecules are designed for leading the assembling framework to adopt a specific geometric and electronic configuration, these very often are supramolecular arrays of surfactants. In other cases, the SDA function is more strictly “structuring”, inducing the formation of a specific topology, opposite in respect with the case of species that act as pore-fillers and are therefore not specific for a topology. It is also important to consider that a given molecule can drive the formation of different materials depending on the synthesis conditions and compositions of the reaction mixtures. The role of structure directing agents will be deepened further on, when hierarchical zeolites will be described, where often SDAs play a fundamental role.
- The solvent: it is usually water. The water content has enormous influence in the zeolite synthesis. It is needed for hydrolysing the precursors and form the

starting gel; then water molecules act as space filler, helping the porous structure formation and directly influencing the zeolite stoichiometry.

Several parameters influence the synthesis trend both regarding the composition (as the nature of the precursors, the relative concentrations and the water content) or the process conditions as the residence time in the different steps, which can vary from hours to days and also the temperature, ranging from 30°C to 200°C. Very often an intermediate step of gel aging is added before crystallization, with a great degree of variation in time and temperature.

The zeolite formation, which is based on a nucleation and growth process can be described in consecutive steps, however considering that exist an enormous variability for different framework and process condition.[59–63]

1. The precursors are dispersed in aqueous alkaline media, where the silica and alumina undergo dissolution. A mixture is formed in which partially reacted species, precipitated from starting materials destabilised by the change in pH (with a high variability of structure precipitated amorphous aluminosilicates, coagulated silica and alumina or unchanged reactants) are present, already influencing the crystal structure. Generally, this is defined as *primary amorphous phase,* which is a non-equilibrium condition. When the synthesis is conducted in colloidal conditions, more defined entities are present in the media.
2. The gel mixture is kept in quiescent conditions for aging, heating at reaction temperature. During this time, the elemental oligomers start to establish connection and larger structures can form.
3. The oligomers that form the solid part of the sol-gel are generally constituted by short chain oxide species of the nutrients Si and Al, surrounded by OH^-, these undergo continuous polymerizations/depolymerisations catalysed by the mineralizing agents. At high Si/Al ratios, the chains are generally longer, since

silica oligomers are favoured (this aspect will be deepened in the description of Silicalite-1 synthesis by clear solution). The remaining part of the sol-gel generally long remains as colloidal solution. For this reason, the zeolites growth is believed to be an heterogenous nucleation process involving both primary (self-production) a secondary nucleation (crystal-catalysed nucleation, that starts when the fist domains are formed). With the aggregation of the first short species (proto-nuclei), a pseudo-equilibrium between the solid and the solution phases is reached, representing the *secondary amorphous phase*. In this stage some short-range order is assumed by action of the structure directing agents.

4. Stable crystal nuclei are formed and the crystallization proceeds by the integration of oligomers from solution and their assembly with the right connectivity toward a specific crystal, until the total consume of the amorphous phase. This is a characterizing feature of the zeolites formation, for which it is believed that the evolution of the amorphous phase pass through the formation of discrete nuclei that evolves in ordered crystals by Ostwald ripening regime, i.e. by the consumption of the smaller nuclei for favouring the growth of the ones that reach the critical radius.

The crystallization can be also promoted by the insertion in the gel mixture of seed crystals. This practice gives the advantages to reduce the synthesis time and moreover to lead the synthesis towards a desired phase (zeolitic framework) in a precise way, by inducing the crystallization of the amorphous gel over the surface of the seeds (secondary nucleation). This avoids the necessity of the gel to self-generate stable nuclei by primary nucleation, facilitating the overall process.

Understanding the exact phenomena involved in the formation of zeolites is a very challenging task, even because it is complicated by the fact that zeolites crystallization occurs in sealed systems as the autoclaves for the hydrothermal treatments.

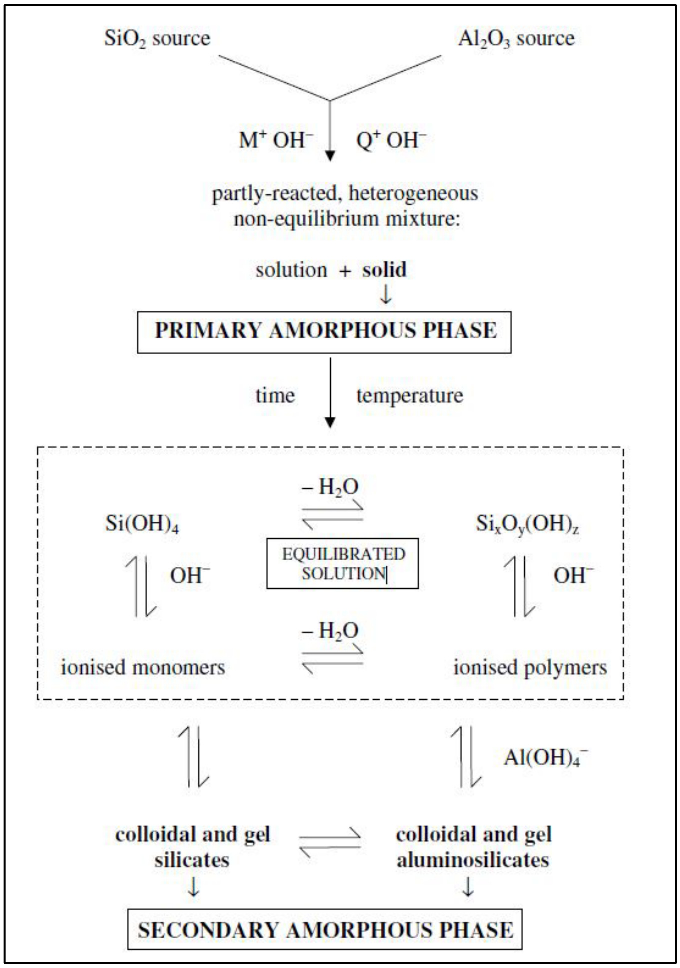

Figure 1. 7. General schematisation of the main phases involved in the zeolites synthesis. Taken from Ref. 62

1.4. Beyond microporosity: Hierarchical Zeolites

Hierarchy defines the concept of subordination between entities that represent the interdependent levels of a gradual and uninterrupted variation scale. The relation of hierarchy supplies characteristics and properties that can be expressed only considering the entire set and not the single components, even if these are self-consistent entities. The term was coined in ancient Greece to define the command and social roles covered by citizens, but the same type of organization can be easily oserved in the structural organization of many natural systems. This is because the subdivision of roles in increasingly specialized units is functional to the performance of many natural activities, as in the case of the root ramification of plants or the circulatory system of mammals, which by adopting hierarchically organized dimensions are able to distribute their inner flow from a single source to the most peripheral and distant areas. This type of organization has inevitably inspired the production of artificial materials, that must fulfil two main aspects: the constituting elements are distributed in more than one length scale, while they have independent but complementary roles. This is the case of the so-called hierarchical zeolites.[64,65] In the case of zeolites, the hierarchy concept is applied to the organization of the porous system, which is structured on different dimensional levels, gradually varied and interconnected. In other words, the most modern synthesis of zeolites has developed methods for creating additional levels of porosity, beyond the microporous one represented by the framework channels. The interconnected web of different pore sized channels modifies the catalytic behaviour of the system, offering new size-shape selectivity and mass transport pathways. This last point is the driving force for the constantly growing interest toward hierarchically structured zeolites, which are the most promising materials when dealing with bulky substrates or reactions that induces easy deactivation of the micro-zeolites. The engineering of zeolites strictly depends on their possible application. In general, traditional zeolites impose strong steric limitations on the substrates to be converted, with a cut-off of 1 nm imposed by the micro-sized dimensions of their channels. Molecules that exceed this size can interact only with the sites located on the external surface of the catalyst, which represent a minority fraction of the total amount. For the same spatial constrictions, the inner diffusion and the mass transport are limited, especially in transformation involving liquid substrates. Limitation in diffusion of the reactants can causes the confinement of the precursors that can evolve in undesired products, moreover it implies a not complete employing of the catalyst surface, resulting in a very low effectiveness factor $\eta = r_{\text{observed}}/r_{\text{intrinsic}}$ (where r is the transformation rate).[66] Even in the so called “large pores zeolites”(with more than 12MR), or zeolites presenting larger cages (as the 8-12MR frameworks), it is common to observe catalytic transformations describable as “ship in a bottle chemistry”: what is generated inside the catalyst is bigger than what had entered it, because it is the result of the assembly of smaller pieces able to diffuse in the microchannels. All these factors, not only limits the possible transformation in which the zeolites are applicable but also facilitates the catalyst deactivation by pore obstruction, especially in reactions involving carbon species that easily degenerate in coke. Different strategies are adopted to overcome these limitations. A general approach for increasing the catalyst lifetime implies the shortening of the diffusion path length. This has led to the well-established use of nanosized catalysts, so as to maximize the external surface area and limit the residence time within zeolites micropores. The nanosized catalysts can be produced by selectively suppressing one or more directions of growth, obtaining nanosheets reducing one dimension, fibres or nanoroads reducing two dimensions or nanocrystals when all the three dimensions are limited. The same result can be obtained by creating an additional level of porosity in the crystal structure and then with the production of proper hierarchical zeolites. Figure 1.8 graphically shows all this type of materials.

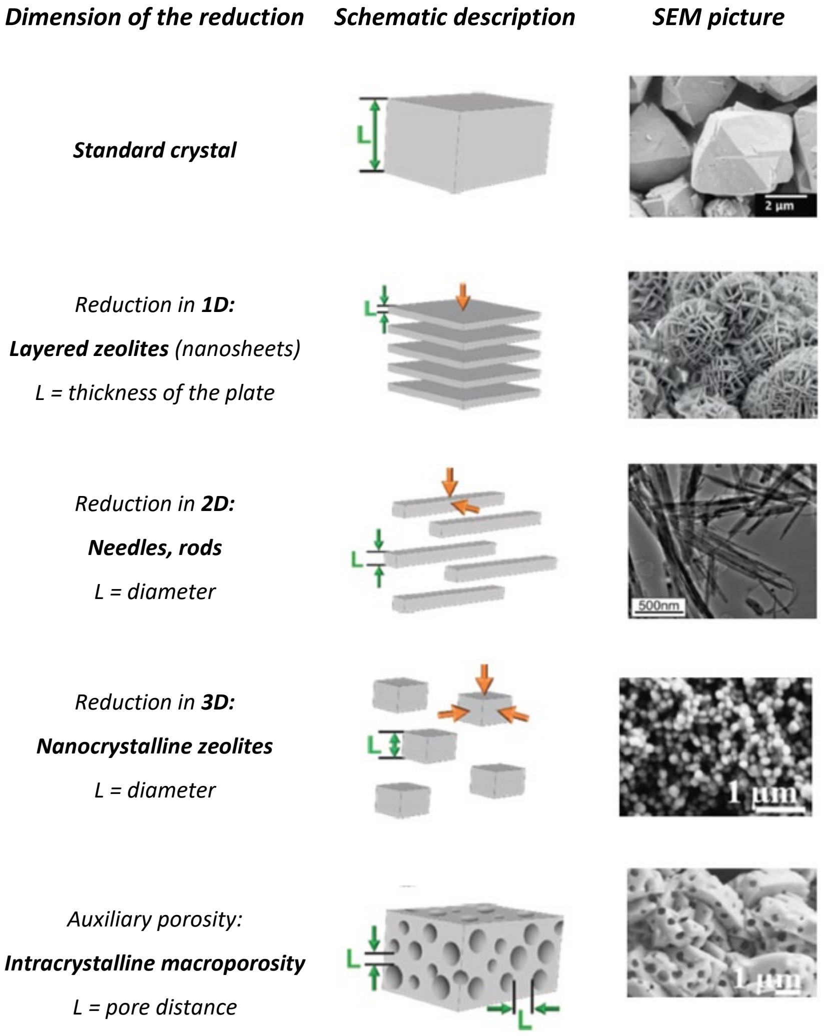

Figure 1. 8. Schematisation of nanomaterials modifications for shortening the inner mass transport path. Adapted from Ref. 67

The benefits offered by presence of multiple level of porosity are not limited in increasing the catalyst lifetime reducing its deactivation. A hierarchical structure is particularly attracting because it can offer new performances compared to its microporous counterpart, even if it is nanostructured. The reasons are multiple.[68] It reduces steric limitations both for the selection of reactants and products releasing. New active sites located in the mesoporous system, which generally greatly increases the specific surface area, allow the conversion of new, bulkier substrates. Thus, it is also possible to be in presence of two kind of active sites, one purely located on the mesopores surface and one at the intersection of micro-mesopores (at the micropore mouth) that confer different types of selectivity. By reducing the spatial constrictions, the diffusion rate is increased as the flow within the mesopores is faster and can reach a classical Knudsen regime. A different mass transport is observed in hierarchical materials with respect to a microporous zeolite.[69] Although selectivity may be thought to be reduced with the increasing of the pore diameter driving to a wider distribution of products, actually different new products can be achieved by the synergic action of the different levels, and also bulkier products can be selectively obtained.

Before deepening the important topic of the catalysis by exposing the cases in which hierarchical zeolites are applied, some structural information is to be provided.

The hierarchical structures have been firstly hypothesized during 1990s, in response to the need to broaden the application possibilities of zeolites by the introduction of mesoporosity. The efforts in obtaining it, opened up new scenarios in silicate synthesis, leading to the production of mesoporous silicas through opportune structure directing agents.[70] The latter materials present an ordered array of mesopores, with controllable size, shape and distribution and suddenly appeared revolutionary. They present extremely high accessible surface areas and can selectively host molecules or nanoparticles of relative high dimensions. Material as MCM-41[71] or SBA-15[72] are still of great interest and find good applications especially as catalysts/functionalization supports or as adsorbent materials. However, the amorphous nature of the walls of ordered silicas cannot give performances comparable to those of the crystalline structures of zeolites in terms of stability, controllable shape selectivity and specific structure of the active site. This led to the first definition of a hierarchical zeolite, the first examples of which were obtained in the early 2000s[73]. The first commercialized example has been a mesoporous containing ultra-stable zeolite Y (USY) produced by Zeolyst.[74] A hierarchical zeolite must in fact retain its bulk properties, maintaining the crystalline structure, which ensures the integrity of the active site and at the same time must provide accessibility pathways extended by the presence of the mesoporous system, which is then able to easily remove products.[75,76] There are many ways to categorize the hierarchical zeolites in order to describe their properties, because the definition groups a very heterogeneous variety of materials in a wide range of structural organization and often the term itself is used inappropriately. The materials can combine micro-/meso- pores or micro-/macro-pores or a mix of the three systems, strictly depending on the synthesis adopted for their production. These are all gathered by the presence of at least one additional porous system with respect to the microcrystalline one, but what is more important is the careful insertion of the porosity allowing the interplay and connection between the levels. This last point is what induces a real effect on the catalytic properties and distinguish a hierarchical system from a traditional zeolite. Therefore, the most rigorous method of defining a hierarchical structure is to evaluate how the catalysis is affected. On the other hand, a material presenting segregated regions with different pore sizes does not properly fall under the definition, since it can hardly influence the catalytic reaction. When mesoporosity is a structural part of the crystal, it is defined as intraparticle porosity, while the interparticle porosity, that intercut the zeolite crystals, involves the organization of the whole catalyst. In general, the principles of hierarchy can be satisfied by both these. Schwieger catalogued as *Hierarchy Type I* and *Hierarchy Type II* [65] the way in which the subdivision from meso-to-micro pores is organized, giving rise to a different mass transport inside the catalyst.

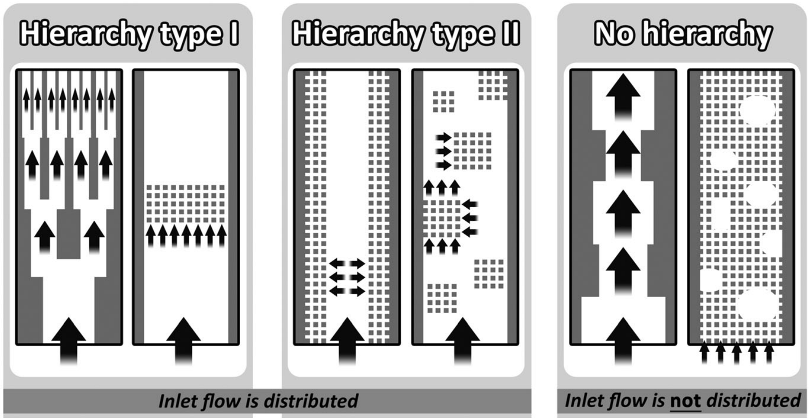

Figure 1. 9. Schematic representation of different hierarchical organizations of pores systems, in which the inner mass flow is represented by the black arrows. The figure is adapted from Ref. 65.

- *Hierarchy Type I* is a gradual subdivision from a larger pore into smaller ones.
- *Hierarchy Type II* is an interconnection in which the larger system alternates the smaller pores ore these represent the ramifications of the former.

To these, the “reverse hierarchy” must be added, indicating the cases in which the flow is collect by the smaller components toward the larger for a fast evacuation.

The way in which the hierarchical zeolite is shaped is strictly dependent by the strategy adopted for its synthesis, that generally involves the zeolitization of preformed mesoporous silicas, the selective aggregation of zeolite precursors, the preferential suppression of the crystal growth along one direction or post-synthesis treatments.[75] A general subdivision distinguishes intraparticle porous crystals from materials presenting interparticle porosity. The latter can regard both aggregates of nanosized crystals (as pillared or random staked nanosheets[77] or tridimentional ordered macroporous materials 3DOm[78]) or monoliths[79] (polycrystals condensed in forming a unique macroscopic body). Moreover, the hierarchical properties can be achieved also by creating composite materials, in which a binder or a scaffold co-works with the zeolite.[65,80] These categories are summarised in Figure 1.10.[67] It is important to underline that, while in proper "hierarchical zeolites" the hierarchy refers to the organization of the crystal structure itself, in case of aggregates of nanostructures, the hierarchy is more properly applied to the way in which the mass transport is forced to interact with the catalyst. The substrate will be first spread through the interparticle mesoporosity and then forced to enter in the zeolitic micropores where the active sites will be mainly located and in the same manner the product are rapidly released. This differentiation does not disagree with the material hierarchy provided by Schwieger.

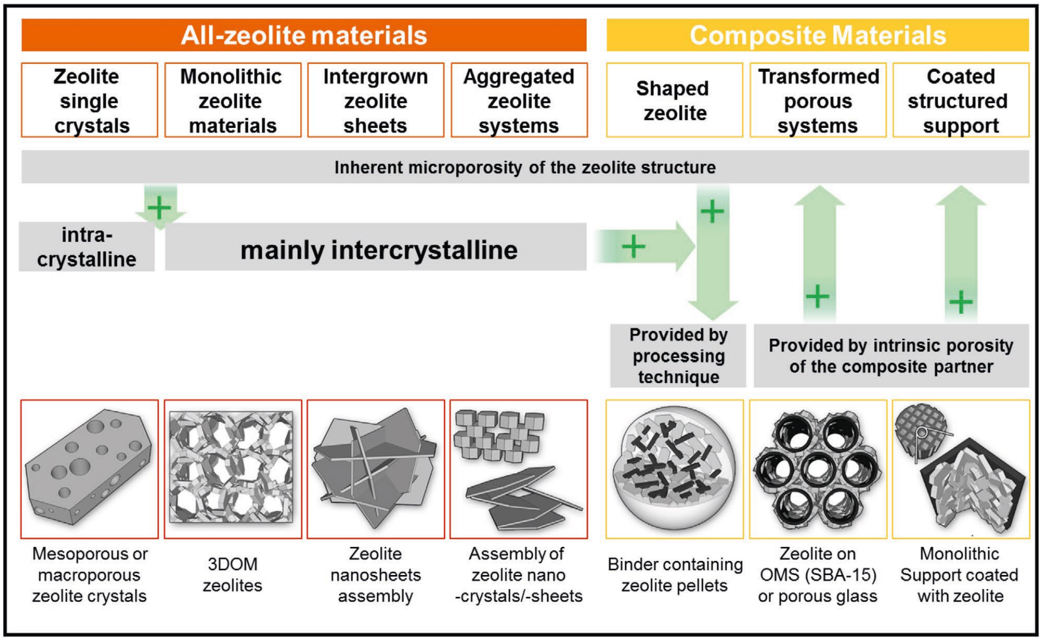

Figure 1. 10. Schematisation of the hierarchy variety applied to zeolitic materials. Taken from Ref. 67.

The developments in creating new structures for new applications must be driven toward the enhancement of the structure-properties relationship, which is the key point in the zeolites catalysis. Aiming to achieve hierarchically structured materials by sophisticated synthetic strategies, is important to guaranty characteristics which are proper of the zeolites, as crystallinity, pore connectivity, distribution of the active sites and thermal/chemical stability. For these reasons, the production must be coupled with a deep knowledge of the materials and their performances, for better understanding the role of the different porosity levels and tune their distribution. This implies different others factor that must be considered, as the determination of the effective mass transport in working conditions, the possibility of catalyst regeneration by subjecting it to consecutive process cycles and determine if the stability is compromised. In the next paragraphs the main aspect of the synthesis and characterization of hierarchically structured zeolites will be provided, with particular attention to these aspects.

The synthesis and the characterization of different hierarchical MFI will be the object of Chapters 3,4 and 5

1.4.1. Synthesis of hierarchical zeolites

The engineering of zeolites offers extensive possibilities for developing new and even more specialised transformation processes. Tailoring the structure-properties relationship is the essential requirement for obtaining target catalysts to be employed in specific applications. In the production of hierarchical systems, particular attention must be posed of course in the successful creation of a well organised porosity, with a certain regularity and accessibility. Moreover, from an out-of-lab scale point of view, it must be considered the employment of not hazardous, environmental friendly and not expensive reactives, to ensure that the final material has real application possibilities, according to the necessary criteria of sustainability and viability.[81]

Although, the scientific approach in obtaining designed porous materials in general, different from proper zeolites, has a relative brief history. It started at the end of 90s with more an empirical than a rationalized approach, based on trial-and-error variation of the synthetic parameters rather than in the understanding of the theoretical physical-chemical principles that lead to a controllable production of designed structures. The effective breakthrough in a controllable creation of designed porosity became with the application of specialized templating agents, firstly applied on materials different from silicates, such es porous oxides, coordination polymers and carbons.[82] This background must be considered in the evolution of the strategy that led to the modifications of zeolitic materials that nowadays can benefit from some well-defined strategies that have achieved a certain degree of controllability over the final material properties.

In the vast literature describing the formation processes of hierarchical zeolites, so many methodologies are presented, as that one of the biggest names in the field, Javier Pérez-Ramírez, entitled one of his editorials "Imagination has no limits"[83] to give a sense of the countless possibilities that lie in front of the synthesizer. There are therefore different ways of categorizing synthesis procedures, whether one looks at the operating methods or at the properties of the material produced. A general distinction in the methodologies is made by dividing into “top-down” or “bottom-up” approaches. The first case refers to the modification of preformed crystal structures in order to create adjunctive porosity, by partial destruction or recombination of the constituting elements, for this is also referred as “destructive approach”. The opposite strategy implies the “constructive” assembly of the constituting units to form the final hierarchical structure and it is opportunely named “bottom-up” approach when it starts from the elemental precursors.[84]

Taking in consideration the characteristics of the final material in which a different hierarchical organization is adopted as presented in paragraph 1.4, three main categories of synthetic strategies, can be defined. I) The formation of mesopores in preformed zeolitic large crystals, limiting the pore blocking and molecular trapping, is commonly obtained by partial destructive post-synthesis treatments, thus from a top-down approach. II) The creation of nanosized crystals presenting interparticle mesoporosity able to drive the mass transport in a hierarchical way, this class involves both not-aggregated nanoparticles (or nanosheets) or mesoporous monoliths formed by the aggregation of nanosized zeolitic domains. III) The bottom-up synthesis of hierarchically ordered micro-meso porous framework, thus proper “hierarchical zeolites”, requires the use of specialized (and often tailor-made) templating agents as SDA that drive the assembly of the growing silicate lattice starting from the elementary components. The SDA can be both molecular organic templates or supramolecular templates, giving origin to differently organized materials.

Some efforts in obtaining this type of structures have also been pointed to the zeolitization of the walls of ordered mesoporous silicas by hydrothermal treatment.[85] This represents an hybrid synthetic strategy which can be defined a combination of “bottom-up templated synthesis” in the formation of the mesoporous structured with the post-synthesis treatment in directing the subsequent zeolite lattice crystallization. The practice has been explored especially at the beginning of the hierarchical zeolites history, but it has resulted difficult to control, because the zeolite formation prevails destroying the mesoporous structure. Therefore, this synthesis method will not be pursued in further detail.

It has been chosen to present the different synthesis methods according to this subdivision in three classes distinguished by the type of hierarchy, since this aspect main affects the catalyst features. Moreover, it helps to better describe the materials that will be presented in the following chapters. Based on the classification provided above, the most relevant synthetic strategies are the following:

I) Post synthesis treatments:

The post-synthesis destructive techniques involve the selective removal of framework cations of a preformed zeolitic crystal (usually of microscopic size) to enlarge the void regions. It implies the use of high temperature steam and/or of drastic pH conditions (acidic or basic) for partially dissolving the structure by leaching in aqueous media or in gas phase. The post synthesis treatments are known since the beginning of the history of synthetic zeolites for improving some characteristics of the catalyst, as enhancing the stability and rising the concentration of acidic sites by modifying the Si/Al ratio.[2] In the last twenty years, with the growing interest for hierarchization of zeolites, these strategies have found a new application: if the procedure is well controlled and applied, it induces the creation of intraparticle mesoporosity. This technique is generally widely employed because it is a good compromise between effectiveness and ease. Moreover, it found an industrialization, which is harder in case of “bottom-up” productions.[81]

The *dealumination* (or demetallation in general) is the selective removal of framework Al by hydrolysis of the (Al)-O-Si bonds, which is usually operated by strong acidic leaching in aqueous media or combined by steaming, complexation with oxalic acid or replacement of Al by Si (usually by gas precursor).[86–88] The strong acidic treatment (usually HCl solutions) first produces the creation of silanol nests and a segregated polymeric gel of extra-framework alumina, which is then leached by subsequent washing. The practice is commonly adopted to produce high silicon zeolites when not possible from direct synthesis, as in the formation of USY (ultra-stable zeolite Y) from preformed FAU framework, which does not allow a Si/Al higher than 3. If the procedure is prolonged in time the extent of the defective zone increases, creating voids.[89] This methodology implies strong modifications of the material, with a variation in the Si/Al ratio that reduces the acidity of the material and often partial amorphization with the consequent decrease of the micropores volume. Moreover, it is attested that the adjunctive voids are created in the inner space of the catalyst, not accessible from the outer, thus an effective impact on the catalytic performances is not always recorded.[87] With the emerging of more sophisticated and efficient techniques, the practice of dealumination is progressively less applied. On the contrary, the alkaline treatments for the partial *desilication* of the framework are much more successful and represent one of the most adopted procedures for the hierarchization of zeolites. The basic hydrolysis of Si-O_4 bonds is more effective in creating mesoporosity because the silicon is more abundant than aluminium in framework and moreover the process is better controllable since the presence of Al can limit the propagation of the hydrolysis, avoiding the total collapse of the structure.[89] Trivalent cations as Al^{3+} (but also Fe^{3+}, Ga^{3+}, B^{3+}) are defined “pores directing agents” (PDA); since their bonds are not subjected to alkaline hydrolysis, their presence in the framework guides the extent of the desilication.[68] The hydrolysis is commonly performed by subjecting the zeolite to strong alkaline baths (at pH> 12) in solutions of inorganic hydroxides as NaOH, KOH, LiOH. The textural properties of the final material can be controlled by tuning the synthetic conditions, as treatment duration, temperature, type, and concentration of base, and solid/liquid ratio. In the easiest and most adopted procedure the zeolite is treated with a 0.2M solution of NaOH for 30 minutes at 65°C, considering a powder to solution ratio of 33 g/L.[68] The first attempt in obtaining mesoporosity by desilication from alkaline treatment has been performed in 2000 by Ogura et al. over a ZSM-5 (Figure 1.11).[90] The same group continued its study evaluating the effect of changing parameters as NaOH concentration or temperature and found that the alkaline treatment effect in a minor extent the aluminium bonds, also for prolonged time. Moreover, it has emerged that the concentration of BAS was univariate after the treatment, which produced instead a an increasing of the LAS. [91]

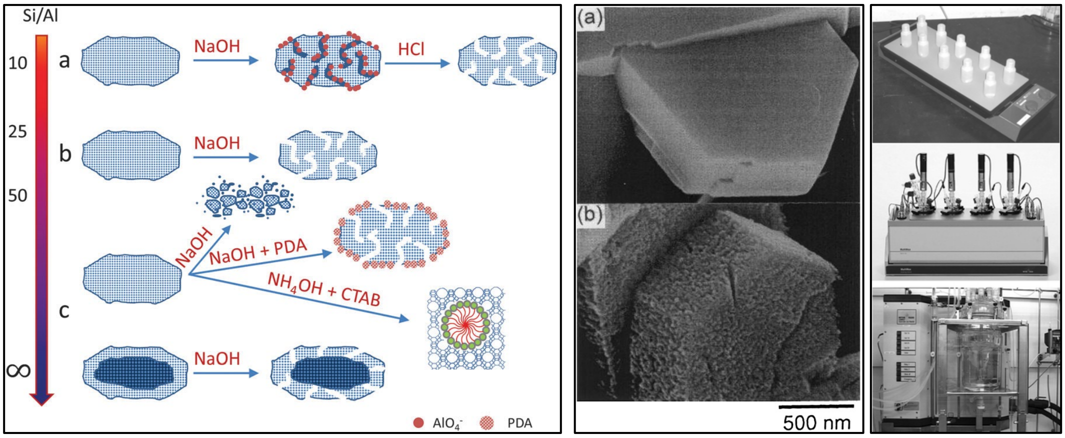

Figure 1. 11. Left panel: schematic representation of the effects of alkaline treatment in function of Si/Al ratio, image taken from Ref. 92*; Central panel: SEM images of ZSM-5 zeolite a) before and b) after alkaline treatment performed by Ogura et al. in Ref.* 90*; Right panel: scaling up representation of the desilication procedure over ZSM-5 zeolites published by Groen et al. in Ref.* 93

After these pioneering works, great interest has been directed to creating mesoporosity by desilication. Pérez-Ramìrez and coworkers outlined the first principles of general validity for the designed application of the method, identifying how the Si/Al of the parent zeolites affects the result of desilication. At low Si/Al (<25) the high aluminium content limits the hydrolysis, resulting in a low mesoporosity level; At intermediate Si/Al (25-50) the mesoporosity is generated in a good extent, while at high Si/Al (>50) the silica removal is excessive, leading to a partial destroying of the structure rather than to mesopores formation.[94] The practice is applied on a great variety of different frameworks, even if it finds the more successful applications on MFI (ZSM-5) because of the high stability of its Al sites. The contrary must be considered for BEA, for which the less stability of Al results in an excessive loss of silicon resulting in the worsening of the zeolite properties as crystallinity and micropores volume.[95] The latter aspect is of prominent importance for evaluating the validity of the synthetic method because the mesoporosity should not be produced at the expense of microporosity reduction. Unluckily this can easily happen with the destructive methods based on hydroxides solutions. At low Si/Al (<25) the prolonged alkaline treatment can easily induce the segregation of extra-framework alumina, which is accumulated in the pores and cavities. For this reason, the process requires the use of acidic washing in order to remove the alumina particle and free the surface of the produced material.[93] For high Si/Al (>50), the technique has been modified with the introduction of organic hydroxides, such as TPAOH and TBAOH, in order to induce a milder hydrolysis.[96] Afterwards the most interesting results have been achieved by adopting a mixed procedure of inorganic/organic oxides, thus a first treatment with NaOH followed by a second with TPAOH keeping constant the total amount of the OH^-.The positive contribution of TPAOH is believed to be the creation of a protective layer around the more external part of the framework, limiting the proceeding of the desilication. This also allows the successful application of the method to frameworks apart from the Si/Al ratio range 25-50.[97]

Despite the progress achieved in the development of this synthetic technique, its main drawback remains the impossibility to selectively produce an ordered mesoporosity. Generally, a broad pore size distribution is obtained, and the interconnectivity cannot be absolutely controlled. Nevertheless, the desilication plays a role of great importance in the production of mesoporous zeolites, also at industrial scale, due to the easy scale-up of the process. The importance of this process is reflected in the adoption of a specific "desilication efficiency index" describing the validity of a new procedure, which is defined as the ratio of the external surface area over the percentage of weight loss.[81]

In more recent works, mixed synthetic methods have been developed, in which the dissolution is combined with subsequent recrystallization to form new structures. This approach found good application also in producing hierarchical zeolites. A very sophisticated synthetic strategy, which is gaining great attention, is the so called "ADOR" (assembly-disassembly-organization-reassembly) which is adopted for layered frameworks.[98] The process involves the chemically selective delamination of pre-synthetized layered framework, to form the so-called “house of cards” (the randomization of the layer orientation) and then the pillaring of the layers to form a new structure. Often the spacing between layers have mesoporous dimensions, ensuring a hierarchical relation with the micropores on the 2D sheet.[67] Less sophisticated methods involves the drastic dissolution of a preformed zeolite in acidic/alkaline media for obtaining part of the framework (ideally the SBU) which are then reassembled by organic surfactant. With this technique, hierarchical materials are not always obtained, it results very poorly controllable and predictable.[67]

II) Assembly of nanosized zeolites:

A different approach considers the zeolitic crystallites as puzzle elements, which can be assembled in a hierarchical organization.[99] In this way prevalently interparticle mesoporosity is obtained between the constitutive units which are nanosized zeolites (with dimensions < 200 nm) . The final material can be different from a strictly defined “hierarchical zeolite”, but the properties achieved by the nano-assembling practice, allow including it in this section, following the criteria exposed in the paragraph 1.4. It is relevant to distinguish this type of synthetic procedure from the two main categories of top-down (use of preformed crystals) and bottom-up (templated synthesis) because a different catalytic behaviour is achieved, even if the technique itself can take cues from both sites. By assembling nanosized zeolite particles, improved conversions and mass transfer are obtained by the reduced dimension and the intercrystallite voids, while at the same time the selectivity is retained by the preserving of the bulk zeolite domains. The strategy is based on avoiding the agglomeration of the nanosized zeolite (or protozeolitic precursors) that must remain as single entities, than aggregates to for a hierarchical architecture.[100] It can be achieved by two principal approaches, as schematized in Figure 1.12: by colloidal synthesis that favours the nucleation of zeolitic domains suppressing their crystal growth, followed by self-organization of the nanoparticles (a) or by the use of seeds with functionalization that act as particle spacer (b).[99]

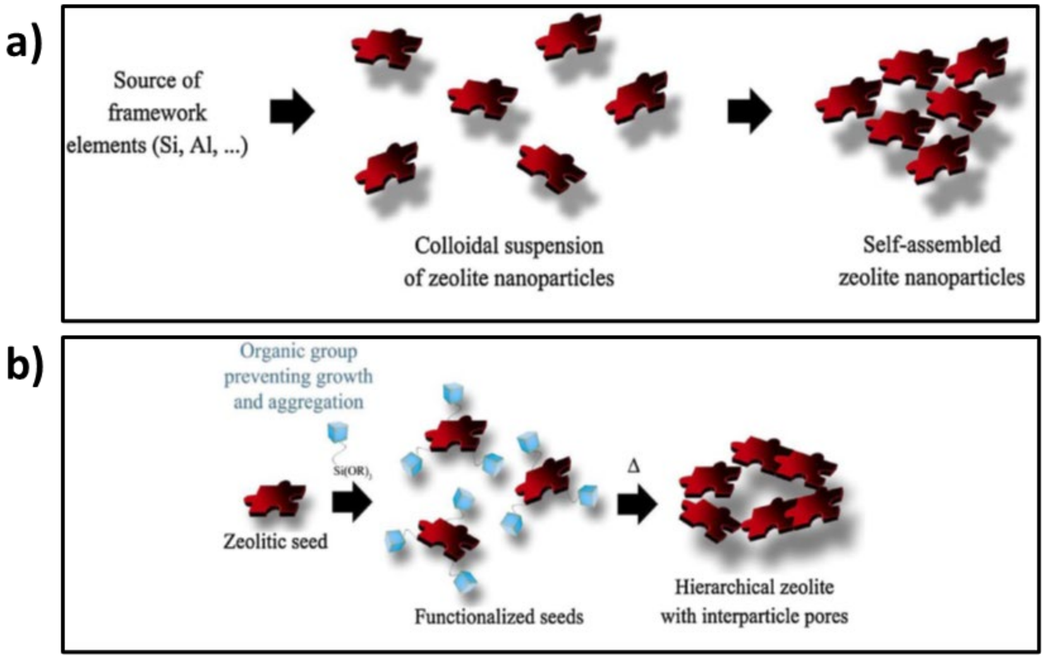

Figure 1. 12. Different approaches to nanoassembling of protozeolitic nuclei. a) involves the self-assembly of colloidal suspension of the nuclei, while b) reports the assembly of functionalised nuclei. Adapted from Ref. 99

The selective production of nanosized zeolites, compared to conventional synthesis, requires specific expedients towards maximizing the crystal nucleation while inhibiting their growth. The first principle is finding the conditions for increase the abundance of stable nuclei at the beginning of the spontaneous formation of the zeolite domains. This because the number of viable nuclei in the synthesis gel determines the crystal size, since the growth process stops when the conversion of the amorphous precursors is completed. Therefore, abundant nucleation induces the creation of small crystallites, while the formation of few and spatially distant nuclei favours the crystal growth.[101] Selectively favour the nucleation represents the main challenge, since it depends on many factors (precursors, concentration within the sol-gel, temperature etc…), it is a not well controllable process. Once obtained the nanocrystals, found the proper conditions, the stabilization of the single entities is usually operated by creating a colloidal suspension of the particles, which is generally reached with very diluted solution and at low concentration of alkali cations, avoiding aggregation.[102] Before describing how a hierarchical organization in achieved starting from nanosized zeolites, some milestones must be listed. The first successes in this field have been reached in the 90s by Schoeman et al., who obtained dispersed crystals of ZSM-5 with average particle sizes in the range 95-170 nm.[103] In 2000, driven by the growing interest in the synthesis of mesoporous structures (inspired by the revolutionary publication on MCM-41)[71] Pinnavaia et al. developed a procedure to assemble protozeolitic domains of zeolite Y (not yet fully crystallized, since they presented not Bragg reflections) by means of the same surfactant used in the synthesis of mesoporous silica, the cetyl-trimethyl ammonium bromide (CTA-Br).[104,105] They obtained a hexagonal mesoporous aluminium silicate presenting improved stability and activity in respect with the amorphous MCM-41, deriving from a partial retaining of the zeolitic organization of AlO_4 and SiO_4 as undefined fragments. They did not define it as a hierarchical structure and not pose attention to the presence of zeolitic microporosity since their goal was the creation of a mesoporous structure, but they sparked the emergence of a new synthetic method. In the same years, Wang et al. obtained micro-macro porous structures by assembling colloidal nanosized Silicalite-1 by means of polystyrene which act as spacer, creating interparticle mesoporosity.[106] Afterwards, a breakthrough contribution became by the work of KU Leuven University operate by Kirschhock et al.[107] with the synthesis of the hierarchical "Zeogrides" [108] and "Zeotiles".[109]

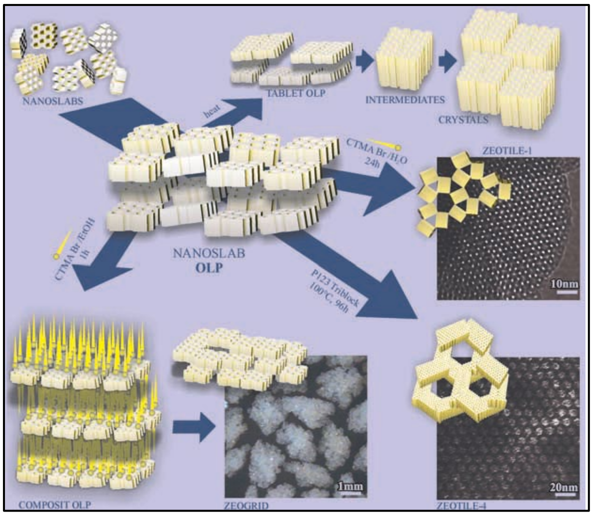

Figure 1. 13. Templated assembling of Silicalite-1 nanoslabs to form hierarchical structures Zeogrides and Zeotiles. Image taken from Ref. 107

They first obtained these two different types of hierarchical structures by combining the colloidal synthesis of Silicalite-1 domains and their assembling by opportune mesoporous templates. Aiming to understand how the crystallization of Silicalite-1 takes place, they have been able to isolate the first organized crystal particle, precursors in the formation of the MFI zeolite crystals (nanoslabs). These were obtained by heating a “clear solution” with the proper concentration of TEOS in water and ethanol, in which the all the Silicon polymerises driven by TPA-OH, forming a colloidal suspensions of the Silicalite-1 nanoslabs.[110] Once the nanoslabs were formed and stable, the hierarchical structures were obtained adding a second templating agent which drives their assembly as building blocks for a second level organization. Zeogrides are formed by effect of CTA-Br that forces the assembly of nanoslabs in stacked concentric layers which are fuse together during the calcination. The resulting material can be described as a Silicalite-1 crystal with about 50% missing framework.[108] Zeotiles are constituted by nanoslabs linked by corners, edges or faces in a pattern determined by the presence of the second template (CTA-Br, but also triblock polymers have been tested). After calcination, the nanoslabs retain the zeolitic microporosity, while an open mesoporosity is created between them, with a geometry depending on the tiling of the building blocks.[109]

Nowadays the nanoassembling practice is a well-established method and it has been developed by studying a great variety of different synthetic conditions for obtaining even more controllable zeolitic building blocks and by varying the second templating agents reaching different mesostructures. Other successes have been obtained by using CTA-Br,[111–113] triblock copolymers,[114] cationic polymer PDDA[115] and even without a second template,[116,117] in a great variety of zeolitic frameworks. When hard templates are involved in the second step, the technique is defined "nano-casting". A slurry of zeolites nanocrystals is deposed on an array of hard templates, filling the voids. The nanocrystals are self-assembled forming a monolith around the hard template which is then removed leaving the mesoporosity.[118]

It is important not to confuse this technique with that of "double templating", which is the combined use of two different templates, placed in the same synthesis mixture with the aim of creating independently micropores and mesopores. It is now well established that double templating is not effective in hierarchization, because the two surfactants often compete inhibiting the micellization of one of the two. This causes the prevalence of one or the other leading to the phase segregation (purely micro or mesoporous) or a physical mixture of both.[68] The main principle of nanoassembly, unlike double templating, is dividing the synthesis in two well-defined steps, first the formation of stable nuclei (not necessarily templated by a surfactant if the selected framework does not require it) and only then, the addition of the mesoporous generator. Some author, as Hartmann et al.[67] are use to define the nanoassembly as "secondary soft templating" underling the two steps process involved.

The syntheses involving organic functionalized zeolite seeds (Figure 1.12 b) represent an evolution of the nanoassembly of protozeolites approach. This method has been proposed for the first time in 2006 by Serrano et al.[119] taking inspiration from the recent discoveries about the clear solution of Silicalite-1.[68,107] They introduced the addition of controlled amounts of organo-silanes (Si-OR_3) molecules in the precursors gel when the zeolites seeds are just formed, for perturbing their growth. The Si-OR_3 are anchored to the zeolites crystals surface by establishing Si-O-Si bonds, while the organic moiety act as a silica chain breaker, stopping the crystal growth. During the hydrothermal treatment the organic parts became the spacers between the forming zeolitic domains, and the free voids are then created during calcination when the -OR_3 groups are combusted. Thus, a hierarchically organized material is obtained by introducing mesoporosity between the zeolitic domains, employing the doble functionality of the organo-silanes molecules grafted on the nanozeolites surfaces (Figure 1.14). In 2006 Serrano obtained sponge-like aggregates of about 300-400 nm, formed by nanocrystals of 5-10 nm that retained a well crystallinity, as testified by XRD and TEM images.[119]

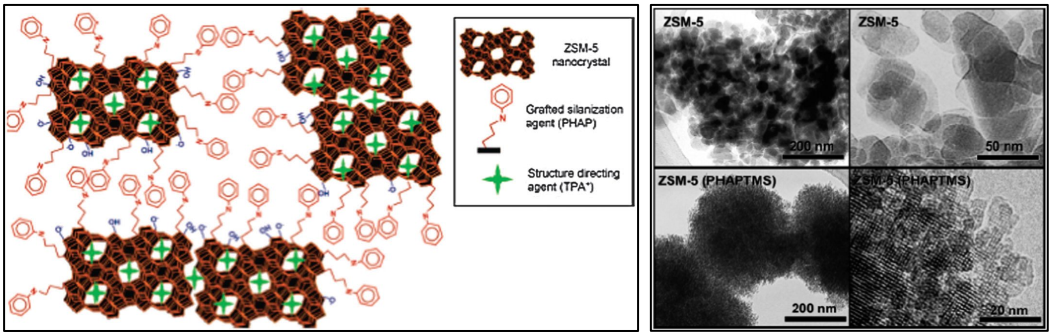

Figure 1. 14. Schematisation of organosilane functionalised zeolites seeds (left), TEM images of materials obtained with seeds functionalisation (right). Adapted from Ref. 119.

Different parameters affect the resulting materials. For frameworks that requires a templated synthesis (as the MFI), the step of zeolites seeds precrystallization is necessary before introducing the silanising agent. This because, as already underlined for other molecules, the competition between TPA^+ and Si-OR_3 leads to the amorphization of the silicate.[119] The temperature of precrystallization (which is favoured by low temperatures, around 40°C) has an influence in stabilizing the protozeolites. Moreover, the concentration of the silanizing agent in the gel is the parameter that mainly influences the textural properties of the hierarchical material, with the great advantage of tuning the mesopores size and shape by the choice of the silane molecule.[120,121] Organo-silanes include a great variety of different molecules which are successfully applied with different approaches apart from nanoassembly. Their employ in bottom-up synthesis is described in the next section.

III) Templated synthesis:

One of the most interesting aspects of zeolite chemistry, that has contributed to widespread use, is the possibility of guiding the assembly of the constituent tetrahedral units by means of specific structures directing agents. These species, of various natures, are normally applied in the synthesis of a wide variety of zeolite frameworks and are defined templates, when they imprint a predetermined shape on the forming silicate. With the evolution of increasingly sophisticated synthetic strategies, the research on ever more specialized templating agents has greatly expanded the variety of structures that can be obtained. With the same approach, it has been possible to directly obtain targeted hierarchical structures through the engineering of appropriate templates, specifically designed to produce systems with dual porosity, determined by the structure of the templating agent itself. Rationalising the action of the template allow having an almost full control during synthesis over the textural characteristics of the final material with a totally bottom-up approach. This represents the field in which the synthesis creativity is mainly expressed for hierarchical structure, since the synthesis design often starts from the creation of the template itself. This technique has been particularly developed in the last twenty years contributing to define some guidelines in the targeted synthesis of hierarchical zeolites, which can depart from a trial-and-error approach and be based instead on a totally rational design. Different kinds of mesopores and connectivity with micropores can be obtained depending not only on the shape of the template but also on the type of interactions that it establishes with the growing framework and the process parameters in which it is inserted.

Two large families of templating are generally defined: *hard templating* and *soft templating*, referring to the nature of the template that imposes different characteristics to the produced material.

Hard templating

The bottom- up assembly of a hierarchical zeolite can be driven by casting the structure with an endo- or exo- pre-shaped solid support, this is defined hard templating. Hard templates are usually applied for leaving a negative imprint of their morphology on the zeolite assembling framework, which is turned into intraparticle mesoporosity, after removal by calcination. With this technique, proper hierarchical zeolites are obtained, embodying interconnected micropores and mesopores in the same particle with tuneable textural properties.[78] The solid template can have a very varied nature, ranging from carbonaceous materials (nanotubes, fibres, porous carbons, or spherical particles)[122–125] and inorganic solids (as porous silica, or calcium carbonate)[126,127] to biological molecules (as starch, wood)[128] and polymers (as polystyrene or polyurethane)[129]. Organo-silane polymers are able to act as “reactive hard templates”, it means that a double function is played, shaping the zeolite structure and providing a Si source for the crystal growth at the same time.[68] The major requirements for the choose of the proper hard templates are to have the right chemical interaction with the precursors for the zeolite production, good stability in the synthesis conditions (generally hydrothermal) and easy removal when the framework is formed.[67]

Soft templating

In the so called soft templated synthesis of hierarchical zeolite the role of structure directing agent is covered by designed surfactants, amphiphilic organic molecules that form supramolecular assemblies in solution. The definition *supramolecular templating* is also valid, since the method exploits the specific supramolecular assembly of surfactants (micellization) for driving the formation of the zeolitic framework by establishing intermolecular interactions with the silicate gel. The assembly way is totally dependent on the type of interaction involved, according to the chemical nature of the surfactant and the free ions concentration in the synthesis conditions, that modify the forces equilibrium in the solution media. Non-ionic surfactants can interact by hydrogen bond or dipolar forces with the inorganic gel. Hydrophilic/hydrophobic interactions, induced by the synthesis solvent, are the driving forces for the surfactant micellization and its thermodynamic stability, which is responsible for directing the mesopore formation of the growing zeolitic framework. Ionic surfactants interact with the forming zeolite trough electrostatic interactions that drive the formation of the mesophase. The different possibilities have been rationalized by Huo et al.[130] who identified four possible pairings of ionic surfactant (S) and a generic inorganic gel (I), depending on the charges involved. $(S^+)(I^-)$ and $(S^-)(I^+)$ are the couples involved when the charges are opposites. When the (S) and (I) present the same charge, the free ions in solution (M) plays a central role, establishing the couplings $(S^+)(M^-)(I^+)$ or $(S^-)(M^+)(I^-)$. The latter is a clear indication of the fact that the synthesis conditions must carefully selected in dependence on the surfactant/inorganic gel nature. In the specific case of zeolites, the inorganic gel is negatively charged, with a net charge in case of aluminium silicate or a partial charge in case of purely silicate gel. Positively charged SDAs, such as quaternary ammonium salts, are effective in driving the assembly of the framework around their point charge. MFI and MOR frameworks templated by TPA$^+$ (tetrapropyl ammonium) or BEA using TEA$^+$ (tetraethyl ammonium) are thus easily obtained. However, if one of the quaternary ammonium substituents is replaced with a long hydrophobic alkyl chain, an amphiphilic molecule (surfactant) is obtained, which in water is capable of micellizing exposing the charged groups to the surface while the hydrophobic tails are oriented toward the inner of the micelles. At this point the silica gel, attracted by the positive charges, can reticulate around the surface of the micelle. This was the revolutionary discovery that brought to the synthesis of M41S mesoporous silicas.[71] The mesoporosity is created by calcining the organic surfactant trapped within the silicate solid, leaving free space with well controllable size and connectivity depending on the organic chain length and micelles shape, Figure 1.15.

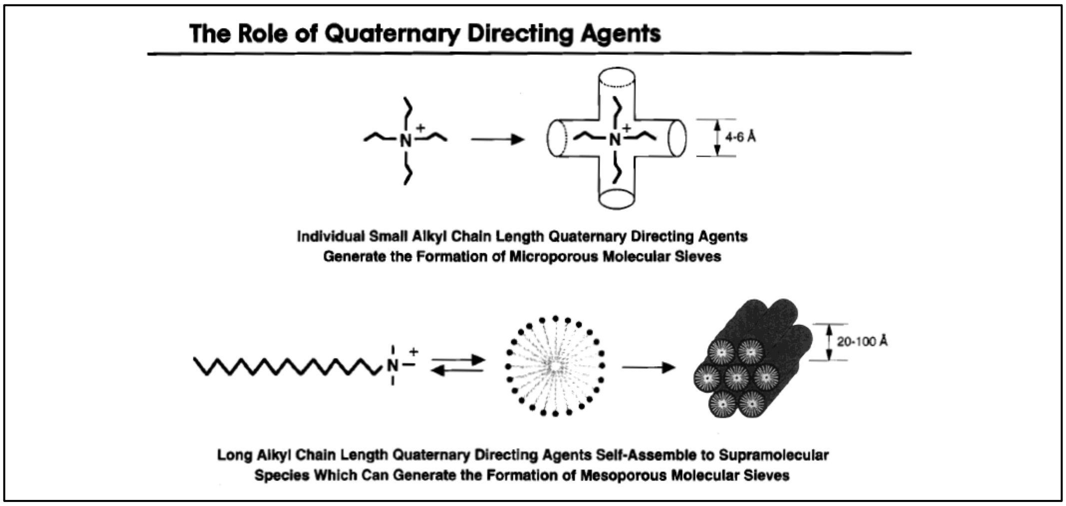

Figure 1. 15. Effect of quaternary ammonium templating agents in driving the formation of the framework. Image adapted from Ref. 82.

At the beginning of the 2000s, the enormous success of surfactant templates synthesis of mesoporous silicas suggested the possibility of functionalizing the hydrophilic head of amphiphilic surfactants for obtaining hierarchical zeolites by the bimodal action of a unique molecule able to create at the same time both mesoporosity and microporosity. This approach overcome in complexity the techniques based on nanoassembly developed in the same years, even taking inspiration from there. The first attempt in producing hierarchical zeolites by the use of amphiphilic surfactant was conducted by Ryoo's group in 2006[131] when designed the amphiphilic surfactant [3-(trimethoxysilyl) propyl]hexadecyl-dimethylammonium- chloride ($[(CH_3O)_3SiC_3H_6N(CH_3)_2C_{16}H_{33}]Cl$ (TPHAC) and analogues. The designed molecule is constituted by a long alkylic tail for mesoporous generation, a zeolite structure directing quaternary ammonium functionality and a hydrolysable methylsilane moiety for interacting with the elemental precursors (SiO_4 and Al_2O_3) by covalent bonds and ensure the formation of the zeolitic framework, overcoming the segregation problems due to doble templating.[132] Ryoo at al. [131] obtained for the first time, the direct synthesis of a mesoporous MFI zeolite through the bimodal action of a single molecule. That represented a revolution in the approach to the synthesis, reaching in practice the ideal concept of hierarchical zeolite. Moreover, the method introduced a certain degree of controllability in the properties of the final material, modulating the mesopores size distribution by varying the length of alkylic functionality of the SDA, the amount of the added organosylane and the duration of the hydrothermal treatment. Afterwards, TPHAC was successfully applied in the synthesis of hierarchical aluminium phosphates (APO-5 and APO-11)[133] and later in creating nanosheets of different frameworks organized in “house of cards” disposition.[134]

The main breakthrough in the surfactant assisted synthesis of hierarchical zeolites was provided again by Ryoo group, introducing the use of poly-quaternary ammonium-based molecules able to produce nanosheets of a single unit cell of MFI with controllable interlayer mesoporosity.[135] Since that moment the production of thin layer of zeolites was very limited, due to the fact that the Ostwald ripening regime of the zeolites growth renders very challenging the formation of anisotropic crystals. The work reports the design of the surfactant $C_{22}H_{45}$-$N_1(CH_3)_2$-C_6H_{12}-$N_1(CH_3)_2$-C_6H_{13} presenting a C_{22} alkylic tail and two quaternary ammonium functionalities spaced by a C_6 chain. The MFI framework is formed by action of the ammonium heads growing in the *ac* crystallographic plane, while the *b* direction is suppressed for the presence of the alkylic tails which are positioned between the layers in a "sandwich like" pillaring. The final material is composed by sheets of 2,5 nm length in the b direction, which can be selectively organized in a multi-lamellar assembly or uni-lamellar randomly staked, by varying the amount of free Na^+ cations in the gel mixture. The materials showed exceptionally higher conversion of bulky organic substrate in acidic catalysed reaction in comparison with standard MFI, with increased catalyst lifetime and retaining the zeolite stability.

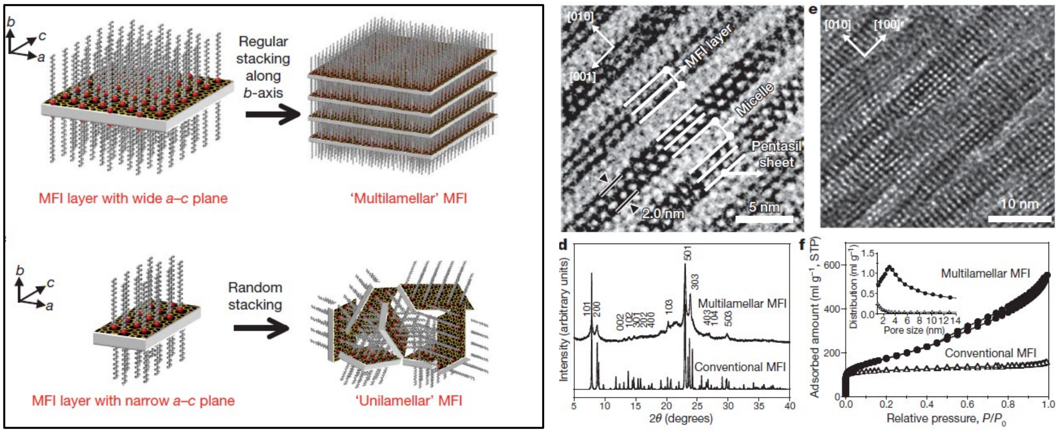

Figure 1. 16. Application of $C_{22}H_{45}$-$N_1(CH_3)_2$-C_6H_{12}- $N_1(CH_3)_2$-C_6H_{13} as templating agent. Schematisation on the left and experimental results on the right.[135]

In 2011 the Ryoo group[136] obtained highly ordered mesoporous materials formed by microporous crystalline aluminium silicate walls, by introducing further functionalization to the bifunctional soft templates. They developed a new series of gemini type surfactants (composed by more than one hydrophobic tail and multiple hydrophilic heads linked together by short spacers)[137] starting with $C_{18}H_{37}$–

N^+ $(CH_3)_2$–C_6H_{12}–**N^+**$(CH_3)_2$–C_6H_{12}–**N^+**$(CH_3)_2$–$C_{18}H_{37}(Br^-)_3$ (C_{18}-N_3-C_{18}). The gemini structure produces large micelles in aqueous media, which expose the hydrophilic heads outward and the hydrophobic tails inwards, ensuring at the same time the nanocrystals formation driven by the quaternary ammonium and the promotion of the crystal-liquid like conditions for the mesostructured assembly. C_{18}-N_3-C_{18} produces an open hexagonal mesoporous structure of about 4 nm in diameter, which walls are constituted by a layer of crystalline MFI of 1,7 nm thickness in the *b* direction, less than one unit cell. The material presented the thinner layer of zeolite ever synthetized until that moment, taking part of a superstructure in which micropores and mesopores are directly interconnected. Moreover, by modifying the chain lengths and introducing aromatic groups in the gemini surfactant, it is possible to selectively obtain different properties of the hierarchical material, as different zeolitic frameworks or modulate the wall thickness and mesopore diameters.[136]

This represent the practical realization of the ideal hierarchical zeolite, as demonstrated in the catalytic tests to which the materials were subjected in the same work. The hierarchical structures, in their acidic forms, proved to be very effective in Friedel-Craft alkylation reactions of very bulky organic substrates, significantly outperforming the properties of the corresponding microporous zeolites in terms of conversion and catalyst lifetime.[136]

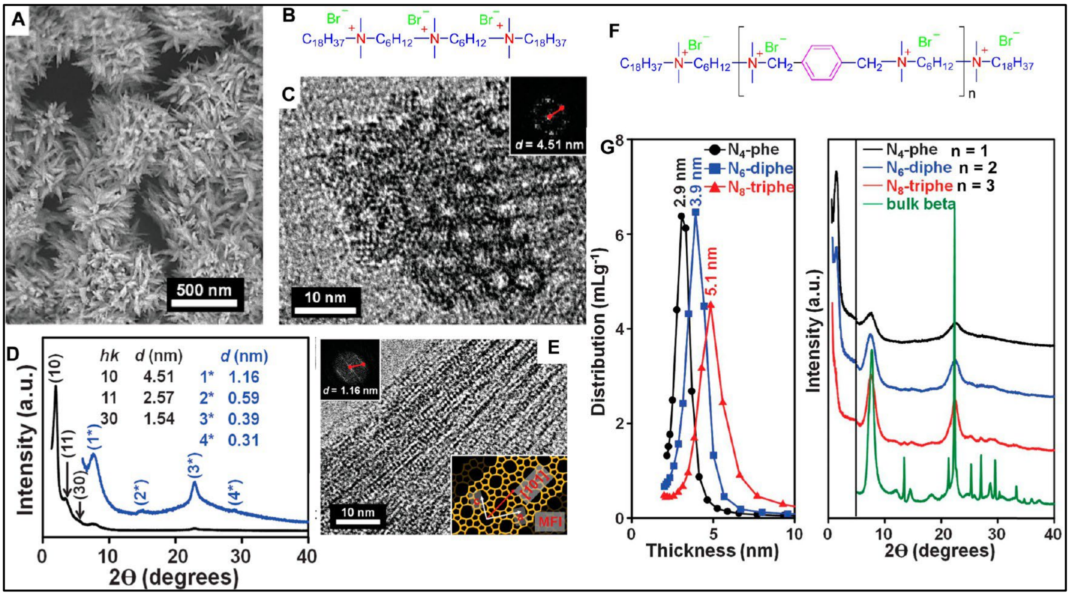

Figure 1. 17. Experimental results obtained with the application of (C_{18}-N_3-C_{18}) in the synthesis of hierarchical MFI.[136]

The pioneering work of Ryoo and co-workers has allowed the development of a true and highly efficient synthesis technique aimed at obtaining hierarchical structures. other functionalisations of gemini-type surfactants have been introduced by other groups later, helping to rationalise the structure-properties relationship.

Che et al. further rationalized the design of amphiphilic surfactants, demonstrating that the insertion of aromatic groups (biphenyls and naphthyls) at the end of the hydrophobic chain of a single ammonium containing surfactant allows exploiting the π-π staking of the tail-tail interaction obtaining a perfect separation between layers to form structures organized in single crystal nanosheets. They also obtained interconnected nanosheets with tuneable mesoporosity by introducing triply branched cationic amphiphilic templates.[138] With the obtainment of cylindrical micelles with bolaform amphiphilic templates (presenting hydrophilic groups at the end of the long alkylic tails) instead, the growth of MFI zeolitic planes can be selectively oriented at 90°C rotational boundary obtaining square structures. [83] All these materials proved to be more active than their microporous zeolitic counterpart in aromatics isomerization reactions, given the greater mass transport and accessibility for bulky substrates, due to the hierarchical structure.

A further development of the gemini-type surfactant has been introduced by Basset et al. with functionalization of the ammonium heads by the insertion of organosilane[139] moieties and polymeric chains,[140,141] allowing a greater crystalline growth of the zeolitic phase in the long range order while maintaining the hierarchical structure.

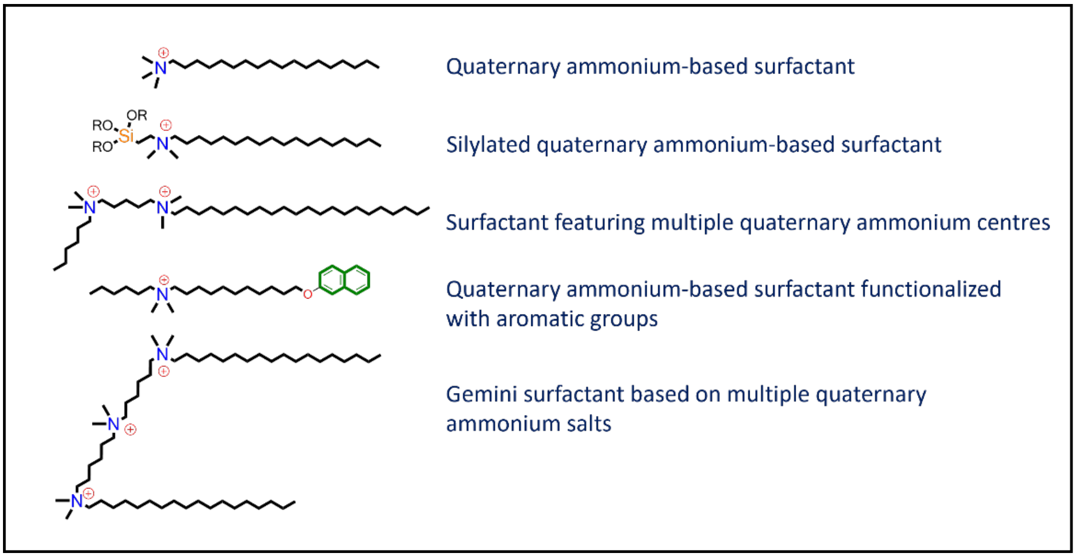

Figure 1. 18. Evolution of amphiphilic quaternary ammonium-based surfactant for the soft templated synthesis of hierarchical zeolites.

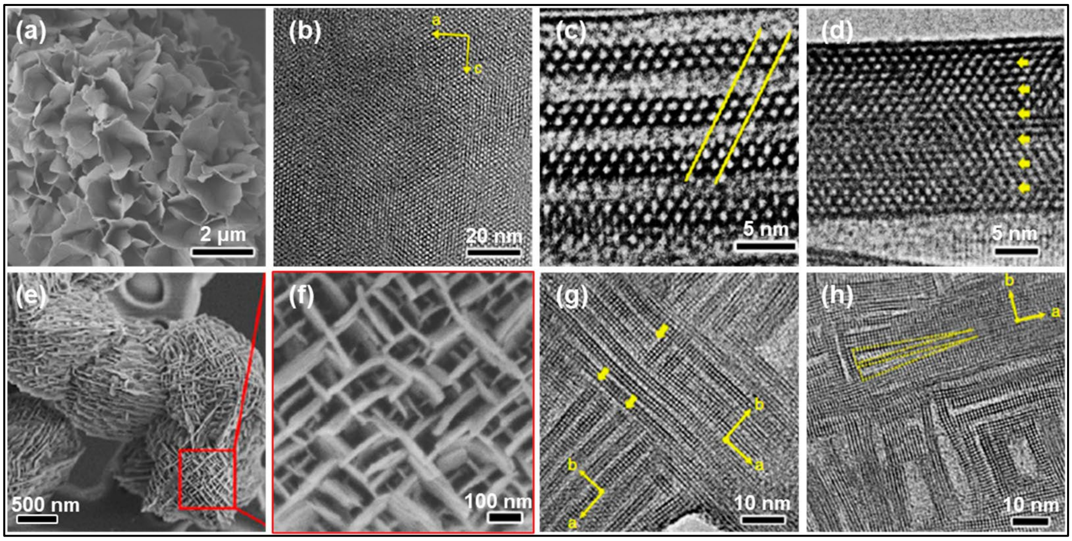

Figure 1. 19. Hierarchical materials developed by Che et al.[138]*by design of amphiphilic templates. (**a**) SEM and (**b**, **c**, **d**) HRTEM images of lamellar mesoporous single-crystalline zeolite nanosheets. (**e**, **f**) SEM and (**g**, **h**) HRTEM images of ZSM-5 nanosheets with a 90°C rotational boundary synthesized using bolaform amphiphilic templates.*

The described approaches for the formation of hierarchical structures proved to be a very sophisticated technique for obtaining very complex materials of great versatility and effectiveness. The evolution of the method reached until now the tools for an entire design concept for the development of mesoporous structures starting from the templating agent. However, the synthesis of such functional surfactants is often complex and expensive and therefore it is difficult to figure out any large-scale production or commercial application for hierarchical structures obtained with this techniques. Also because, except for the admiring examples described above, the method often leads to amorphous materials or aggregated nanosized zeolites due to intergrowth phenomena. In any case these strategies have contributed to the comprehension of the interaction between surfactants and the zeolite precursors and provided exceptional materials which represent extremely innovative case studies.

1.4.2. Characterization of hierarchical zeolites

The process of hierarchization induces several changes in the properties of a zeolite, that must be taken in consideration both during its preparation and then in characterizing it. It is common to observe an increased concentration of defect and a partial loss of the crystallinity with respect to bulk zeolites, that inevitably induces a reduction in the number of active sites. The control of the crystallization is one of the main aspect to consider for developing a synthetic strategy.[75] The partial amorphization, often induced by the secondary porosity, complicates the structure determination by conventional analysis of the X-Ray diffraction. The resulting pattern can differ from that of a bulk framework for different reasons, starting from the abundant presence of lattice imperfections and new geometrical strains that easily reduce the lattice planes in coherent interference. In case of 3D nanosized zeolites, a broadening of the diffraction peaks must be expected, since the extension of the crystallites is reduced in all the directions; while in case of the suppression of one direction (as in case of zeolitic nanosheets), it must be considered that the corresponding reflections will be systematically suppressed. Different is the case of intraparticle crystals, in which mesoporous arranged in a very regular and narrow distribution generate additional reflections at very low 2θ angles; these are totally absent in the pattern of a bulk zeolite, but commonly found for ordered mesoporous silicas. The low angles reflections, if well resolved, give information regarding the shape/geometry of the pores and their size, represented by the distance enclosed between the silicate walls. However, in the practice, the high degree of amorphization in hierarchical structures complicates the structural resolution requiring unusual ways of characterization, and often the combination of different techniques is needed. Techniques as small angle X-Ray and neutron scattering (SAXS and SANS) and solid-state NMR are more often successfully employed for their structural determination. A relevant role is held by electron microscopy techniques that are able to prove the presence of pores, their distribution, shape and extent.[75,142] SEM (scanning electron microscopy) has proven to be an effective technique for obtaining information about the surface topology of materials. In case of hierarchical zeolites, it is particularly useful for comparing or monitoring changes in the morphology of different samples[131] (for example before and after a desilication treatment or comparing the bulk with the hierarchical form of the same framework) and allows the visualization of mesopores and macropores. The FIB-SEM (ion beam scanning electron microscopy) is also a powerful technique that allows the visualization of the internal surface; it is applied for the characterization of the pore architecture in hierarchical zeolites,[143] since it can provide 3D imaging of the section of the sample. TEM (transmission electron microscopy) is one of the most relevant techniques providing information on the mesopore array in hierarchical zeolites. It can provide imaging at atomic level, combining also a structural determination by diffracted electrons. It is possible to discriminate the presence of crystalline and amorphous phases and accurately measure the dimension and extent of pores family. Size, shape and homogeneity/inhomogeneity of mesopores are directly appreciable by TEM imaging. Due to the high variability and complexity of the textural properties, which is the main characterizing aspect of hierarchical zeolites, the analysis of the pore structure is the most relevant topic. The volumetric measurements by gas physisorption as N_2 or Ar at cryogenic temperature is the leading technique, allowing the determination of the pore sizes in all the ranges, their shape, distribution and accessibility. The technique also provides the evaluation of the surface area value, which is crucial for all heterogeneous catalysts and moreover for porous materials. In case of such complex system as multi-sized porosity, anyway, the technique requires expertise in the choice of target experiments and the data elaboration through opportune models. The characterization of hierarchical structures has required the application of the most sophisticated adsorption methods but, at the same time, it has provided a training ground for the implementation of the technique itself over the years. The efforts are oriented in obtaining even more ordered nanostructured materials with uniform tailor-made pore structures, this implies the development of high-resolution experimental protocols of adsorption of cryogenic fluids for their characterization.[144–146]

The physisorption data can be directly employed in a very simplistic way, defining what is called "hierarchical factor" (HF).[97,147] It is a ready to use tool for correlating the porous structure with a hypothetical catalytic performance. The HF is defined as the product:

$$(V_{micro}/V_{pore}) \times (S_{meso}/S_{BET})$$

where V_{micro} and V_{pore} indicate the micropores and total volume respectively, while S_{meso} and S_{BET} are the surface of mesopores and the total surface are calculated by BET equation. It is important for evaluating the portion of zeolitic microporosity, which is the most active phase, that is retained in the multiparous system in relation with the total available surface. Even if the HF can give an indication of the portion of the catalyst represented by the different porosity and it can be useful for comparing different materials, it is unable to describe the interconnectivity and the accessibility of the pores, which is the main aspect of hierarchical structures. The last point is mandatory in discriminating between an actual hierarchical zeolite and in materials presenting segregated fraction of pores with different sizes, that, without the correct interpretation of the isotherm curve of adsorption, would provide the same value of HF. It is necessary to identify the fluid path by pore filling for understanding the pore interconnectivity. This requires more advanced experimental procedures to be determined.[147–149]

The identification of the nature and location of the active sites is of prominent importance in zeolite catalysis, and it assumes aspect of increased complexity when deal with hierarchical structures. It must be kept in mid that the proper active site of a zeolite arises from the perfectly tetrahedral coordination of the framework cations when the charge imbalance needs to be compensated by extra-framework species. The high defective nature of hierarchical zeolites, as unconventional shaping of the framework (geometrical strain) or extended surfaces (as in case of 2D structures), is responsible for the abundance of other potentially active centres. The leading techniques for identify these species, both generated by regular assembly or induced by defectivity, are the spectroscopies. The solid-state NMR spectroscopy is gaining enormous importance in the zeolites word, allowing the determination of the local environment that can provide information about the coordination sphere of selected nuclei. It is possible, for example, to achieve the coordination number of the Al^{3+} species, and unambiguously distinguish between framework and extra-framework species providing their relative abundance, but the technique lacks a spatial resolution that can inform about the location of different sites. This aspect, in contrast, is perfectly satisfied by advanced methodologies based on the use of Fourier Transformed InfraRed (FT-IR) vibrational spectroscopy. In case of hierarchical zeolites, it is possible to obtain valuable information on the location of active sites and how they are distributed on the surface, differentiating between micropores and mesopores by means of target probe molecules with different steric hindrance. Pyridine and substituted pyridines are particularly useful.[150–152] Pyridine (Py) is a heteronuclear aromatic cycle of 0.57 nm diameter, with nucleophilic Lewis character and high proton affinity (930 kJ/mol) able to quantitatively deprotonate a zeolitic BAS when interacting with it. Due to the steric encumbrance of pyridine, it can diffuse only in zeolitic micropores larger than its kinetic diameter and selectively reach only the BAS exposed on the accessible surface. In case of 8MR zeolites, the Py diameter exceeds the pore openings (0.38 nm in APO-18, AEI framework), thus it can selectively interact only with the acidic sites exposed on the outer surface, leaving unaffected which ones are enclosed in the microporous system. For larger frameworks, as 10MR or more, the pore opening diameters (about 0.6 nm for MFI framework) allow the diffusion of Py all over the internal surface of the micropores, inducing the quantitative deprotonation of the acidic sample. The resulting spectrum will show the disappearance of the BAS νOH vibrational band and at the same time the formation of the vibrational ring modes of the pyridinium ion (Py^+). Known the molar extinction coefficient of the Py^+ band (product of the acid-base reaction) the quantification of the amount of the acidic sites titrated by pyridine, is directly achievable by the intensity of the considered signal. In case of 8MR ring the percentage of inner/outer BAS distribution can be obtained. For hierarchical zeolites, the distinction between differently accessible areas can be performed by employing substituted pyridines. Methyl (or longer chain) substituents on the aromatic ring increases the kinetic diameter, hampering the diffusion of the substituted pyridine in micropore openings in the range of the MFI framework. The most employed methyl substituted pyridines are 2,6-dimethyl pyridine (2,6 lutidine) with 0.67 nm diameter and 2,4,6-trimethyl pyridine (2,4,6 collidine) with 0.74 nm diameter. The selective use of these differently sized bases allows discriminating the position of acidic sites distributed in the multimodal porous system of hierarchical MFI zeolites (or comparable sized framework). On the basis of the *in situ* adsorption of bulky probes the pore architecture of a hierarchical zeolite can be described by means of IR spectroscopy defying the accessibility index (AI) parameter.[153] The AI was defined by Pérez-Ramìrez as the ratio between the number of Brønsted acid sites probed by the employed substituted methylpyridine (directly reliable with extra-micropores sites) and the total amount of Brønsted acid sites, quantified by pyridine adsorption. The screening of a series of desilicated ZSM-5, from which the AI were developed, resulted in 2,6-lutidine having access to roughly 50% of the acid sites of the parent zeolite, while collidine only probes the acid sites present over the external surface. The study demonstrated that the accessibility index increased with the mesopore surface area of the desilicated sample. Generalizing, the AI is a useful tool for directly comparing different hierarchical structure.

The use of size-selective probe molecules can be also coupled with a molecular probe with suitable dimensions to spread inside the micropores (namely CO at 77 K).[154–156] Indeed, the consecutive adsorption of Col and CO helps to discriminate the fraction of sites not accessible to collidine, but available to interact with a probe that can easily enter the microchannels of all dimensions. Knowing the distribution of active sites can be a very useful tool for the selection of the proper catalyst in a specific catalytic process, in which a substrate can be differently selectively converted by the action of different located active sites. The acid-base interaction regards also weaker acidic sites on the catalysts surface which are generally represented by silanols (Si-OH) in silicate zeolites and phosphanols (P-OH) in aluminium phosphate zeotypes, characterized by distinctive vibrational bands. These hydroxyls groups present a weak acidic character that allow the interaction with basic molecules, in addition to establishing hydrogen bonding with H acceptors. Generally, these groups represent points defect since they correspond to chain breakers of the framework and have a moderate reactivity that allows them to take part in some catalytic reactions. The speciation of these groups by interaction with probe molecules, provides information about the defectivity of the sample and their distribution. The latter point is particularly useful for evaluating, in the comparison with a bulk zeolite, the effect of hierarchization, either induced by a post-synthesis process or obtained bottom-up. Especially if run with steric selective probes (as methyl pyridines), the distribution of defects all over a multilevel porous system can be disclosed.

Chapter 2: Techniques and experimental strategies

2.1. Synthetic strategies adopted

2.1.1. Hydrothermal synthesis

Zeolites with MFI framework, namely ZSM-5 with Si/Al= 15 and TS-1 have been obtained by hydrothermal synthesis. In general, a hydrogel composed by hydrolysed elemental precursors is obtained at low temperature (Si^{4+} and Al^{3+} precursors are hydrolysed in a range of 40°-60°C, while for Ti^{4+}at 4°C in ice bath) under stirring in high alkaline media, in presence of TPA^{+}. The gel is then converted in a defined crystal structure by a slow hydrothermal treatment at 140°C-170°C for 1 to 3 days.

2.1.2. Soft templating synthesis of mesoporous structures

Mesoporous silicas MCM-41 and MCM-48 has been obtained by sol-gel synthesis mediated by CTA-Br, followed by hydrothermal treatment.

With reference to the work of Na et all. in 2011[136] the synthesis of a **hierarchical MFI** by soft templating technique has been reproduced. The material has been fully characterized as reported in the paper Airi et al. 2021 and resumed in Chapter 3.[157]

The amphiphilic gemini surfactant based on three quaternary ammonium functionalities C18-N3-C18 has been successfully synthetized following the procedure reported by Na et al.[136], the details are reported in Chapter 3. The molecule has been then employed for directing the synthesis of a ZSM-5 like material with Si/Al=15 by hydrothermal synthesis. The aluminosilicate gel is formed adding Si (TEOS) and Al (sodium aluminate) precursors in an ethanol/water solution in which C18-N3-C18 micellises. The conditions for the correct crystallisation have been evaluated, monitoring the temperature for the gel formation and the duration of the hydrothermal conditions. The latter has been conducted in stainless steel autoclave at 170°C under rotation, obtaining the desired material with an 8-day long treatment.

2.1.3. Clear solution based synthesis

Silicalite-1 samples have been synthetized by clear solution. The same technique has been tested also for the synthesis of TS-1, as described in Chapter 4.

The so-called "clear solution" is a colloidal solution of the elemental precursors that replaces the sol-gel method. TEOS is added in aqueous solution of tetrapropylammonium hydroxide (TPA-OH) at room temperature and it is hydrolysed under continuous stirring. The hydrolysis of TEOS releases ethanol, resulting in a final ethanol/water solution in which nanometric sized MFI domains (nanoslabs) are formed by self-assembling. TPA^+ being encapsulated by the silicate growing framework, act as structure directing agent imposing hydrophilic/hydrophobic interaction between the silicate and the surrounding water medium. The particles are not visible at naked eye, thus the solution is transparent and for this called "clear". After a colloidally stable particle distribution in the clear solution is reached, heating is required for the aggregation to proceed further.[107]Silicalite-1 crystallises in mild conditions and the hydrothermal treatment is not required. The clear solution is kept in quiescent conditions at temperature ranging between 80°C and 100°C within polypropylene bottles for the crystallization of the MFI materials.

2.1.4. Nanoassembling of zeolitic precursors

The clear solution has been tested also as precursor for the synthesis of mesoporous and hierarchical materials. Assuming that stable nuclei are formed in the colloidal solution, attempts to assembly them by the use of a second templating agent have been performed. These are the subject of Chapters 4, 5. The selected sondary templating agents are commercial organic compouds, known in the zeolite synthesis world as mesoporous generators mesoporegen). These are, an ammonic surfactant CTA-Br, a triblock-copolymer P123 and a non-ionic surfactant Triton-X. the possibility to obtain hierarchical structure by inducing the nanossambly of zeolitic nuclei around the different mesoporogens has been critically evaluated. For increment the stabilization of the crystal nuclei and push the nucleation at the expenses of crystal growth, some expedients have been adopted:[158]

- Aging the precursors gel at the room temperature. It has significant influence on the nucleation rates, since it is favoured at room temperature, while the growth rate is inhibited.
- Controlling the alkalinity of the starting solution. The concentration of OH^- ions strongly increases the solubility of the silicate species promoting the formation of small ordered domains.
- Modulating the concentration of the clear solution. Considering that, the dilution of the solution can cause the formation of large crystals (considering the Ostwald ripening regime for the zeolites crystallisation) high concentration is a desired parameter for promoting high nucleation rates.
- A low crystallization temperature (80–100°C) is often applied, considering that the large zeolitic crystal formation is contrary favoured by hydrothermal treatments.

2.2. Structural and textural determination

2.2.1. Powder X-Ray diffraction

The powder X-Ray diffraction measurements have been operated using the Bragg-Bretano geometry with a PANalytical PW3050/60 X'Pert PRO MPD diffractometer working with a Cu anode ($K\alpha = 1.5418$ Å) and an X'Celerator detector. The XRD has been employed for determining the crystal phase of the synthetized sample, by simple comparison with reference patterns. MFI patters have been recorded in the range 5-50° 2θ, while for samples for which mesoporosity was expected the measurement has been performed in the range 0.5-5° 2θ. Evaluation of the phase purity has been performed comparing the pick list with tabulated data, while the dimensions of the crystals domains are evaluated on the pick width.

2.2.2. Transmission Electron Microscopy

The TEM analysis has been conducted using a TEM JEOL JEM 3010 UHR microscope (0,17 nm of theoretical resolution) equipped with a LaB_6 electron source working at 300 kV of accelerating potential and EDS OXFORD X-STREAM Energy dispersion detector. The images have been collected by a CCD camera Gatan, Model 894 US1000 (2k x 2k).

The sample has been prepared depositing a small amount of powder over a 200-mesh lacey carbon copper grid.

2.2.3. N_2 physisorption at low temperature

Isothermal N_2 physisorption measurements at liquid nitrogen temperature (LNT - 196°C) were performed on a Micromeritics ASAP 2020.

Prior volumetric measurements, all the samples have been subjected to the removal of surface pre-adsorbed species by thermal activation in vacuum. Turbomolecular pumping is needed for reaching the conditions for the analysis of zeolitic ultramicropores, that starts from 10^{-8} mbar of relative pressure. To avoid structural damages induced by the activation procedure, special heating programs were adopted, in particular for hierarchical structures that mostly suffer from steaming. The programs involve all a slow ramp of 1°C/min until 100°C. This temperature is kept constant overnight, for ensuring a delicate removal of adsorbed water from the pores. Before the measurements, the materials are subjected to another thermal treatment at higher temperature, nominally 250°C for mesoporous silicas, 350°C for hierarchical structures and 400°C for bulk zeolites until complete removal of adsorbates (stable outlet pressure) in some hours. The difference in the temperature reflects the facility in removing the adsorbed species in relation with the size of the pores.

Specific of the technique:

Nitrogen at its boiling point (-196°C) is a suitable probe molecule for the volumetric analysis of porous materials, allowing the determination of pores in different sizes. [145,146] The adsorption isotherm (originated by reversible physisorption of a gas over a solid surface) is the results of the mechanism with which the surface of the adsorbent solid is fully covered by the adsorbate and is built point by point at increasing gas pressure dosage. The quantity adsorbed is correlate to the volume occupied by the gas at the equilibrium pressure (known the dead space of the adsorbent), following the gas laws. If the desorption follows different stages, it will result delayed with respect to the adsorption and a hysteresis loop will be recorded in the isotherm curve. The different types of isotherms and shape of hysteresis loops are classified by IUPAC[146] as reported in Figure 2.1. Type I isotherm is found for physisorption in microporous materials. It is distinguished in two variations. Type I (a) regards ultramicropores filling, that occurs at very low relative pressures always below $p/p_0 < 0.01$, where the interaction adsorbent-adsorptive is enhanced. Type I (b) is obtained by supermicropores that are filled in the range $p/p_0 = 0.01$-0.15. Type IV isotherms regard mesoporous materials. It is characterized by the presence of a plateau at high relative pressures. Again, the differentiation in Type IV (a) and (b) depends on the pore size, higher for (a) and lower for (b). Type IV (a) isotherm is generated when the pore with exceeds a critical dimension for which capillary condensation/evaporation produces a hysteresis loop, this corresponds to about 4 nm in case of nitrogen (or argon) physisorption. When the pore size is lower or in case of closed pores, the totally reverse isotherm Type IV (b) is obtained.[145,146]

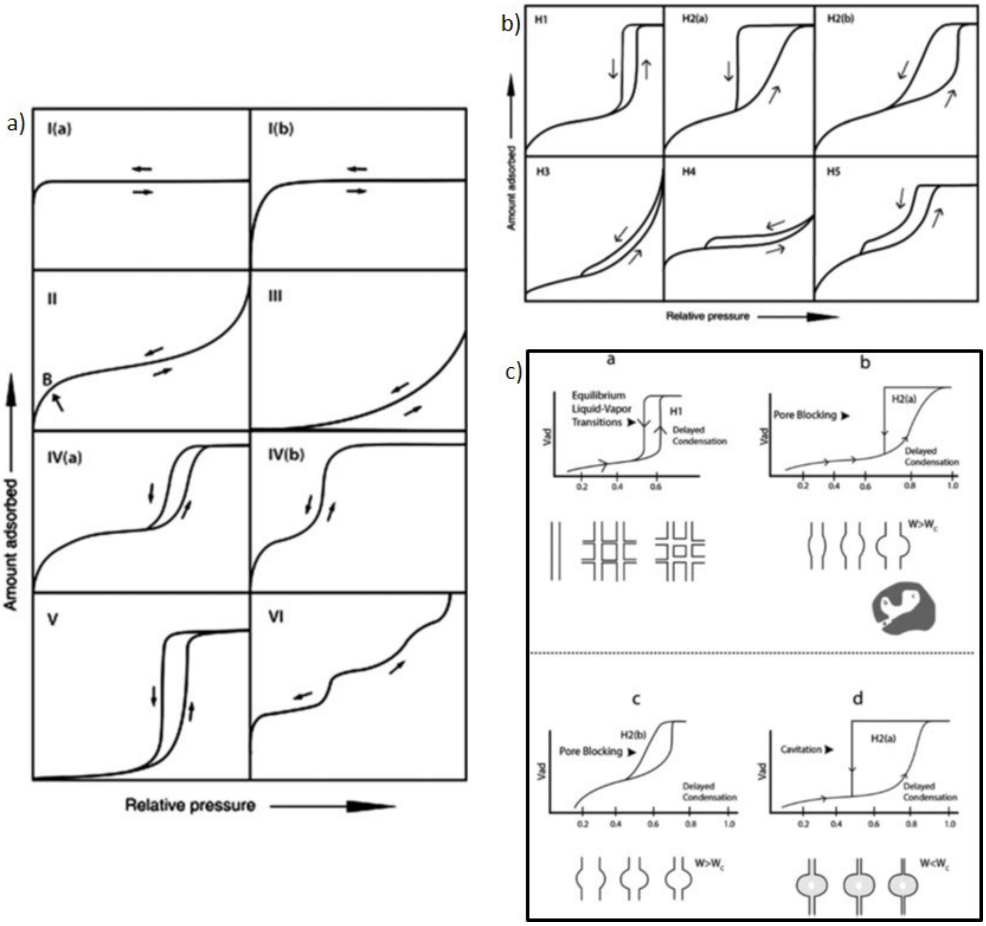

Figure 2. 1. a) IUPAC classification of physisorption isotherms. b) IUPAC classification of possible hysteresis loops.[146] *c) Adsorption hysteresis in correlation with the pore structure.*[159]

Proper hierarchical zeolites, due to the presence of multilevel porous systems, usually shows composite isotherms that are combination of Type(I) and Type (IV). The presence and therefor the analysis of the hysteresis loop can give precious information about the connectivity of the pores, because its shape can depend on pore geometry and/or network effects.[146]

The evaluation of the surface area is another important data achievable by the analysis of the isotherm curves. The most commonly adopted method for the surface area calculation is the B.E.T (Brunauer, Emmett, and Teller), which has been developed for non-porous materials (Type II isotherm). Certain expedients must be considered in case of porous materials and mostly for hierarchical ones, for which the value must be considered an apparently surface area and not the real accessible one. Anyhow, it still is a useful indication for materials comparison and a fingerprint for their characterization.

Contrary, the pore volume and size determination are a straightforward characteristic achievable by physisorption. As the total pore volume is determined at p/p_0 close to the unit, the calculation from the quantity adsorbed is admitted for both microporous and mesoporous materials, since both Type I and Type IV present a plateau at high relative pressure (different is the case of macropores). Several methods have been developed for the determination of pore sizes, based on different mathematical and physical assumptions. Nowadays, prominent importance is covered by DFT methods, based of non-local density function of confined fluids.[144] Providing an accurate modelling of both the isotherm curve and the hysteresis loops, these methods (provided by specialised software) allow the accurate determination of pore size and volume in both the micro and mesopore range and are indispensable for the textural characterization of hierarchical materials.

2.2.4. Raman Spectroscopy

Raman spectra of activated samples in form of self-supporting pellet, were collected with a Renishaw InVia Raman microscope working with a 785 nm laser diode and a 20X objective, accumulating for 20 seconds with 1 mW laser power. The 244 nm Raman was performed on a Renishaw inVia Raman microscope spectrometer, equipped with a Coherent Innova 300C motoFreD frequency doubled Ar+ laser as excitation source, a 3600 line/mm grating and UV-enhanced CCD detector. The light was focused on samples through a 15 x objective. In order to prevent degradation phenomena induced by the intense, highly energetic excitation light, samples were kept under continuous rotation by exploiting a home-made sample holder.[160] Three spectra were collected for each samples and averaged to three different points for yield a better signal-to-noise ratio.

2.3. Active sites characterization

Ex situ **high temperature treatments: catalysts activation.**

Thermal activation in vacuo at high temperature is a mandatory pre-treatment to remove all molecules adsorbed on the zeolitic surface that otherwise would perturb the catalyst spectral features.

All the samples considered in this work have been treated before each experiment of FT-IR and DR-UV-vis spectroscopies directly in the customized sample older (cell) of home-made design specific for each technique. The quartz cells were connected to a glass-line equipped with vacuum pumps, allowing the thermal treatments and gas dosage. The template removal of uncalcined samples (referred also as high temperature O_2 treatments in the next paragraphs) was conducted by controlled heating 5°C/minute until 550°C, with intermediate steps of 50 mbar O_2 dosages alternated to vacuum removal of gaseous species, following literature reference.[161] When the temperature of 550°C was reached, the samples were kept in pure oxygen atmosphere for 2 hours, then cooled to room temperature in O_2. Finally, the system was outgassed by vacuum pumps, until reaching $5 \cdot 10^{-4}$ mbar of residual internal pressure. High temperature H_2 treatments has been performed over the calcined samples, by first outgassing the system while rising in temperature 5°C/minute until 400°C. Once the internal pressure of $5 \cdot 10^{-4}$ mbar was reached, 50 mbar of pure H_2 were introduced in the system and kept in contact with the samples for 1 hour. Followed outgassing and cooling down to room temperature.

Simple activations consisted in heating treatments of 5°C/minute until 400°C in dynamic vacuum outgassing conditions until reaching $5 \cdot 10^{-4}$ mbar pressure.

2.3.1. Infra-Red Spectroscopy

ATR-IR experiments: the spectra were collected on Bruker Alpha compact spectrophotometer, equipped with a Bruker Platinum ATR accessory with a diamond single reflection internal refraction element and a DTGS detector, collecting 32 scans for each acquisition with 2cm^{-1} of resolution. The samples have been analysed upon previous activation treatment in the protected atmosphere of a N_2 glovebox, where the spectrophotometer is located.

Transmission FT-IR experiments: the activated samples were analysed in the form of self-supporting pellets inserted in a home-made quartz cell with KBr windows for *ex situ* and *in situ* experiments. The IR spectra were acquired in transmission mode with a Bruker Vertex 70 spectrophotometer equipped with a MCT cryodetector working at 20 KHz, collecting 32 scans for each spectrum with 2 cm^{-1} of resolution. Under acquisition, the samples were kept connected to the vacuum glass-line which allowed the dosage of gaseous probe molecules for *in situ* measurements, recording the spectral changes during adsorption/desorption. The probe molecule interaction experiments were carried on following procedures reported by literature.[162,163]

The covalent nature of the bonds in zeolite frameworks makes them particularly suitable samples for investigation by vibrational spectroscopy. Zeolites and zeotypes are characterized by diagnostic vibrational modes that give very important information on the framework surface and especially on the nature of their active site. The population of Brønsted acid sites, with different strength, can be determined by observing the ν (OH) stretching bands. The length of the O-H bond, and consequently the acid strength of the group involved, determines the vibration frequency, which becomes lower as the length of the O-H distance and acidic strength increase.[164] Also, the insertion of heteroatoms affects the vibrational features of the zeolites mostly in the framework mode region (about 1200-400 cm^{-1}), even if some changes are also observed in the ν(OH) region due to a change in the acidity strength arising from the isomorphous substitution.

For the characterization of zeolitic active sites, i*n situ* techniques are extensively used since allow acquiring IR spectra when the sample is subjected to modifications as temperature treatments, adsorption/desorption of gases and interaction with reactive molecules, obtaining information about the physicochemical behavior of the catalysts.[165] Monitoring by in situ FT-IR spectroscopy the adsorption of opportune probe molecules (at the proper conditions of temperature and equilibrium pressure) with the zeolite surface give a wide range of information regarding the nature, location and distribution of the active sites. The adsorbed molecule interacting with the surface induces spectral changes in the diagnostic vibrational mode of the catalyst or generate completely new informative signals which can be spectroscopically appreciate with high sensitivity. Basic molecules are particularly suitable probes for the characterization of acidic zeolites and zeotypes, establishing with the surface the interaction reported in Scheme 2.1. Different information can be achieved depending on the proton affinity (PA) or Lewis basic character of the probe, enabling the identification of Brønsted and Lewis acidic sites, their strength and accessibility.[31,153,166,167] The vibrational modes of Brønsted sites are influenced by the PA of the probe and also by the dimensions of the cavities and by the degree of pore filling. Contrary, the interaction of a bases (B) with Lewis acidic sites can be only monitored by the modification of the IR spectrum of the base.[30]

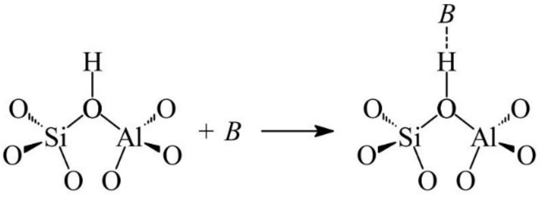

Scheme 2. 2. Formation of acid-base adduct between a zeolitic Brønsted acid and a base B via a classical acid-base reaction.[31]

N_2 adsorption at LNT:[168] the interaction of N_2 with the surface hydroxyl groups of zeolites can be observed at low temperature. The establishment of a weak H-bond induces a downward shift of the ν(OH) involved and an upward shift of ν(N≡N), which is proportional to the acidic character of the OH group.[167] Also Lewis acidity can be detected observing the shift of ν(N≡N) (only Raman active mode, falling at 2321 cm^{-1}) due to electronic σ-donation or π-backdonation of transition metals to the diatomic molecule.[169]

The adsorption of N_2 has been performed by employing home-made cells for in situ measurements at the temperature of liquid nitrogen. The activated samples, in form of self-supporting pellets are located in the cell and the system is cooled down with liquid nitrogen. Then, increasing pressure of gas N_2 are dosed by means of a glass line connected to the FT-IR cell, while acquiring consecutive spectra.

CO adsorption at RT and LNT: the dipolar CO molecule interacts with the positive charges located on the catalysts surface by sharing the HOMO electronic pair localised on the C atom. This polarisation induces an upward shift of the free molecule IR vibrational band (2143 cm^{-1}). If CO interacts with the localised positive charge of metal cations, the hypsochromic shift can be appreciated also upon adsorption of the molecule at Room Temperature (RT). This experiment is conducted by subjecting the samples to increasing pressure of gas CO by means of a glass line connected to the FT-IR cell, while acquiring consecutive spectra. If the system is cooled down with liquid nitrogen, the CO adsorption is enhanced, and the molecule can establish interaction also with the Brønsted acidic sites. The CO in contact with the surface at LNT condenses and generates a strong signal of the liquid-like vibration. Therefore, for appreciating the spectral features arising from the CO interaction with the active sites, the excess of molecule must be desorbed from the surface, by static vacuum outgassing. The spectra are collected when the equilibrium pressure is reached at each outgassing step.

Pyridine and methyl substituted pyridines (Py): the strong pyridine bases interact with zeolites surface as already described in Section 1.4.2. The experimental procedure involves the direct dosage of Py vapour tension over the sample surface at RT, by means of the *in situ* IR cell connected to the glass line. Once the first spectrum has been acquired, the sample must be then subject to *ex situ* thermal treatment at 200°C for 1 hour, in order to remove the excess of adsorbed Py. A last spectrum is now acquired for exclusively visualising the effect of the irreversibly adsorbed fraction of Py over the sample.

2.3.2. UV-Visible spectroscopy

Diffuse Reflectance DR-UV-visible spectra have been collected with a Varian Cary 5000 UV-vis-NIR spectrophotometer working in diffuse reflectance mode in the 200-2500 nm, with resolution of 1 nm.

This spectroscopic investigation is particularly useful for the characterization of zeolitic active sites constituted by metal centres in isomorphic substitution. It is possible defying the oxidation state or the coordination sphere of the heterometal, by the assignation of the electronic transition induced by the light absorption.

2.4. Catalysis

2.4.1. Hydroconversion of n-decane catalysed by ZSM-5 zeolites

The materials described in Chapter 3 (acidic hierarchical MFI zeolites H-mM-Z) have been tested in the catalytic hydroconversion of n-decane and compared with two reference materials, a commercial ZSM-5 and an Al-MCM-41. The analysis of the products obtained during the hydroconversion reaction of a model long chain n-alkane can give precious information about the location of active sites and about the inner space architecture of a zeolitic structure. To this purpose, the acidic zeolite was loaded with Pt particles constituting a bifunctional catalyst. these catalytic test set of experiment have been performed at Professor Martens' laboratories at KU Leuven University.

The samples were firstly loaded with the 0.3% (w/w) of Pt, by wet impregnation with an aqueous solution of $Pt(NH_3)_4Cl_2$ (Sigma-Aldrich, 98%). Once dried, the powders were pelletized and inserted in a high throughput reactor, from home-made design of KU Leuven University.[170] In each experiment, 50 mg of bifunctional catalyst pellets were loaded in quartz reactor tubes with internal diameter of 2 mm. The materials have been pre-treated in situ by heating to 400°C at 5°C/min under O_2 flow for 1 h, then flushed with N_2 for 25 min, and finally reduced in pure H_2 atmosphere at 400°C for 1 h. Before starting the feed n-decane injection the reactor has been cooled down to 100°C. The H_2/n-decane molar ratio in the catalytic experiments was 214, and the space time (W/F_o) 1400 kg s/mol. The reaction temperature was increased stepwise at constant space time. The reaction products were sampled for in-line gas chromatographic (GC) analysis 1 h after reaching a temperature set point with a rising slop of 5°C for every step until complete conversion of the feed n-decane was reached.

The catalytic hydroconversion involves two different types of active sites, the noble metal particles and the Brønsted acid of the zeolite. The reaction is initiated by the dehydrogenation of the alkane by the action of the noble metal functionality to form an alkene. The acidic Brønsted site is able to protonate the alkene forming an alkylcarbenium ion. The rearrangement of this cationic intermediate drives the generation of structural isomers passing by a cyclic iso-alkylcarbenium ion intermediate and then the cracked products can be generated by β-scission.[171] The shape selectivity of a zeolite is expressed by driving the location of the positive charge along the linear chain and thus the positional selectivity of chain branching or breaking.[172–174] The steric limitations imposed by a zeolitic lattice, combined with the distribution of the active sites stabilizes specific conformation of the alkylcarbenium ion intermediates, thus reflected in the selectivity for specific isomers and cracked products. Consequently, applying the backwards reasoning, knowing the nature of the products along all possible reaction pathways, it is possible to envision the shape and size of the zeolitic inner space. A list of specific criteria and the tabulation according to the opening diameter of the channels of the most common zeolite frameworks, makes the “n-decane test” an easy-to-read tool for disclosing new structures and their modifications.[172,175–177] It was applied on the materials reported in Chapter 3 to investigate the activity as well as the spatial constraints around the active sites contributing to the catalytic shape selectivity.

2.4.2. Partial oxidation HPPO catalysed by TS-1

The epoxidation of propylene using H_2O_2 as an oxidizing agent (HPPO process) has been performed over Ti containing materials and followed by in situ IR spectroscopy. The reaction has been selected as test for evaluating the catalytic activity of the samples synthetized as reported in Chapter 5. The IR spectra were acquired in transmission mode with a Bruker Vertex 70 spectrophotometer equipped with a MCT cryodetector working at 60 KHz, collecting 16 scans for each spectrum with 2 cm^{-1} of resolution. The high working speed is needed for identify very rapid spectral changes expected for the instantaneous reaction of propylene epoxidation.

The reaction has been carried out on a thin pellet of the material insert in a home-made quartz cell for in situ FT-IR acquisitions, connected to a glass line for gas dosages. Before IR measurements, the one drop of H_2O_2 (30wt% in water, Sigma Aldrich) has been carefully deposited on the pellet which was then inserted in the cell and connected to the glass vacuum line. Afterward, the cell has been outgassed in order to remove the excess of the hydrogen peroxide from the reaction environment. When the diagnostic vibrational modes of H_2O_2 were significantly reduced (meaning that the excess fraction leaved the system) 50 mbar of propylene has been sent to contact the catalyst. The reaction was monitored spectroscopically, following the evolution of vibrational bands reliable to propylene oxide. To unequivocally identify the spectral features of different reagents/products, the spectra of TS-1 interacting with pure propylene and propylene oxide were used as comparison. In addition, the reactivity of the synthesized materials has been compared with the one of a commercial TS-1.

2.4.3. Methanol to olefins conversion catalysed by acidic MAPO-18

The conversion of methanol to olefins has been performed over H-SAPO-18 and H-CoAPO-18 at 400°C and followed by IR spectroscopy “in continuo” (i.e repeated, not delayed, *in situ* measurements), as reported in Chapter 9. The spectra have been collected by a Bruker Invenio R spectrophotometer with a MCT cryodetector working at 40 KHz, equipped with a AABSPEC 2000 multi-mode FT-IR cell operating in transmission, allowing high temperature and high pressure *in situ* measurements (Schematized in Figure 2.2).[178] The cell has been connected to a mass flow controller for the direct gas dosage within the measure chamber where the sample is located in form of self-supporting pellet of about 10 mg of pressed powder.

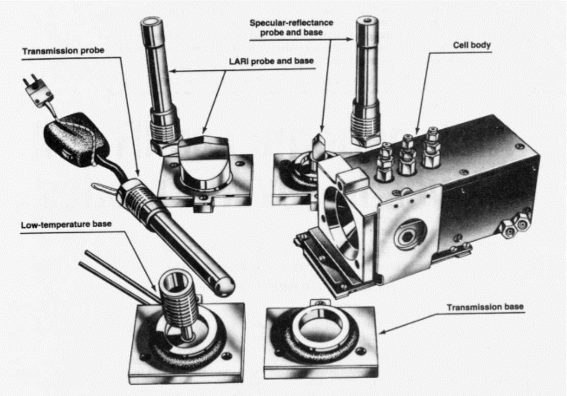

Figure 2. 2. Art graphic schematization of AABSPEC 2000 multi-mode FT-IR cell for high temperature and high pressure in situ measurements.[178]

***In situ* calcination experiments:** the samples (SAPO-18 and CoAPO-18) calcination has been conducted fluxing a mixture of N_2 (60 ml/min) and O_2 (20 ml/min) rising the temperature from 30°C to 550°C at 5°C/min rate while collecting IR spectra each three minutes, keeping the temperature constant until the disappearance of template (N,N-Diisopropylethyl amine) IR signals from the sample surface.

The methanol conversion experiments (MTO): it has been performed carrying the methanol vapours at RT (25°C) by N_2 (60 ml/min) passing through a saturator, directly into the AABSPEC cell where the catalysts (SAPO-18 and CoAPO-18 previously calcined) were kept at 400°C and ambient pressure. The reaction, at constant temperature, was followed for 1 or 4 hours by continuous acquisitions (not delayed) of IR spectra, accumulating 32 scans for each spectrum with 2 cm^{-1} of resolution. Considering the interferometer speed of 40KHz, each acquisition required 16 seconds which should be taken into account as a time-resolution for the interpretation of the spectral changes described in the results section. The regeneration of spent CoAPO-18 followed the same procedure of the catalyst calcination, implying a thermal treatment of 4 hours at 550°C under synthetic air flow: N_2 (60 ml/min) and O_2 (20 ml/min), acquiring no delayed spectra of 32 scans with 2 cm^{-1} of resolution.

Chapter 3: The hierarchical zeolites mM-Z

The possibility of obtaining a hierarchical material constituted by a thin layer of MFI framework have been critically evaluated by reproducing the synthesis published by Na et al. in 2011,[1] starting from the production of the non-commercial gemini type surfactant. The obtained materials have been finely characterized discovering all the aspects of the structural arrangement and the nature and distribution of the active sites. The unique shape size selectivity arising from the hierarchical organization has been then disclosed by testing the material in the catalytic hydroconversion of n-decane. All the process has been attended by the parallel study of two reference materials, a commercial ZSM-5 and a mesoporous Al-MCM-41 synthetised for the scope.

3.1. Synthesis

- **Synthesis of the bifunctional template ($C1_8$-N_3-C_{18})**

The synthesis of the non-commercial organic template was performed following the procedure published by Na et al. in 2011.[1] It is divided in three steps of nucleophilic substitution of a linear primary alkylic halide by a tertiary amine, in order to finally obtain a gemini surfactant containing 3 quaternary ammonium functionalities, presenting tow long alkylic chains C_{18}: **C_{18}-N_3-C_{18}**.

Step 1.

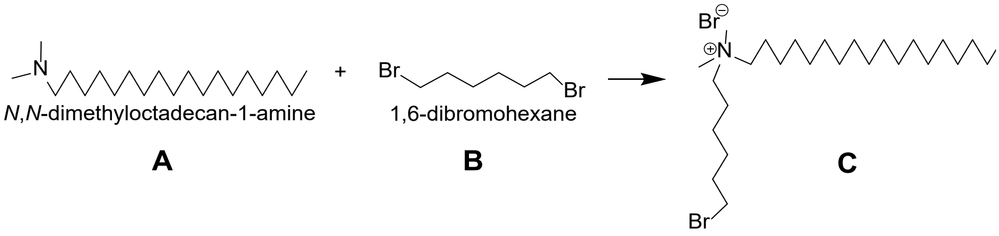

Scheme 3. 1

The reactants are introduced in a ratio A : B = 1 : 10 and solubilized dropwise (through a drip funnel) with a mixture 1:1 of acetonitrile and toluene within a three necks flask. The reaction is carried forward for 24h in reflux under stirring at 65°C. At the end of the reaction (monitored by TLC) the solvents are removed by evaporation under vacuum, obtaining an oily raw product. The product is then crystallized and washed from reactant residues by ethyl ether baths, under stirring for 2 hours and repeating the process three times. It is obtained a white precipitate, isolated by in vacuum filtration.

Step 2.

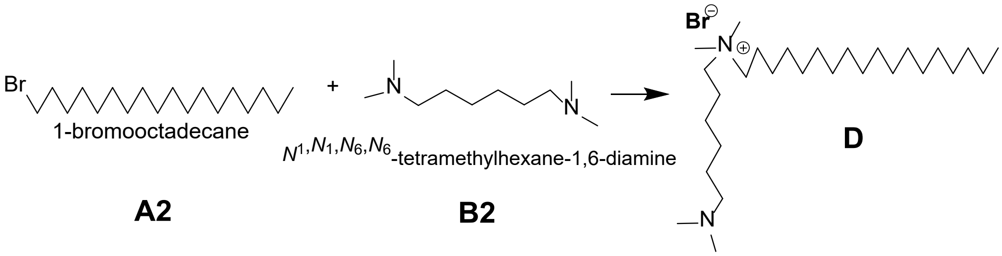

Scheme 3. 2

Same procedure applied in step 1.

Step 3.

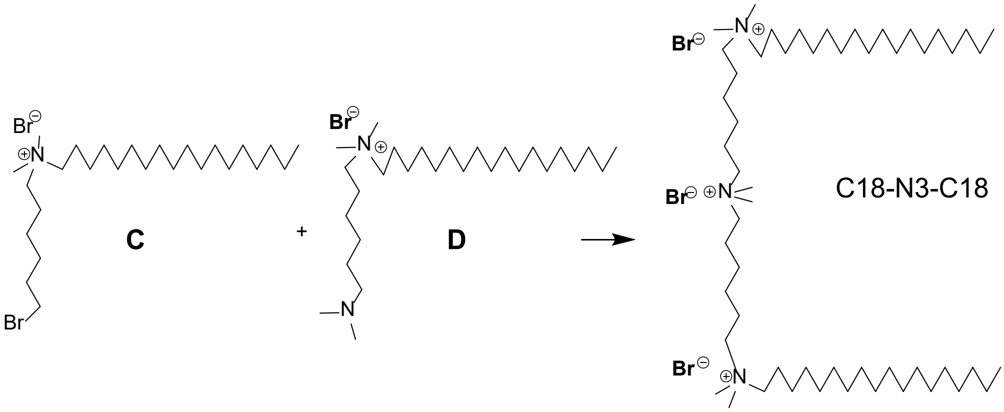

Scheme 3. 3

The products of Step 1 and 2 (C and D) are mixed together in ratio 1:1 and solubilized dropwise in acetonitrile (200% respect of the weight of one reactant) at 65°C. The reaction is conducted in reflux under stirring and monitored by frequent sampling and analysis by mass spectrometry. It is visible the progressive formation of a white solid, separated from the mother liquor by filtration. When no more solid is formed the reaction can be considered finished. All the produced solid (C18-N3-C18) is then repeatedly washed with ethyl ether, then air dried.

All the products have been analyzed by ^{1}H-NMR spectroscopy, confirming the success of the synthesis.

- **Synthesis of the hierarchical zeolite: mM-Z series**

The aluminum silicate materials denoted as mM-Z samples have been synthetized with sol-gel method followed by hydrothermal treatment, using the surfactant C_{18}-N_3-C_{18} as templating agent. The synthetic procedure has been repeated several times in order to evaluate the efficacy of the method and its reproducibility.

The gel composition is:

6.62 Na_2O: 0.75 Al_2O_3: 30 SiO_2: 1.5 C_{18}-N_3-C_{18}: 240 EtOH: 2132 H_2O

First an ethanol/ water (using half of the total necessary water) solution of C_{18}-N_3-C_{18} is prepared and kept under stirring, in reflux at 60°C until obtaining a clear liquid, with the formation of surfactant micelle. Then $NaAlO_2$ and NaOH are solubilized in the rest of the water, where it is also added the right volume of TEOS (Si source). This second solution is added dropwise in the first one and then kept for 6 hours under stirring at 60°C for the gelification. The temperature control has been performed by external electronic control of the heating system. The procedure has been also performed with a different temperature control: by direct measurement immersing a thermometer directly in the reaction liquor and adjusting the system heating to 65°C.

The white gel is then inserted in a steal autoclave for the tumbling hydrothermal treatment, in oven at 140°C for 8 days.

At the end, the obtained powder is in vacuum filtered and washed with water, then calcined in a tubular oven at 550°C for 7 hours fluxing dry air.

- **Synthesis of the mesoporous reference Al-MCM-41**

The mesoporous silicate MCM-41 was synthetized by sol-gel method followed by hydrothermal treatment, according to the procedure published by Vaschetto et al. in 2013.[179] As silicon source it was selected the tetraethyl orthosilicate (TEOS), sodium aluminate ($NaAlO_2$) as aluminum source, NaOH as mineralizer and Cetyl Trimethyl Ammonium Bromide (CTA-Br) as organic tamplate. The gel composition was chosen as follows:

Si/Al= 20; NaOH/Si= 0.50; CTA-Br/Si= 0.12; H_2O/Si= 132.

First, the NaOH is solubilized in H_2O within a tow necks flask, under stirring at 40°C in reflux, then the CTA-Br is added, followed by the TEOS, inserted dropwise. The aqueous solution is kept under stirring for 30 minutes at constant temperature. After this time, it is added the $NaAlO_2$ and the mixture is stirred for 4 hours at room temperature, to promote the formation of the gel. At the end, the solution is inserted in an autoclave for the hydrothermal treatment at the constant temperature of 100°C for 2 days. Finally, the material is separated by filtration, washed with water and then calcined overnight at 550° in N_2/O_2 atmosphere for removing the organic template.

- **Cation exchange of the aluminosilicate materials**

In the present work, all the aluminum silicates (Al-MCM-41; mM-Z series) are synthetized in sodic form. In order to obtain Brønsted acidity, the cation Na^+ must be exchanged with H^+. The strategy adopted for this cation exchange is: washing per 6 hours the materials with a solution 1M of NH_4NO_3 at 80°C, centrifuge and repeating the treatment three times. NH_4^+ substitutes Na^+ in the aluminum silicate structure and finally, NH_3 is removed by calcination at 500°C, leaving only H^+ for charge balancing, giving the material acid character.

3.2. Characterization of the hierarchical mM-Z materials

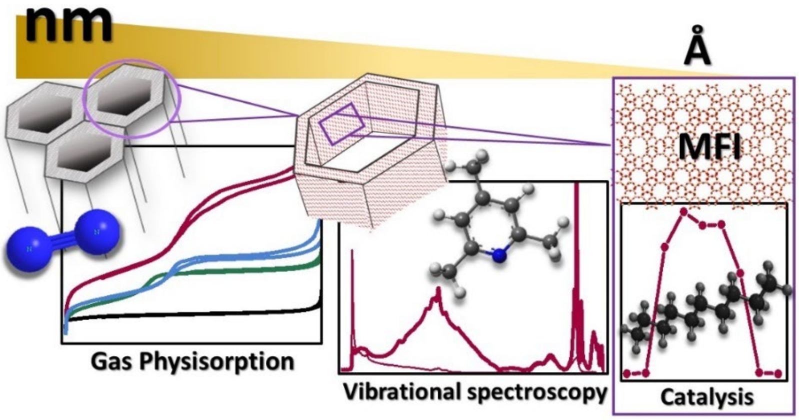

Figure 3. 1. Graphical abstract created for the work Airi et al. 2021.[157] *The picture highlights the interplay between the different techniques for describing the material from the structural arrangement to the active sites.*

After the replication and optimization of the synthetic strategy we carried out a tailor-made advanced characterization procedure for disclosing the nature, abundance and distribution of the catalyst active sites, highlighting how the peculiar hierarchical organization affects the shape-size selectivity of the MFI framework. The multi-technique approach was principally based on crossing the results of vibrational (Infra-Red and Raman) spectroscopies with a targeted catalytic test, taking in consideration the textural properties emerged from the application of different models of N_2 physisorption at liquid nitrogen temperature. More in depth, an extensive investigation was carried out for identifying the nature and the arrangement of the active sites of the catalyst in its acidic form by *in situ* IR spectroscopic[31] coupled with the adsorption of appropriate probe molecules with both different basic character and steric hindrance.[152,180,181]The catalytic hydroconversion reaction of n-decane has been applied in the so-called “decane test” , which represents a powerful “characterization” technique for disclosing the inner space of a zeolitic material, through the evaluation of isomerization and cracking products during all the conversion pathway (See section 2.4.1). The same characterization approach has been carried out on two reference materials, an aluminum containing MCM-41 as mesoporous model and a commercial ZSM-5 as zeolite reference, in order to rationalize the results and find differences and similarities with the two known systems.

The complete work is reported in the publication Airi et al. 2021 (Appendix I).[157] Reproducing several times the synthesis reported in the literature, a considerable influence of the gel aging temperature on the final characteristics of the material emerged, in particular on the level of crystallinity. The products described, named mM-Z1 and mM-Z2, present considerable difference in terms of structure and crystallinity. While the first one evidently presents characteristics traceable to the MFI framework (vibrational modes of pentasil units) and has an ordered mesoporous structure (visible in the TEM images), the second instead seems to have structural characteristics very close to those of an amorphous silica. At the same time, however, from the results obtained through the physisorption of N_2 at 77K the presence of an ultra-microporous system of comparable size to those of a bulk ZSM-5, as well as a heterogeneous system of mesoporosity, were found for both. The nature of the acid sites was determined by means of *in situ* IR spectroscopy. The adsorption of CO showed that the nature and acid strength of the Brønsted sites is equivalent to that of a bulk ZSM-5; while their concentration (quantified by pyridine adsorption) is significantly lower than the parent zeolite. It is due to the frequent distorted coordination of partially in-framework aluminium, that generates Lewis acidity, comparable to that of Al-MCM-41. However, the proof the samples includes the MFI zeolite framework becomes from the results of the decane test, finding correlation also with other hierarchical structures.[111,182] Both samples show the shape selectivity of a 10RM lattice and the distribution of decane conversion products typical of a ZSM-5, which is operated by the action of acid sites located at the mouth of the ultra-micropores. In addition, the material has improved characteristics compared to bulk zeolite in terms of transport and diffusion of reaction products (it can easily release structural isomers) due to the mesoporous system, which at the same time limits secondary cracking. These characteristics are more pronounced in the mM-Z2 sample, which deviates more from the bulk zeolite ZSM-5 than mM-Z1, which probably presents segregated regions of MFI crystal domains. It was possible to exclude that mM-Z2 corresponds to an amorphous silica, as evidenced by the total absence of activity and selectivity of the reference Al-MCM-41. Therefore, it can be concluded (also comparing the data of the decane test with two-dimensional hierarchical systems as MFI nanosheets),[183] that the mM-Z hierarchical structure is constituted by mesoporous channels, with hexagonal section, whose walls are made up of MFI framework that exposes the totality of its acidic sites, in correspondence with the mouths of the micropores, on the mesopores surface, which is accessible also for bulky substrate (as also demonstrated by the adsorption of 2,4,6 collidine).

The structure of mM-Z can be effectively categorized in the definition of reverse hierarchy.[145] Moreover, it should be noted that a higher level of crystallinity does not improve the performance of this material in reactions such as the hydroconversion of the decane. Instead, it is the synergy between the different levels of porosity that defines its peculiar characteristics and influences its catalytic properties.

Chapter 4: Synthesis of mesoporous Silicalite-1 employing commercial templating agents

The technique of nanoassembling proto-zeolitic domains of Silicalite-1 (S1) has been tested for the production of hierarchical materials employing commercial surfactants as mesoporogen agents. The synthesis of Zeotiles-2 from Kirschhock et al.[184] has been reproduced employing CTA-Br for assembling the S1 domains. Then, the same procedure has been adopted substituting CTA-Br with the non-ionic surfactant *p-tert-octylphenoxy polyethylene ether* (Triton-X100), for evaluating the changing in morphology induced by the different molecule.

The study proceeded trying to modify the micellization conditions of Triton-X100 by the addiction of cinnamic acid solution. As reported in the literature, this should induced the formation of road like micelles of Triton-X100 instead of spherical ones, depending on the concentration of the cinnamic acid solution in which the surfactant is solubilised.[185] The scope of this research is to find the conditions for the hierarchization of the MFI framework by adopting an easy synthetic way and employing cheap, environmental friendly templating agents.

4.1. Synthesis

- **Synthesis of Zeotiles-2**

The synthesis has been performed replicating the procedure described by Kremer et al.[184] starting with the production of a solution with the molar composition:

1 TEOS: 0.35 TPAOH: 93.09 H2O

TEOS was solubilized in an aqueous solution of TPA-OH resulting in a clear solution, which was left under stirring for 24 hours at RT within a PP bottle, in order to allow the full hydrolysis of the silicon precursor and the formation of the nanoslabs. The day after, an aqueous solution of CTA-Br (25 %) was introduced into the clear solution for reaching the ratio TEOS : CTA^+ = 1 : 0.46 and adding the water content needed for satisfying the stoichiometry above reported. The resulting slurry was left at RT under stirring for other 24 hours. Afterwards, the crystallization has been induced by thermal treatment in quiescent conditions at 97°C for 80 hours within PET bottles.

The characterization results of this synthesis are not reported here since the obtained materials were totally comparable with the literature reference.[184]

- **Modified synthesis of Zeotiles-2 with Triton-X100 and cinnamic acid**

The same procedure has been reproduced by substituting CTA-Br with the same amount of Triton-X100 solubilized in a 0.40 M solution of cinnamic acid, keeping the total water content univariate, for a molar composition:

1 TEOS : 0.35 TPAOH : 0.46 Triton-X100 : 0.1 CinAc : 93.09 H_2O

The sample S1_TX100_A (Table 4.1) has been obtained.

The synthesis has been reproduced again halving the Triton-X100 molar content, obtaining a solution with the composition:

1 TEOS : 0.35 TPAOH : 0.23 Triton-X100 : 0.1 CinAc : 93.09 H_2O

for the production of the sample S1_TX100_B (Table 4.1).

- **Modification of the synthesis with Triton-X100 and cinnamic acid**

The sample S1_TX100_Ref (Table 4.1) has been synthesized without cinnamic acid and avoiding the use of TPA-OH, for evaluating the real impact of the acidic additive in modifying the behavior of Triton-X100 as templating agent for the mesoporous silicate formation.

The sample has been produced with a solution composition:

1 TEOS : 0.23 Triton-X100 : 93.09 H_2O

The clear solution has been stirred at 50°C for favoring the Triton-X100 solubilization, which forms a viscous mixture with water. This parameter has been kept constant in the synthesis described below.

In order to understand the action of combining Triton-X100 and cinnamic acid, the same synthetic procedure has been repeated and modified as follows.

The stoichiometry was kept fixed to

1 TEOS : 0.23 Triton-X100 : 0.1 CinAc : 93.09 H2O

while the process parameters have been systematically changed.

The first synthetic screening, obtained by variating the main process parameters, produced the set of samples listed in Table 4.1. Each type of synthesis is indicated with a capitol letter from C to F, indicating the variations of four main parameters: aging time and temperature, crystallization time and temperature.

Table 4. 1. List of the most representative samples synthetised in presence of Triton-X100 and the process conditions adopted.

Sample name	**Additive**		**Si/Triton X100**	**Clear solution**		**Aging time with TX100**	**Crystallization conditions**	**Crystallization**	
	TPA-OH	**CinAc**		**Temperature**	**Stirring time**			**Time**	**Temperature**
S1_TX100_A	x	x	1 : 0.46	RT	24 h	/	Quiescent	80 h	97°C
S1_TX100_B	x	x	1 : 0.23	RT	24 h	24 h	Quiescent	80 h	97°C
S1_TX100_Ref			1 : 0.23	50°C	24 h	/	Static autoclave	80°C	97°C
S1_TX100_C		x	1 : 0.23	50°C	24 h	24 h	Static autoclave	48 h	110°C
S1_TX100_D		x	1 : 0.23	50°C	12 h	4 h	Static autoclave	24 h	140°C
S1_TX100_E		x	1 : 0.23	50° C	3 h	24 h	Quiescent	80 h	97°C
S1_TX100_F		x	1 : 0.23	50°C	30 h	none	Static autoclave	4 days	110°C

After crystallisation, all the solid precipitates appeared as hydrated gels, which have been separated to the solution by in vacuum filtration and washed with abundant deionised water, then left to exsiccate at 80°C. S1_TX100_F has been tested for freeze drying template removal, operating the sublimation of the water/surfactant solution trapped in the pores after calcination.

The obtained powders have been finally calcined at 550°C under air flow.

4.2. Structure characterisation of the first screening set of samples

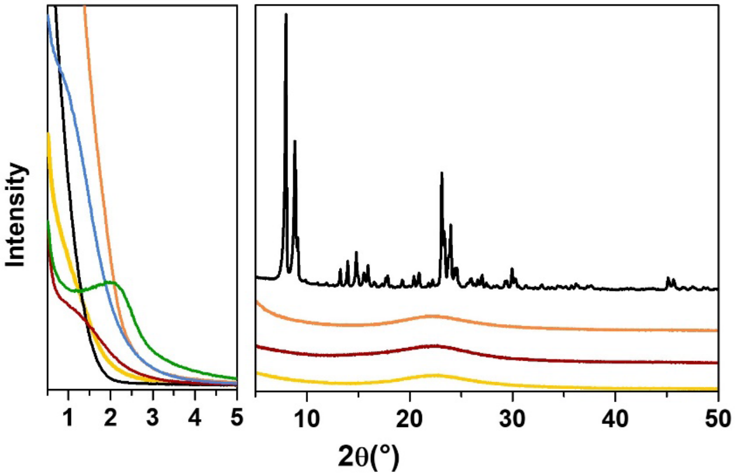

Figure 4. 1. P-XRD patterns of S1_TX100_B (black), S1_TX100_Ref (yellow), S1_TX100_C (red), S1_TX100_D (blue), S1_TX100_E (green), S1_TX100_F (orange) in the low angles region (left panel) and in wide angle region (right panel, only selected samples).

Merging the structural and textural information arising from the analyses of XRD (Figure 4.1), N_2 physisorption at liquid nitrogen temperature (LNT) (Figure 4.2 and Table 4.1) and TEM micrographs (Figure 4.3) it is possible to rationalize the results obtained with the modified synthesis. Samples S1_TX100_A and S1_TX100_B differs from the others, since they have been produced in presence of TPA-OH. Only the characterization of S1_TX100_B is reported here because the materials did not present any difference, indication that the concentration of Triton-X100 does not affect the structural characteristics of the sample. S1_TX100_B present the diffraction pattern of the MFI framework[186] (Figure 4.1).

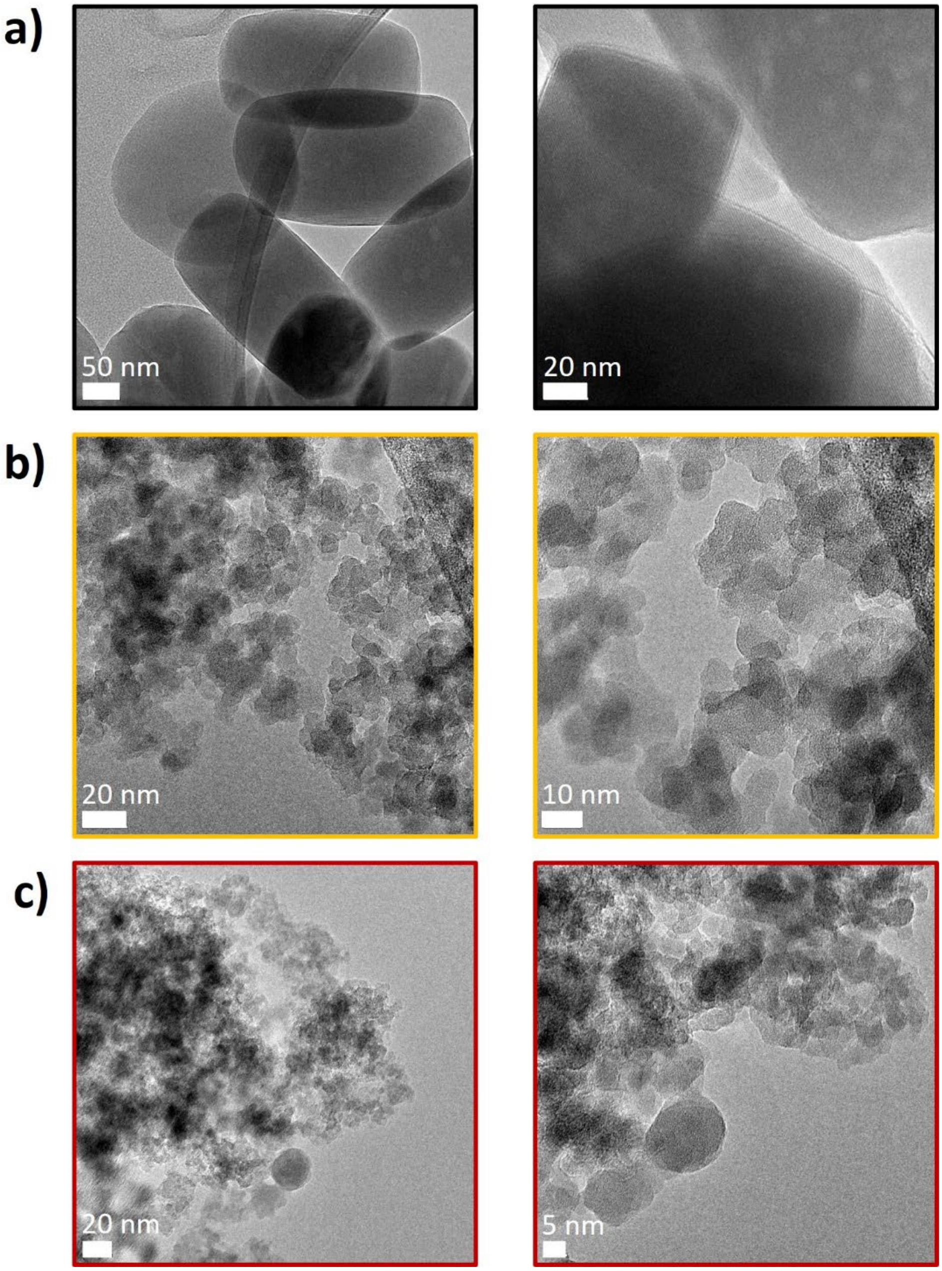
a)
50 nm
20 nm
b)
20 nm
10 nm
c)
20 nm
5 nm

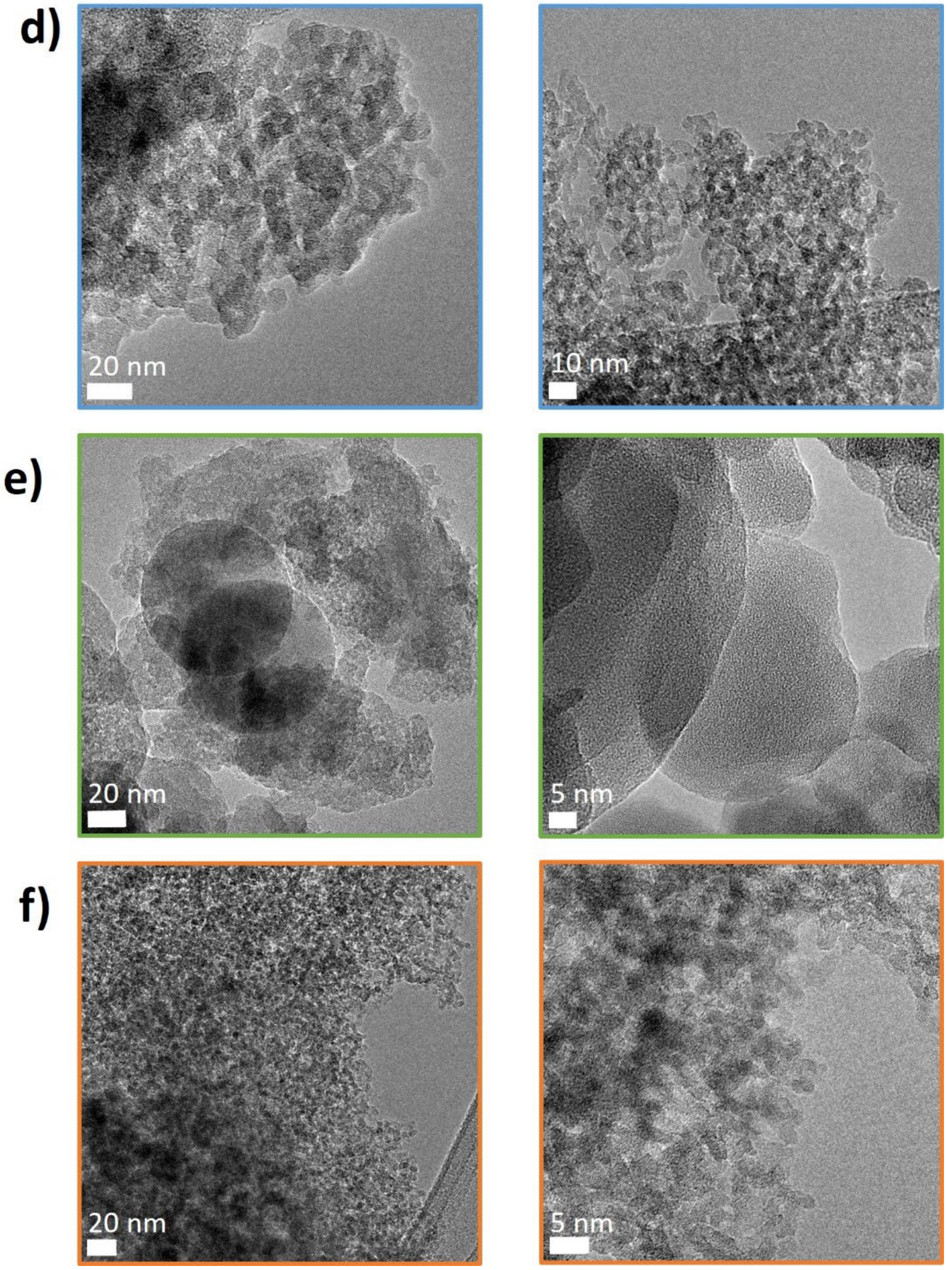

Figure 4.2. TEM micrographs of: S1_TX100_B (a), S1_TX100_Ref (b), S1_TX100_C (c), S1_TX100_D (d), S1_TX100_E (e), S1_TX100_F (f).

The textural characterization performed by N_2 physisorption and analysed by NL-DFT, are in agreement with the XRD results, showing a Type I isotherm due to the adsorption at low T within of a single family of ultramicropores with a diameter of 0.55 nm, compatible with the MFI framework. The TEM micrographs (Figure 4.2 a) show uniformly sized plate particle with average dimensions of 200-300 nm, well visible in the left panel of Figure 4.2. At higher magnification (right panel Figure 4.2 a) the parallel microporous channels of the MFI are distinguishable in the bright zone of the image. The very regular particle shape together with the diffractogram obtained for the sample S1_TX100_B indicate the formation of perfectly crystallized Silicalite-1 zeolite. The elongated plate morphology is typical of Silicalite-1 crystals, compatible with the best examples collected in the literature. Therefore, it is possible to assert that the synthetic strategy failed in assembling the S1 nanoparticles in a mesostructured hierarchy, reasonably because the presence of TPA-OH hampers the micellization of Triton-X100. At the same time, however, extremely regular zeolitic crystals have been obtained under mild conditions (sub-hydrothermal). A positive influence of Triton-X100 in dispersing the S1 nuclei and allowing a favourable nanocrystal formation is supposed, even if the latter observation requires to be confirmed by producing reference materials in comparable conditions.

Due to the results obtained with the samples S1_TX100_A and S1_TX100_B, the study proceeded evaluating the effect of Triton-X100 as mesoporogen in absence of TPA-OH. The sample S1_TX100_Ref has been produced with this purpose. In Figure 4.1 (yellow line) it is possible to see that S1_TX100_Ref presented none XRD reflections and the profile of a completely amorphous material. Accordingly, the TEM micrographs (Figure 4.2 b) do not show a regular organization, indeed the particles are organized in globular disordered clusters. The N_2 physisorption at LNT revealed a quite low N_2 uptake resulting in Type II isotherm (Figure 4.3 b), generally found for non-porous materials with a resulting BET specific surface area of 298 m^2/g, lower than that of the previously reported samples (Table 4.2). The BJH[187] model has been applied to the adsorption isotherm for the pores description, taking in mind that the application of such a model is a very strong assumption, since the presence of cylindrical pores is required for the correct calculation. BJH has been applied to all samples (excluding the microporous ones) as comparison element for evaluating the results of next synthesis. For S1_TX100_Ref a pore volume of 0.47 cm3/g for a family of mesopores with 5 nm diameter has been obtained by BJH analysis. This is considered a non-significant value, but only a term of comparison. The very low surface area and the totally amorphous nature of S1_TX100_Ref induced to consider that the spherical micelles of Triton-X100 in water are unable to drive the formation of an ordered mesoporous silicate structure (with accessible open pores). These observations stimulated the idea of modifying the Triton-X100 micelles from spherical to road like, aiming to form cylindrical mesopores (tunnel like) inducing the silicate growth around the micelles. The formation of road like micelles of Triton-X100, as reported in the literature, can be achieved by solubilizing the surfactant in an aqueous solution of enolic acids, among which cinnamic acid is the most effective.[185] The surfactant dissolved in cinnamic acid was directly applied to the synthesis of the silicates to evaluate its effect on the structure. Until now, to adequately evaluate the shape of the micelles in acid solution was not possible, since it requires expertise belonging to surfactants chemistry, but it is planned for the near future for deepen the ongoing research. The next samples obtained are those labelled from C to F, as described above. These four samples have been carefully characterized through XRD, TEM and N_2 physisorption at LNT. In Figure 4.1 it can be observed that none of them shows diffraction reflections, demonstrating a substantially amorphous nature, except for sample S1_TX100_E (the diffractograms shown were obtained on calcined samples). It is very interesting to observe that sample S1_TX100_E (green line) shows a reflection at 2.5° 2θ, suggesting the presence of a long-distance order, compatible with the diffraction of the planes that constitute the walls of a mesoporous silicate system, sufficiently ordered to generate such a reflection (similar to ones observed in M40s silicas).[71] The sample S1_TX100_C present a quite disordered morphology, as visible in TEM micrographs (Figure 4.2 c), which is more organized in S1_TX100_D and S1_TX100_F, which are formed by rather uniform spherical particles with average diameter of average 5 nm (Figure 4.2 d and f). These three amorphous samples present type IV N_2 isotherms with differently shaped hysteresis loops, indicating the presence of mesopores. A relevant increasing of the pore volume and BET surface areas respect to S1_TX100_B and S1_TX100_Ref is attested, with values higher than 600m^2/g (Table 4.2). However, the pores size distribution, determined by BJH analysis (again the application of the model requires a strong assumption, since it is based on a cylindrical geometry of pore diameter > 2nm) is very broad, ranging from 4 to 12 nm and reasonably with not uniform shape. Comparing the physisorption data with the TEM images it is assumed that the recorded mesoporosity is reasonably represented by interparticle voids in which capillary condensation occurs, while the very high BET surface is due to the very low particle size. The synthesis C, D and F where not successful in obtaining ordered mesoporous materials, anyhow the produced material present same element of interest, which are the nanosized dimensions (around 5 nm) and the very relevant interparticle mesoporosity, important features for catalytic applications. Different observations must be reserved to S1_TX100_E. As mentioned above, this samples present a low angle diffraction peak, indicating a long-distance order. Moreover, regular shaped particles of about 100 nm with spherical morphology are visible in the TEM micrographs (Figure 4.2 e). No mesoporous openings are distinguishable in the images, but this may be due to the sensitivity of the sample to the electron beam damage and to the difficulties of focusing such a light material. In fact, the sample has a very low density, as can be seen from the exceptionally high BET surface area value of 1273 m^2/g as reported in Table 4.2. Accordingly, with the XRD pattern, this material presents the characteristics of a narrow mesoporous solid, with a Type IV (b) N_2 physisorption isotherm. The BJH pore size analysis (which is more realistic for this sample, due to the low angle XRD reflection) shows a monodispersed and narrow distribution of pores with 3 nm diameter that represents a significant pore volume of 0.79 cm^3/g.

Table 4.2. Textural properties of the most relevant samples obtained by N_2 physisorption at LNT. The reference for the MFI framework is the commercial ZSM-5 Zeolyst CBV3024E.

Sample name	**B.E.T SSA (m^2/g)**	**Langmuir SSA (m^2/g)**	**[a] NL-DFT Total pore volume (cm^3/g)**	**[c] BJH Total pore volume (cm^3/g)**	**[b] NL-DFT Average Micropore size (nm)**	**[d] BJH Average Mesopore size (nm)**
Reference MFI	381	507	0.19	/	0.55	/
S1_TX100_B	353	466	0.25	/	0.55	/
S1_TX100_Ref	298	406	/	0.47	/	5
S1_TX100_C	866	1210	/	1.04	/	4-8
S1_TX100_D	659	924	/	0.84	/	4-8
S1_TX100_E	1273	1795	/	0.79	/	3
S1_TX100_F	642	898	/	1.24	/	4-12

[a] Calculated by cumulative pore volume graph obtained from NL-DFT analysis of the adsorption isotherm.

[b] Calculated by pore size distribution graph obtained from NL-DFT analysis of the adsorption isotherm

[c] Calculated by cumulative pore volume graph obtained from BJH model applied to the adsorption isotherm.

[d] Calculated by pore size distribution graph obtained from BJH model applied to the adsorption isotherm

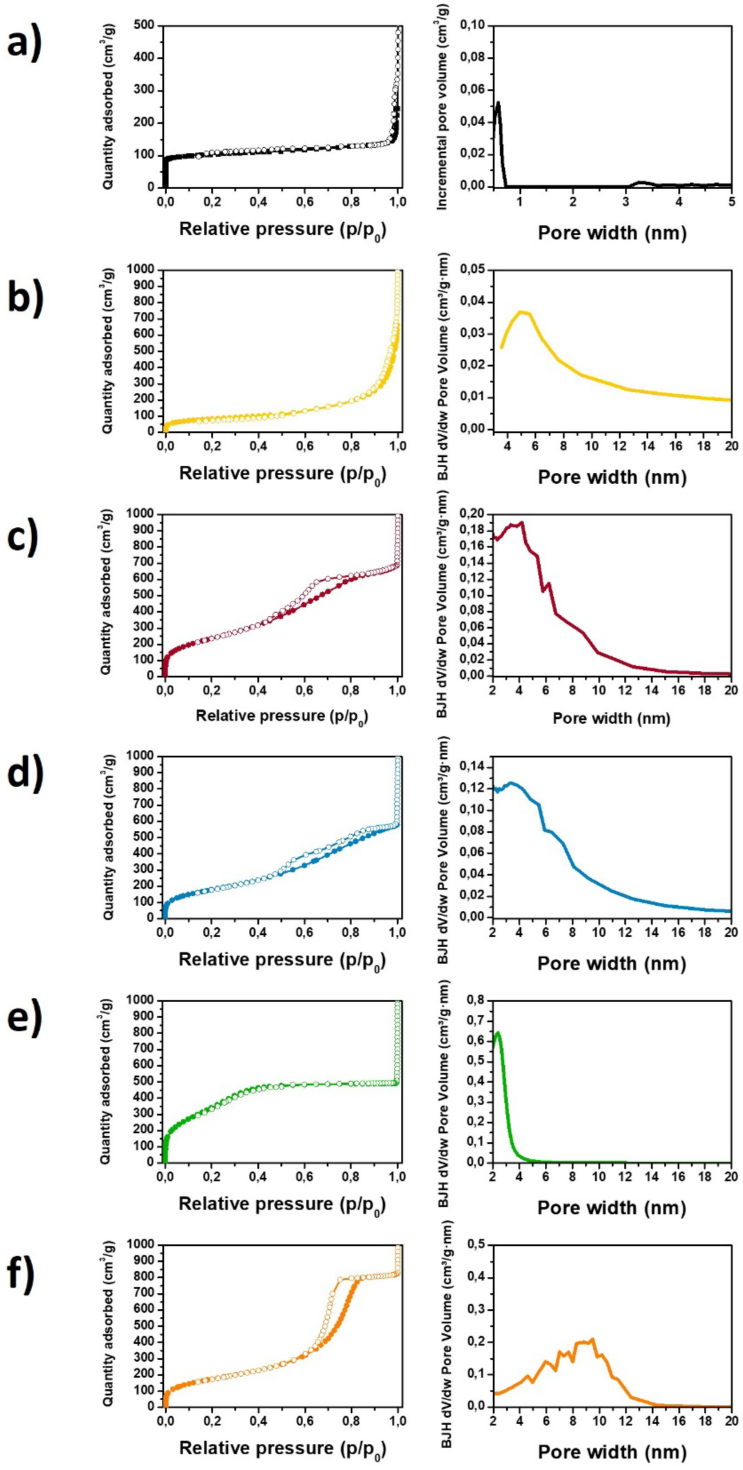

Figure 4.3. N_2 physisorption isotherms at LNT (right panels) and pore size distributions of S1_TX100_B (a), S1_TX100_Ref (b), S1_TX100_C (c), S1_TX100_D (d), S1_TX100_E (e), S1_TX100_F (f).

4.3. Further screening sets of samples

Afterward, due to the promising results obtained for the sample S1_TX100_E, the type of synthesis E has been selected for a second screening of the synthesis variables, pointed to rationalize the conditions that favors the structural order and the monodisperse distribution of the mesopores population. Therefore, the aging and crystallization conditions have been systematically observed by producing the samples collected in the table 4.3. In particular, three different series of samples have been produced: samples E23_A have been crystallized at 80°C, E23_B at 140°C and E23_C at 110°C. Samples E23_P are attempts in changing the Triton-X100-Cinnamic acid ratio. The Table reports the process parameters adopted and the most relevant information reached from each sample from preliminary characterization by XRD of the calcined materials.

Table 4. 3. Screening sample sets, obtained variating the process parameters of synthesis E. The coloured cells highlight the sample that present a significant variation from the parent S1_TX100_E.

Sample name	**Aging time**	**Aging T**	**Crystalliz. time**	**Crystalliz. T**	**Crystalliz. cond**	**Observations**
E23_A0	24h	RT	96 h	80°C	autoclave	2.5° 2θ reflection
E23_A1	24h	40°C	96 h	80°C	autoclave	2.5° 2θ reflection
E23_A2	24h	50°C	96 h	80°C	autoclave	2.5° 2θ reflection
E23_A3	24h	60°C	96 h	80°C	autoclave	amorphous
E23_A4	24h	50°C	48 h	80°C	quiescent	2.5° 2θ reflection
E23_A5	24h	50°C	48 h	80°C	autoclave	2° 2θ reflection
E23_A6	24h	50°C	24 h	80°C	autoclave	2.5° 2θ reflection
E23_A7	24h	50°C	72h	80°C	autoclave	2° 2θ reflection

E23_A8	24h	50°C	72h	80°C	quiescent	amorphous
E23_P1 (2x CinAc)	24h	50°C	24h	110°C	autoclave	amorphous
E23_P2 (½ CinAc)	24h	50°C	24h	110°C	autoclave	2° 2θ reflection
E23_B1	24h	40°C	96h	140°C	autoclave	1° 2θ reflection
E23_B2	24h	50°C	96h	140°C	autoclave	1° 2θ reflection
E23_B3	24h	60°C	96h	140°C	autoclave	amorphous after calcination
E23_B4	24h	50°C	24h	140°C	autoclave	1° 2θ reflection
E23_B5	24h	50°C	48h	140°C	autoclave	1° 2θ reflection
E23_C4	24h	50°C	24h	110°C	autoclave	not analyzed yet
E23_C5	24h	50°C	48h	110°C	autoclave	not analyzed yet

The screening sets reported in Table 4.3 brings out some interesting information that allows to outline a certain trend in the results, identifying an influence of temperature and duration of crystallization conditions on the final material. In general, it is observed that shortening the crystallization time produces samples presenting XRD reflection at slightly lower 2θ angles (ideally larger pores). In particular the E23_A samples, crystallised for less than 96 hours present a single reflection at 2° 2θ (grey boxes). The synthesis performed in proper hydrothermal conditions (autoclave at 140°) produced the E23_B samples, for which the reflection is shifted to 1° 2θ (yellow boxes). The textural characterisation is required for evaluating if the XRD results find some correspondence with an ordered and narrow distributed pore population. If the correspondence between XRD reflection and pore size (achievable by gas physisorption, which will be performed soon) will be confirmed, the results showed in Table 4.3 would indicate that the pore size of these silicates is modulable by controlling time and temperature of crystallisation.

The synthesis type B has been deepened as well, in order to identify the conditions for avoiding the exclusively formation of MFI crystals, as discussed for sample S1_TX100_B. The preliminary screening produced the samples listed in Table 4.4. Unfortunately, non-significant differences from the S1_TX100_B have been recorded. This can confirm the hypothesis of TPA-OH hampering the micellization of Triton-X100 in cinnamic acid solution, which, as demonstrated with the previous results, is effective in driving the formation of mesoporous silicates.

Table 4. 4. Screening sample set, obtained variating the process parameters of synthesis B.

Sample name	Aging time	Aging T	Crystalliz. time	Crystalliz. T	Crystalliz. cond	Remarks
B23_A0	24h+24h	RT	80h	110°C	autoclave	MFI
B23_A1	24h+24h	RT	72h	80°C	autoclave	MFI
B23_A3	24h+24h	RT	24h	80°C	autoclave	no precipitate
B23_A4	24h+24h	RT	48h	80°C	autoclave	MFI
B23_A5	24h+24h	RT	96h	80°C	autoclave	MFI

Chapter 5: Synthesis of mesoporous Ti-Silicalite-1

Following different literature references a synthetic strategy for the production of a hierarchical form of Titanium Silicalite-1, employing cheap precursors and templating agents, has been proposed. Again, the synthesis of Zeotiles-2[184] has been chosen as starting point for the creation of a hierarchical structure, while the literature regarding TS-1 has been followed as model for the careful insertion of Ti(IV) in framework.[188] Some attempts of this synthesis procedure are reported, testing two different commercial mesopore templating agents. Other synthesis parameters taken into account, were the crystallization temperature and the aging treatment duration. The target material should respect the definition of hierarchy, presenting both the MFI microporous framework and the mesoporosity induced by the second template. At the same time particular attention was devoted to the evaluation of the correct insertion of Ti^{4+} as isomorphous substitute of Si^{4+} in the lattice, determined through diagnostic DR-UV-vis, ATR-IR and Raman signals.[189–193] Finally, the existence of proper active sites has been tested performing the Hydrogen Peroxide to Propylene Oxide (HPPO) reaction over the most promising sample, followed by in situ FT-IR spectroscopy.

5.1. Synthesis

- **Synthesis of conventional TS-1**

The synthesis has been performed adapting the procedure described by Zile Hua, Jianlin Shi et al.[194] producing a solution with the molar composition:

1 TBOT: 50 TEOS: 13.5 TPAOH: 100 i-POH: 1460 H_2O

The hydrolysis of silicon and titanium precursors (TEOS and TBOT) respectively has been performed separately, in parallel. 6.35 ml of TPAOH have been solubilized in 13.1 ml of H_2O within a round bottom flask with the capacity of 50 ml, after what

5.58 ml of TEOS was added. The resulting solution (noted as solution A) was left for stirring for 4 h at 40°C, being connected to water-cooler condenser.

In a second 50 ml two-neck round bottom flask 0.061 ml of TBOT was added dropwise into 3.74 ml of isopropanol (solution B). The hydrolysis was performed in an ice bath, keeping the temperature at 4°C for 4 h. Low temperature conditions are needed in order to slow down the kinetics of TBOT hydrolysis preventing the formation of bulk TiO_2 and promoting the Ti(IV) insertion in the MFI framework. After 4 hours, both solutions A and B were cooled down to 4 °C. Then, the content of the solution A was added dropwise into the solution B. Subsequently, the final solution is left under stirring at 40°C for 24 h.

The resulting solution was transferred into 45 ml Teflon lined stainless steel autoclave and crystallized for 20 hours at 140°C in tumbling oven with 20RPM rotation speed. After crystallization, the product was separated by centrifugation and washed with abundant quantity of deionized water. The precipitate was left for drying in oven at 70 °C for 24 hours. Afterwards, the template removal has been performed to remove the microporous agents in tubular oven under air flow, heating up to 550 °C, with a heating rate of 2 °C min^{-1} and then keeping for 7 hours at reached temperature.

- **Synthesis of mesoporous Titanium Silicalite-1 by nano-assembling of protozeolitic units**[195]

The synthetic strategy chosen for the production of TS-1 starts from the precipitation of Titanium containing protozeolitic MFI nuclei formed by action of a quaternary ammonium surfactant, forming a colloidal solution. Then they are assembled together by action of different mesoporous generator commercial templates and crystallized by hydrothermal treatment.[184,196–199] The starting gel composition adopted is:[194]

88.8 SiO_2: 1.0 TiO_2: 13.5 TPA-OH: 1460 H_2O: 100 i-POH

For a Titanium content corresponding to TiO_2/SiO_2 = 1.12%.[18]

The general procedure implies the separate hydrolysis of Silicon and Titanium sources (Tetra ethyl orthosilicate TEOS and tetra butyl orthotitanate TBOT respectively) into different solutions. The first is composed by TEOS, tetrapropyl ammonium hydroxide and water and is kept under stirring for 4 hours at 40°C, contemporary TBOT is hydrolysed in iso-propanol at 4°C (ice bath) under stirring for the same time. After this aging period, the TBOT solution is inserted dropwise in the first one, then iso-propanol is removed by in vacuum evaporation. An amount of $(NH_4)_2CO_3$ is now added to the solution to facilitate the inclusion of Ti^{4+} in the silicalite lattice.[188] The resultant solution is kept under stirring for 24h at 40°C in order to favour the nucleation of microporous zeolitic domains by action of TPA-OH, forming a colloidal suspension. At the end of this first step the second template, for the generation of the mesopores, has to be added to the clear solution for inducing the assembling of the little zeolitic nuclei. Different commercial templates, usually applied for the synthesis of mesoporous silica, are being evaluated, that are: cetyltrimethylammonium hydroxide (CTA-OH) and Triton X100.[200] The percentage of template moles with respect to the Silicon content is also matter of investigation. The crystallization is generally conducted in a Teflon-lined steel autoclave, operating a screening of temperatures of crystallisation (100-140°C) and of the residence time (1-8 days) within a tumbling or static oven, the different synthesis conditions are listed in Table 5.1. At the end, the obtained powder is filtered under vacuum or centrifuged and washed with water, then calcined at 550°C for 7 hours in dry air flow.

- **Synthesis of TS1-CTAOH samples**

The synthesis of hierarchical TS-1 by nanoassembling driven by CTAOH surfactant has been performed, starting from a clear solution with the following molar composition:

1 TEOS : 0.35 TPAOH : 0.02 TBOT : 2 i-POH : 0.46 CTAOH : 93.09 H_2O : 0.03 $(NH_4)_2CO_3$ the general procedure is the following:

0.0613 ml of TBOT was hydrolyzed with 3.75 ml of isopropanol in ice bath at 4°C for four hours (solution A). In parallel, the hydrolysis of 5.59 ml of TEOS with 8.83 ml of TPAOH was performed for same quantity of time at room temperature (solution B). Then it was added to solution A and left for stirring at room temperature for 24 hours (solution C). In parallel, preliminary preparation of mesoporosity template has been done. In this case CTAOH or CTA-Br was used, 13.91 g of which was mixed with 42 ml of deionized water and left for stirring at 40°C with water-cooled condenser to avoid evaporation of components and change in molar ratio of the gel. This step has been done in order to promote the formation of stable micelles that act as SDA, creating desired mesoporosity level. The day after, the solution C was combined with the CTA^+ solution and the resulting gel was left under agitating at 60°C for one day. The crystallization (110°C, 72 hours, tumbling at 20RPM) was performed as listed in Table 5.1. During the last stage, when sample was transferred in autoclave, formation of silicon-like clumps was observed.

- **Synthesis of TS1-Triton X100**

The nanoassembling of TS-1 driven by Triton X100 has been designed, starting from the preparation of the precursors solution with composition:

1 TEOS: 0,.5 TPA-OH: 0,02 TiO_2: 2 i-POH: 93.09 H_2O: 0.2 Triton X-100: 0.2$(NH_4)_2CO_3$

The general procedure is:

the hydrolysis of Ti and Si precursors has been performed as described in the above reported synthesis. After the unification of the hydrolyzed TBOT and TEOS solutions, 0.346 g of ammonium carbonate was added, observing the formation of white clumps. After 20 minutes, the solution has been completely jellified, so the flask was connected to water-cooler condenser and heated up to 50°C in order to liquidize the gel and subsequently it was left for 24 hours under stirring. Next day, 2 ml of Triton X-100 with 30 ml of deionized water were added to reaction gel, keeping under mixing for 5 hours at 50°C. Then solution has been transferred to an autoclave for crystallization at 140°C for 72 h.

Table 5. 1. List of the synthetic conditions applied in the presence of mesoporogen templates.

Name	Mesopores Template	Temperature	Time	Crystallization conditions
TS1_CTA-OH_a	CTA-OH	Water reflux	24 hours	Flask, magnetic stirring
TS1_CTA-OH_b	CTA-OH	140°C	4 days	Tumbling autoclave
TS1_CTA-OH_c	CTA-OH	140°C	24 hours	Tumbling autoclave
TS1_CTA-OH_k	CTA-OH	110°C	72 hours	Tumbling autoclave
TS1_CTA-Br	CTA-Br	110°C	72 hours	Tumbling autoclave
TS1_TX100	Triton-x100	140°C	72 hours	tumbling autoclave

- **Synthesis of reference MCM-48**

MCM-48 has been synthetized following the rapid, RT, procedure reported by Kumar et al.[201] A starting gel with the molar composition:

1 TEOS: 12.5 NH_4OH: 54 EtOH: 0.4 CTABr: 174 H_2O

has been produced by solubilizing CTABr in water and ethanol within a PET bottle, followed by the addition of NH_4OH. The resulting solution was stirred for 10 min. Subsequently, TEOS was added, and the solution was stirred for 2 hours at ambient temperature. The formation of a white gel has been observed after 10 minutes since TEOS was added signaling the formation of the product. The precipitate was recovered by vacuum filtration, washed with deionized water, and dried at room temperature. The template was removed by calcination in air flow at 550 °C for 7 hours in a tubular oven.

5.2. Samples characterization

The full characterization of the most interesting products obtained is reported in the following paragraphs to outline the effect of the different mesoporogens on the final materials. The PXRD patterns of the calcined samples are reported in Figure 5.1, where the diffractograms are compared in the low angle region (0.5-5° 2θ) with the mesoporous reference MCM-48 (Figure 5.1, yellow curve). This structure has been selected, since the 3D mesoporous cubic lattice is expected as result of the synthesis of Zeotiles-2.[184] This disposition is attested in the sample TS1_CTA-OH_k (orange line) which shows a broad reflection peak at around 2.5 and 3° 2θ, while the same signal is very less intense in the sample TS1_CTA-Br. The long-distance order demonstrated by the low angle reflection is instead totally absent for the sample synthetized in presence of Triton-X100 (blue line), as already observed in Chapter 4. This sample presents the pattern of the MFI framework, which is, on the contrary absent for TS1_CTA-OH_k (orange) and TS1_CTA-Br (green).

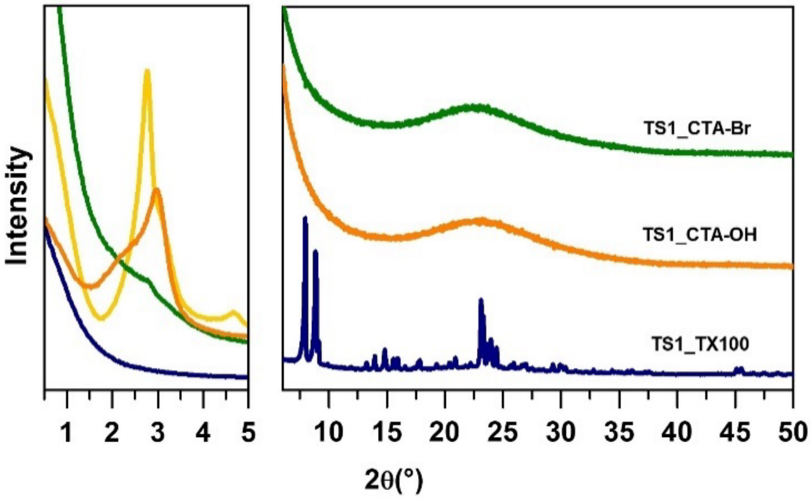

Figure 5. 1. Low angles (left panel) and wide angles (right panel) P-XRD patterns of TS1_TX100 (blue), TS1_CTA-OH_k (orange), TS1_CTA-Br (green) and MCM-48 (yellow, only low angles).

The textural properties of the same samples are described from the results of N_2 physisorption at LNT. Figure 5.2 presents the experimental N_2 isotherms (left panel) and the pore size distribution obtained by the application of NL-DFT model, while the results are summarised in Table 5.2.

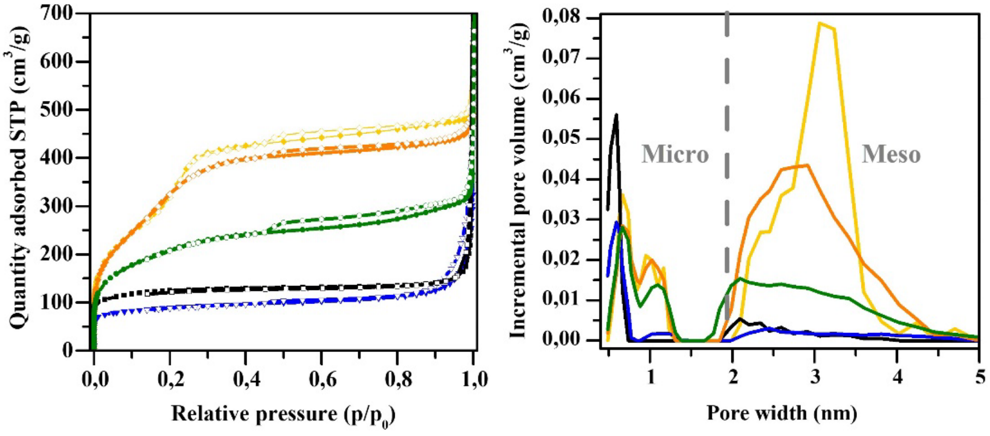

Figure 5. 2. Left panel: N_2 adsorption-desorption isotherms collected at liquid nitrogen temperature of: reference TS-1 (black), TS1_TX100 (blue), TS1_CTA-OH_k (orange), TS1_CTA-Br (green) and MCM-48 (yellow). Right panel: compared pore size distribution calculated by NL-DFT model of the same samples.

As preliminarily observed in the diffractograms, the samples are clearly distinguished into two families with significantly different characteristics. Triton-X100 leads to the formation of a material presenting the diffraction pattern of the MFI framework, in agreement with the type I isotherm which identifies a fully microporous material reported in Figure 5.2. The isotherm is comparable with that of a commercial TS-1 (black curve, Figure 5.2), such as the size of 0.55 nm, typical of the MFI micropores (blue and black curve, Figure 5.2, right). These data confirm the formation of a MFI zeolite in the presence of Triton-X100, as already observed in chapter 4. On the contrary, the syntheses conducted in the presence of CTA^+ induce the formation of materials similar to MCM-48 (yellow isotherm in Figure 5.2). Composed isotherms arising from the combination of Type I and Type IV isotherms are recorded for MCM-48, TS1_CTA-Br and TS1_CTA-OH_k. The application of the NL-DFT model to the whole N_2 adsorption isotherm considering cylindrical pores geometry gave a good fit for all these three samples. The pore size distribution and volume reported in Table 5.2. Surprisingly different families of pores have been identified in MCM-48 which is supposed to be a fully mesoporous material with uniform mesopore diameter of 3 nm. Both ultramicropores (of 0.7 nm) and supermicropores (of 1.2 nm) have been observed in MCM-48, contributing to a significant micropore volume of 0.24 cm^3/g. Moreover, a family of mesopores of 3 nm is present, corresponding to what is usually reported for the MCM-48 cubic structure[201] Since no bibliographic references were found for the presence of micropores in MCM-48, it was assumed that the identification of these families was obtained here only thanks to the application of the most advanced model of N_2 physisorption. The hypothesis of an incorrect synthesis leading to the formation of a different material from the usual is excluded, since the diffractogram and the BET surface area value is fully comparable to the reference.[201] It is supposed, instead, that these micropores have traditionally been ignored because it is a common practice to the use of the BJH model for describing mesopores, which can only be applied to pores larger than 2nm. In contrast, the NL-DFT model, applied here, can adequately describe even ultramicropores. However, given the amorphous nature of the MCM-48 walls, a non-regular distribution of the different pore families can be assumed, and despite the multilevel porosity, this is not definable as hierarchical structure. It is interesting to note in Table 5.2 that the Ti(IV) containing samples TS1_CTA-Br and TS1_CTA-OH_k present the same textural properties. In particular, TS1_CTA-OH_k possesses the same pore size distribution of the MCM-48 reaching comparable pore volume and BET specific surface area. The values are lower for TS1_CTA-Br, suggesting a less ordered porous system, as already observed by XRD (Figure 5.1, green pattern).

Table 5.2. Textural properties of the TS-1 samples compared with a commercial TS-1 reference and a mesoporous MCM-48 obtained by N_2 physisorption at LNT.

Sample name	B.E.T SSA (m^2/g)	Lang. SSA (m^2/g)	[a] Total pore volume(V) (cm^3/g)	[a] V micro (cm^3/g)	[b] V meso (cm^3/g)	[c]Average Micropore size (nm)	[c]Average Mesopore size (nm)
Commercial TS-1	430	572	0.22	0.19	/	0.55	/
MCM-48	1200	1715	0.74	0.24	0.50	0.7 (um)* + 1.2 (sm)	3
TS1_CTA-OH_k	1255	1821	0.67	0.23	0.44	0,6 (um) + 1.2 (sm)	3
TS1_CTA-Br	756	1045	0.47	0.21	0.26	0.6 (um) +1.2 (sm)	2-3.5
TS1_TX100	308	412	0.22	0.14	negligible	0.55	negligible

[a] Calculated by cumulative pore volume graph obtained from NL-DFT analysis of the adsorption isotherm.

[b] Obtained by difference between Total Pore Volume and Micropore Volume values

[c] Calculated by pore size distribution graph obtained from NL-DFT analysis of the adsorption isotherm

* um refers to ultramicropores and sm to supermicropores.

Considering the textural properties described above, TS1_CTA-OH_k is presumed to be an analogous of MCM-48. More information is achievable observing the TEM micrographs reported in Figure 5.3 reporting MCM-48 on the top and TS1_CTA-OH_k on the bottom. The openings of about 3 nm in diameter of the pores determined by N_2 physisorption at LNT are clearly visible in both samples. Although the well-ordered pores and particles distribution of MCM-48 (yellow boxes) is not completely reached for TS1_CTA-OH_k (orange boxes). The TS1_CTA-OH_k can be described as a Ti(IV) containing analogous of MCM-48, indeed the Ti content of this sample has been quantified by TEM-EDS (energy dispersive X-Ray spectroscopy) resulting in an average value compatible with the nominal Ti quantity expected from the synthesis composition. However, it is worth noting that the distribution of the Ti content is very broad and not homogeneous, since the 5 points examined by TEM resulted in very different compositional values.

Table 5. 3. Elemental composition of TS1_CTA-OH_k determined by TEM-EDS as average values obtained on five different points.

TS1_CTA-OH_k	**Nominal Ti/Si**	**Nominal atomic %**	**Real Ti/Si (EDS)**	**Real atomic % (EDS)***
Ti	0.02	0.2	0.02 ± 0.01	0.31
Si		16.68		13.18
O		83.13		86.51

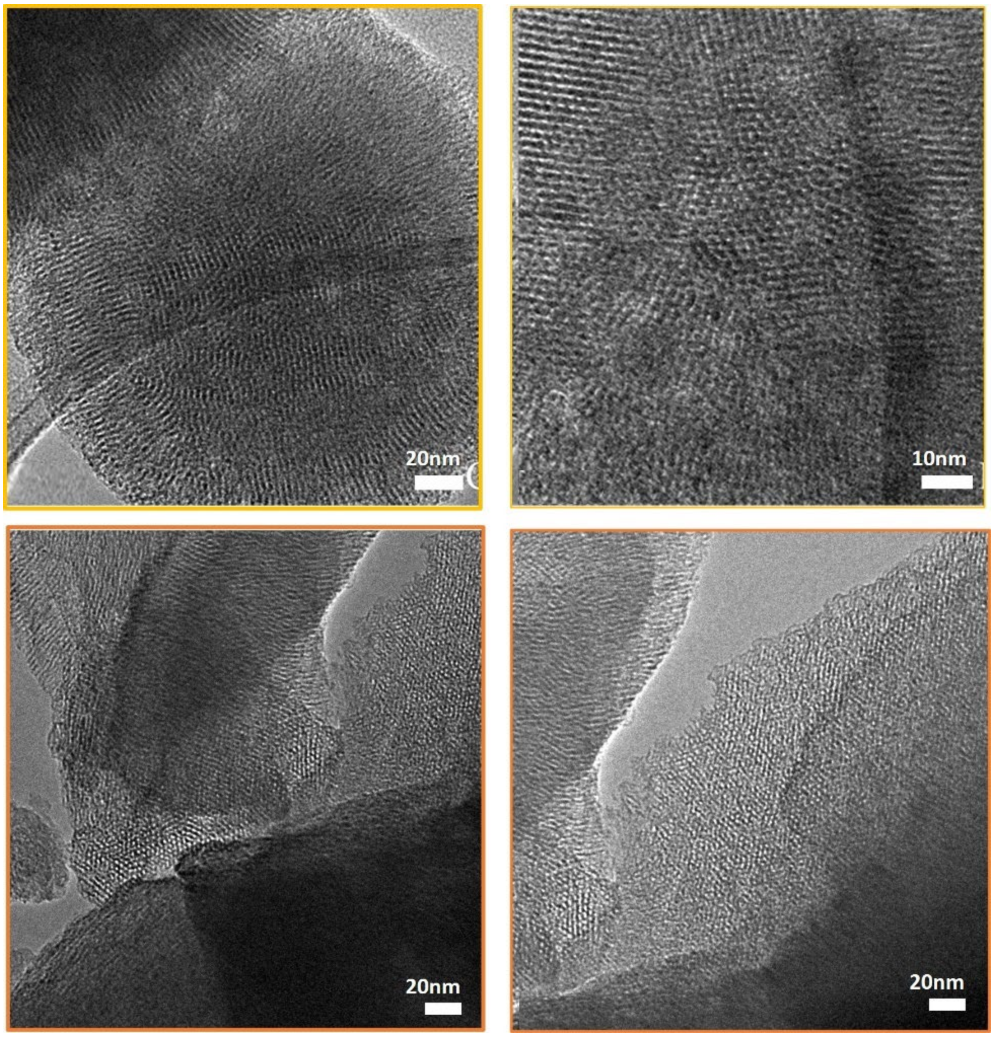

Figure 5. 3. TEM micrographs of MCM-48 (top, yellow) and TS1_CTA-OH_k (bottom, yellow).

5.2.1. Ti (IV) incorporation

From the results obtained by TEM-EDS it turned out that the synthesis of TS1_CTA-OH_k allowed the complete insertion in the silicate of the Ti(IV) present in the raw synthesis mixture. However, the heteroatom was quite randomly distributed in the final material. After having demonstrated the insertion of Ti inside the framework, it was important to determine its coordination state in TS1_CTA-OH_k, considered the most interesting material. To this purpose, it has been compared with the other Ti-containing samples and with the reference materials, performing a spectroscopic investigation by means of ATR-IR, Uv-vis and Raman spectroscopies.

The activated samples have been first studied by means of ATR-IR spectroscopy performed within the controlled atmosphere of a N_2 glovebox for avoiding external moisture adsorption. This is necessary for observing the unperturbed framework vibration at surface. The collected spectra are reported in Figure 5.4 (left panel) in the spectral region of framework Si-O fundamental vibrations bands (1400-400 cm^{-1}). All the samples are characterised by the presence of some typical fingerprints of silicates: the very intense asymmetric stretching modes (ν_{asym}) at 1200-1050 cm^{-1} and the symmetric stretching (ν_{sym}) at 800 cm^{-1} of SiO_4 units, and the out of plane rocking of Si-O-Si units signal at 435 cm^{-1}. The signal at 540 cm^{-1} is considered the spectroscopic signature of zeolites with MFI topology, being the collective vibrational mode of condensed five-membered units of Si atoms (pentasil units).[202–206] This signal is recorded for the sample TS1_TX100 (blue spectrum) as in the commercial TS-1 (black). In contrast, it is totally absent in the spectra of TS1_CTA-Br (green) and TS1_CTA-OH_k (orange).

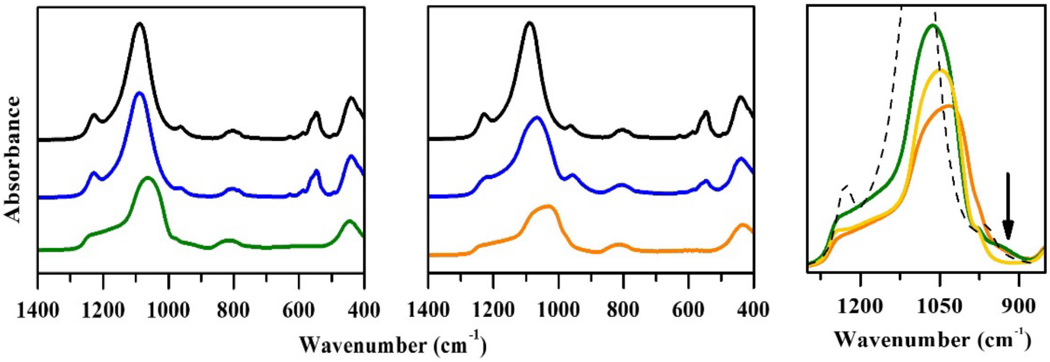

Figure 5.4. ATR-IR spectra of activated Ti-containing samples: reference TS-1 (dotted black), TS1_TX100 (blue), TS1_CTA-OH_k (orange), TS1_CTA-Br (green). Right panel shows the spectral region between 1300 cm^{-1} and 850 cm^{-1}, the Ti-samples are compared with MCM-48 (yellow). All the spectra intensities have been normalized to arbitrary units and vertically translated.

All these results are in agreement with the corresponding XRD patterns and textural properties described above.

The region enclosed between the intense ν_{asym} and ν_{sym} (1000–850 cm^{-1}) modes is known as the transparency window, where distinctive features deriving from the perturbation of SiO_4 tetrahedra modes can be determined. These can be induced by internal silanol nests (generated by Si vacancies), by strong interactions of extra-framework cations with the framework or by the isomorphic insertion of heteroatoms.[164,207] The presence of the heavier Ti(IV) in isomorphous substitution within Ti-Silicalite-1, induces a shift of the SiO_4 tetrahedra vibrations frequency, activating new vibrational modes in the transparent window region. The band at 960 cm^{-1} is an IR and Raman active mode arising from the presence of Ti(IV) species incorporated in the framework in tetrahedral or nearly tetrahedral coordination, perturbing the ν_{asym} of SiO_4.[196] This signal is clearly visible in the reference spectra of the commercial TS-1 (black) and in the one of TS1_TX100 (blue) reported in Figure 5.4 (left panel) suggesting a good insertion of the heteroatom in the framework of this sample. Contrary, a defined signal centred at the same frequency is not visible in the samples synthesized using CTA$^+$ (green and orange spectra of Figure 5.4, left). The magnification of the 1300-850 cm^{-1} region, reported in the right panel of Figure 5.4, compares the CTA$^+$ templated samples with MCM-48 (Ti free) and TS-1, for which some similarities are found. The intense band of SiO_4 ν_{asym} is centred at 1050 cm^{-1} in MCM-48 (yellow) TS1_CTA-OH_k (orange) and TS1_CTA-Br (green) samples, with a maximum at slightly lower frequency compared with the same mode of TS-1 (dotted black line). TS1_CTA-OH_k and TS1_CTA-Br both show a weak shoulder band at 927 cm^{-1} (black arrow) emerging from the profile of the more intense ν_{asym} band. This is totally absent in the spectrum of Ti free MCM-48. The band at band at 927 cm^{-1} could be ascribed to the asymmetric stretching mode of Ti-O-X (X= Si or H) bridges groups, proving the presence of Ti(IV) in M40s amorphous Ti-silicas.[208] In the spectrum of TS1_CTA-Br (green) the two components (ν_{asym} (SiO_4) and ν(Ti-O-X)) are separate and clearly distinguishable, while in the case of TS_CTA-OH (orange), the band with maximum at 1050 cm^{-1} extends its profile to lower frequencies until encompasses the signal at 927 cm^{-1}. The ν_{asym} mode band is clearly more asymmetrical than that of the other two amorphous samples, suggesting that several contributions in the region between 1000 and 920 cm^{-1}are convolved in the most intense signal. This suggests that several different species generate vibrational modes between ν_{asym} (SiO_4) and ν(Ti-O-X), which may reasonably be intermediate some structures enclosed between the Si tetrahedra and the Ti bridges. One possible situation is a coordination more similar to the tetrahedral TiO_4 present in TS-1, characterised by the 960 cm^{-1} mode (dotted black spectrum). At this regard, more information arises from the analysis of the DR-UV-visible spectra of the same samples.

Tetrahedral Ti(IV) centres in Ti(IV)-containing zeolites and siliceous mesoporous materials are characterised by typical electronic transition in the 200-220 nm range of the DR UV-vis spectra. These signals are associated to oxygen to tetrahedral Ti(IV) charge-transfer transitions (LMCT).[208] Coordination that deviate from this induces the shift of the same electronic transition toward higher wavelength, until 310-330 nm for the purely octahedral Ti(IV) in TiO_2. When Ti(IV) presents an intermediate coordination sphere, as distorted tetrahedra toward the more energetically favourable octahedral geometry, the LMCT ranges between 230 and 280 nm. [209]

The isomorphic insertion of Ti(IV) in the zeolitic framework strictly depends on the synthesis conditions and different Ti(IV) sites are frequently found, whose coordination is other than tetrahedral, including penta- and hexa-coordinated Ti(IV) species.[55]

Before performing the UV-vis analysis, each sample has been previously activated at 500°C in vacuum (as described in Section 2.3.2) to avoid interferences with the spectral signal of Ti(IV) species. In addition, the adsorbed molecules on the surface can contribute to the coordination sphere of Ti(IV) that possibly can alter the LMCT energy. DR-UV-vis spectra have been collected on all the Ti-containing samples and compared with the reference TS-1, known to contain only tetrahedral centers.[55] The spectra are reported in the left panel of Figure 5.5 in the range 200-500 nm. The reference TS-1 (black), as expected, exhibits a single intense absorption maximum at 200 nm, that is ascribed to the O(2p) → Ti(3d) charge transfer transition, which is characteristic of the isolated and tetrahedral TiO_4 species in the zeolite framework.[194] Interestingly, the sample TS1_CTA-Br (green) presents a quite similar energy absorption profile, with a maximum at 202 nm and a tail extended until 300 nm. This is the indication of an important fraction of Ti(IV) tetrahedra involved in the absorption at 202 nm and the contemporary presence of slightly distorted species that enlarges the transition range until 300 nm. On the contrary, the samples TS1_CTA-OH_k (orange) and TS1_TX100 (blue) present a broader absorption extended until 340 nm with the maximum around 220 nm. The broad band indicate the presence of a variety of differently coordinated Ti(IV) species. Reasonably also the presence of segregated nano-sized TiO_2 can be attested by the absorption tail at 340 nm of hexa-coordinated Ti(IV). The percentage of TiO_2 is reasonably limited and localised in small domains not able to induce XRD reflections (totally absent in Figure 5.1). For this reason, the CTA$^+$ templated samples have been characterised by means of Raman spectroscopy, by which the distinctive features of TiO2 can be identify with very high sensitivity. The Raman spectra are reported in Figure 5.5 and compared with the reference TS-1.

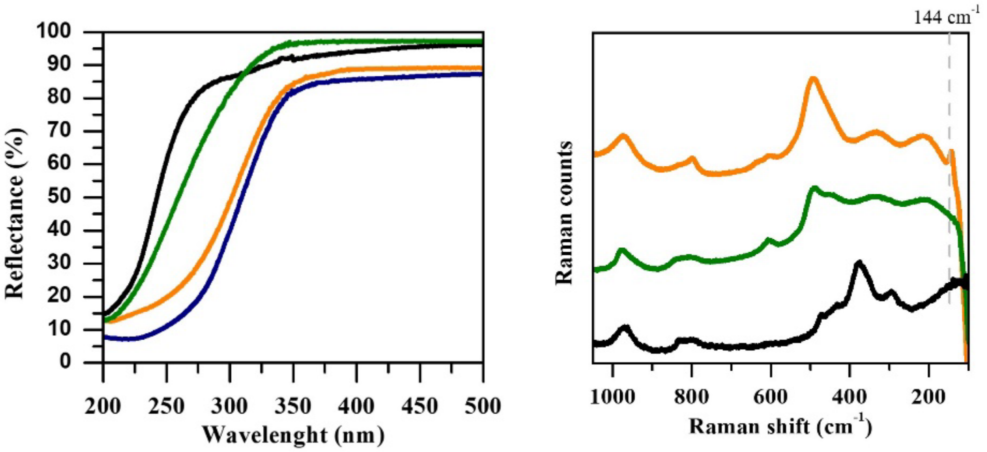

Figure 5. 5. Left panel: DR-UV-vis spectra of activated reference TS-1 (black), TS1_CTA-OH_k (orange), TS1_CTA-Br (green) and TS1_TX100 (blue). Right panel: Non-resonant Raman spectra (incident λ= 785 nm) of reference TS-1 (black), TS1_CTA-OH_k (orange), TS1_CTA-Br (green) collected in air. The spectra have been normalized to 800 cm^{-1} overtone intensity and vertical translated for the sake of clarity.

All the represented samples show an absorption signal centered at 810 cm^{-1} associated with ν_{sym} (Si-O-Si).[210,211] The 960 cm^{-1} band is observed in all of the samples. It can be attributed to Ti(IV) tetrahedrally coordinated or to a localized ν (O_3Si-OH) of hydroxylated defects that are commonly found on high-surface-area silica and on defective silicalites. For this reason, it cannot be considered unequivocally related to the presence of tetrahedral Ti(IV) species. [211] The Raman spectra of anatase TiO_2 typically show four main bands at 144 cm^{-1}, 638 cm^{-1}, 517 cm^{-1}, and 396 cm^{-1}, in approximate order of intensity.[212] The more intense Raman signal of anatase TiO_2 is detected only in TS-1_CTA-OH sample, confirming what observed by DR-UV-vis spectroscopy. On the contrary TS-1_CTA-Br does not present any signal reliable to the presence of TiO_2, confirming the better Ti(IV) insertion suggested by the DR-UV-vis spectrum. This is a quite surprising result, since the structural techniques identified TS-1_CTA-OH as better organized than TS-1_CTA-Br. This induced to think that the Ti(IV) insertion in the Silicalite-1 framework would be favored also by the presence of OH^- anions in the synthesis mixture.

5.3. Catalytic HPPO reaction test

The sample TS-1_CTA-Br resulted to be a micro/mesoporous amorphous material with dispersed framework Ti(IV) centers in tetrahedral coordination. Therefore, this sample has been tested in the catalytic epoxidation of propylene by H_2O_2 (HPPO process) its catalytic activity. The reaction has been studied, by means of *in situ* IR spectroscopy. The reaction has been carried out by depositing one drop of H_2O_2 (30wt% in water, Sigma Aldrich) on the sample pellet which then was inserted in the FT-IR cell and connected to the glass vacuum line. Afterward, the material has been outgassed in order to remove the excess of the hydrogen peroxide (observing the intensity variation of the H-O-O bending mode at 1350 cm^{-1}), then 50 mbar of pure propylene has been sent in contact with the catalyst. The reaction was monitored spectroscopically, collecting IR spectra every 30 seconds. To unequivocally identify the spectral features of different reagents/products, the same experiment has been performed on the reference TS-1 was. The commercial material has been put in contact with pure propylene and propylene oxide (PO) as well. The resulting spectra are reported in Figure 5.6.

The initial spectrum of TS1_CTA-Br sample is reported in green in Figure 5.6. After the contact with propylene, it is possible to observe a broad structured band cantered at 1640 cm^{-1}, assigned to the C-C stretching of propylene, appearing. The composite band at 1450 cm^{-1} is attributed to propylene out-of-plane and in-plane antisymmetrical deformations of CH_3 groups. [213] 15 minutes after the reaction start, a new signal centred at 1410 cm^{-1} has been detected (red curve in Figure 5.6, magnified in the inset). This band can be assigned to the CH_3 deformation of the propylene oxide [214] (the same feature is observed in the spectrum of pure propylene oxide in contact with reference TS-1 with, blue curve in Figure 5.6). The appearance of this band is considered to be a direct proof of conversion of propylene into the desired reaction product (PO).

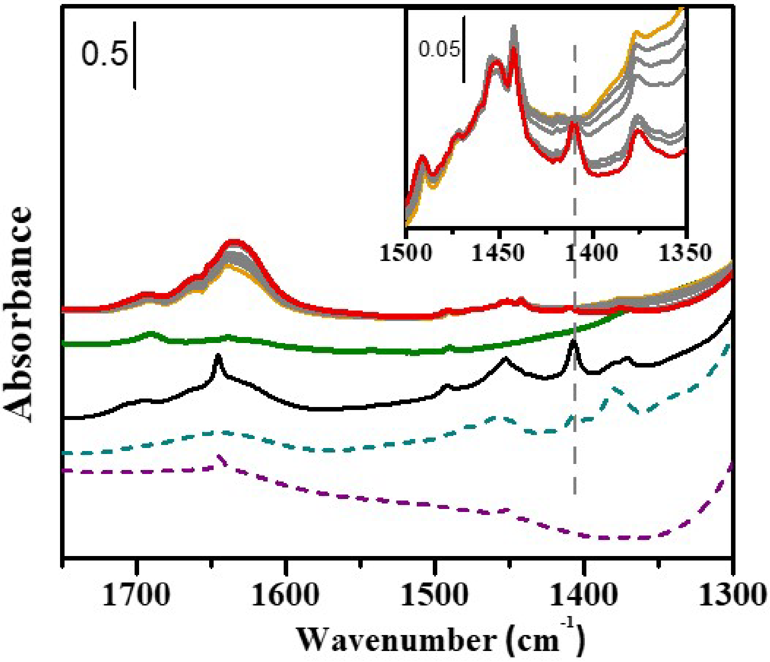

Figure 5. 6. FT-IR spectra of TS1_CTA-Br sample, after contact with H_2O_2 solution (orange), after the contact with 50 mbar of propylene (black), during diffusion (light grey) and after 15 min (red). The spectra of TS-1 in contact with PO (light violet) and with propylene only (purple) as well as the spectrum of reference TS-1 in contact with H_2O_2 and 40mbar of propylene (dark violet solid line, spectrum taken immediately after contact with propylene) are reported for supporting the bands attributions.

The reaction can be considered successfully performed since the formation of propylene oxide has been detected. However, the kinetics of the reaction is rather slow since the formation of the final product has been observed only after 15 minutes from the beginning of the catalytic process (i.e. the contact of propylene with the H_2O_2 loaded catalyst). Comparing this result with the reaction occurred in the presence of the reference TS-1 (black spectrum), collected immediately after the catalyst contact with propylene, it can be observed that the 1410 cm^{-1} band has appeared instantly, pointing out the immediate formation of propylene oxide, with an intensity 10 times higher. More interesting results could be obtained trying the same reaction test with bulkier substrates, as a cyclic olefin, for evaluating the effect of the mesoporosity present in the sample TS1_CTA-Br. Indeed, as demonstrated by the characterization step, this sample possesses active sites like ones of TS-1 and a structure comparable to the one of MCM-48.

Chapter 6: Characterization of ZSM-5 hierarchical Monolith

A novel sol-gel synthesis has been developed at Cambridge University. The strategy is based on shaping ZSM-5 nanoparticles, by controlled removal of the of the water content with consecutive steps of dehydration of the framework, to form self-supported and mechanically stable hierarchical monoliths with ordered mesostructures. The resulting material appears uniformly distributed in the centimeter-scale dimensions without using additional binders, applied high pressures, extruders or replicas. The produced material showed exceptional catalytic properties in the MTO conversion achieving high light olefin selectivity up to 70% at 100% methanol conversion with improved catalyst lifetimes, outperform conventional commercial and hierarchical ZSM-5 powders and extrudes. The synthesis details and catalytic tests are not reported here, since the unpublished results belongs to prof. D. Fairen-Jimenez of Cambridge University. We received the calcined ZSM-5 monolith in protonic form, and we operated the complete characterization of the material in order to understand how the hierarchical organization is built, providing the experimental data for supporting the development of a computed model of the structure and the MTO mechanism within the catalyst, by molecular dynamics simulation. This study is currently on going, performed by the group of prof. V. Van Speybroeck at Gent University.

6.1. Textural properties

Figure 6.1a reports the N_2 physisorption isotherms at liquid nitrogen temperature (LNT) of the ZSM-5 monolith compared with a commercial ZSM-5 Zeolyst CBV3024E, while the resulting textural data are collected in Table 6.1.

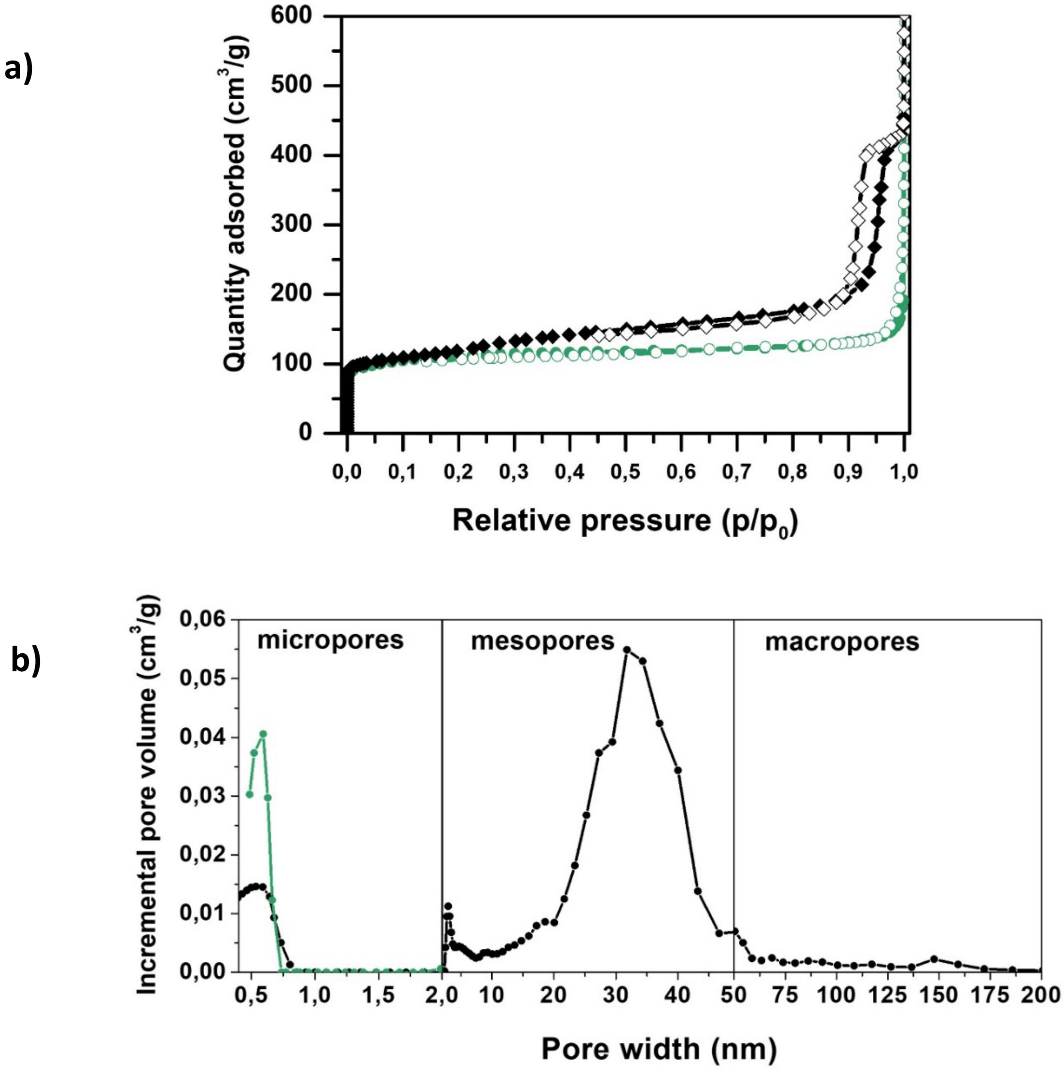

Figure 6. 1. a) Nitrogen physisorption isotherms at LNT and b) Pore sizes distribution of ZSM-5 monolith (black) compared with the commercial ZSM-5 CBV3024E (green), calculated by NL-DFT.

The material presents a composite isotherm generated by the combination of Type I and Type IV. It presents a strong uptake at very low relative pressure ($<10^{-6}$ p/p^0) indicating the micropores filling and a second step at higher relative pressure (around 0.25 p/p^0) due to the capillary condensation in the mesopores. A H1 type hysteresis loop is observed at high p/p^0 (around 0.9) and its symmetrical shape indicates a gradual process of filling/evacuation of the mesopores, that allow excluding pore obstruction or cavitation. The surface area values, calculated both by BET and Langmuir models, are close to ones of the reference, around to 400 m^2/g as commonly found for MFI zeolites.

Table 6. 1. Textural properties of monolith and reference ZSM-5 zeolites calculated by NL-DFT of Micromeritics ASAP 2020

Sample name	B.E.T SSA (m^2/g)	Lang. SSA (m^2/g)	[a] Total pore volume(V) (cm^3/g)	[a] V micro (cm^3/g)	[b] V meso + macro (cm^3/g)	[c]Average Micropore size (nm)	[c]Average Mesopore size (nm)	[c]Macropore size (nm)
Monolith	411	550	0.63	0.11	0.52	0.55	30	150
Reference	381	507	0.19	0.19	/	0.55	/	/

[a] Calculated by cumulative pore volume graph obtained from NL-DFT analysis of the adsorption isotherm.

[b] Obtained by difference between Total Pore Volume and Micropore Volume values

[c] Calculated by pore size distribution graph (Figure 6.1b) obtained from NL-DFT analysis of the adsorption isotherm

The pore size distribution and the cumulative pore volume (Table 6.1) have been calculated by pore modelling based on non-localized density functional theory (NL-DFT), considering a slit pore geometry of N_2 adsorption. The model perfectly fits with the experimental adsorption isotherm showing a family of ultra-micropores, with the dimensions of MFI channels (0.55 nm) and two different families of mesopores, one with average diameter of 2 nm and one with average diameter of 30 nm, which represent a huge contribution in the pores population. It is also present some macroporosity with a diameter that exceeds 100 nm, not well defined due to the poor retention of N_2 in macropores, which requires other techniques for the volumetric evaluation. The NL-DFT analysis indicates that the presence of a multilevel porosity allows increasing the MFI total pore volume reaching the value of 0.63 cm^3/g in the monolith. This value mainly arises from the contribution due to pore volume represented by meso and macropores taking part of the hierarchical structure, while the volume represented by the micropores, is not far from how reported for a commercial ZSM-5 (0.11 compared to 0.19 cm^3/g). The contribution represented by the mesoporosity represent an excess of 0.52 cm^3/g. It is possible to assume that the material is organized in perfectly crystallized domains of MFI spaced by open channels with mesoporous range size. At this level it is not possible to describe the interconnection between the porous levels, however, more information about the structure displacement is now under evaluation by building a computational model of the structure starting from the experimental data here reported.

6.2. Vibrational spectroscopies study

Figure 6.2 presents the IR spectrum of the activated monolith sample (black line) compared with the commercial ZSM-5 Zeolyst CBV3024E (green line).

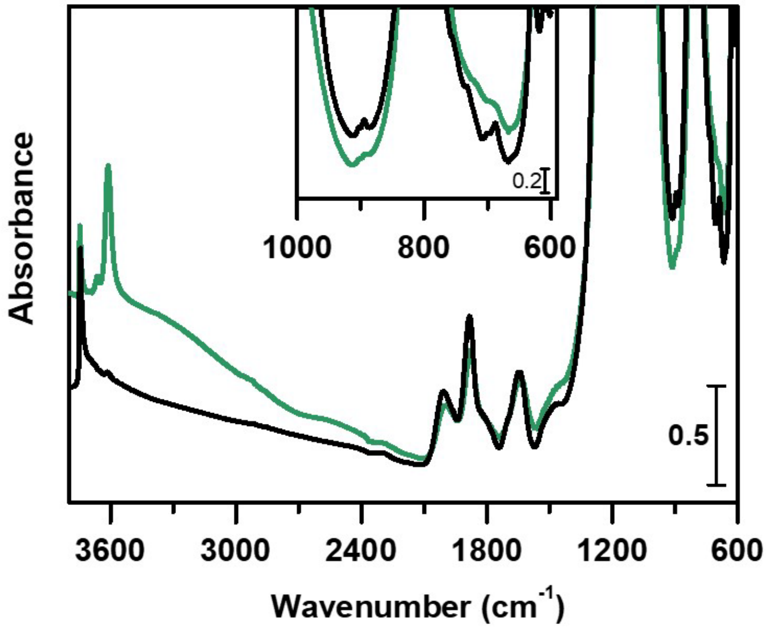

Figure 6. 2. IR spectra of: ZSM-5 monolith (black) compared with the commercial ZSM-5 CBV3024E (green), samples outgassed at 500°C. The intensity of spectra has been normalized to the 1700 cm^{-1} overtone band for the sake of visualization.

The monolith spectrum in the high frequencies region is characterized by the sharp and strong hydroxyl stretching ν(OH) modes typically found in protonic zeolites. A very intense band at 3747 cm^{-1} corresponds to the ν(OH) of isolated free silanol groups Si-(OH), commonly found in pure silica materials. This band is much more intense than the analogue seen in CBV3024E, suggesting a significantly higher concentration of silanol species (defects) in the monolith sample. Contrary, the signal at 3610 cm^{-1} corresponding to the ν(OH) of bridged Si-OH-Al, the Brønsted acidic site (BAS) of the zeolite, appears much less intense than the one of the commercial ZSM-5 (green curve). This is in line with the different Al loading (Monolith Si/Al = 50, CBV3024E = 15).

In the low frequency region, in which the Si-O framework vibrational modes fall, a band centred at 895 cm^{-1} is present in the monolith spectrum while it is totally absent in the commercial ZSM-5 (Inset Figure 6.2). It can be explained as the stretching mode of strained siloxanes (Si-O-Si bonds) bridges,[215] which are generally generated by thermal condensation of silanols releasing water, following the reaction:[216]

$2\ Si\text{-}OH \rightarrow Si\text{-}O\text{-}Si + H_2O$

These group are reasonably formed during the sol-gel synthesis, that involves the low releasing of water from the silicate framework toward the formation of the stable monolith. Siloxanes bridges are commonly found in pure siliceous structures, upon thermal activation that induces the condensation of silanols. Due to the presence of a significant concentration of aluminium in the ZSM-5 monolith, it is reasonable assuming that the formation of bridges is concentred in the region with high silicon content, while it is prevented in the region where Al is insert in the framework. The presence of Al induces both the formation of Si-OH-Al and isolated Si-OH, reasonably accompanied by extraframework Al. The identification of all the reactive species, with particular attention to the Al state, has been operated by coupling the IR spectroscopy with the adsorption of basic probe molecules.

6.2.1. Acidic sites speciation

Figure 6.3 reports the monolith IR spectra, the one in presence of adsorbed Carbon Monoxide (CO) at LNT and the progressive desorption of the probe molecule by static vacuum outgassing at the same temperature. [30,217,218] The probe molecule at LNT, with its weak basic character is able to probe the presence of both Lewis and Brønsted sites that induces a $\Delta\nu$ (CO) which is proportional to the strength of the surface-molecule interaction giving precious information about the nature of material active sites (the complete experimental description is reported in section 2.3.1).

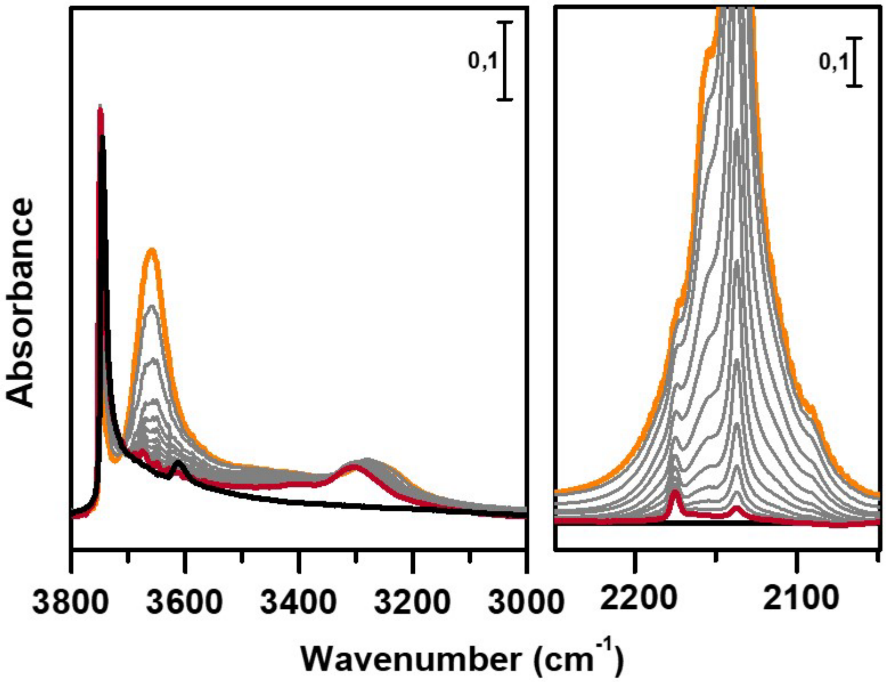

Figure 6.3. In situ IR spectra recorded following the desorption of Carbon Monoxide at 77K over the surface of ZSM-5 monolith. Activated sample (black), CO 35mbar, ep (orange), decreasing CO pressure (grey), ep CO < 1mbar (red).

In figure 6.3 the left panel focuses the ν(OH) region, while the right panel presents the ν(CO) region. The black line corresponds to the spectrum of the activated monolith sample, the orange line corresponds to the spectrum in the presence of CO at the equilibrium pressure of 35 mbar over the sample surface, recorded after liquid nitrogen cooling. The adsorbed gas has been then progressively outgassed by static vacuum, recording a spectrum at each equilibration step (grey lines) until reaching ep < 1mbar (red line) in order to distinguish the different strength of interaction sites.

In the left panel of the figure is visible the interaction with 35 mbar of CO with the hydroxyls population of the material (orange line), which induces the partial erosion of the silanol vibrational mode (3747 cm^{-1} in the black spectrum) which is shifted to 3660 cm^{-1} in the orange spectrum. In the same moment the νOH band of the acidic Brønsted site (3610 cm^{-1} in the black spectrum) is completely eroded and downward shifted to 3300 cm^{-1} upon interaction with the CO (orange spectrum). The entity of Δν of the band corresponds to the value commonly found for ZSM-5 zeolites, indicating that this acidic site possesses the same acidic strength of the parent zeolite. Contemporary, in the right panel (ν(CO) region) at high CO equilibrium pressure, the region is dominated by a very strong vibrational mode centred at 2140-2138 cm^{-1} raising while cooling down the system (out of scale in the orange spectrum), due to the liquid-like vibration of the retained CO on the catalyst surface. A so strong band is not usual for microporous zeolites (it is possible to compare this Figure with Figure 5 in Airi et al. 2021)[157]. The surprisingly strong and persistent signal in the monolith can be therefore explained with the large amount of the liquid-like gas trapped in the mesoporosity, in accordance with the volumetric data collected by N_2 physisorption (see Figure 6.1 and Table 6.1). Other two signals are visible in the same region at 2155 and 2175 cm^{-1} generated by the upward shift of the ν(CO) in interaction with the surface groups of the monolith. These signals became progressively structured by removing the excess CO by outgassing (grey spectra). The first one, decreases in intensity until disappearing while the silanol band in the left panel is completely restored and therefore can be attributed to the CO in interaction with the poor acidic surface silanols. Contrary, the component at 2175 cm^{-1} persists and it is still visible at very low CO coverage (red spectrum) indicating the strong interaction with the BAS, confirmed by the contemporary decreasing of the signal at 3300 cm^{-1} in the right panel (perturbed Al-(OH)-Si). At the same step (red spectrum) the component at 2138 cm^{-1} of the liquid-like CO (which usually is easily removed by outgassing) is still present, indicating again an extraordinary CO retention within the sample pores.

It is worth nothing that no signal reliable to CO interacting with the Lewis sites represented by the electron density of tricoordinate tetrahedral Al (partially extra-framework species) are visible. Generally, such interaction generates a diagnostic ν(CO) band at 2230 cm^{-1} also at room temperature, which is not recorded for the monolith. Therefore, the presence of such species can be confidently excluded, giving however, further information for the description of the material.

Further insight on the monolith acidic sites has been reached by *in situ* IR spectroscopy performed in the presence of adsorbed pyridine (Py).[181,219,220] This base interacts with acidic solids by quantitatively deprotonating accessible BAS to form the piridinium ion (Py^+) in strong interaction with the surface, and with LAS by establishing a strong Lewis acid-base couple. As already mentioned in Section 1.4.2, Py is supposed to diffuse in the MFI micropores without steric limitation, due to its kinetic diameter smaller than the MFI ring opening. Therefore, it is assumed that the base interacts with every acidic site exposed on the accessible surface, which corresponds to the totality in an ideal MFI sample. For the evaluation of the probe molecule interaction with the strong active sites, it is necessary to comment the spectrum obtained after prolonged in vacuum thermal removal of the Py excess, leaving on the sample surface only the irreversibly adsorbed fraction. Therefore, Figure 6.4 shows the IR spectra of the activated sample (black), after first Py vapours contact (orange) and following *ex situ* outgassing at 200°c for 2 h (red). The spectra are reported in the ν(OH) and ν(CH) region (left panel) and in the Py ring vibrational modes in the right panel.

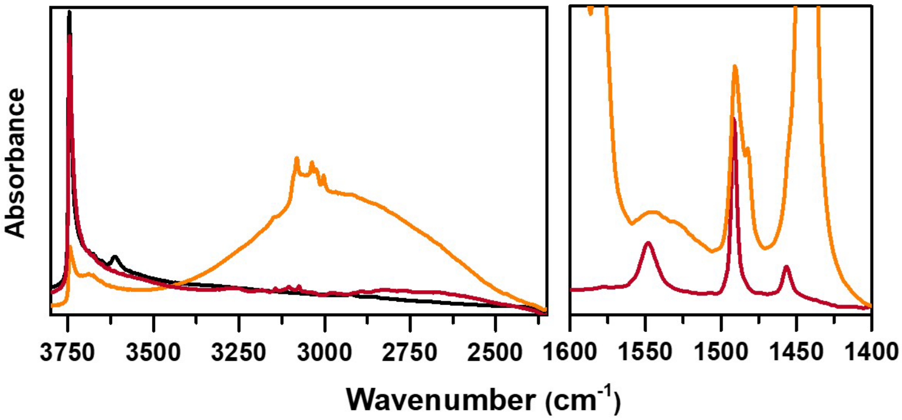

Figure 6.4. In situ IR spectra recorded following the adsorption/desorption of pyridine over the surface of ZSM-5 monolith. Activated sample (black), Py vp (orange), Py outgassed at 200°C 2h (red).

The interaction with Py vapours (orange spectrum) suddenly causes the erosion of most of the free silanols exposed to the surface accessible to the probe molecule, since the pristine band at 3747 cm^{-1} is significantly reduced in intensity. The non-interacting silanols responsible for the less intense band at 3747 cm^{-1}, in the orange spectrum, are reasonably represented by local defective zones not directly exposed to the surface. It is possible to assume the presence of silanols nests, which are formed by groups of close Si-OH involved in H-bonding interaction and therefore less accessible to the Py, formed upon displacement of one Si atom.[215,221] At lower frequency, a band at 3686 cm^{-1}, becomes visible upon the erosion, by Py contact, of the principal contribution due to intense isolated silanols band. This can be attributed to hydroxyls groups bonded to extraframework Al (Al-OH).[217] In parallel, the band related with the Brønsted sites is completely consumed by the strong interaction with Py vapours, accompanied by the parallel growth of a broad band cantered at 3000 cm^{-1} generated by the constitution of a large envelope of H-bonding in which the surface and the molecule are involved. After vacuum outgassing at 200°C, all the reversibly adsorbed Py is removed and the red spectrum is obtained, showing the vibrational modes generated by the irreversible fraction of adsorbed Py. The result is particularly evident in the right panel of Figure 6.4, in which the thermal outgassing allows the definition of some diagnostic modes in the region of Py ring vibrations (from orange to red spectrum). It is worth noticed that the total population of silanols is recovered, when freed by the reversible interaction with the base (red spectrum). Contrary, after thermal removal, the band at 3610 cm^{-1} is not restored, indicating that the whole population of BAS is still involved in the irreversible interaction with Py. This produces the formation of Py^{+} over the sample surface, which is testified by the presence of the component at 1545 cm^{-1} corresponding to the 8a Py ring vibrational mode (red spectrum Figure 6.4 right panel) and one at 1492 cm^{-1}. The contemporary interaction of Py with LAS sites generates the band a 1455 cm^{-1} which corresponds to the 19b ring stretching mode (red spectrum Figure 6.4 right panel). These sites are reasonably represented by octahedrally coordinated Al in extra-framework position, since the same band is attested when Py is adsorbed over the surface of alumina polymorphs.[222]

Integrating the area of the analytical 8a and 19b Py vibrational ring modes generated by the irreversible interaction with the acidic sites, the quantitative evaluation of BAS and LAS is achievable, according to the Lambert-Beer law, by using the experimental molar extinction coefficients available in the literature[223] and applying the equations:[180,219]

$$BAS(\mu mol/g) = \frac{A_{1545}(cm^{-1})}{\varepsilon_{BAS}(cm/\mu mol)} \cdot \frac{S(cm^{2})}{w(g)} \qquad \text{Eq. 2}$$

$$LAS(\mu mol/g) = \frac{A_{1455}(cm^{-1})}{\varepsilon_{LAS}(cm/\mu mol)} \cdot \frac{S(cm^{2})}{w(g)} \qquad \text{Eq. 3}$$

In which A is the integrated area (absorbance) of the irreversible diagnostic bands positioned at 1545 cm^{-1} (Py^{+}) and 1455 cm^{-1} (Py-LAS). ε is the extinction coefficients calculated for the same bands: ε BAS = 0.73 cm/µmol and ε LAS = 1.11 cm/µmol. S and w are respectively the surface and the weight of the sample, which ratio is considered as optical path for the Lambert-Beer law application. The results are reported in table 6.2.

Table 6.2. Concentration of Brønsted acidic sites (BAS) and Lewis acidic sites (LAS) in a monolith pellet, calculated by Py adsorption

BAS (µmol/g)	**86**
LAS (µmol/g)	**91**

Due the general stoichiometry of a defect free ZSM-5 unit cell:

$$[H_n\,Al_n\,Si_{96-n}\,O_{192}]\cdot 16\ H_2O$$

The expected quantity of the total amount of active sites (ideally described as H^+ concentration), for the monolith with Si/Al =50 is expected to be 326 µmol/g, which is quite far from the sum of the values reported in Table 6.2 (LAS+BAS = 177 µmol/g). this must be traced in the deviation from the ideal stoichiometry that the monoliths presents, as testified by the rich hydroxyls population, siloxanes bridges and extraframework Al, which covers a great part of the total content. For the full description of the structure, allowing the computational model formulation, it is important determine the location of such species. This can be achieved by applying IR spectroscopy coupled with the adsorption of steric selective methyl substituted pyridines, as described in section 1.4.2.

6.2.2. Hydrophilicity evaluation

In situ IR spectroscopy following adsorption /desorption of water[224] has been than applied for completing the description of the groups characterizing the monolith surface. Silica derived materials generally presents polar character arising from the abundant presence of surface silanols, that confers them high hydrophilicity. As already described, the monolith present at the same time a significant concentration of surface silanol and siloxane bridges, which contrary are considered highly hydrophobic species. These two elements confer an ambivalent nature to the material that has been investigated by IR spectroscopic experiments in presence of adsorbed water vapours at RT.

Figure 4.5a presents the spectra collected in the presence of progressive adsorption of water molecules over the monolith. The black line corresponds to the spectrum of activated sample, the violet line is the first H_2O dosage (vapour pressure), while the blue lines (from dark to light) correspond to consecutive doses of H_2O and a prolonged contact of the molecule with the monolith surface. In general, this experiment revealed the prevalence of an extremely hydrophobic character of the material. This fact is very peculiar and unusual for a zeolite, especially for a H-ZSM-5 rich of hydrophilic groups.

The first dose of H_2O (purple spectra) lead to a very weak erosion of the ν(OH) band of the free silanols at 3747 cm^{-1} (left inset Figure 6.5a) while the signal of Brønsted groups at 3610 cm^{-1} is only partially eroded. The presence of adsorbed H_2O is attested by the δ(OH) at 1625 cm^{-1} and it slowly grows with the same trend of silanols dectrasing, indicating the interaction with the hydrophilic groups. The purple spectra are delayed of few minutes, in order to observe the effect of water vapour diffusion. These spectra appear perfectly overlapped in the hydroxyls region, while a significative changing is observed in the Si-O region in the right inset

Figure 6.5a. The band at 890 cm^{-1} attributed to bridged siloxanes is focused. This band undergoes an erosion induced by progressive water adsorption until disappearing in the last purple lines.

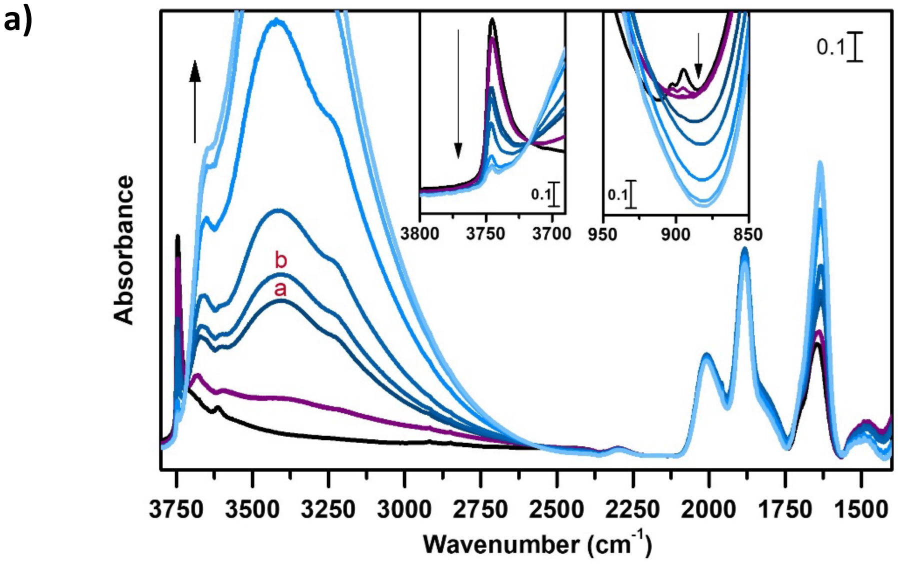

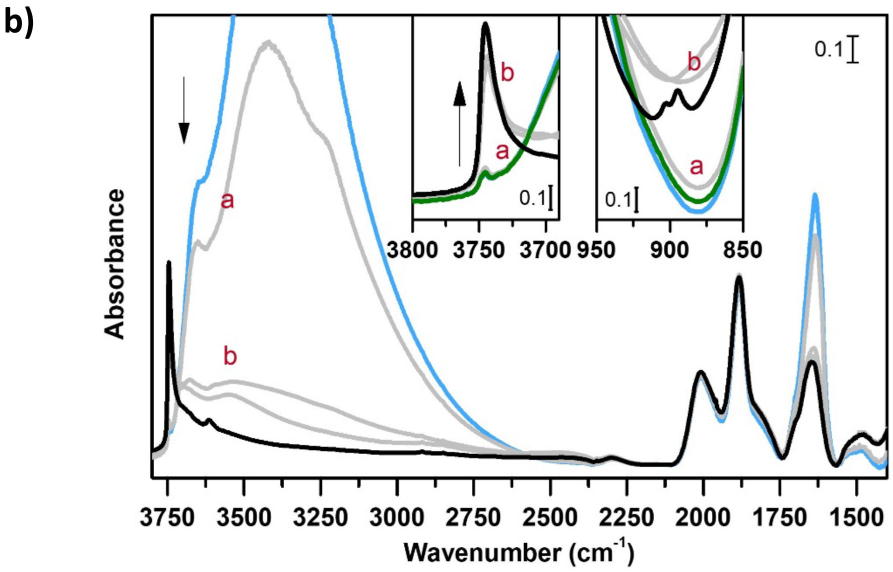

Figure 6. 5. In situ IR spectra recorded following a) the adsorption of H_2O over the surface of ZSM-5 monolith. Activated sample (black), first H_2O vp dosage (violet lines), prolonged contact with H_2O vp, time evolution (blue lines). b) the desorption of H_2O over the surface of ZSM-5 monolith. Activated sample (black), H_2O saturation (blue), H_2O outgassing (grey), last H_2O vp dosage (inset, green).

Water adsorption induces the hydrolysis of the highly hydrophobic siloxane bridges, when the necessary p_0 is reached. Therefore, the disappearance of the 890 cm^{-1} (in the last purple spectrum, Figure 6.5a, inset right) can be explained as the siloxane hydrolysis to form silanols.[225] It is interesting to note that a significant reduction of the silanols band is reached only when the siloxanes bridges signal is totally consumed (line a, Figure 6.5a). Thus, it is reasonable hypothesize that the hydrophobic siloxane bridges constitute a sort of protective layer that prevents the water contact with the hydrophilic surface of the zeolite (polar groups). Siloxane bridges may be disposed in the most accessible surface of the monolith, reasonably exposed on the mesoporous channels, where the water diffusion is faster, while the silanols are part of the MFI domains. As determined by Py adsorption they are distinguished in internal and external groups. Indeed, the second H_2O dosage (Figure 4, dark blue curve a) induces the first significant erosion of silanol band (magnification in the left inset). Around 3300 cm^{-1} the spectrum is now dominated by a very broad signal due to the ν(OH) which are starting to be involved in a hydrogen bond network. Waiting an hour for the H_2O diffusion (Figure 4, dark blue curve b) the trend proceeds, even if not significantly changes are recorded. Reasonably the hydrophobic layer is not completely hydrolysed, even if the 890 cm-1 band is no more visible. Only after a subsequent H_2O vp dosages (Figure 4, light blue lines) and further time of diffusion, the complete erosion of silanol band has been reached (left inset, light blue lines), while the overall spectra are again dominated by ν(OH) of H_2O molecules interacting by H bond and the δ(OH) at 1625 cm^{-1} rises in intensity. The difficulty in perturbing all the silanols population is extremely indicative of the hydrophobic character of the monolith, significantly different from more conventional ZSM-5 zeolites.[30]

In Figure 6.5b the water desorption is shown to verify the reversibility of the interactions. The first spectrum has been recorded after static outgassing of the excess of water from the zeolite surface (Grey curve a Figure 6.5 b). The spectrum still presents the very intense and broad signal of H_2O interacting by H-bond (around 3300 cm^{-1}) with the surface polar group, as confirmed by the fact that the silanol band is still eroded. After dynamic outgassing of adsorbed water, the grey spectra b have been recorded (Figure 6.5). It is observed that the intense and broad signal of H_2O interacting by H-bond suddenly decreases and at the same time the silanol band is quickly restored (3647 cm^{-1}, focus in left inset). This indicates again a weak interaction of the monolith with water and an easy restoring of the surface groups. Upon a subsequent dosage of water over zeolite surface, the green spectra in insets Figure 6.5 have been obtained, in which the instantaneous erosion of the silanol band is visible. This indicates an increased hydrophilicity of the material, which is significantly changed after water treatment. Siloxanes bridges are not restored (right panel Figure 6.5b) since their formation requires thermal water removal. However, the monolith superior stability to water is attested. This aspect is particularly useful for a suitable MTO catalyst, since the methanol conversion release water as main byproduct and generally the catalyst lifetime is shortened by structure collapse after steaming. Therefore, the increased lifetime recorded for the monolith in the MTO conversion can be explained, both with the reduced deactivation rate induced by cocking (since the products are easily removed through mesopores) and in with the high tolerability for steaming determined by the presence of hydrophobic surface groups.

6.2.3. Raman spectroscopy

The Raman spectrum of the monolith has been recorded in air, with an incident λ = 785 nm of the excitation laser.[226]The collected spectrum is reported in figure 6.6 and compared with the one of the commercial ZSM-5 Zeolyst CBV3024E (green). As the ZSM-5 reference spectrum, the monolith presents a maximum at 800 cm^{-1} corresponding to the symmetric Si-O-Si framework stretching and a broad signal below 500 cm^{-1} that corresponds to the Si-O-Al stretching where the Al partially substitute the Si atoms. The intense component at 380 cm^{-1}, is attributed to the ring stretching Raman active mode of pentasil-units, typical of the MFI framework, [227] that appears particularly intense and sharp in the monolith spectrum. Moreover, the monolith presents two main peculiarities: the band at 500 cm^{-1} appears composed by different contribution and it presents a band at 290 cm^{-1}, totally absent in the reference spectrum. A right assignation of these bands requires the comparison with computed Raman modes, arising from the model structure, currently under optimization.

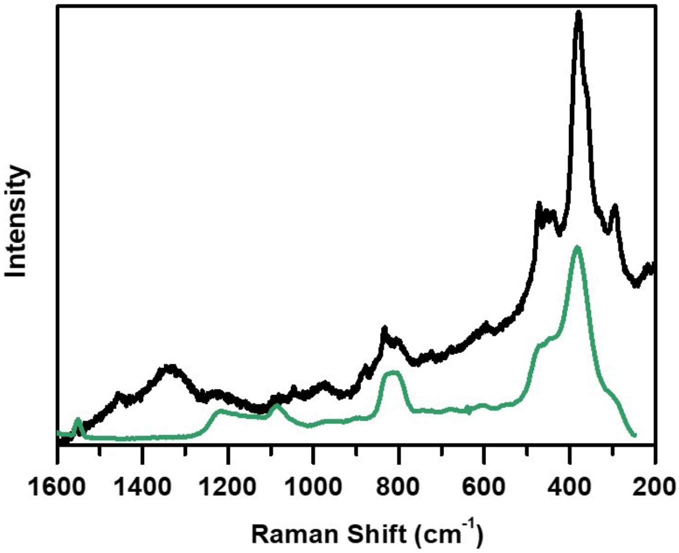

Figure 6. 6. Raman spectra of: ZSM-5 monolith (black) compared with ZSM-5 CBV3024E (green). The intensity of spectra has been normalized to an arbitrary factor for the sake of visualization.

Chapter 7: Characterization of different SAPO-18 and MAPO-18 for MTO conversion

A series of heteroatoms containing AlPO-18 has been synthetized at Oslo University and tested in the MTO conversion, showing excellent activity and selectivity toward light olefins. The complete work is reported in the publication Xie et al. 2022,[162] presented in Appendix I. These were a SAPO-18 and three different MAPOs-18, where M is a bivalent metal cation, namely, Mg^{2+}, Co^{2+} and Zn^{2+}, listed in Table 7.1. We operated the spectroscopic characterisation of the materials for fully describe their acidic features, which is one of the main determining parameters for the catalyst activity in the MTO conversion.

Table 7. 1. Textural and acidic properties of the MAPO-18s.

	Crystal shape [a]	Crystal size (µm)[a]	BET SSA (m^2/g)[b]	Elemental Composition [c]			Density of M (mmol/gcat)[c]	Brønsted Acidity (mmol/g_{cat})[d]
				P/Al	M/Al	M/(Al+P)		
SAPO-18	rods	~ 0.5	750	1.0	0.12	0.06	0.61	0.29
MgAPO-18	cubes	~ 0.5	730	1.1	0.12	0.05	0.55	0.17
CoAPO-18	cubes	≤ 0.5	639	1.0	0.16	0.08	0.78	0.27
ZnAPO-18	irregular	~ 1.0	96	1.1	0.14	0.07	0.66	0.04

Properties determined using [a] SEM, [b] N2-physisorption using BET method, [c] SEM-EDS, [d] propylamine-TPD.

In Table 7.1 the main properties of the samples are summarised. The heteroatom density of all the zeotypes, determined by SEM-EDS, are consistent with the nominal synthesis composition. However, propylamine-TPD measurements, used to characterize the Brønsted acidity and the Brønsted acid sites (BAS) density of the samples, probed a much lower amount of BAS than expected. Therefore, an advanced characterisation of the acidic properties and active sites of SAPO-18 and MAPO-18s have been performed by means of *in situ* IR Spectroscopy, for understanding the reasons for such discrepancy. In Figure 7.1, the spectra of the activated samples (treated in high vacuum at 400 °C) are shown in the left panel, in the ν(OH) region, where several groups with different acidic properties can be identified. Except for ZnAPO-18 (grey), the ν(OH) of Al–OH terminal groups are visible at 3795 and 3770 cm^{-1} for all the catalysts, that all show a band at 3680 cm^{-1} assigned to the stretching modes of phosphanols, ν(P–(OH)) terminal groups. An additional band at 3745 cm^{-1}, due to terminal silanols Si–OH, is observed for SAPO-18 (blue). With the exception of ZnAPO-18 (grey) all the catalysts shows signals reliable to the presence of BAS.[23] SAPO-18 (blue curve) showed two bands at 3627 and 3600 cm^{-1} attributed to ν Si–(OH)–Al, corresponding to BAS located in two different crystallographic positions.[23] MgAPO-18 (red curve) and CoAPO-18 (yellow curve) IR spectra are characterized by quite broad absorption at much lower frequency, centred at 3582 and at 3570 cm^{-1}, respectively. The progressive downward shifts of these bands in the series SAPO-18, MgAPO-18, and CoAPO-18, can be explained in terms of an increased BAS acidity strength in relation with the heteroatom, that follows the order Si ≪ Mg < Co.

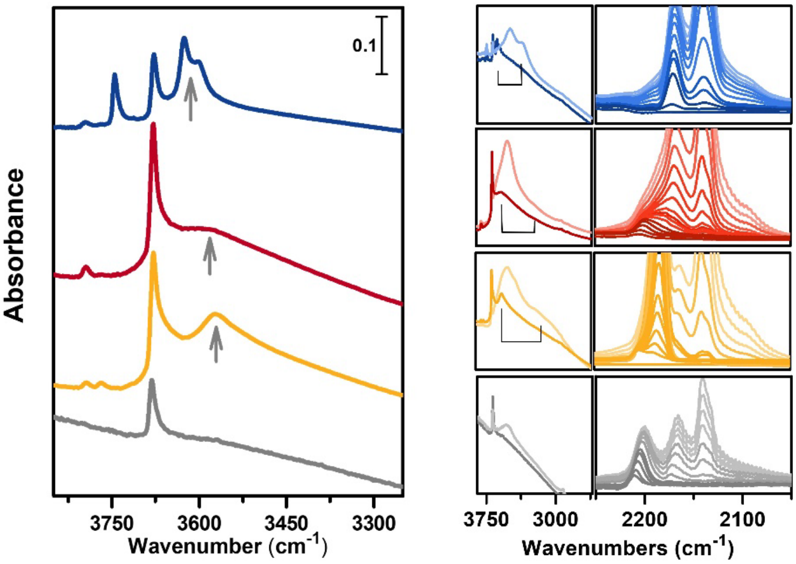

Figure 7. 1. Left panel: IR spectra of activated samples SAPO-18 (blue), MgAPO-18 (red), CoAPO-18 (yellow) and ZnAPO-18 (grey). Right panel: CO adsorption at LNT over SAPO-18 (blue), MgAPO-18 (red), CoAPO-18 (yellow) and ZnAPO-18 (grey), in the left inset the dark lines correspond to ν(OH) region the unperturbed activated

sample spectra, while the light line is the higher CO pressure coverage. On the right inset the ν(CO) spectral region is reported at decreasing CO pressure (outgassing) from lighter to darker lines).

Figure 7.1 (right) displays the IR spectra of MAPOs-18 in presence of adsorbed CO at liquid nitrogen temperature (LNT). In the left panels the OH stretching region of each sample is reported (dark lines refer to the activated samples, light lines to higher coverage of CO). Upon interaction with CO, the BAS signals are downward shifted to 3350 cm^{-1} for SAPO-18, 3280 cm^{-1} for MgAPO-18 and 3064 cm^{-1} for CoAPO-18, with Δν proportional to the acidic strength of the site, mainly dependent on the electropositivity of the heteroatom. Right panels show the corresponding CO stretching range. All the samples are characterized by a strong component due to physiosorbed CO (liquid-like) at 2140 cm^{-1}. In case of SAPO-18 a second, quite symmetric band is observed at 2170 cm^{-1} due to CO interacting with BAS sites and a very similar component, is observed also in case of MgAPO-18 at 2178 cm^{-1}. This sample also presents a minor contribution at 2205 cm^{-1} corresponding to the interaction with Mg^{2+} cations. As regards the CoAPO-18, a very strong band is centred at 2183 cm^{-1}. ZnAPO-18 does not show signals attributable to the presence of BAS sites; in contrast, an extraphase was determined. In the ν(CO) region a signal at 2210 cm^{-1} is visible, indicating the interaction of the probe molecule with the electronic density of Zn(II). It suggests a significant presence of segregated ZnO, giving an explanation for the lack of BAS in this sample.

To explain the reason for the discrepancy between the concentration (mmol/g$_{cat}$) of heteroatoms and BAS sites in SAPO-18 and MgAPO-18 samples, two series at increasing concentrations of Si and Mg, respectively, were synthesized. The samples, also produced by the University of Oslo, are listed in Table 7.2. The characterisation of the two series is functional to identify the actual incorporation of the heteroatom into the AlPO-18 framework, as its nominal concentration varies.

Table 7. 2. Textural and acidic properties of the SAPO-18 and MgAPO-18 catalysts with varied M/T atomic ratios prepared by varying M/T ratios in the synthesis gel recipes.

	Crystal size (μm)[a]	BET SSA (m^2/g)[b]	Elemental Composition [c]			Density of M ($mmol/g_{cat}$)[c]	Brønsted Acidity ($mmol/g_{cat}$)[d]
			P/Al	M/Al	M/T Atoms		
SAPO-18_a	~ 0.5	729	1.0	0.06	0.03	0.51	0.33
SAPO-18_b	~ 0.5	772	1.0	0.09	0.04	0.71	0.41
SAPO-18_c	~ 0.5	685	0.9	0.12	0.06	0.94	0.45
SAPO-18_d	~ 0.5	749	0.9	0.12	0.06	1.01	0.25
MgAPO-18	~ 0.5	730	1.1	0.12	0.05	0.55	0.17
MgAPO-18_a	~ 0.5	748	1.0	0.06	0.03	0.49	0.23
MgAPO-18 _b	~ 0.5	755	1.0	0.08	0.04	0.65	0.30
MgAPO-18_c	~ 0.5	741	1.0	0.11	0.05	0.81	0.39

Properties determined using [a] SEM, [b] N_2-physisorption using BET method, [c] SEM-EDS, [d] propylamine-TPD.

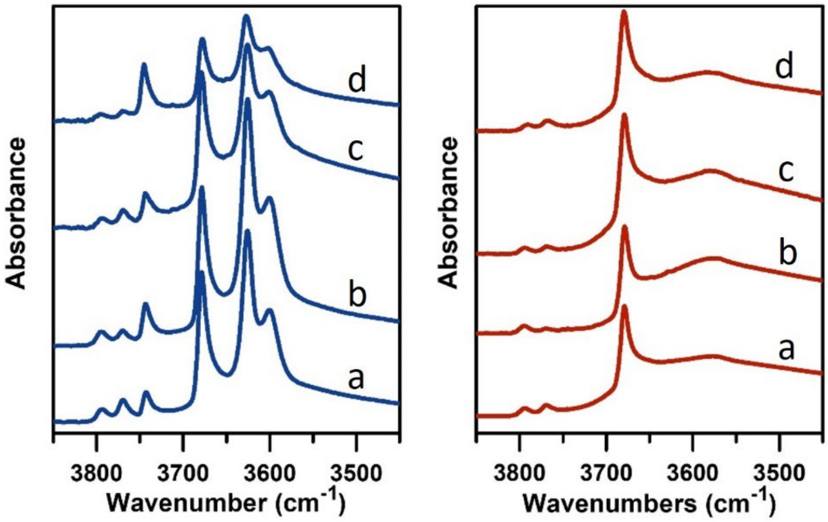

Figure 7. 2. Left panel: OH stretching region of IR spectra of activated SAPO-18s (a) SAPO-18_a, (b) SAPO-18_b, (c) SAPO-18_c, (d) SAPO-18_d. Right panel: OH stretching region of IR spectra of activated MgAPO-18 (a) MgAPO-18, (b) MgAPO-18_a (c) MgAPO-18_b and (d) MgAPO-18_c. The spectra are normalized to the pellets thickness.

From the results shown in Table 7.2 (last two columns), it can be observed that, while the experimental concentration ($mmol/g_{cat}$) of the heteroatoms is close to the nominal one, the concentration of the BAS sites is significantly lower. This indicates that the heteroatom is incorporated into the framework in a form other than the perfect tetrahedron, capable of generating the Brønsted site. This trend finds agreement with the intensity variation observed for the BAS signals of SAPO-18s and MgAPO-18s reported in Figure 7.2. Notably, the variation of BAS bands intensities, moving from the bottom to the top of the series is not proportional to the increment of the heteroatom contents but it follows the trend evaluated by propylamine-TPD. In case of SAPO-18s, an intensity increasing is observed from samples SAPO-18_a to SAPO-18_b, substantially similar to SAPO-18_c and with a significant drop in SAPO-18_d, which is nominally the higher Si containing material. In case of MgAPO-18s the intensity of the BAS bands is essentially unchanged as the nominal concentration of Mg^{2+} changes (Figure 7.2, right panel). This suggests that the amount of Mg^{2+} incorporated into the framework of the different samples is average the same, regardless of the nominal content present in the synthesis mixture. This corresponds to approximately 0.30 mmol/g_{cat} (Table 7.2).

Target experiments of *in situ* FT-IR spectroscopy combined with adsorbed probe molecules, have been performed for identify the nature of the heteroatoms fraction that is not involved in the BAS formation. The spectra of SAPO-18_a (top) and SAPO-18_d (bottom) are compared in Figure 7.3 in an experiment of pyridine (Py) irreversible adsorption (see Section 2.3.1). The two samples have been selected since they represent the two extremes in the nominal Si content (Table 7.2). Py, having a kinetic diameter of 0.57 nm, exceeds the size of AEI framework (AlPO-18) micropores openings (0.38 nm). Therefore, Py can only interact with external surface sites. In case of SAPO-18_a (Figure 5.3, top), the contact with Py vapors (after thermal removal of the reversibly adsorbed fraction at 200°C) induces a significant erosion of the BAS and silanols bands and partially of one associated to phosphanols. This indicates a dispersion of acidic sites, distributed between the inner and outer surface of the sample. In the right panel, where the region of Py ring modes is reported, the contribution related to the protonated Py at 1550 cm^{-1}

is clearly visible. The band at 1450 cm^{-1} is in general associated to Py interacting with LAS, explainable in case of SAPO-18 only with the presence of silica-alumina areas.[222] The presence of the so-called ‘Silica islands’ is responsible for the BAS loss with respect to the Si content, since the Si is found out of the AlPO framework.[15] This species are even more significant in the sample SAPO-18_d (more intense Py-silica bands in Figure 5.3, bottom), indicating that a more abundant fraction of the total Si content is segregated in silica islands, explaining the lowest BAS content reported in Table 7.2. Considering again the Py dimensions, it is possible to assert that the BAS of this sample, are almost completely located in the internal surface, not accessible to the bulky probe molecule. Contrary, all the Si-OH population is exposed to the external surface, reasonably being part of the silica formations. The P-OH are distributed both in the inner and in the outer surface.

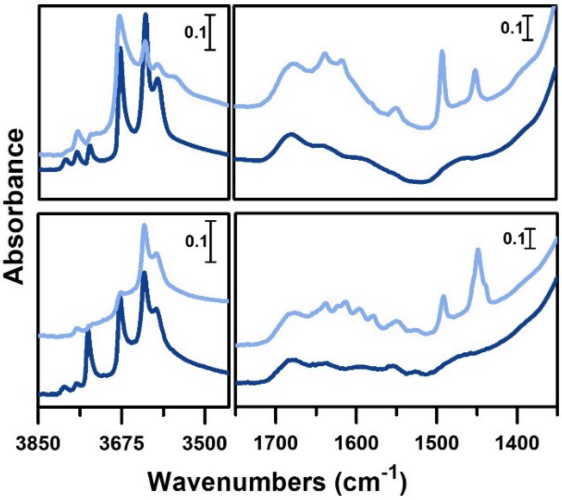

Figure 7.3. IR spectra of activated samples (dark lines) of SAPO-18_a (top panels) compared with SAPO-18_d (down panels), and after Py evacuation at 200°C for 1 h (light lines).

MgAPO-18_c and MgAPO-18 have been compared in a further experiment of FT-IR spectroscopy coupled with CO adsorption at LNT (Figure 7.4). Again, the two extremes in the nominal Mg content have been selected. As already discussed above, MgAPO-18 (Figure 7.4, bottom), at low CO equilibrium pressure, presents a persistent signal at 2210 cm^{-1}. This is compatible with the upward shift of the ν(CO) induced by the interaction of the molecule with the electron density of a cationic center, reasonably Mg^{2+}. The same signal is very less intense for MgAPO-18_c (Figure 7.4, top), which presents a higher BAS concentration. Therefore, it is possible to conclude that part of the Mg^{2+} content, inserted during synthesis, does not take part of the framework for generating BAS. Instead, it interacts with the MgAPO-18 framework in counter-ion position, as free cation in place of a proton. Considering the divalent charge of Mg^{2+}, when it substitutes H^+, two P-(O^-)-Mg sites are involved, therefore the extra framework fraction overcomes the framework one. This is even enhanced at high Mg^{2+} content as in the case of the sample MgAPO-18 compared with MgAPO-18_c.

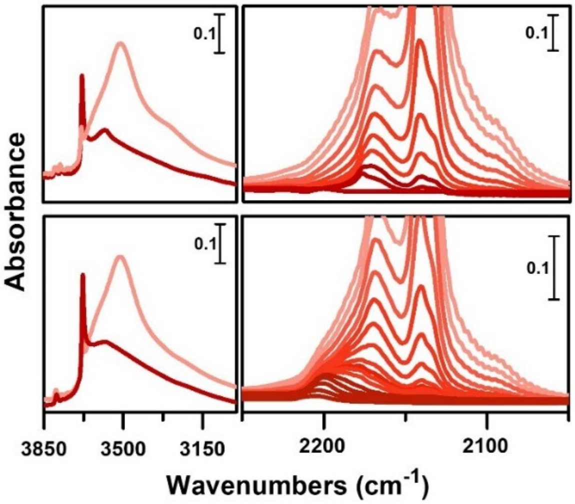

Figure 7.4. IR spectra of MgAPO-18_c (top) and MgAPO-18 (bottom) in presence of adsorbed CO at 77K at decreasing coverages. Left panels: OH stretching region (from 3800 to 3000 cm^{-1}) of activated samples (dark lines) and in presence of the highest CO coverage (light lines). Right panels: CO stretching region (from 2250 to 2050 cm^{-1}) of spectra recorded in presence of decreasing CO equilibrium pressure (from lighter to darker lines).

The case of CoAPO-18 was found significantly different with respect to other MAPOs, for this, its full description is deepened in Chapter 8.

Chapter 8: Spectroscopic investigation of CoAPO-18

The content of Chapters 8 and 9 are part of the manuscript “**Catalyst sites and active species in the early stages of the MTO conversion over Cobalt AlPO-18 followed by IR spectroscopy**” By A. Airi et al., which has been revised with minor revisions by *Catalysis, Science and Technology* in early March 2022.

8.1. Outlook on CoAPO-18

The sample under investigation is the cobalt containing AlPO-18 reported in the publication Xie at al.[162] The powder has been synthetized at the Oslo University by hydrothermal synthesis templated by N,N-Diisopropylethylamine, with alumina (AlO(OH) Pural), orthophosphoric acid and cobalt(II) acetate as Al, P and Co(II) sources respectively, for a gel composition of Co/Al = 1.6. The elemental analysis performed by ICP-OES, revealed a final Co/Al ratio equal to 1.3. In the present chapter the sample has been presented in two different forms:

- **CoAPO-18u**. Calcined *in situ* in small aliquots under controlled atmosphere only prior to each experiment to meticulously avoid contact with atmospheric oxygen and moisture.
- **CoAPO-18c.** Calcined *ex situ* and stocked in air for months, without any preservation from atmospheric agents.

We compared CoAPO-18u and CoAPO-18c in different experiments to outline the spectroscopic features of the presence of cobalt in the AlPO-18 framework and to identify which are closely related to the oxidation state of the heteroatom, which the reactivity of the material depends on. Since the early stages of this research, the process of template removal has turned out to be crucial in the formation of the active site and in influencing the oxidation state and the coordination sphere of the metal.

The first problem encountered in approaching CoAPO-18 material was navigating and finding unambiguous information in a rather old literature. The material was the subject of a prolific moment in the early 90's and then tended to be abandoned by the literature. Therefore, a thorough and careful analysis of the literature of that period was essential to fully comprehend the material and understand the results of the experiments that will be described later. This analysis revealed that the historical literature suffered from several bias related to the technological limitations of the time, particularly in the analysis of XAS simulations. To shed light on this and better understand the intent of the experiments conducted, a literature outlook on CoAPO-18 is reported here.

The work of professor Thomas and co-workers represents a precious feedstock of information, since they first synthesized the material and deeply characterized it by spectroscopic tools.[23,228] As demonstrated by Marchese et al.[163] trough *ex situ* experiments of IR spectroscopy during the calcination, the acidic form of the zeotype is obtained by the decomposition of the ammonic functionality R_3NH^+ of templating agent. Thus, the template removal represents a dramatic stage in the CoAPOs activation. Moreover, the oxidative atmosphere required for the template combustion (high temperature and O_2) easily lead to think that the cobalt oxidation can be favoured. The calcination process has therefor studied step by step by different techniques to monitor the local changes in the cobalt coordination, with several attempts in determining the oxidation state changes involved. Thomas et al. report that cobalt cations incorporation in the AlPO-18 framework is very diluted (with a concentration below 2wt.%)[229] as the tetrahedral coordination in which Co(II) d^7 is forced by the AlPO lattice, is energetically disfavoured in respect with the octahedral one.[230] Since the local order is too less extended for a determination by X ray diffraction, information about the symmetry of cobalt centres come instead from XAS analysis.[229,231,232] Sankar et al.[229] first determined in 1995 the Co(II) in the as-prepared CoAPO-18 by Co K-edge XANES and measured four equivalent Co-O bond of 1.9 Å in the first Co shell by EXAFS, for a tetrahedral coordination of the Co(II). Recently, the structural parameters have been refined by more advanced techniques, resulting in four equivalent O atoms surrounding the tetrahedral Co(II) with a radius of 1.94 ± 0.003 Å.[232] Sankar et al.[229] proceeded their study evaluating the calcination effect on the CoAPO-18 XANES spectrum, which undergoes pronounced changes due to the Co-O distance decreasing. The authors formulated a model involving the Co centre surrounded by three equivalent O and one at longer distance, which generate two distinct EXAFS oscillations. Based on this bond shortening and the shift in the Co K-edge position, the authors postulated, with the processing tools available at the time, a total oxidation of the metal to Co(III) in a distorted high spin tetrahedral coordination with average Co-O of 1.82 Å. It was only a later study that measured the length of Co-O equal to 1.79 Å in purely tetrahedral compounds of Co(III).[233] Upon reduction, further changes occurred, resulting in three short Co-O bonds of 1.90 Å and a longer of 2.04 Å. The latter has been associated to the bridged Co-OH-P which corresponds to the BAS and implies the restored Co(II) state.[231]

The model developed by Sankar et al. on the XAS, based on Co-O shortening in calcined CoAPO-18, convinced the group of authors that the totality of Co(II) present in CoAPO-18 was oxidizable to Co(III) in a fully reversible process that would restore the tetrahedral Co(II) upon reducing treatment. The monolithic work of this extremely important group, which does not admit the coexistence of the two oxidation states in the calcined compound, clashes with the results obtained by UV-vis spectroscopy conducted by other groups and made its interpretation difficult. The interpretation of Diffuse-Reflactance (DR) spectra of CoAPOs has in fact generated an intense debate, aggravated by the difficulty in finding reference models of tetrahedral Co(III) complexes that tend to be energetically disfavoured by the ligand field.

A preliminary indication of the redox process involving Co is given by the pronounced colour change affecting the material. Accordingly, CoAPO-18 as-synthetized appears as a blue powder, indicative of the tetrahedral Co(II). Upon calcination the material presents a green coloration which turns to blue after reduction. The DR-UV-visible spectroscopy has been extensively applied by using many different compounds to attribute the contributions of the complex spectrum of CoAPO-18 and its changes throughout the treatment steps. Tetrahedral oxocomplexes of Co(II) are characterized by an LMCT $O^{2-} \rightarrow Co^{2+}$ transition that falls in the UV region and three main d-d transitions from the ground state, which are:[230]

- $\nu_1 \equiv {}^4A_2 (F) \rightarrow {}^4T_2 (F)$ InfraRed region
- $\nu_2 \equiv {}^4A_2 (F) \rightarrow {}^4T_1 (F)$ Visible region
- $\nu_3 \equiv {}^4A_2 (F) \rightarrow {}^4T_1 (P)$ Visible region

ν_2 and ν_3 are located around 19 000-15 000 cm^{-1}, combined and split in three spectral components, due to Jahn-Teller effect and spin-orbit coupling. The band splitting is more pronounced in as-synthetized CoAPO structure in respect with the homogeneous references, indicating a more distorted tetrahedral coordination in which the $[CoO_4]^{2-}$ are forced by the lattice.[163] It is common for different CoAPOs frameworks to observe two adjunctive absorption bands rising at higher frequencies when the sample undergoes a calcination process. These bands, located around 30 000 and 25 000 cm^{-1}, are attributed to the LMCT transition involving tetrahedral Co(III) centres. Since the same transition is observed as a lonely band in homogeneous systems, the splitting in a doublet suggests a slight distortion from the pure tetrahedral coordination in case of Co(III)APOs.[234–236] In contrast to the XAS work mentioned above, who have studied the UV-vis spectroscopy of these materials have found evidence that a portion of the Co(II) present in CoAPO-18 as-synthetized does not undergo oxidation but more likely a distortion toward the more stable octahedral coordination. First, mention must be made of the work of Marchese et al. who in 1996 observed that after calcination the Co(II) triplet is reduced in intensity for about 50%, but its permanence is evidence of a portion of unoxidized Co(II) in CoAPO-18[163] (and more for CoAPO-5[237]). After a subsequent reduction process, they observed a larger splitting of the Co(II) triplet, suggesting a more distorted coordination. Moreover, they indicate a new band falling at 22 000 cm^{-1} that they assigned to a coordinatively unsaturated Co(II) or a weaker Co-O sphere, suitable of ligand exchange when adsorbates interact with the metal. They conclude that the calcination process causes the oxidation of only 50% of the total Co (the pure tetrahedral portion) while the rest appears as coordinatively unsaturated Co(II). In 2004 Moden et al.[235] have come to similar conclusions through observations of different sort. Through H_2 TPR (temperature programmed reduction) measurements they deduced that the active redox fraction corresponds to 64% of the total Co. During the reduction process however, a fraction of the Co(II) would undergo a coordination distortion. In parallel they also recorded a decrees of Co(II) visible triplet of about 45% after oxidation, but they added that a subsequent reduction recovers only a 15% of the initial intensity. This indicates that a fraction of Co(II) cannot be restored to its initial structure following a redox cycle and persists as distorted Co(II) centres, in agreement with Marchese observations. These considerations must be taken into account when approaching the study of CoAPO-18 behaviour and interpreting its changes during the reactions and catalytic processes in which it is involved. At the same time, it helps in reading the results of other techniques such as vibrational spectroscopy which has been widely adopted to characterize this material. The IR spectroscopy gave very important information about CoAPO-18 active sites, especially when coupled with specific adsorbed probe molecules.[161,228,238] The literature reports the only signal of P-OH group in the hydroxyl stretching region, for the calcined material spectrum. On the contrary, the reduced material presents in addition a very intense band at lower frequency, which has been attributed to the Brønsted centre, thanks to *in situ* experiments in the presence of basic probe molecules.[161,239] This profound change in the spectrum has been justified by the presence of Co(III) in the first case and Co(II) in the second. Little space has been given to the characterization of distorted and redox-inactive species of which there is UV-visible evidence. This chapter, through the combination of different spectroscopic techniques and the investigation of samples that have undergone different activation treatments, aims to understand the incidence of such species and what are the phenomena that promote their formation at the expense of the tetrahedral coordination that guarantees the Brønsted site.

8.2. Cobalt state and active sites

8.2.1. *Ex-situ* DR-UV-visible spectroscopy

The DR-UV-visible spectra collected in air atmosphere of CoAPO-18u and CoAPO-18c and their correspondence upon *ex situ* high temperature O_2 and H_2 treatments (see Section 2.3 for details) are here reported and discussed. The electronic transitions found in the spectra of Figure 8.1 are listed in Table 8.1. The data collected here, find good agreement with what reported by the literature.

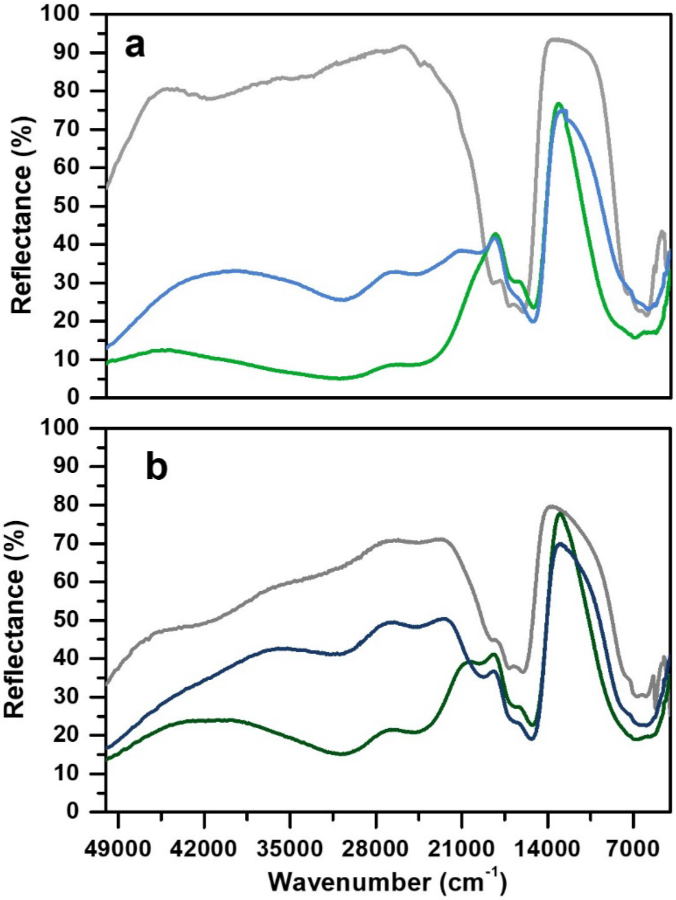

Figure 8. 1. Diffuse reflectance UV-visible spectra of a) CoAPO-18u and b) CoAPO-18c. Grey lines refer to the spectra collected in air on the pristine samples, green after O_2 treatment at 550°C and blue to H_2 treatment at 400°C.

Table 8. 1. Average frequency of principal absorption maxima identified in the DR-UV-visible spectra of CoAPO-18u and CoAPO-18c in air and upon ex situ high temperature O_2 and H_2 treatments.

Spectral Region	CoAPO-18u			CoAPO-18c		
	Air	O2	H2	Air	O2	H2
UV	50000		50000	50000	50000	50000
Uv-vis				41500		
		30600	30600	30600	30600	30600
		24600	24600	24600	24600	24600
Visible	18500		19 723	18700	19400	19400
	17200	17000	17 000	17250	17000	17000
	16000	15200	15 200	16000	15200	15200
NIR	7500-5800	8800-5000	7900-5500	From 7800	8800-5000	8000-5000

The spectrum of CoAPO-18u before any treatment (Figure 8.1 a, grey line) presents the principal absorption bands of the tetrahedral Co(II) as previously reported for CoAPO-18 before template removal.[238] A broad band in the UV region is compatible with the LMCT, while the visible region is dominated by the narrow triplet between 18500 and 16000 cm^{-1} typical of Co(II) *d-d* transition in tetrahedral coordination. A broad signal is present in the NIR region, around 7000 cm^{-1}. The sample was then subjected to calcination at 550°C in a pure oxygen atmosphere within a closed system consisting of a quartz line and a pumping system (as described in Section 2.3). The second spectrum (Figure 8.1 a, green line) was then recorded while maintaining the conditions of isolation from the external atmosphere. A deep variation of the absorption profile in the UV-visible region is observed with the establishment of two very broad and intense bands that have approximately maxima at 30600 and 24600 cm^{-1}. These are compatible with the Co(III) doublet aforementioned. In the visible region, the signal associated with Co(II) has undergone some change, being distorted in a band with two maxima at lower frequencies in respect with the triplet of the first spectrum (1700-15200 cm^{-1}). In the NIR region, the absorption is more extended and more intense. The third spectrum (Figure 8.1 a, blue line) was collected after treatment in pure H_2 at 400°C under the same conditions of atmospheric isolation (see Section 2.3). A decrease in the intensity of the bands at 30600 and 24600 cm^{-1} can be observed, indicating a lower amount of Co(III) species; while in the visible zone a partial restoration of the triplet can be seen with the appearance of a signal at 19700 cm^{-1} which is added to the signals at 17000 and 15200 cm^{-1}. These observations indicate an incomplete process of reduction, as Co(III) is still present, while Co(II) is being restored by passing through a distorted intermediate coordination, compared to the one of the starting spectrum.

The CoAPO-18c spectrum collected in air (Figure 8.1 b, grey line) shows at the same time features reliable to both Co(II) and Co(III). The transition at 50000 cm^{-1} and the frequencies of the three bands constituting the visible triplet, indicate the presence of tetrahedral Co(II) as in the CoAPO-18u first spectrum (Figure 8.1 a, grey line). However, it is evident that these bands in CoAPO-18c spectrum have lower intensity and thus a lower concentration of species, with respect to the case of CoAPO-18u. This observation finds agreement with the contemporary presence of signals related to Co(III) (UV region, 30000-24000 cm^{-1}). It follows that the total cobalt in CoAPO-18c is simultaneously present in the structure with both the oxidation states. An extra band is present around 42000 cm^{-1} probably due to $\pi \rightarrow \pi^*$ transitions of aromatic structures trapped in the CoAPO-18 pores, deriving from the template combustion, as it disappears after the subsequent O_2 treatment at 400°C (Figure 8.1 b, green line). This process causes the growing of the Co(III) UV bands, as the concentration of the species is increased, even if the signal is less intense in CoAPO-18c than in CoAPO-18u. Indeed, a portion (greater than the case of oxidized CoAPO-18u) of the total Co is still present as Co(II), as testified by the triplet. This signal is broader in respect with the grey spectrum, suggesting a slight distortion of the coordination sphere; its occurrence is even further pronounced after the H_2

treatment (Figure 8.1 b, blue line), indicating that the Co(II) fraction is rising. Also in this last case the persistence of the Co(III) bands, indicates a not fully completed reduction process.

The overall analysis of these data demonstrates that the calcination treatments do not lead to the total oxidation of the Co(II) structure. In the case of CoAPO-18u (observed since the templating removal step), most of the Co is oxidized to Co(III) while the remaining part seems to pass throw a distorted Co(II) intermediate form (the triplet assumes a doublet form), while the tetrahedron is gradually restored after reductive treatment (the triplet reappears, but is enlarged compared to the initial state). These data line up well with what is reported in the literature cited in the introductory section, as the experimental procedure is comparable. It involves *ex situ* treatments in a closed environment, with continuous removal of products by vacuum pumping. Instead, the results obtained for CoAPO-18c are more surprising. This sample, which was calcined in air and never protected by it, is less similar to the case studies. In this case, the simultaneous presence of tetrahedral Co(II) and Co(III) is observed, while the sole presence of the oxidized state would be expected in absence of a reductive process (Figure 8.1 b, grey and green spectra). It is also observed that there is a limit to the fraction of Co(III) that can be formed and that it coexists with a fraction of distorted Co(II) upon treatments. These new observations suggest that the traditional literature may have reached biased conclusions due to experimental practices. At the same time, indeed, similar considerations have been reached through IR spectroscopy, strengthening these conclusions.

8.2.2. *Ex-situ* FT-IR Spectroscopy

In Figure 8.2 a and b, the IR spectra of CoAPO-18u and CoAPO-18c are shown upon *ex situ* high temperature O_2 (green lines) and subsequent H_2 (blue lines) treatments. The spectra of CoAPO-18 present different vibrational bands related with surface hydroxyl species visible after catalyst activation, as reported in Figure 8.2.

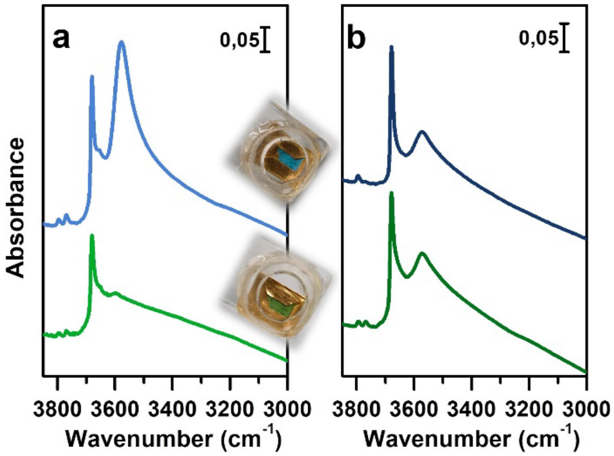

Figure 8. 2. IR spectra in the hydroxyl stretching region (3850 to 3000 cm^{-1}) of a) CoAPO-18u upon calcination (green line) and reduction (blue line) and b) CoAPO-18c after O_2 (green line) and H_2 (blue line). The spectra are normalized to the overtone's intensity for sake of comparison. The inset images show CoAPO-18u after high temperature O_2 (green) and H_2 (blue) treatments, inserted in the homemade cell for in situ FT-IR acquisitions.

At highest frequencies, two bands ascribable to Al-OH groups in different framework positions fall at 3793 and 3768 cm^{-1} in each spectrum. At 3678 cm^{-1} an intense and sharp band is assigned to the P-OH groups (free phosphanols) typical of all the aluminophosphates material which represent framework local defects. The large signal at 3578 cm^{-1} is due to the stretching mode of bridged P-(OH)-Co hydroxyls which represent the Brønsted acidic sites (BAS). The intensity of the latter two bands significantly differs in the various spectra reported in Figure 8.2 upon the different treatments the samples have been subjected to. Looking to the CoAPO-18u spectra (Figure 8.2 a) some differences are suddenly visible. Upon O_2 treatment (green line) the BAS signal in CoAPO-18u is almost absent, while the same band is extremely intense and overcomes the P-OH one upon H_2 action (blue line). These results are in line with what the literature reports. The case of CoAPO-18c is different (Figure 8.1 b) as the compared spectra show no notable differences.

The 3578 cm^{-1} is an evidence of the tetrahedral Co(II) in framework (as the charge compensating proton is needed to balance the charge of the phosphate groups [3-]), its variations give information about the Co state, especially if the analysis is coupled with the UV-vis spectroscopy results. On the other hand, there is no direct evidence of the presence of Co(III), since there are no vibrational bands traceable to it, but only indirect considerations can be raised. From these statements, it is reasonable to assume that the cobalt in CoAPO-18u (Figure 8.2 a green spectrum) is present almost entirely in the oxidised Co(III) state, given the absence of the band associated with BAS. In contrast, the presence of a relatively intense band at 3578 cm^{-1} in the case of CoAPO-18c (Figure 8.2 b green line) testifies the persistence of a fraction of Co(II), in agreement with the UV-vis results. The remaining fraction may be Co(III). It should be noted, however, that the intensity of the band related to P-OH is higher than in the case of CoAPO-18u, indicating an increase in these defective species. This finding suggests that a fraction of Co may have been leached from the framework generating free P-OH. Consequently, the fraction of the heteroatom that does not contribute to constitute BAS sites, reasonably may consist partly of tetrahedral Co(III) and distorted Co(II). Again, this description is in full agreement with the UV-vis data. After treatment in H_2 of CoAPO-18u, it can be presumed that all Co(III) is reduced back to framework Co(II), as a huge increase in the BAS signal is observed, while the leaching can be essentially excluded as the phosphanol band does not vary in intensity. If the intensity of the CoAPO-18u BAS band is thought as an indication of the maximum concentration of in-framework Co(II) species, it is confirmed that this situation is never reached by CoAPO-18c. Indeed, the spectrum collected after treatment in H_2 leaves essentially unchanged the intensity of the

BAS band. As the maximum level of Co(II) is reached after treatment in H_2, the samples at this stage will be considered "activated" hereafter.

The vibrational features of activated samples are summarised in Table 8.2 and highlighted in Figure 8.3, where the CoAPO-18u and CoAPO-18c are also compared in the “transparent window region” (Figure 8.3 b) i.e. the spectral portion enclosed between $\nu_{asymmetric}$ and $\nu_{symmetric}$ of framework T-O_4 units, where some diagnostic modes fall. The three bands visible in the CoAPO-18u spectrum (Figure 8. b, light line) find correspondence with ones that have been assigned by Marchese et al.[161,239] as CoAPO-18 fingerprints. Following their interpretation, the 955 cm^{-1} and the 905 cm^{-1} signals corresponds to the δ (P-OH) and δ (P-OH-Co) respectively, while the 945 cm^{-1} would be the perturbation of the νT-O_4 due to the presence of the heavier Co atom in the framework. The last attribution is based on the intensification of this band when the concentration of Co(II) is increased in CoAPO-18 and it is considered as the correspondent of the 960 cm^{-1} in TS-1 zeolites.[193] In CoAPO-18c (Figure 8.3 dark line) these three components are not distinguishable, as they probably take part of the larger $\nu_{asym}(TO_4)$ mode. This represents a further relevant difference in the CoAPO-18c nature with respect to the fresh sample.

Table 8. 2. Fundamental vibrational modes of activated CoAPO-18 CoAPO-18u and CoAPO-18c.

Vibrational mode attribution	**Frequency (cm^{-1})**	
	CoAPO-18u	**CoAPO-18c**
ν Al-(OH)	3793 3768	3793 3768
ν P-(OH)	3678	3678
ν P-(OH)-Co	3578	3578
ν_{asym}(TO4)	1200-1100	1200-900
δ (P-OH)	955	/
ν (TO_3-Co)	945	/
δ (P-OH-Co)	905	/
$\nu_{sym}(TO_4)$	770-600	770-600

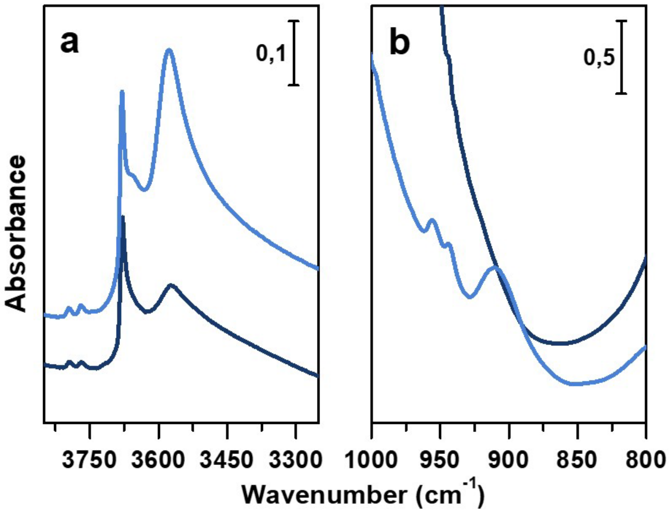

Figure 8. 3. The OH stretching region (a) and "transparent window region" (b) of IR spectra of CoAPO-18u (light blue line) and CoAPO-18c (dark blue line). The spectra are normalized to the overtone's intensity for sake of comparison.

8.2.3. *In-situ* FT-IR Spectroscopy

The interaction of adsorbed probe molecules with the CoAPO-18 surface during *in situ* IR spectroscopy experiments provides a wide range of information about the possible active sites. The activated materials are shown here in interaction with N_2 at LNT (Figure 8.4), CO at RT (Figure 8.5) and CO at LNT (Figure 8.6). The different proton affinity and the different degree of adsorption due to the temperature, highlight the behaviour of active species allowing better their identification. [240,241] In Figure 8.4 the vibrational spectra of the activated samples in presence of N_2 adsorbed at LNT, are shown. The very weak nature of the interaction of N_2 with CoAPO makes this molecule suitable as probe, ensuring any modification of the system. In the left panels of Figure 8.4 the perturbation of hydroxyl groups of CoAPO-18u (a) and CoAPO-18c (b) in presence of N_2 is observed inducing similar effects on the two samples. The Al-OH groups vibration is unaffected by the interaction, while the P-OH and bridged P-OH-Co components are suddenly eroded by the formation of the H-bonding. At the same time the perturbation of these two oscillators generates two components at lower frequencies, at 3653 cm^{-1} and 3475 cm^{-1} respectively (red spectra). In case of CoAPO-18u, the erosion involves also the δ(P-OH-Co) mode (Figure 8.4 a, Inset). At the same stage of adsorption, the appearance of a new component in the ν(N≡N) region is also recorded at 2339 cm^{-1} (Figure 8.4 a-b, right panels). When the interaction with N_2 is enhanced by increasing cooling of the system (from grey to black spectra) the shifted components are stabilized and intensified, while adjunctive signals appear in the ν(N≡N) region (Figure 8.4 a-b, right panels). These are a less intense signal at 2325 cm^{-1} due to N_2 in interaction with P-(OH) and one at 2234 cm^{-1} due to N_2 interacting with the BAS, more intense for CoAPO-18u.[239] The component at 2339 cm^{-1} is persistent in all spectra and is significantly more pronounced in the case of CoAPO-18c. It is compatible with the N_2 perturbed by the electronic density of a coordinatively unsaturated metal centre, reasonably a distorted tetrahedral Co(II) which represent a Lewis acidic site (LAS). The δ(P-OH-Co) in CoAPO-18u at low temperature is upward shifted, consistently with a strong acidic site.

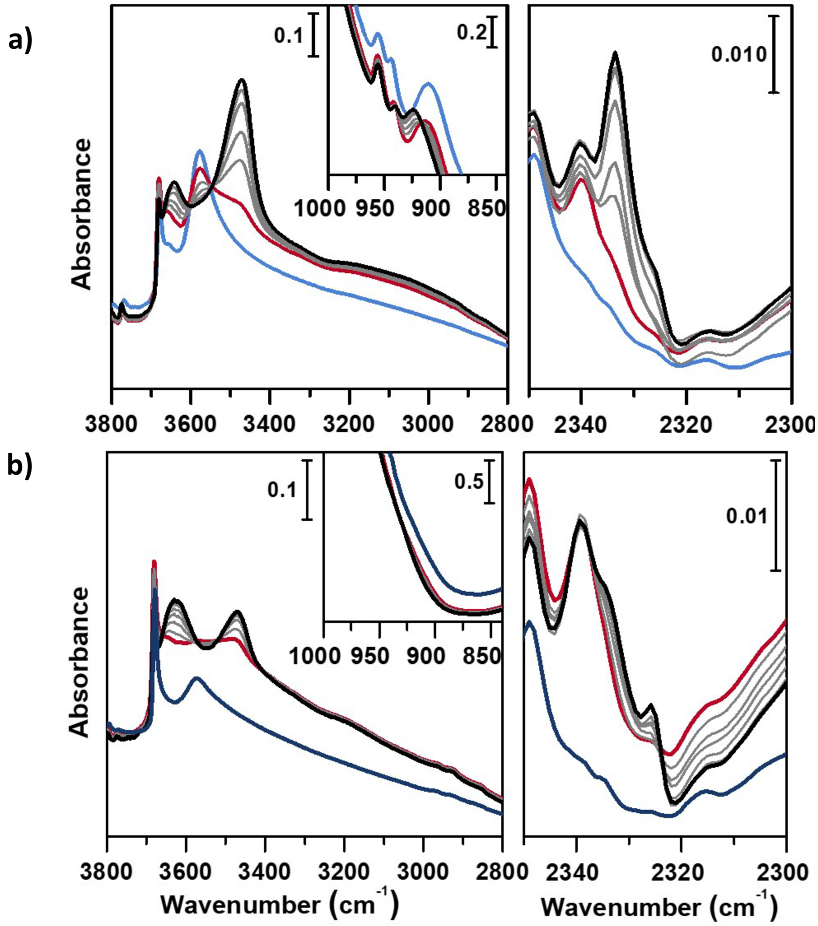

Figure 8. 4. IR spectra of a) CoAPO-18u and b) CoAPO-18c in presence of adsorbed N_2 at LNT in the OH stretching region (left panels), N≡N stretching region (right panels) and transparent window region (Insets). Blue lines are the activated sample spectra, red lines correspond to the first interaction with the probe, grey lines to the increasing of the adsorption and black to the maximum of coverage.

The adsorption of N_2 revealed in general that the BAS site remains unaltered in the two forms of the sample and that it presents a significant acidic strength. Indeed, the 3578 cm^{-1} band (BAS) undergoes a Δν, which define a spectroscopic acidity scale (lability of the O-H bond, excluding spatial constraints), equivalent to 110 cm^{-1}, and its extent is comparable to that of a ZSM-5, one of the most acidic of solid catalysts.[239] Moreover, the presence of coordinatively distorted Co(II) is probed consistently with the UV-vis spectroscopy results.

The case of CoAPO-18 is again peculiar in respect with other cobalt free analogous materials (zeolites and zeotypes), as the transition metal easily coordinate basic molecules bringing to the brake of (Co-OH)-P bond.[163,228,242] In other words, it has been observed that different molecules presenting Lewis basicity can coordinate the tetrahedral cobalt and substitute the bridged -OH group. This implies the loss of the BAS, and the occurrence of a Lewis acid-base couple (Scheme 8.1) instead; the interaction is reversible after the desorption of the molecule.

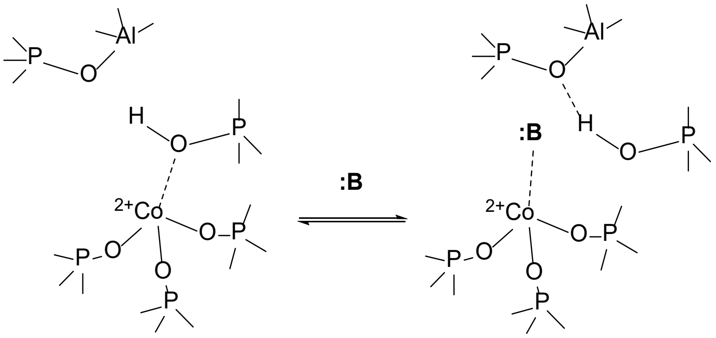

Scheme 8. 1. Establishment of the Lewis acid-base couple represented by framework Co (II) and a generic Lewis base :B, inducing the (Co-OH)-P bond displacement.

This behaviour justifies some observations in the IR spectra of CoAPO-18 in presence of relative strong bases as H_2O, CH_3CN and NH_3, while what is observed in case of a weak base as CO is not totally explained. Due to poor reactivity of CO, its adsorption at RT allow to evidence only the strongest interaction sites with the material surface, which are generally represented by coordinatively unsaturated metals (LAS) or the localized density of free cations.

Figure 8.5 displays the interaction of activated CoAPO-18u (a) and CoAPO-18c (b) with CO at RT.

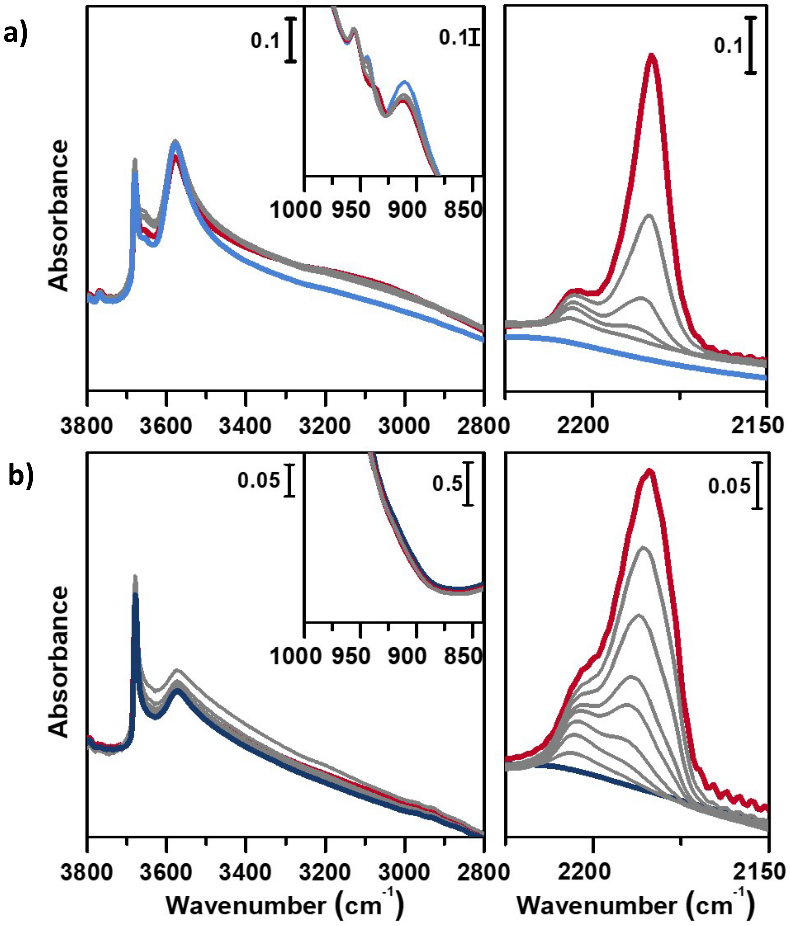

Figure 8. 5. IR spectra of a) CoAPO-18u and b) CoAPO-18c in presence of adsorbed CO at RT in the OH stretching region (left panels), C≡O stretching region (right panels) and transparent window region (Insets). Blue lines are the activated sample spectra, grey lines correspond to progressive CO dosage and red lines to the maximum of coverage (15 mbar).

In the left panel of Figure 8.5 a little perturbation of the OH stretching is visible at 3578 cm^{-1} (BAS), which band is slightly eroded and downward shifted to 3060 cm^{-1}, while in the inset a, the associated bending mode (905 cm^{-1}) undergoes a comparable decrease in intensity (the supposed upward shifting is not distinguishable from the dominating $\nu_{asym}(TO_4)$). This effect is more pronounced for CoAPO-18u (a), since it presents a significantly higher concentration of BAS in respect with CoAPO-18c (b) and an intense and visible bending mode. Although the perturbation of the spectroscopic modes appears to be weak, it reflects an extraordinarily strong interaction, as generally no shift of the hydroxyls is observed upon CO at RT, but only at low temperature. In the ν (C≡O) region (Figure 8.5 a, b, right panels) two contributions for each sample clearly appear increasing the dose of adsorbed CO (from grey to red spectra; red spectra correspond to equilibrium pressure of 15 mbar CO). These bands, falling at 2206 and 2183 cm^{-1}, are generated by the upward shift of the free C≡O vibrator interacting with a localized electron density. The 2206 cm^{-1} band finds correspondence with the direct interaction of the probe molecule with Co(II). Since the same signal is recorded also in Co(II) exchanged zeolites, it is reasonably identified as a Co(II) cationic site, in counter-ion position.[243,244] This signal is more intense in the CoAPO-18c spectra, indicating again a higher concentration of the extra-framework species in that sample. The attribution of the 2183 cm^{-1} band is of more complex interpretation and a more complete description will be given by coupling these with the results of the experiments at LNT. This signal is commonly attributed to CO linearly interacting with a Co(II) LAS centre, stable in different systems.[163,242,243] Marchese et al.[163] explain the presence of such species with the mechanism reported in Scheme 8.1, for which a fraction of the framework Co(II) undergoes a ligand displacement of the bridged OH groups by CO action. Under this hypothesis, the formation of the Co(II)—CO adduct would explain at the same time the perturbation of the stretching and bending mode of bridged OH which are forced to interact to framework oxygens by H-bond, stiffening the vibration. It must be noted also that the lattice vibration at 945 cm^{-1} is slightly shifted to 938 cm^{-1} by the probe adsorption (Figure 8.5 a, right panel). This description agrees with Marchese's results, which are valid for CoAPO-18u, as already occurred in the case of previous experiments (UV-vis and ex situ IR spectroscopies). According to this interpretation, the band at 2183 cm^{-1} would be generated by the action of CO adsorption and not by the pre-existing extra-framework Co(II). With all this, however, the behaviour of CoAPO-18c once again contrasts. Indeed, as observed in the left panel 8.5 b, it exhibits a band at 2183 cm^{-1} more intense (or at least comparable) than CoAPO-18u. If this band were generated by ligand displacement of BAS sites, the behaviour should be exactly opposite, as it is well established that CoAPO-18c has a lower concentration of these centres. In addition, the higher intensity of this band also clashes with the lower perturbation of the hydroxyls of CoAPO-18c. Therefore, in this case the LAS centre would not be generated by CO, but more reasonably would correspond to Co(II) in distorted coordination, of which there is UV-vis evidence.

More consideration can be made from the analysis of the IR spectra recorded in presence of CO adsorption at LNT. The low temperature enhances the adsorption rate allowing the determination of weaker interactions which can be discriminated following the progressive probe desorption from the zeotype surface. In Figure 8.6, the activated samples CoAPO-18u (a) and CoAPO-18c (b) are reported as blue spectra, they are then subjected to 30 mbar CO ep at LNT (first grey spectrum) and at progressive CO desorption (from grey to red spectra) by static vacuum evacuations until a CO ep < 0.06 mbar when a dynamic vacuum outgassing regime has been imposed (yellow spectra) at the same temperature. The strongest interaction, in respect with the RT adsorption, is visible in a more pronounced perturbation of both the O-H (left panels) and C≡O (right panels) spectral regions. At higher CO ep (30 mbar), when the cryogenic temperature is reached (first grey spectrum) it is possible to observe the erosion of both the phosphanols and BAS signals which are downward shifted. Contemporary in the CO region, the doublet band centred at 2138 cm^{-1} corresponding to the liquid-like vibration of the molecule and two other bands at 2167 cm^{-1} and at 2183 cm^{-1} (very intense) can be noted. The attributions of these bands will be described in details.

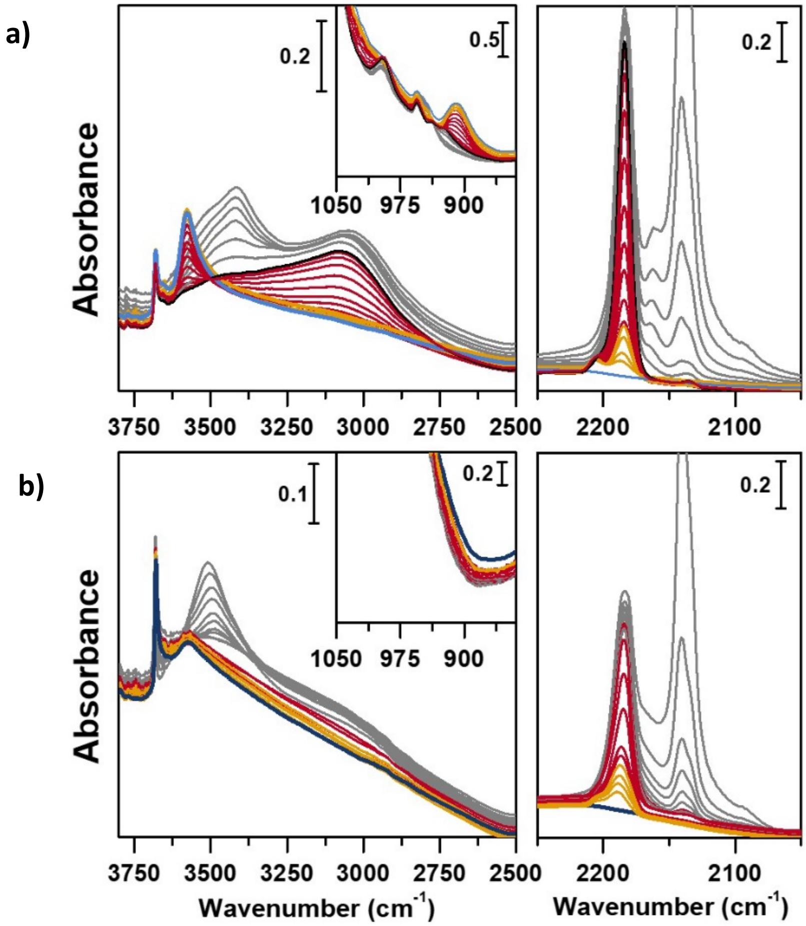

Figure 8. 6. IR spectra of a) CoAPO-18u and b) CoAPO-18c in presence of adsorbed CO at LNT in the OH stretching region (left panels), C≡O stretching region (right panels) and transparent window region (Insets). Blue lines are the activated sample spectra, grey lines correspond to decreasing CO ep from 30mbar to 0.3 mbar, black line to CO ep 0.3 mbar and red lines to decreasing CO ep from 0.2 mbar to 0.06 mbar by static vacuum evacuation; yellow lines correspond to decreasing CO below ep < 0.06 mbar by dynamic vacuum outgassing.

At LNT the poor acidic P-OH of both samples (a, b) can establish a H-bonding with the probe; the 3678 cm^{-1} band is eroded and downward shifted to 3422 cm^{-1}, while the ν C≡O is upward shifted at 2167 cm^{-1} by the same interaction (first grey spectrum CO ep 30 mbar), explaining the lower frequency component in the CO spectral region. This weak interaction is underlined by the grey lines of Figure 6 and represents the first site of CO desorption, as the related bands are easily consumed outgassing the probe by static vacuum. At CO ep 0.3 mbar (black spectrum) the pristine band of free phosphanols is completely restored while the 3422 and 2167 cm^{-1} components are consumed. In the same moment the disappearance of the liquid-like CO signal (2138 cm^{-1}) is also attested, while the component at 2183 cm^{-1} persists as very intense and narrow signal. As already noticed with the RT experiment, the interaction of CO with the BAS results in an outstanding spectral modification; the effect is more pronounced for CoAPO-18u where the concentration of the sites is much higher. At the maximum covering (CO ep 30mbar) the 3578 cm^{-1} band is consumed while a very intense and broad band at 3059 cm^{-1} is stabilized. Thus, the ***v*** P-(OH)-Co undergoes a downward shift of 518 cm^{-1} (Figure 8.6) indicating an extremely acidic site, since the Δv value significantly overcomes the one of common protonic zeolites, even the H-SSZ-13 (zeolitic homolog of AlPO-18). Therefore, it can be stated that the strongly ionic nature of the Co-O bond weakens the neighbour O-H, while increasing the acidic strength of the site. During the probe outgassing, the shifted component of the ***v*** P-(OH)-Co mode persists up to low CO ep (0.3 mbar, black spectrum), indicating a relative strong adsorption site. This band is gradually consumed only below 0.2 mbar CO ep while the 3578 cm^{-1} is recovering with the same trend (red spectra). Looking to the right panels of Figure 6, where the CO modes region is reported, in the same moment it is possible to observe the contemporary consumption of the 2183 cm^{-1} band starting (red spectra), while the BAS signal is being restored. This component is much more intense in the CoAPO-18u spectra, but in both cases its lessening has the same rate of the BAS band regrowth. Once reached the pressure of 0.06 mbar, the complete restoration of the 3578 cm^{-1} band (BAS signal) is attested for both samples but a fraction of the 2183 cm^{-1} band is still persistent (yellow spectra). Moreover, an additional band at 2206 cm^{-1} becomes visible. The frequency of these two bands and their shape (the band at 2206 cm^{-1} is lower and wider) coincides perfectly with the signals recorded in the RT experiment and therefore represent the interaction of CO with the sites of strongest adsorption. Indeed, these signals remain persistent even after prolonged dynamic vacuum degassing. Given the frequency and the strength of the site, it is reasonable to attribute them to Lewis sites, as already assumed in the case of CO at RT. The band at 2206 cm^{-1} probably corresponds to the interaction with a Co(II) as counter-ion, while the persistent fraction of the one at 2183 cm^{-1} corresponds to framework Co(II) with distorted geometry capable of coordinating CO. All these species are represented in Scheme 8.2. This interpretation of the IR spectra would disprove the hypothesis that CO adsorption induces the mechanism of Scheme 8.1. The band at 2183 cm^{-1} is the result of the convolution of two contributions, one given by the adsorption of CO on the Brønsted site and one due to the Lewis site, which appear overlapping at high pressures and can only be distinguished with a slow progressive degassing of the probe. This interpretation (Scheme 8.2) is in perfect agreement with the trend of the signals in the OH region, which otherwise could hardly be explained by the mechanism of Scheme 8.1.

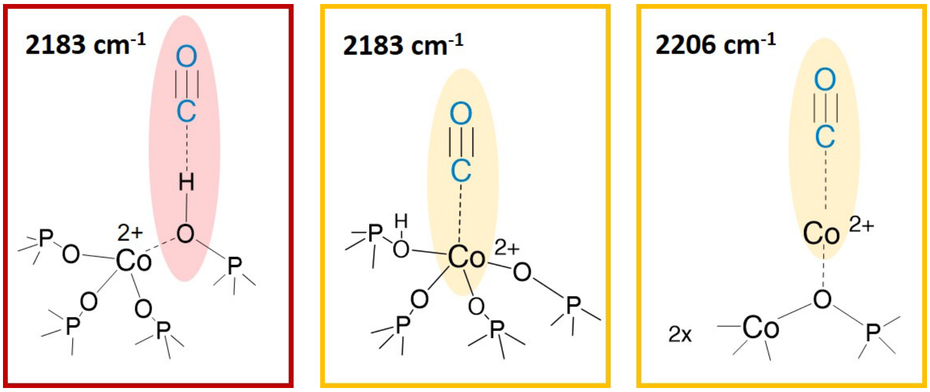

Scheme 8. 2. Graphical representation of the CO interaction sites at LNT. From left to right: Brønsted acid site, Co(II) as generic Lewis acid site, Co(II) in counter-ion position. The images are only intended to indicate the vibrational modes highlighted, none suggestion of structure is provided here.

The adsorption of CO over CoAPO-18u also induces the perturbation of the low frequency modes enclosed in the transparent window region (Figure 8.6 a, inset). The δ (P-OH-Co) at 905 cm^{-1} is suddenly eroded by the first CO interaction and upward shifted to 995 cm^{-1}, the pristine band is recovered only at very low CO ep in parallel with the ***ν*** P-(OH)-Co component. At the same time, the ***ν*** (TO_3-Co) is first slightly downward shifted to 938 cm^{-1} and then restored after the complete CO desorption (yellow spectra), indicating again the establishment of a CO- adduct with the Lewis site.

The perturbative effect of the different probe molecules on the activated CoAPO-18u is summarized in Table 8.3 and expressed as Δν of the pristine vibration frequency upon the surface interaction.

Table 8. 3. Δν of the fundamental vibrational modes of CoAPO-18u after probe molecules interaction.

Vibrational mode attribution	Frequency (cm^{-1})	Δν (cm^{-1})		
		N_2 (LNT)	CO (RT)	CO (LNT)
ν Al-(OH)	3793 3768	/	/	/
ν P-(OH)	3678	-25	/	-256
ν P-(OH)-Co	3578	-103	-518	-518
δ (P-OH)	955	/	/	/
ν (TO_3-Co)	945	/	-7	-7
δ (P-OH-Co)	905	+30	Partially eroded	+90

The overall analysis of the spectroscopic data demonstrates that the conditions with which the calcination treatment is performed induces relevant modification to the active sites population of CoAPO-18. The amount of BAS, which strictly depends on the presence of Co(II) in framework position (tetrahedral coordination) is subjected to variations deriving from the calcination/activation treatments to which the material is exposed. The zeotype, synthetized in presence of solely Co(II) can be subjected to redox cycles involving the metal centres in a different amount if the treatments are performed in controlled atmosphere or opened to air. It is possible to selectively obtain the oxidized form Co(III)APO-18 by pure oxygen treatment or the acid catalyst H-Co(II)APO-18 by after-calcination reductive treatment with pure H_2, as long as the cobalt sites retain the tetrahedral coordination, in accordance with the reactions in Scheme 8.3, valid for CoAPO-18u:[235]

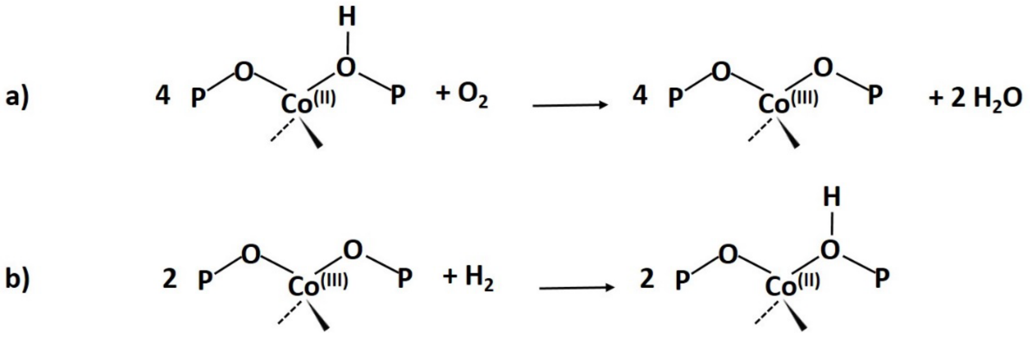

Scheme 8. 3.a) Oxidation reaction involving Co(II) by action of molecular oxygen. b) Reduction of Co(II) in H_2 to form Co(II) and the zeolitic BAS.

This is guaranteed by controlled processes that avoid the interaction of the material with atmospheric moisture or with the H_2O molecules produced during the combustion of the template. The water molecules are believed to coordinate the Co(II) vicinal oxygen atoms, distorting the coordination from tetrahedral toward the more energetically stable octahedral one.[236] For this reason, exposing the template-free material to air (CoAPO-18c) and then removing the adsorbed water by thermal treatment, irreversibly increases the amount of coordinative distorted Co(II), decreasing the number of redox active centres. This corresponds to an irreversibly lower amount of BAS and a correspondent enhanced concentration of LAS. It is worth notice also that the reactions described in Scheme 8.3, in particular the oxidation reaction, require prolonged exposure to oxidative/reductive treatment for being quantitative. This can be guaranteed in the closed system adopted for the CoAPO-18u sample, where temperature and atmosphere homogeneity are ensured and the combustion products are removed by pumping. In the case of natural air treatment of the sample (as in the case of CoAPO-18c) or under synthetic air flow, an intermediate and complex situation is reached. In addition to tetrahedral Co(II), several forms of cobalt are reasonably present at the same time, decreasing the nominal amount of BAS sites, i.e. distorted tetrahedral Co(II), which is responsible for LAS sites, Co(III) derived from partial oxidation and free Co(II) in the counter ion position derived directly from the synthetic precursor.

Chapter 9: CoAPO-18 in the MTO conversion:
a FT-IR Spectroscopy study

Since the discover of the APO-18 framework in 1994,[23] its potential as catalyst for methanol to olefins reaction suddenly appeared, as structurally related with the SAPO-34. MAPO-18 compounds have stability comparable to that of their Si containing analogous and provide excellent performance as catalysts of the MTO reaction over the same temperature range. The presence of the divalent metal confers to the CoAPO-18 increased acidity (due to the more ionic character of the anionic framework) that promotes the methanol conversion, reaching the 100% at 350°C (the same for Mg-APO and ZnAPO-18); at the same time the 70% of selectivity for light olefins is observed.[23]

In the present chapter the MTO reaction over CoAPO-18 and SAPO-18 has been followed by FT-IR spectroscopy in continuo, by means of a custom set-up constituted by a mass flow controller for the direct methanol dosage into a temperature-controlled IR cell operating in transmission mode (all the details are listed in Section 2.4.3). No outlet flow analyser was connected to the system, since the object of interest of this analysis was the identification of the species adsorbed on the catalyst surface and their evolution within the porous system during all the reaction pathways.

9.1. Samples calcination

Before fluxing methanol and initiating the MTO reaction, the sample was specifically calcined within the same set-up, simulating a catalyst pre-activation step, common to many catalytic processes. The details are reported in Section 2.4.3.

The evolution of the IR spectra during the template decomposition from the CoAPO-18 pore system is summarized in Figure 9.1, in which the effect of the rising temperature and duration of the treatment are highlighted.

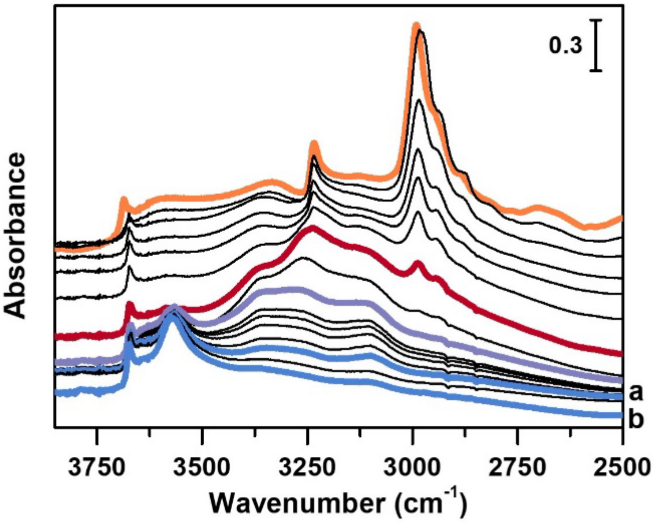

*Figure 9. 1. IR spectra of CoAPO-18u between 3850 and 2500 cm^{-1} (OH, NH, CH stretching regions) collected in N_2/O_2 mixture flux at rising temperature. Selected spectra are highlighted with different colour remarking the most significant changes in the profile due to temperature (orange spectrum at 180°C, red spectrum at 280°C, violet spectrum at 550°C) or prolonged heating treatment (blue spectrum **a** at 550°C for 4 hours and blue spectrum **b** after 24 hours). The spectra are shifted along the y axis for sake of clarity.*

The evolution of the decomposition of the templating agent (N,N-Diisopropylethyl amine) has been previously studied step by step by Marchese et al.[163] through a series of *ex situ* IR acquisitions and finds correspondence with what is reported in Figure 9.1. In the figure, the initial steps of desorption of atmospheric water that saturates the OH zone due to the strong H-bonding on the surface, are omitted. Starting from a temperature at which the material is considered free from adsorbed species (180°C orange spectrum) it is possible to clearly distinguish the characteristic signals of the organic template, i.e. the ν (C-H) of the isopropyl and ethyl functionalities between 3000 and 2700 cm^{-1} and the ν (N-H) of the amine at 3235 cm^{-1}. Also, regarding the CoAPO-18 profile, the ν P(O-H) signal emerges at 3678 cm^{-1}, while the Brønsted site signal is not yet distinguishable. Increasing the temperature, the decrease of ν (CH) signals intensity and the enlargement of ν (NH) signals are observed, indicating that alkyl functionalities decompose first, releasing the amine that start to establish intermolecular H-bonds (red spectrum, recorded at 280°C). Once 550°C is reached (temperature commonly used for calcination of this type of materials, violet spectrum) the total removal of the carbonaceous fraction is observed, while the N-H signals of the amine persist, indicating a rather strong interaction of this species with the surface of CoAPO-18. N-H signals undergo a noticeable decrease as the duration of treatment increases. In the violet spectrum, the appearance of the 3578 cm^{-1} signal of the BAS is recorded for the first time, as it is gradually released as a free oscillator while the concentration of the H-bonding acceptors decreases. In fact, the signal increases in intensity from the blue spectrum **a** to the spectrum blue **b**. The two blue spectra will be further investigated; the first corresponds to the result of a standard calcination treatment (comparable to that undergone by CoAPO-18c, 4 hours at 550°C, see previous chapter) while the second corresponds to the moment in which no more amine signals are recorded, i.e. a calcination treatment of 4 hours followed by a synthetic air flow overnight at RT and a second activation at 400°C. It is relevant to note that, despite undergoing oxidative treatment, H-CoAPO-18 exhibits its characteristic Brønsted site-related signal, indicating the presence of Co(II) in the framework. This suggests that the metal oxidation in framework is not a favoured process and requires rather drastic conditions such as prolonged pure oxygen atmosphere treatments to occur.

9.2. Methanol conversion over SAPO-18 and CoAPO-18

The reaction of methanol conversion has been performed over a H-SAPO-18 (Figure 9.2) and a H-CoAPO-18 (Figure 9.3) monitoring the process by means of transmission FT-IR spectroscopy under continuous MeOH vapour stream (vapour pressure 0.167 bar at 25°C), simulating the operative conditions of the MTO reaction at 400°C (see the Experimental section for further details). The development of the MeOH conversion is here described as the evolution of the surface adsorbed species during the proceeding of the reaction, assuming a working interval in which the catalysts activity relies above the 80% of conversion.[162] The description then can be focused on the transformations of active species before and during the mechanism of HCP, starting from the earliest interactions of methanol with active sites. The interpretation of the results obtained can be based on the most recent literature that has been able to spectroscopically give a profile to the complex set of species composing the HCP within different systems, such as acidic zeolites (H-ZSM-5,[245,246] H-Beta,[41,245] H-SSZ-13[247]) or APOs (H-SAPO-34)[248,249]. Two spectral portions mainly involved can therefore be identified, namely that of ν (OH) and ν (CH) stretching (3850-2450 cm^{-1}) and the region of ν (C=C) stretching and C-H bending modes (1900-1300 cm^{-1}). Figures 9.2 and 9.3 report in addition the ν (C≡O) IR spectral region (2250-2000 cm^{-1}), which requires specific description.

Comparing Figures 9.2 and 9.3 it is possible to qualitatively observe a similar behaviour of H-SAPO-18 (Figures 9.2) and H-CoAPO-18 (Figures 9.3) catalysts in terms of species produced, identifiable through the frequency of the vibrational modes involved. Instead, a profound difference is observed in the activity of the two zeotypes, which can be expressed in terms of signal intensity and growth rate of the same.

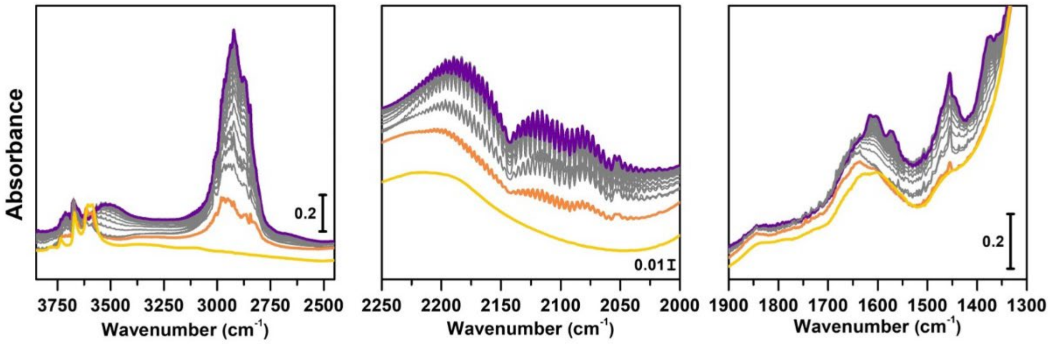

Figure 9. 2. Conversion of methanol catalysed by SAPO-18 at 400°C followed by IR spectra acquired in continuo. Left panel: O-H and C-H stretching regions (3850-2450 cm^{-1}); central panel: C=O stretching region (2250-2000 cm^{-1}); right panel: C=C region (1900-1300 cm^{-1}). The yellow spectrum corresponds to the activated SAPO-18, orange is the first interaction with methanol, grey are subsequent acquisitions at increasing time of methanol stream, violet after 1h conversion.

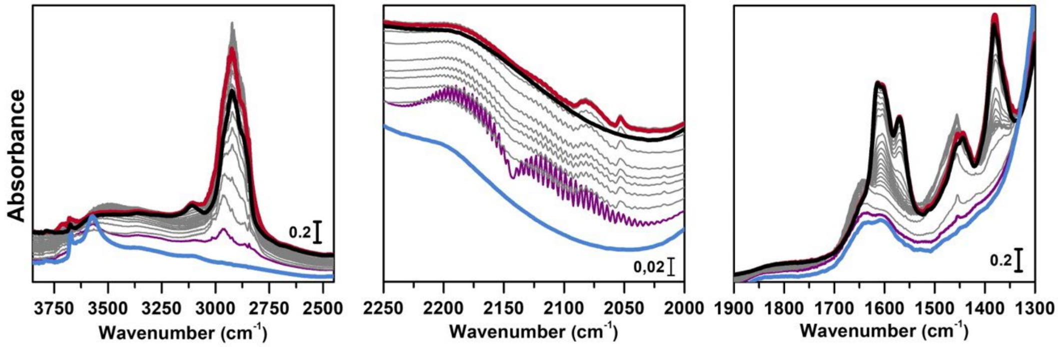

Figure 9. 3. Conversion of methanol catalysed by CoAPO-18 at 400°C followed by IR spectra acquired in continuo. Left panel: O-H and C-H stretching regions (3850-2450 cm^{-1}); central panel: C=O stretching region (2250-2000 cm^{-1}); right panel: C=C modes region (1900-1300 cm^{-1}). The blue spectrum corresponds to the CoAPO-18, purple is the first interaction with methanol, grey are subsequent acquisitions at increasing time of methanol stream, red after 4h conversion, black after inert gas flux.

The activated samples, before interaction with the substrate are highlighted in Figure 9.2 as yellow line (H-SAPO-18) and in Figure 9.3 as blue line (H-CoAPO-18) and have been obtained as reported in Experimental section. The H-CoAPO-18 spectrum corresponds to the blue spectrum **b** of Figure 9.1. The spectra have in common the presence of an intense signal due to the ν (OH), reliable with the BAS at 3620 cm^{-1} and 3580 cm^{-1} for H-SAPO-18 and H-CoAPO-18 respectively (a complete description is provided in Chapter 7). The very first interaction with methanol vapours (orange spectrum in Figure 9.2 and purple in Figure 9.3) suddenly induces, in both cases, a partial consumption of the BAS band accompanied by the formation of two families of new signals. In the ν (CH)zone, bands (left panels) at 3012, 2981, 2950, 2923, 2843, 2819 cm^{-1} are recorded, while in the low frequency region (right panels) a weak signal emerge 1454 cm^{-1}, and all signals appear intensified in the spectrum immediately following. These signals are associable to small methylated molecules, deriving from the instantaneous degradation of methanol and adsorption on the catalysts active sites, which indeed decreases in intensity. The 3012-2819 cm^{-1} group of signals corresponds to the vibrations of CH_3 complicated by Fermi resonance between stretching and overtones modes,[41] among which the signal around 2980 cm^{-1} is attributed to CH asymmetric stretching of methoxy groups (OCH_3) with its bending counterpart at 1454 cm^{-1} (symmetric deformation mode) reasonably corresponding to (Ze)-OCH_3, while the two components at 2950 and 2843 cm^{-1} are related to the methyl groups of DME.[248–251] This very first phase corresponds to the induction period, in which the building blocks of the HCP species are formed, whose evidence has allowed to postulate the direct coupling theory (See Section 1.2.1.1).[33] It is very interesting to note that in this phase, as soon as the methanol interacts with the catalyst surface, the typical roto-vibrational profile of carbon monoxide is recorded, characterized by two relatively intense maxima at 2183 and 2114 cm^{-1} (central panels). The intensity of this signal is comparable only in the first spectrum recorded for the two samples (orange and purple respectively) while it is significantly reduced in the case of H-CoAPO-18 remaining equally intense in the case of H-SAPO-18 (grey spectra). This signal is associated with two others that retain the same rotational profile, positioned at 2080 and 2060 cm^{-1}, that still requires a proper attribution. In the following spectra the behaviour of the two catalysts is deeply different. In both cases we observe the growth of a signal at 1645 cm^{-1} that can be attributed to C=C stretching of linear olefins[251] indicative of the initiation of chain reactions that drive the HCP. In the case of SAPO-18 the changes are very slow while for CoAPO-18 they are instantaneous. During the continuation of the reaction the signal at 1640 cm^{-1} is gradually substituted by the bands at 1614-1600 and 1597 cm^{-1}, which become extremely intense in the case of H-CoAPO-18, indicating the condensation of olefines occurring to form aromatic cycles. In parallel a component at 1382 cm^{-1} grows and that at 1454-1443 cm^{-1} is being partially consumed (violet spectrum in Figure 9.2, red in Figure 9.3). In the case of H-SAPO-18 there is a correspondence of frequencies, but not in the intensity of the signals and their growth rate. The first two bands around 1600 cm^{-1} are generated by the formation of aromatics (C=C ring vibrations), which shift at 1597 cm^{-1} with the evolution into polycondensed structures (coke precursor species), already observed within the HCP induced by SAPO-34. While the lower frequency one corresponds to the bending modes of the alkyl substituents on the aromatic structures. This is also confirmed by the structuration of the signals in the stretching region, which acquire three defined maxima at 2955, 2925 and 2870 cm^{-1}, corresponding to ν (C-H) stretching of the same groups.[247,248] In case of H-CoAPO-18 a completely new signal is visible in the last stages of the conversion at 3109 cm^{-1}, corresponding to ν C-H aromatic, which will be described later. It is worth noting that the formation of aromatic structures in H-SAPO-18 is very low and the associated bands (skeletal modes at 1614 and 1597 cm^{-1} and bending of methyl substituents at 1382 cm^{-1}) are poorly intense and their growth is slow (little changes in grey spectra), while the band at 1453 cm^{-1}, due to the CH_3 deformation of virtually isolated methoxy groups, continuously grows, overcoming the intensity of the other signals in the region. The same signal is instead reduced on H-CoAPO-18. This reasonably indicates that the H-SAPO-18 cavities keep trapping the unreacted methanol and its degradation products, which continuously occurs during all the time of stream (as attested by the intense roto-vibrational signal of CO), while the autocatalytic transformation of the HCP aromatic species is slower and inhibited. On the contrary H-CoAPO-18 quickly converts the small methyl intermediates which are involved in the HCP growing, that produces aromatic species dominating at the end of the conversion (red spectrum). The intensity of the CO signals individuated in the central panels, give support to this observation. A correlation can be found between the different capacity of the two catalysts in producing hydrocarbons and the trend of the bands of the precursors of the first C-C bond, which according to the most recent theories, correspond to CO and the surface methoxy groups -OCH_3. The higher conversion operated by H-CoAPO-18 (which gives rise to significantly more intense signals in the aromatic zone, with a higher growth rate) coincides with a decrease in the signal intensity of free CO and a stop in the growth of the signal at 1454 cm^{-1} related to the CH_3 bending of surface adsorbed methanol (Ze-OCH_3), at the proceeding of the conversion. It is reasonable to think that the CO is produced *in situ* from the decomposition of the methanol fraction not adsorbed by the BAS and it is continuously consumed during the process by the reaction with the -OCH_3 groups, explaining the modifications of the signals. This observation finds a logical answer in the Koch carbonylation mechanism, which involves the formation of a carbonyl by direct interaction of CO with a methoxy group, as proposed by Lercher et al.[51] As further confirm, the black spectrum of Figure 9.3 has been collected at the end of the conversion in absence of methanol stream, under inert flow only. The total absence of the CO signal in this spectrum demonstrates that the gas is instantaneously produced *in situ* by the methanol degradation and it stops when methanol stream is off. The CO is continuously generated by the methanol excess, and it is trapped in the catalyst cages all over the process. Reasonably it takes part in the conversion not only in the first stage but also in the HCP growth as carbon source.

The minor conversion by H-SAPO-18 is accompanied by the constant presence of free CO, indicated by the roto-vibrational gas signal with unchanged intensity. The less production of hydrocarbons by action of this catalyst is accompanied by a larger presence of unreacted precursors CO e -OCH_3, giving support to what described above. Further considerations will be provided in the next paragraphs.

9.3. Regeneration of CoAPO-18 catalyst after methanol conversion.

The same spectroscopic approach has been applied during the regeneration of the spent H-CoAPO-18. The full process is reported in Figure 9.4. The experiment described in Figure 9.4 is composed of three phases: the methanol conversion on H-CoAPO-18 (Figure 9.4a), the regeneration of the spent catalyst by thermal treatment at 550°C for 4 hours (Figure 9.4b) and the repetition of the reaction over the regenerated catalyst (Figure 9.4c). Moreover, the full experiment provides an opportunity to gain insight on various aspects of methanol conversion and on CoAPO-18 as a catalyst. First, the reaction was carried on the zeotype presenting the blue spectrum **a** of Figure 9.1 (it has undergone a rapid calcination, see Experimental section) and thus makes it possible to assess how the catalyst activation process affects the reaction. Secondly, by observing in real time how the species adsorbed in the porous system evolve during a thermal treatment, it is possible to obtain information on the deactivation/reactivation processes of the material. Finally, by subjecting the regenerated catalyst to a second cycle of catalysis, it is possible to observe how it has an influence on the catalytic activity.

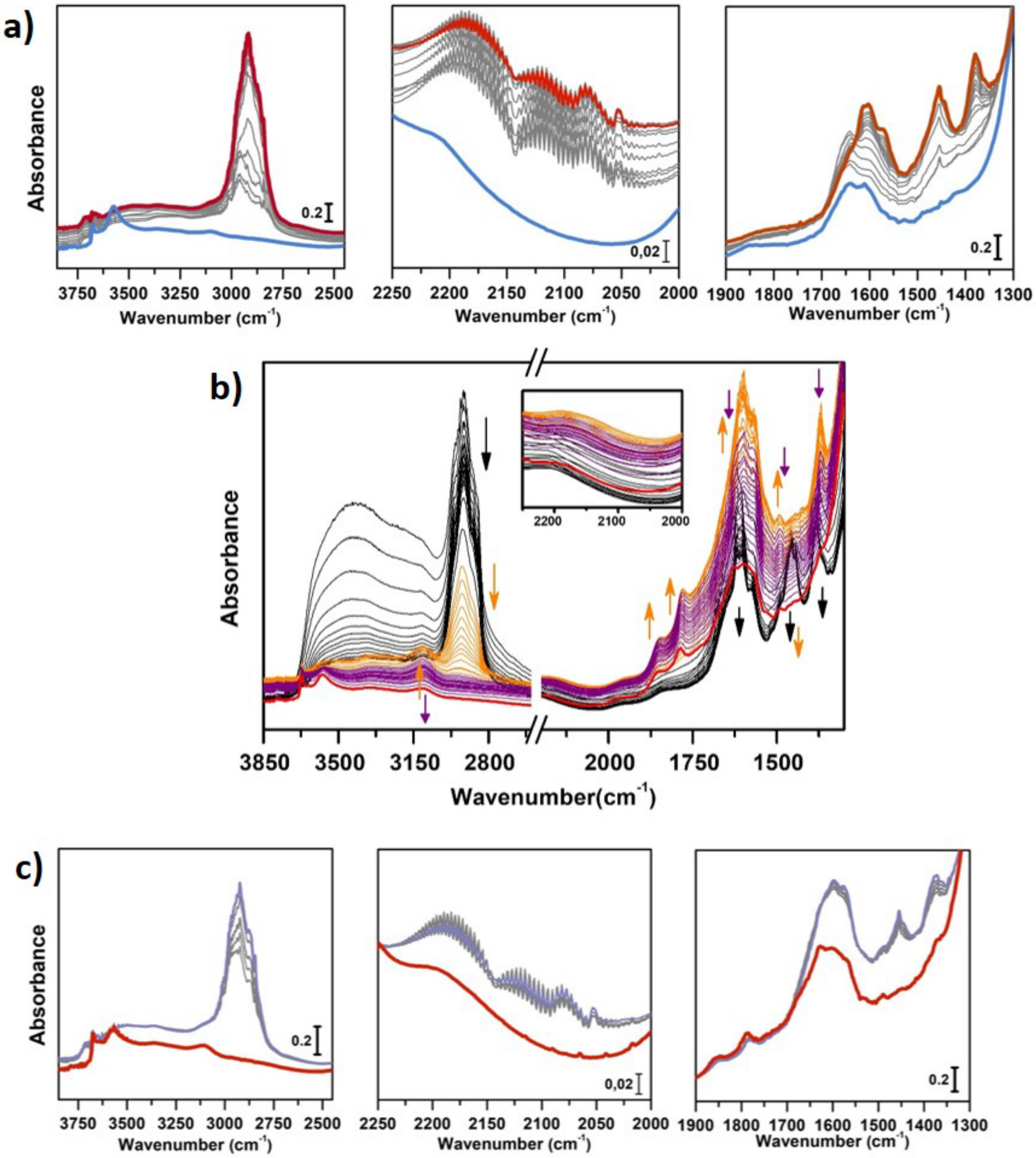

Figure 9. 4. ***Regeneration of CoAPO-18****. a) Conversion of methanol catalysed by CoAPO-18 at 400°C followed by IR spectra acquired in continuo before regeneration. Left panel: O-H and C-H stretching regions (3850-2450 cm^{-1}); central panel: C=O stretching region (2250-2000 cm^{-1}); right panel: C=C modes region (1900-1300 cm^{-1}). The blue spectrum corresponds to the CoAPO-18, purple is the first interaction with methanol, red after 4h conversion. b) Regeneration of CoAPO-18 followed by IR spectra acquired in continuo for 4h at 550°C; black spectra have been acquired rising temperature from RT to 550°C; orange spectra represent the first hour at 550°C; in purple the spectra acquired in the last 3 hours at 550°C; in red is reported the spectrum of CoAPO-18 after 4h of regeneration. c) Conversion of methanol catalysed by regenerated CoAPO-18 at 400°C followed by IR spectra acquired in continuo. Right panel: O-H and C-H stretching regions (3850-2450 cm^{-1}); central panel: C=O stretching region (2250-2000 cm^{-1}); right panel: C=C modes region (1900-1300 cm^{-1}). The red spectrum corresponds to the regenerated CoAPO-18; purple is after 1h conversion.*

Figure 9.4a must be compared with Figure 9.3, as the conversion of methanol has been performed over H-CoAPO-18 in two different conditions. In case of Figure 9.3, the sample has been activated operating a 4-hour calcination at 550°C under synthetic air flow and subsequently it has been fluxed by pure N_2 overnight at RT, while in Figure 9.4a the experiment has been carried out directly after 4 hours of calcination. In Figure 9.1 the result of the different calcination is reported as blue spectrum **a** (the one of Figure 9.4a) and blue spectrum **b** (Figure 9.3). It is evident from Figure 9.1 that the process of "fast calcination" does not lead to the complete desorption of the species originating by the template combustion, as the band at 3100 cm^{-1} due to the ν (N-H), is still present in blue spectrum **a.** The amine interacts with the CoAPO-18 by H-bonding involving the Brønsted sites, which ν (O-H) band result less intense in respect with blue spectrum **b** and generates a downward shifted component at 3356 cm^{-1}. This implies a reduced availability of the active sites to take part of the methanol adsorption and the catalytic conversion when stream is on. It results in a slower conversion of the substrate especially at the early stage, since the close-up spectra in Figure 9.4a indicate less pronounced changes in respect with ones of Figure 9.3. The vibrational profile of the adsorbed species after 4 hours of reaction (Red spectra Figure 9.3 and 9.4a) appears the same, with the prevalence of methylated aromatic structures. However, the higher intensity of the ring modes at 1614-1600 and 1597 cm^{-1} together with the methyl bending at 1380 cm^{-1} of Figure 9.3 suggest a more advanced level of development of aromatic species. While in Figure 9.4a the same signals present comparable intensity with the band at 1454 cm^{-1} of isolated OCH_3, as similarly observed for H-SAPO-18. This could suggest that the less availability of active sites (or weaker acidic strength in case of H-SAPO-18) limits the conversion to aromatics and so the HCP developing. The reaction relies at the stage of methanol decomposition which does not requires strong acidity (it occurs also on pure Silicalite-1 at comparable temperature)[51]. It must be underlined that during all the process the signal of CO is recorded with unchanged intensity. Again, this trend agrees better with the one of H-SAPO-18 in respect with the H-CoAPO-18 of Figure 9.3. The precursors rely unreacted in the catalyst cages giving rise to the vibrational mode of isolated species, while the hydrocarbon species have a slower growth rate. From this observation, it is allowed assuming that the rate of Koch carbonylation does not depend only on the catalyst composition (and therefore on the acidic strength) but more probably by the availability of active sites.

During the regeneration of the sample, the adsorbed species have been followed with the IR spectra reported in Figure 9.4b. The sample has been heated from RT to 550°C acquiring the black spectra. The first phenomenon observed is the desorption of water (the sample has been exposed to air before its regeneration) through the rapid decrease of the very intense and broad band in the ν(OH) region, generated by the interaction of H_2O with surface hydroxyls and the corresponding bending signal at 1600 cm^{-1}. Only in the last moments of this phase the signal related to the adsorbed methanol is disappearing (1454 cm^{-1}) while a significant decrease in the C-(CH_3) signals (2960-2860 and 1380 cm^{-1}) and aromatic ring modes is observed. The latter evolves in a signal that is gradually structured in three defined maxima at 1624, 1596 and 1572 cm^{-1} indicating the increasing condensation of the aromatic systems. The orange spectra describe the first hour at 550°C. It is initially observed an increase in the intensity of the ring modes of the condensed molecules (coke forming). At the same time there is an indication of the loss of ring substituents as the first step of degradation: the CH_3 stretching modes are progressively decreasing, leaving space to the appearance of a 3107 cm^{-1} and 1495 cm^{-1} bands, that corresponds to the aromatic C-H stretching and bending respectively. The 3107 cm^{-1} signal has already been recorded in the last stages of Figure 9.3 corresponding to an advanced stage of thermal evolution within the pores, which can be identified as a sign of recognition for the deactivating species. Completely new signals appear at 1857 and 1781 cm^{-1} corresponding to ν_{asym} and ν_{sym} C=O stretching of carbonyl substituents of a five-membered aromatic ring.[251] During the progress of the thermal treatment, underlined by violet spectra, the progressive consumption of the coke related bands is observed until reaching, after 4 hours, the situation represented by the red spectrum. In this, few signals can be identified in the region of aromatic ν (C-H) and carbonyl ν (C=O) stretching, indicating the nature of the persistent species at the end of the calcination treatment. It is worth noting that the roto-vibrational signal of CO is never recorded during the catalyst regeneration, during which the sample is subjected only to N_2 and O_2 flow (Figure 9.4b, inset). This attests that the combustion of the hydrocarbon species does not produces the syngas, which is, on the contrary, generated exclusively from methanol decomposition. The sample was then subjected to a new cycle of methanol conversion reaction, under the same conditions used in the previous cases, obtaining the results shown in Figure 9.4c. The reaction proceeds, as already observed, starting with the formation of CO and surface (Ze)-OCH_3 groups and then giving rise to bands related to polycondensed aromatic systems, which probably grow from the pre-existing aromatic fragments, surviving the calcination process (witnessed by the bands at 3107 and 1495 cm^{-1}) and not from the olefinic fragments (the 1645 cm^{-1} signal is missing). The conversion is slower compared to that carried out by the fresh catalyst, but still gives evidence of the possibility of using the regenerated catalyst, despite a lower activity.

9.4. The role of Carbon Monoxide

It is not surprising to observe the formation of CO during the conversion of methanol at 400°C over the surface of an acidic zeolite/zeotype. It is attested that in such conditions MeOH degrades, by action of the acidic functionalities combined with the high temperature, forming formaldehyde, CH_4, H_2, CO and water.[51] What we observed in the experiments of methanol conversion over AlPO-18s is the retaining of the gas CO trapped the in pore structure of the catalysts at working temperature along all the reaction. Considering that at 400°C the adsorption is thermodynamically inhibited, the appearance of the roto-vibrational profiles of the carbon monoxide can by explained only by the gas rotor hampered by the spatial constriction of the AlPO-18 cages. This signal is recorded in every experiment of methanol conversion reported in Figures 9.2, 9.3, 9.4a, 9.4c. In the central panel of the four figures above, the roto-vibrational CO signal presents comparable intensity in the first spectrum acquired for each, corresponding to the very first interaction between the catalyst and the substrate. This moment reasonably corresponds to the breaking of the methanol bonds, before the coupling reaction cascade to form the HCP, begins. Part of the methanol is adsorbed on the catalyst active sites producing surface methoxy species $-OCH_3$ and releasing water, with a 1:1 ratio in accordance with Scheme 9.1.[252,253]

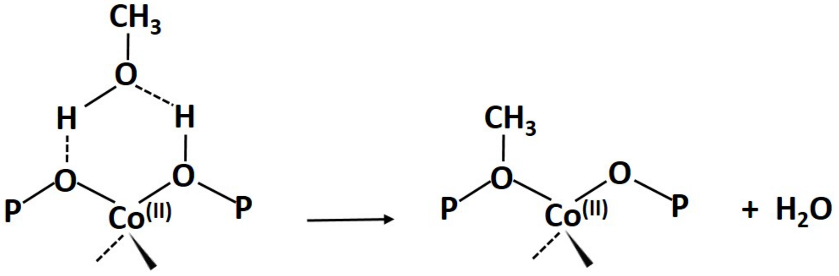

Scheme 9. 1. Methoxy groups formation upon methanol adsorption on CoAPO-18 BAS sites.

Reasonably, the excess of MeOH is decomposed giving origin to small methylated molecules as formaldehyde and dimethyl ether and CO, which are spectroscopically identified, as mentioned earlier. In this work, a correlation between the trend of the CO bands, generated by the methanol decomposition, and the band at 1454 cm^{-1}, which must be considered diagnostic of the presence of surface methoxy species $-OCH_3$, has been identified. Thus, the spectroscopical evidence reported in the present work can give support to the occurrence of a Koch carbonylation involving the $-OCH_3$ and the CO generated in situ, in accordance with the newest theories in the field. The role of CO in the formation of the first C-C bond has never been ignored or underestimated, but often rejected because it was believed that its concentration in the reaction environment could not be high enough. Moreover, prior to the decisive work of Lercher et al.[51] it was considered that the presence of CO could only result from impurities in the reactants. This was compounded by the lack of monitoring of reactor outgoing CO during catalytic experiments. The approach adopted in this work provides a new point of view, showing what is formed within the system and not what it releases and can be helpful in completing the overall picture. We believe that the experiments reported in this chapter provide robust evidence of the generation of CO *in situ* from methanol degradation and its subsequent involvement in the hydrocarbons formation starting from the carbonylation of the $-OCH_3$ groups. Summarising what previously noticed, in the conversion catalysed by H-CoAPO-18 properly activated (Figure 9.3) a significant reduction of the intensity of the roto-vibrational profile of the gaseous CO is observed at the proceeding of the reaction while the diagnostic $-OCH_3$ band appears constant in intensity. This behaviour of the spectroscopic signals suggests a continuous consumption and regeneration of the species involved which carry on the proceeding of the conversion into aromatic methylated hydrocarbons. The fact that a constant growth of the same signal is attested in presence of H-SAPO-18

(Figure 9.2) and H-CoAPO-18 rapidly activated or regenerated (Figure 9.4a and 9.4c) indicates the presence of the unreacted precursors within the porous system, which evolution into HCP species is more restricted. The reason can be traced in the higher acidity and availability of the active sites of H-CoAPO-18 (Figure 9.3) that continuously allow the formation of -OCH_3 and release of a carbonyl intermediated instantaneously converted into hydrocarbon molecules releasing water. The free BAS sites of H-CoAPO-18 of Figure 9.4 a and c are in less concentration in respect with the sample of Figure 9.3, thus they are more easily saturated by methanol. It follows that the concentration of -OCH_3 is lower and the fraction of not adsorbed methanol is pushed to the decomposition to CO, which prevails over the carbonylation.

It is not surprising that carbonyls are not detected by the set up adopted in this work, because molecules as ketones, esters or carbonyls acids can easily leave the surface of the catalyst.

In conclusion, the work reported in this chapter provides robust evidence of the involving of Carbon monoxide in the methanol conversion operated by different acidic AlPO-18, giving support to the occurrence of Koch carbonylation process. With a view of this findings, more information about the chemistry of the methanol conversion can be achieved with the same approach if combined with an outlet analyser for the product identification.

Conclusion remarks

The variety of case studies presented in this thesis collectively exemplifies the complexity of the world of zeolitic materials. This PhD work tried to combine skills that are usually strictly sectorized and investigated by different specialists, namely the synthesis, the characterization and the catalysis. It is important to parallelly consider each of these aspects with the aim to enhance the materials development and their employment, but their combination may be even a more powerful tool. Indeed, the catalytic application cannot dispense with the full understanding of the material that derives from its characterization, but at the same time this can be completed by the knowledge of the synthetic mechanisms, since it allows studying the system starting from the moment of its assembly.

Particular attention has been posed to the production and the determination of zeolitic active sites by different phisico-chemical techniques. This is mainly expressed in the topic of Chapter 3. The knowledge acquired in spectroscopies, allowed the investigation of different active systems. Acidic properties have been principally investigated by means of *in situ* FT-IR spectroscopy coupled with opportune probe molecules, while transition metal containing systems were principally studied through DR-UV-Visible spectroscopy. The correlation between the structural array of the porous structure of zeolitic materials and the way in which the active sites are located, giving the material shape-selective catalytic properties, has been the main focus of this doctoral research. The interaction surface-molecules, often studied by *ad hoc* created experiments, has been the primary means of investigation, also allowing the determination of the catalytic activity of materials synthesized personally or by others (as in case of Chapters 6-8). All this is due to the deep knowledge of the research group in the physico-chemical study of heterogeneous catalysts, within which this work was developed. Chapter 9 is a good example of the advanced application of these competencies.

The approach to the synthesis of zeolites is instead a new topic for the tradition of the group and those reported in this work, in particular in Chapters 4 and 5, are the first results of the new line of research. The synthetic techniques of complex materials such as zeolites requires, above all, a long experience and observation. The logical principles that guide the processes are not the only factors at play, but a high degree of empiricism is involved. For the development of the synthesis of a new material, every possible experimental variable must be considered, such as times, temperature, nature of the reagents, additives and instrumentation. Although a screening of the synthesis conditions of different materials has been carried out, in some cases it is still necessary a systematic study of the variables that leads to targeted production, limiting the trial-and-error approach. Compared to traditional inorganic synthesis, the world of porous materials adds an additional level of difficulty as it is often based on the use of organic molecules as templating agents. In the light of these considerations, the results reported in Chapters 4 and 5, although rather preliminary, can be considered satisfactory and represent a good starting point for the continuation of the research in that field.

Looking to the near future, the characteristics that emerged from the study of MAPOs discussed in Chapters 7-9 are particularly promising for their application in the MTO process. For this reason, this study will be carried out as part of the European COZMOS project, in participation with the University of Oslo, which aims to produce the next generation of catalysts for the production of light olefines starting from waste CO_2. The process involves the hydrogenation of CO_2 followed by the MTO conversion, in which zeolites play a crucial role.

Bibliography

(1) Na, K.; Jo, C.; Kim, J.; Cho, K.; Jung, J.; Seo, Y.; Messinger, R. J.; Chmelka, B. F.; Ryoo, R. Directing Zeolite Structures into Hierarchically Nanoporous Architectures. *Science (80-.).* **2011**, *333* (6040), 328–332. https://doi.org/10.1126/science.1204452.

(2) Kulprathipanja, S. *Zeolites in Industrial Separation and Catalysis*; Kulprathipanja, S., Ed.; Wiley, 2010. https://doi.org/10.1002/9783527629565.

(3) Baerlocher, C.; Meier, W. M.; Olson, D. H. ATLAS OF ZEOLITE FRAMEWORK TYPES Fifth Revised Editon. *Framework* **2001**.

(4) Weitkamp, J. Zeolites and Catalysis. *Solid State Ionics* **2000**, *131* (1–2), 175–188. https://doi.org/10.1016/S0167-2738(00)00632-9.

(5) Wright, P. A.; Pearce, G. M. Structural Chemistry of Zeolites. In *Zeolites and Catalysis*; Wiley-VCH Verlag GmbH & Co. KGaA: Weinheim, Germany, 2010; pp 171–207. https://doi.org/10.1002/9783527630295.ch7.

(6) Zdravkov, B. D.; Čermák, J. J.; Šefara, M.; Janků, J. Pore Classification in the Characterization of Porous Materials: A Perspective. *Cent. Eur. J. Chem.* **2007**, *5* (2), 385–395. https://doi.org/10.2478/s11532-007-0017-9.

(7) Sing, K. S. W.; Everett, D. H.; Haul, R. A. W.; Moscou, L.; Pierotti, R. A.; Rouquerol, J.; Siemieniewska, T. Reporting Physisorption Data for Gas/Solid Systems with Special Reference to the Determination of Surface Area and Porosity (Recommendations 1984). *Pure Appl. Chem.* **1985**, *57* (4), 603–619. https://doi.org/10.1351/pac198557040603.

(8) Corma, A.; Diaz-Cabanas, M. J.; Jiang, J.; Afeworki, M.; Dorset, D. L.; Soled, S. L.; Strohmaier, K. G. Extra-Large Pore Zeolite (ITQ-40) with the Lowest Framework Density Containing Double Four- and Double Three-Rings. *Proc. Natl. Acad. Sci.* **2010**, *107* (32), 13997–14002. https://doi.org/10.1073/pnas.1003009107.

(9) Database of Zeolite Structures http://www.iza-structure.org/databases/.

(10) DENT, L. S.; SMITH, J. V. Crystal Structure of Chabazite, a Molecular Sieve. *Nature* **1958**, *181* (4626), 1794–1796. https://doi.org/10.1038/1811794b0.

(11) FLANIGEN, E. M.; GROSE, R. W. Phosphorus Substitution in Zeolite Frameworks. In *Journal of the American Chemical Society*; American Chemical Society, 1974; Vol. 104, pp 76–101. https://doi.org/10.1021/ba-1971-0101.ch006.

(12) Wilson, S. T.; Lok, B. M.; Messina, C. A.; Cannan, T. R.; Flanigen, E. M. Aluminophosphate Molecular Sieves: A New Class of Microporous Crystalline Inorganic Solids. *J. Am. Chem. Soc.* **1982**, *104* (4), 1146–1147. https://doi.org/10.1021/ja00368a062.

(13) Pastore, H. O.; Coluccia, S.; Marchese, L. Porous Aluminophosphates: From Molecular Sieves to Designed Acid Catalysts. *Annu. Rev. Mater. Res.* **2005**, *35* (2), 351–395. https://doi.org/10.1146/annurev.matsci.35.103103.120732.

(14) Corà, F.; Catlow, C. R. A. Ionicity and Framework Stability of Crystalline Aluminophosphates. *J. Phys. Chem. B* **2001**, *105* (42), 10278–10281.

https://doi.org/10.1021/jp0107053.

(15) Potter, M. E. Down the Microporous Rabbit Hole of Silicoaluminophosphates: Recent Developments on Synthesis, Characterization, and Catalytic Applications. *ACS Catal.* **2020**, *10* (17), 9758–9789. https://doi.org/10.1021/acscatal.0c02278.

(16) Degnan, T. F.; Chitnis, G. K.; Schipper, P. H. History of ZSM-5 Fluid Catalytic Cracking Additive Development at Mobil. *Microporous Mesoporous Mater.* **2000**, *35–36*, 245–252. https://doi.org/10.1016/S1387-1811(99)00225-5.

(17) Flanigen, E. M.; Bennett, J. M.; Grose, R. W.; Cohen, J. P.; Patton, R. L.; Kirchner, R. M.; Smith, J. V. Silicalite, a New Hydrophobic Crystalline Silica Molecular Sieve. *Nature* **1978**, *271* (5645), 512–516. https://doi.org/10.1038/271512a0.

(18) Taramasso, M.; Donato Milanese, S.; Perego, G.; Notari, B. Preparation of Porous Crystalline Synthetic Material Comprised of Slicon and Titanum Oxdes. **1983**, No. 19, 410–501.

(19) G. T. Kokotailo; S. L. Lawton; D. H. Olson; W. M. Meier. Structure of Synthetic Zeolite ZSM-5. *Nature* **1978**, *272(5652)* (March), 437–438. https://doi.org/https://doi.org/10.1038/272437a0.

(20) van Koningsveld, H. Localization of Non-Framework Species in MFI. *J. Mol. Catal. A Chem.* **1998**, *134* (1–3), 89–95. https://doi.org/10.1016/S1381-1169(98)00025-9.

(21) Simmen, A.; McCusker, L. B.; Baerlocher, C.; Meier, W. M. The Structure Determination and Rietveld Refinement of the Aluminophosphate AlPO4-18. *Zeolites* **1991**, *11* (7), 654–661. https://doi.org/10.1016/S0144-2449(05)80167-8.

(22) Chen, J.; Thomas, J. M.; Wright, P. A.; Townsend, R. P. Silicoaluminophosphate Number Eighteen (SAPO-18): A New Microporous Solid Acid Catalyst. *Catal. Letters* **1994**, *28* (2–4), 241–248. https://doi.org/10.1007/BF00806053.

(23) Chen, J.; Thomas, J. M. MAPO-18 (M ? Mg, Zn, Co): A New Family of Catalysts for the Conversion of Methanol to Light Olefins. *J. Chem. Soc. Chem. Commun.* **1994**, *18* (5), 603. https://doi.org/10.1039/c39940000603.

(24) Wagner, P.; Nakagawa, Y.; Lee, G. S.; Davis, M. E.; Elomari, S.; Medrud, R. C.; Zones, S. I. Guest/Host Relationships in the Synthesis of the Novel Cage-Based Zeolites SSZ-35, SSZ-36, and SSZ-39. *J. Am. Chem. Soc.* **2000**, *122* (2), 263–273. https://doi.org/10.1021/ja990722u.

(25) Sankar, G.; Raja, R. On the Structure of Cobalt-Substituted Aluminophosphate Catalysts and Their Catalytic Performance. In *Nanostructured Catalysts*; Springer US: Boston, MA, 2008; pp 195–212. https://doi.org/10.1007/978-0-387-30641-4_8.

(26) Franklin, I. L.; Beale, A. M.; Sankar, G. On the Activity, Longevity and Recyclability of Mn(II) and Co(II) Substituted AlPO-18 Catalysts for the Conversion of Methanol to Light Olefins. *Catal. Today* **2003**, *81* (4), 623–629. https://doi.org/10.1016/S0920-5861(03)00160-3.

(27) Thomas, J. M. Design, Synthesis, and In Situ Characterization of New Solid Catalysts. *Angew. Chemie Int. Ed.* **1999**, *38* (24), 3588–3628. https://doi.org/10.1002/(SICI)1521-3773(19991216)38:24<3588::AID-ANIE3588>3.0.CO;2-4.

(28) Thomas, J. M.; Raja, R. Catalytically Active Centres in Porous Oxides: Design and Performance of Highly Selective New Catalysts. *Chem. Commun.* **2001**, No. 8, 675–687. https://doi.org/10.1039/b100369k.

(29) Marthala, V. R. R.; Jiang, Y.; Huang, J.; Wang, W.; Gläser, R.; Hunger, M. Beckmann Rearrangement of 15N-Cyclohexanone Oxime on Zeolites Silicalite-1, H-ZSM-5, and H-[B]ZSM-5 Studied by Solid-State NMR Spectroscopy. *J. Am. Chem. Soc.* **2006**, *128* (46), 14812–14813. https://doi.org/10.1021/ja066392c.

(30) Zecchina, A.; Spoto, G.; Bordiga, S. Probing the Acid Sites in Confined Spaces of Microporous Materials by Vibrational Spectroscopy. *Phys. Chem. Chem. Phys.* **2005**, *7* (8), 1627. https://doi.org/10.1039/b418763f.

(31) Bordiga, S.; Lamberti, C.; Bonino, F.; Travert, A.; Thibault-Starzyk, F. Probing Zeolites by Vibrational Spectroscopies. *Chem. Soc. Rev.* **2015**, *44* (20), 7262–7341. https://doi.org/10.1039/C5CS00396B.

(32) Chang, C. D.; Lang, W. H. Process for Manufacturing Olefins. US4025576 A, 1977.

(33) Yarulina, I.; Chowdhury, A. D.; Meirer, F.; Weckhuysen, B. M.; Gascon, J. Recent Trends and Fundamental Insights in the Methanol-to-Hydrocarbons Process. *Nat. Catal.* **2018**, *1* (6), 398–411. https://doi.org/10.1038/s41929-018-0078-5.

(34) Yarulina, I.; De Wispelaere, K.; Bailleul, S.; Goetze, J.; Radersma, M.; Abou-Hamad, E.; Vollmer, I.; Goesten, M.; Mezari, B.; Hensen, E. J. M.; Martínez-Espín, J. S.; Morten, M.; Mitchell, S.; Perez-Ramirez, J.; Olsbye, U.; Weckhuysen, B. M.; Van Speybroeck, V.; Kapteijn, F.; Gascon, J. Structure–Performance Descriptors and the Role of Lewis Acidity in the Methanol-to-Propylene Process. *Nat. Chem.* **2018**, *10* (8), 804–812. https://doi.org/10.1038/s41557-018-0081-0.

(35) Stöcker, M. Methanol-to-Hydrocarbons: Catalytic Materials and Their Behavior. *Microporous Mesoporous Mater.* **1999**, *29* (1–2), 3–48. https://doi.org/10.1016/S1387-1811(98)00319-9.

(36) Chen, D.; Moljord, K.; Holmen, A. A Methanol to Olefins Review: Diffusion, Coke Formation and Deactivation on SAPO Type Catalysts. *Microporous Mesoporous Mater.* **2012**, *164*, 239–250. https://doi.org/10.1016/j.micromeso.2012.06.046.

(37) Olsbye, U.; Svelle, S.; Lillerud, K. P.; Wei, Z. H.; Chen, Y. Y.; Li, J. F.; Wang, J. G.; Fan, W. B. The Formation and Degradation of Active Species during Methanol Conversion over Protonated Zeotype Catalysts. *Chem. Soc. Rev.* **2015**, *44* (20), 7155–7176. https://doi.org/10.1039/c5cs00304k.

(38) Olsbye, U.; Svelle, S.; Bjrgen, M.; Beato, P.; Janssens, T. V. W.; Joensen, F.; Bordiga, S.; Lillerud, K. P. Conversion of Methanol to Hydrocarbons: How Zeolite Cavity and Pore Size Controls Product Selectivity. *Angew. Chemie - Int. Ed.* **2012**, *51* (24), 5810–5831. https://doi.org/10.1002/anie.201103657.

(39) Dahl, I. M.; Kolboe, S. On the Reaction Mechanism for Propene Formation in the MTO Reaction over SAPO-34. *Catal. Letters* **1993**, *20* (3–4), 329–336. https://doi.org/10.1007/BF00769305.

(40) Dahl, I. M.; Kolboe, S. On the Reaction Mechanism for Propene Formation in the MTO Reaction over SAPO-34. *Catal. Letters* **1993**, *20* (3–4), 329–336. https://doi.org/10.1007/BF00769305.

(41) Bjørgen, M.; Bonino, F.; Kolboe, S.; Lillerud, K.-P.; Zecchina, A.; Bordiga, S. Spectroscopic Evidence for a Persistent Benzenium Cation in Zeolite H-Beta. *J. Am. Chem. Soc.* **2003**, *125* (51), 15863–15868. https://doi.org/10.1021/ja037073d.

(42) Bjørgen, M.; Bonino, F.; Arstad, B.; Kolboe, S.; Lillerud, K. P.; Zecchina, A.; Bordiga, S. Persistent Methylbenzenium Ions in Protonated Zeolites: The Required Proton Affinity of the Guest Hydrocarbon. *ChemPhysChem* **2005**, *6* (2), 232–235. https://doi.org/10.1002/cphc.200400422.

(43) Saepurahman; Visur, M.; Olsbye, U.; Bjørgen, M.; Svelle, S. In Situ FT-IR Mechanistic Investigations of the Zeolite Catalyzed Methylation of Benzene with Methanol: H-ZSM-5 versus H-Beta. *Top. Catal.* **2011**, *54* (16–18), 1293–1301. https://doi.org/10.1007/s11244-011-9751-5.

(44) Li, T.; Shoinkhorova, T.; Gascon, J.; Ruiz-Martinez, J. Aromatics Production via Methanol-Mediated Transformation Routes. *ACS Catal.* **2021**, *11* (13), 7780–7819. https://doi.org/10.1021/acscatal.1c01422.

(45) Song, W.; Marcus, D. M.; Fu, H.; Ehresmann, J. O.; Haw, J. F. An Oft-Studied Reaction That May Never Have Been: Direct Catalytic Conversion of Methanol or Dimethyl Ether to Hydrocarbons on the Solid Acids HZSM-5 or HSAPO-34. *J. Am. Chem. Soc.* **2002**, *124* (15), 3844–3845. https://doi.org/10.1021/ja016499u.

(46) JIANG, Y.; WANG, W.; REDDYMARTHALA, V.; HUANG, J.; SULIKOWSKI, B.; HUNGER, M. Effect of Organic Impurities on the Hydrocarbon Formation via the Decomposition of Surface Methoxy Groups on Acidic Zeolite Catalysts. *J. Catal.* **2006**, *238* (1), 21–27. https://doi.org/10.1016/j.jcat.2005.11.029.

(47) Yamazaki, H.; Shima, H.; Imai, H.; Yokoi, T.; Tatsumi, T.; Kondo, J. N. Evidence for a "Carbene-like" Intermediate during the Reaction of Methoxy Species with Light Alkenes on H-ZSM-5. *Angew. Chemie - Int. Ed.* **2011**, *50* (8), 1853–1856. https://doi.org/10.1002/anie.201007178.

(48) Wu, X.; Xu, S.; Zhang, W.; Huang, J.; Li, J.; Yu, B.; Wei, Y.; Liu, Z. Direct Mechanism of the First Carbon–Carbon Bond Formation in the Methanol-to-Hydrocarbons Process. *Angew. Chemie - Int. Ed.* **2017**, *56* (31), 9039–9043. https://doi.org/10.1002/anie.201703902.

(49) Hutchings, G. J.; Gottschalk, F.; Hall, M. V. M.; Hunter, R. Hydrocarbon Formation from Methylating Agents over the Zeolite Catalyst ZSM-5. *J. Chem. Soc. Faraday Trans. 1* **1987**, *83* (3), 571.

(50) Wang, C.; Chu, Y.; Xu, J.; Wang, Q.; Qi, G.; Gao, P.; Zhou, X.; Deng, F. Extra-Framework Aluminum-Assisted Initial C−C Bond Formation in Methanol-to-Olefins Conversion on Zeolite H-ZSM-5. *Angew. Chemie - Int. Ed.* **2018**, *57* (32), 10197–10201. https://doi.org/10.1002/anie.201805609.

(51) Liu, Y.; Müller, S.; Berger, D.; Jelic, J.; Reuter, K.; Tonigold, M.; Sanchez-Sanchez, M.; Lercher, J. A. Formation Mechanism of the First Carbon-Carbon Bond and the First Olefin in

the Methanol Conversion into Hydrocarbons. *Angew. Chemie - Int. Ed.* **2016**, *55* (19), 5723–5726. https://doi.org/10.1002/anie.201511678.

(52) Chowdhury, A. D.; Houben, K.; Whiting, G. T.; Mokhtar, M.; Asiri, A. M.; Al-Thabaiti, S. A.; Basahel, S. N.; Baldus, M.; Weckhuysen, B. M. Initial Carbon–Carbon Bond Formation during the Early Stages of the Methanol-to-Olefin Process Proven by Zeolite-Trapped Acetate and Methyl Acetate. *Angew. Chemie - Int. Ed.* **2016**, *55* (51), 15840–15845. https://doi.org/10.1002/anie.201608643.

(53) Chowdhury, A. D.; Paioni, A. L.; Houben, K.; Whiting, G. T.; Baldus, M.; Weckhuysen, B. M. Bridging the Gap between the Direct and Hydrocarbon Pool Mechanisms of the Methanol-to-Hydrocarbons Process. *Angew. Chemie - Int. Ed.* **2018**, *57* (27), 8095–8099. https://doi.org/10.1002/anie.201803279.

(54) Yang, L.; Yan, T.; Wang, C.; Dai, W.; Wu, G.; Hunger, M.; Fan, W.; Xie, Z.; Guan, N.; Li, L. Role of Acetaldehyde in the Roadmap from Initial Carbon-Carbon Bonds to Hydrocarbons during Methanol Conversion. *ACS Catal.* **2019**, *9* (7), 6491–6501. https://doi.org/10.1021/acscatal.9b00641.

(55) Signorile, M.; Braglia, L.; Crocellà, V.; Torelli, P.; Groppo, E.; Ricchiardi, G.; Bordiga, S.; Bonino, F. Titanium Defective Sites in TS-1: Structural Insights by Combining Spectroscopy and Simulation. *Angew. Chemie - Int. Ed.* **2020**, *59* (41), 18145–18150. https://doi.org/10.1002/anie.202005841.

(56) Prestipino, C.; Bonino, F.; Usseglio, S.; Damin, A.; Tasso, A.; Clerici, M. G.; Bordiga, S.; D?Acapito, F.; Zecchina, A.; Lamberti, C. Equilibria between Peroxo and Hydroperoxo Species in the Titanosilicates: An In Situ High-Resolution XANES Investigation. *ChemPhysChem* **2004**, *5* (11), 1799–1804. https://doi.org/10.1002/cphc.200400427.

(57) Berlier, G.; Crocellà, V.; Signorile, M.; Borfecchia, E.; Bonino, F.; Bordiga, S. Characterization of Metal Centers in Zeolites for Partial Oxidation Reactions. In *Applications Of Evolutionary Computation In Chemistry*; 2018; pp 91–154. https://doi.org/10.1007/430_2018_24.

(58) Mintova, S.; Barrier, N. *Verified Syntheses Of Zeolitic Materials*, Third Edit.; Mintova, S., Ed.; Published on behalf of the Synthesis Commission of the International Zeolite Association, 2016.

(59) Cubillas, P.; Anderson, M. W. Synthesis Mechanism: Crystal Growth and Nucleation. In *Zeolites and Catalysis*; Wiley-VCH Verlag GmbH & Co. KGaA: Weinheim, Germany, 2010; pp 1–55. https://doi.org/10.1002/9783527630295.ch1.

(60) Grand, J.; Awala, H.; Mintova, S. Mechanism of Zeolites Crystal Growth: New Findings and Open Questions. *CrystEngComm* **2016**, *18* (5), 650–664. https://doi.org/10.1039/c5ce02286j.

(61) Cundy, C. S.; Cox, P. A. The Hydrothermal Synthesis of Zeolites: History and Development from the Earliest Days to the Present Time. *Chem. Rev.* **2003**, *103* (3), 663–701. https://doi.org/10.1021/cr020060i.

(62) Cundy, C. S.; Cox, P. A. The Hydrothermal Synthesis of Zeolites: Precursors, Intermediates and Reaction Mechanism. *Microporous Mesoporous Mater.* **2005**, *82* (1–2), 1–78. https://doi.org/10.1016/j.micromeso.2005.02.016.

(63) Aerts, A.; Kirschhock, C. E. A.; Martens, J. A. Methods for in Situ Spectroscopic Probing of the Synthesis of a Zeolite. *Chem. Soc. Rev.* **2010**, *39* (12), 4626. https://doi.org/10.1039/b919704b.

(64) Lakes, R. Materials with Structural Hierarchy. *Nature* **1993**, *361* (6412), 511–515. https://doi.org/10.1038/361511a0.

(65) Schwieger, W. Hierarchy Concepts: Classification and Preparation Strategies for Zeolite Containing Materials with Hierarchical Porosity. *Chem. Soc. Rev.* **2016**, *45* (12), 3353–3376. https://doi.org/10.1039/C5CS00599J.

(66) Hartmann, M.; Machoke, A. G.; Schwieger, W. Catalytic Test Reactions for the Evaluation of Hierarchical Zeolites. *Chem. Soc. Rev.* **2016**, *45* (12), 3313–3330. https://doi.org/10.1039/C5CS00935A.

(67) Hartmann, M.; Thommes, M.; Schwieger, W. Hierarchically-Ordered Zeolites: A Critical Assessment. *Adv. Mater. Interfaces* **2021**, *8* (4). https://doi.org/10.1002/admi.202001841.

(68) Serrano, D. P.; Escola, J. M.; Pizarro, P. Synthesis Strategies in the Search for Hierarchical Zeolites. *Chem. Soc. Rev.* **2013**, *42* (9), 4004–4035. https://doi.org/10.1039/c2cs35330j.

(69) Schneider, D.; Mehlhorn, D.; Zeigermann, P.; Kärger, J.; Valiullin, R. Transport Properties of Hierarchical Micro-Mesoporous Materials. *Chem. Soc. Rev.* **2016**, *45* (12), 3439–3467. https://doi.org/10.1039/c5cs00715a.

(70) Corma, A. From Microporous to Mesoporous Molecular Sieve Materials and Their Use in Catalysis. *Chem. Rev.* **1997**, *97* (6), 2373–2419. https://doi.org/10.1021/cr960406n.

(71) Kresge, C. T.; Leonowicz, M. E.; Roth, W. J.; Vartuli, J. C.; Beck, J. S. Ordered Mesoporous Molecular Sieves Synthesized by a Liquid-Crystal Template Mechanism. *Nature* **1992**, *359* (6397), 710–712. https://doi.org/10.1038/359710a0.

(72) Zhao, D. Triblock Copolymer Syntheses of Mesoporous Silica with Periodic 50&Nbsp;to 300&Nbsp;Angstrom Pores. *Science (80-.).* **1998**, *279* (5350), 548–552. https://doi.org/10.1126/science.279.5350.548.

(73) Hartmann, M. Hierarchical Zeolites: A Proven Strategy to Combine Shape Selectivity with Efficient Mass Transport. *Angew. Chemie Int. Ed.* **2004**, *43* (44), 5880–5882. https://doi.org/10.1002/anie.200460644.

(74) Purusottam Sahoo, Sugar Land, T.; (US); Shane M. Richard, Deer Park, Magnolia, T. (US) T. (US); C. S. Patent Application Publication (10) Pub . No .: US 2005 / 0034197 A1, 2005.

(75) Mitchell, S.; Pinar, A. B.; Kenvin, J.; Crivelli, P.; Kärger, J.; Pérez-Ramírez, J. Structural Analysis of Hierarchically Organized Zeolites. *Nat. Commun.* **2015**, *6*. https://doi.org/10.1038/ncomms9633.

(76) Pérez-Ramírez, J.; Christensen, C. H.; Egeblad, K.; Christensen, C. H.; Groen, J. C. Hierarchical Zeolites: Enhanced Utilisation of Microporous Crystals in Catalysis by Advances in Materials Design. *Chem. Soc. Rev.* **2008**, *37* (11), 2530–2542. https://doi.org/10.1039/b809030k.

(77) Jung, J.; Jo, C.; Cho, K.; Ryoo, R. Zeolite Nanosheet of a Single-Pore Thickness Generated by

a Zeolite-Structure-Directing Surfactant. *J. Mater. Chem.* **2012**, *22* (11), 4637–4640. https://doi.org/10.1039/c2jm16539b.

(78) Fan, W.; Snyder, M. A.; Kumar, S.; Lee, P.-S.; Yoo, W. C.; McCormick, A. V.; Lee Penn, R.; Stein, A.; Tsapatsis, M. Hierarchical Nanofabrication of Microporous Crystals with Ordered Mesoporosity. *Nat. Mater.* **2008**, *7* (12), 984–991. https://doi.org/10.1038/nmat2302.

(79) Hasan, F.; Singh, R.; Li, G.; Zhao, D.; Webley, P. A. Direct Synthesis of Hierarchical LTA Zeolite via a Low Crystallization and Growth Rate Technique in Presence of Cetyltrimethylammonium Bromide. *J. Colloid Interface Sci.* **2012**, *382* (1), 1–12. https://doi.org/10.1016/j.jcis.2012.05.027.

(80) Lopez-Orozco, S.; Inayat, A.; Schwab, A.; Selvam, T.; Schwieger, W. Zeolitic Materials with Hierarchical Porous Structures. *Adv. Mater.* **2011**, *23* (22–23), 2602–2615. https://doi.org/10.1002/adma.201100462.

(81) Verboekend, D.; Pérez-Ramírez, J. Design of Hierarchical Zeolite Catalysts by Desilication. *Catal. Sci. Technol.* **2011**, *1* (6), 879–890. https://doi.org/10.1039/c1cy00150g.

(82) Barton, T. J.; Bull, L. M.; Klemperer, W. G.; Loy, D. A.; McEnaney, B.; Misono, M.; Monson, P. A.; Pez, G.; Schere, G. W.; Vartuli, J. C.; Yaghi, O. M. Tailored Porous Materials. *Chem. Mater.* **1999**, *11* (10), 2633–2656. https://doi.org/10.1021/cm9805929.

(83) Pérez-Ramírez, J. Imagination Has No Limits. *Nat. Chem.* **2012**, *4* (4), 250–251. https://doi.org/10.1038/nchem.1310.

(84) Chal, R.; Gérardin, C.; Bulut, M.; VanDonk, S. Overview and Industrial Assessment of Synthesis Strategies towards Zeolites with Mesopores. *ChemCatChem* **2011**, *3* (1), 67–81. https://doi.org/10.1002/cctc.201000158.

(85) Trong On, D.; Lutic, D.; Kaliaguine, S. An Example of Mesostructured Zeolitic Material: UL-TS-1. *Microporous Mesoporous Mater.* **2001**, *44–45*, 435–444. https://doi.org/10.1016/S1387-1811(01)00218-9.

(86) Müller, M.; Harvey, G.; Prins, R. Comparison of the Dealumination of Zeolites Beta, Mordenite, ZSM-5 and Ferrierite by Thermal Treatment, Leaching with Oxalic Acid and Treatment with SiCl4 by 1H, 29Si and 27Al MAS NMR. *Microporous Mesoporous Mater.* **2000**, *34* (2), 135–147. https://doi.org/10.1016/S1387-1811(99)00167-5.

(87) Kortunov, P.; Vasenkov, S.; Kärger, J.; Valiullin, R.; Gottschalk, P.; Elía, M. F.; Perez, M.; Stöcker, M.; Drescher, B.; McElhiney, G.; Berger, C.; Gläser, R.; Weitkamp, J. The Role of Mesopores in Intracrystalline Transport in USY Zeolite: PFG NMR Diffusion Study on Various Length Scales. *J. Am. Chem. Soc.* **2005**, *127* (37), 13055–13059. https://doi.org/10.1021/ja053134r.

(88) Valdiviés-Cruz, K.; Lam, A.; Zicovich-Wilson, C. M. Full Mechanism of Zeolite Dealumination in Aqueous Strong Acid Medium: Ab Initio Periodic Study on H-Clinoptilolite. *J. Phys. Chem. C* **2017**, *121* (5), 2652–2660. https://doi.org/10.1021/acs.jpcc.6b09794.

(89) Silaghi, M. C.; Chizallet, C.; Raybaud, P. Challenges on Molecular Aspects of Dealumination and Desilication of Zeolites. *Microporous Mesoporous Mater.* **2014**, *191*, 82–96. https://doi.org/10.1016/j.micromeso.2014.02.040.

(90) Ogura, M.; Shinomiya, S.; Tateno, J.; Nara, Y.; Kikuchi, E.; Matsukata, M. Formation of Uniform Mesopores in ZSM-5 Zeolite through Treatment in Alkaline Solution. *Chem. Lett.* **2000**, *29* (8), 882–883. https://doi.org/10.1246/cl.2000.882.

(91) Ogura, M.; Shinomiya, S. Y.; Tateno, J.; Nara, Y.; Nomura, M.; Kikuchi, E.; Matsukata, M. Alkali-Treatment Technique - New Method for Modification of Structural and Acid-Catalytic Properties of ZSM-5 Zeolites. *Appl. Catal. A Gen.* **2001**, *219* (1–2), 33–43. https://doi.org/10.1016/S0926-860X(01)00645-7.

(92) Möller, K.; Bein, T. Mesoporosity – a New Dimension for Zeolites. *Chem. Soc. Rev.* **2013**, *42* (9), 3689. https://doi.org/10.1039/c3cs35488a.

(93) Groen, J. C.; Moulijn, J. A.; Pérez-Ramírez, J. Alkaline Posttreatment of MFI Zeolites. From Accelerated Screening to Scale-Up. *Ind. Eng. Chem. Res.* **2007**, *46* (12), 4193–4201. https://doi.org/10.1021/ie061146v.

(94) Groen, J. C.; Jansen, J. C.; Moulijn, J. A.; Pérez-Ramírez, J. Optimal Aluminum-Assisted Mesoporosity Development in MFI Zeolites by Desilication. *J. Phys. Chem. B* **2004**, *108* (35), 13062–13065. https://doi.org/10.1021/jp047194f.

(95) Groen, J. C.; Abelló, S.; Villaescusa, L. A.; Pérez-Ramírez, J. Mesoporous Beta Zeolite Obtained by Desilication. *Microporous Mesoporous Mater.* **2008**, *114* (1–3), 93–102. https://doi.org/10.1016/j.micromeso.2007.12.025.

(96) Abelló, S.; Bonilla, A.; Pérez-Ramírez, J. Mesoporous ZSM-5 Zeolite Catalysts Prepared by Desilication with Organic Hydroxides and Comparison with NaOH Leaching. *Appl. Catal. A Gen.* **2009**, *364* (1–2), 191–198. https://doi.org/10.1016/j.apcata.2009.05.055.

(97) Pérez-Ramì-rez, J.; Verboekend, D.; Bonilla, A.; AbellÃ^3, S. Zeolite Catalysts with Tunable Hierarchy Factor by Pore-Growth Moderators. *Adv. Funct. Mater.* **2009**, *19* (24), 3972–3979. https://doi.org/10.1002/adfm.200901394.

(98) Eliášová, P.; Opanasenko, M.; Wheatley, P. S.; Shamzhy, M.; Mazur, M.; Nachtigall, P.; Roth, W. J.; Morris, R. E.; Čejka, J. The ADOR Mechanism for the Synthesis of New Zeolites. *Chem. Soc. Rev.* **2015**, *44* (20), 7177–7206. https://doi.org/10.1039/c5cs00045a.

(99) Opanasenko, M. Zeolite Constructor Kit: Design for Catalytic Applications. *Catal. Today* **2018**, *304* (May 2017), 2–11. https://doi.org/10.1016/j.cattod.2017.08.026.

(100) Vuong, G.-T.; Do, T.-O. Nanozeolites and Nanoporous Zeolitic Composites: Synthesis and Applications. In *Mesoporous Zeolites*; Wiley-VCH Verlag GmbH & Co. KGaA: Weinheim, Germany, 2015; pp 79–114. https://doi.org/10.1002/9783527673957.ch3.

(101) Mintova, S.; Jaber, M.; Valtchev, V. Nanosized Microporous Crystals: Emerging Applications. *Chem. Soc. Rev.* **2015**, *44* (20), 7207–7233. https://doi.org/10.1039/c5cs00210a.

(102) Schoeman, B. .; Sterte, J.; Otterstedt, J.-E. Colloidal Zeolite Suspensions. *Zeolites* **1994**, *14* (2), 110–116. https://doi.org/10.1016/0144-2449(94)90004-3.

(103) Persson, A. E.; Schoeman, B. J.; Sterte, J.; Otterstedt, J. E. Synthesis of Stable Suspensions of Discrete Colloidal Zeolite (Na, TPA)ZSM-5 Crystals. *Zeolites* **1995**, *15* (7), 611–619. https://doi.org/10.1016/0144-2449(95)00070-M.

(104) Liu, Y.; Zhang, W.; Pinnavaia, T. J. Steam-Stable Aluminosilicate Mesostructures Assembled from Zeolite Type Y Seeds [8]. *J. Am. Chem. Soc.* **2000**, *122* (36), 8791–8792. https://doi.org/10.1021/ja001615z.

(105) Liu, Y.; Zhang, W.; Pinnavaia, T. J. Steam-Stable MSU-S Aluminosilicate Mesostructures Assembled from Zeolite ZSM-5 and Zeolite Beta Seeds. *Angew. Chemie - Int. Ed.* **2001**, *40* (7), 1255–1258. https://doi.org/10.1002/1521-3773(20010401)40:7<1255::AID-ANIE1255>3.0.CO;2-U.

(106) Wang, Y. J.; Tang, Y.; Ni, Z.; Hua, W. M.; Yang, W. L.; Wang, X. D.; Tao, W. C.; Gao, Z. Synthesis of Macroporous Materials with Zeolitic Microporous Frameworks by Self-Assembly of Colloidal Zeolites. *Chem. Lett.* **2000**, *29* (5), 510–511. https://doi.org/10.1246/cl.2000.510.

(107) Kirschhock, C. E. A.; Kremer, S. P. B.; Vermant, J.; Van Tendeloo, G.; Jacobs, P. A.; Martens, J. A. Design and Synthesis of Hierarchical Materials from Ordered Zeolitic Building Units. *Chem. - A Eur. J.* **2005**, *11* (15), 4306–4313. https://doi.org/10.1002/chem.200401329.

(108) Kremer, S. P. B.; Kirschhock, C. E. A.; Tielen, M.; Collignon, F.; Grobet, P. J.; Jacobs, P. A.; Martens, J. A. Silicalite-1 Zeogrid: A New Silica Molecular Sieve with Super- and Ultra-Micropores. *Adv. Funct. Mater.* **2002**, *12* (4), 286–292. https://doi.org/10.1002/1616-3028(20020418)12:4<286::AID-ADFM286>3.0.CO;2-M.

(109) Kremer, S. P. B.; Kirschhock, C. E. A.; Aerts, A.; Villani, K.; Martens, J. A.; Lebedev, O. I.; Van Tendeloo, G. Tiling Silicalite-1 Nanoslabs into 3D Mosaics. *Adv. Mater.* **2003**, *15* (20), 1705–1707. https://doi.org/10.1002/adma.200305266.

(110) Kirschhock, C. E. A.; Buschmann, V.; Kremer, S.; Ravishankar, R.; Houssin, C. J. Y.; Mojet, B. L.; van Santen, R. A.; Grobet, P. J.; Jacobs, P. A.; Martens, J. A. Zeosil Nanoslabs: Building Blocks InnPr4N+-Mediated Synthesis of MFI Zeolite. *Angew. Chemie Int. Ed.* **2001**, *40* (14), 2637–2640. https://doi.org/10.1002/1521-3773(20010716)40:14<2637::AID-ANIE2637>3.0.CO;2-7.

(111) Reichinger, M.; Schmidt, W.; Berg, M. W. E. Van Den; Aerts, A.; Martens, J. A.; Kirschhock, C. E. A.; Gies, H.; Grünert, W. Alkene Epoxidation with Mesoporous Materials Assembled from TS-1 Seeds – Is There a Hierarchical Pore System ? *J. Catal.* **2010**, *269* (2), 367–375. https://doi.org/10.1016/j.jcat.2009.11.023.

(112) Liu, M.; Li, J.; Jia, W.; Qin, M.; Wang, Y.; Tong, K.; Chen, H.; Zhu, Z. Seed-Induced Synthesis of Hierarchical ZSM-5 Nanosheets in the Presence of Hexadecyl Trimethyl Ammonium Bromide. *RSC Adv.* **2015**, *5* (12), 9237–9240. https://doi.org/10.1039/c4ra14955f.

(113) Jin, Y.; Li, Y.; Zhao, S.; Lv, Z.; Wang, Q.; Liu, X.; Wang, L. Synthesis of Mesoporous MOR Materials by Varying Temperature Crystallizations and Combining Ternary Organic Templates. *Microporous Mesoporous Mater.* **2012**, *147* (1), 259–266. https://doi.org/10.1016/j.micromeso.2011.06.023.

(114) Lv, G.; Deng, S.; Zhai, Y.; Zhu, Y.; Li, H.; Wang, F.; Zhang, X. P123 Lamellar Micelle-Assisted Construction of Hierarchical TS-1 Stacked Nanoplates with Constrained Mesopores for Enhanced Oxidative Desulfurization. *Appl. Catal. A Gen.* **2018**, *567* (July), 28–35. https://doi.org/10.1016/j.apcata.2018.09.009.

(115) Möller, K.; Yilmaz, B.; Müller, U.; Bein, T. Hierarchical Zeolite Beta via Nanoparticle Assembly with a Cationic Polymer. *Chem. Mater.* **2011**, *23* (19), 4301–4310. https://doi.org/10.1021/cm103533e.

(116) Wang, Z.; Li, C.; Cho, H. J.; Kung, S. C.; Snyder, M. A.; Fan, W. Direct, Single-Step Synthesis of Hierarchical Zeolites without Secondary Templating. *J. Mater. Chem. A* **2015**, *3* (3), 1298–1305. https://doi.org/10.1039/c4ta05031b.

(117) Möller, K.; Yilmaz, B.; Jacubinas, R. M.; Müller, U.; Bein, T. One-Step Synthesis of Hierarchical Zeolite Beta via Network Formation of Uniform Nanocrystals. *J. Am. Chem. Soc.* **2011**, *133* (14), 5284–5295. https://doi.org/10.1021/ja108698s.

(118) Lu, A.-H.; Schüth, F. Nanocasting: A Versatile Strategy for Creating Nanostructured Porous Materials. *Adv. Mater.* **2006**, *18* (14), 1793–1805. https://doi.org/10.1002/adma.200600148.

(119) Serrano, D. P.; Aguado, J.; Escola, J. M.; Rodríguez, J. M.; Peral, Á. Hierarchical Zeolites with Enhanced Textural and Catalytic Properties Synthesized from Organofunctionalized Seeds. *Chem. Mater.* **2006**, *18* (10), 2462–2464. https://doi.org/10.1021/cm060080r.

(120) Serrano, D. P.; Aguado, J.; Morales, G.; Rodríguez, J. M.; Peral, A.; Thommes, M.; Epping, J. D.; Chmelka, B. F. Molecular and Meso- and Macroscopic Properties of Hierarchical Nanocrystalline ZSM-5 Zeolite Prepared by Seed Silanization. *Chem. Mater.* **2009**, *21* (4), 641–654. https://doi.org/10.1021/cm801951a.

(121) Srivastava, R.; Iwasa, N.; Fujita, S. I.; Arai, M. Synthesis of Nanocrystalline MFI-Zeolites with Intracrystal Mesopores and Their Application in Fine Chemical Synthesis Involving Large Molecules. *Chem. - A Eur. J.* **2008**, *14* (31), 9507–9511. https://doi.org/10.1002/chem.200801113.

(122) Valtchev, V.; Schoeman, B. J.; Hedlund, J.; Mintova, S.; Sterte, J. Preparation and Characterization of Hollow Fibers of Silicalite-1. *Zeolites* **1996**, *17* (5–6), 408–415. https://doi.org/10.1016/S0144-2449(96)00089-9.

(123) Jacobsen, C. J. H.; Madsen, C.; Houzvicka, J.; Schmidt, I.; Carlsson, A. Mesoporous Zeolite Single Crystals [2]. *J. Am. Chem. Soc.* **2000**, *122* (29), 7116–7117. https://doi.org/10.1021/ja000744c.

(124) Schmidt, I.; Boisen, A.; Gustavsson, E.; Ståhl, K.; Pehrson, S.; Dahl, S.; Carlsson, A.; Jacobsen, C. J. H. Carbon Nanotube Templated Growth of Mesoporous Zeolite Single Crystals. *Chem. Mater.* **2001**, *13* (12), 4416–4418. https://doi.org/10.1021/cm011206h.

(125) Tao, Y.; Tanaka, H.; Ohkubo, T.; Kanoh, H.; Kaneko, K. Pore Structures of ZSM-5 Synthesized in the Mesopore Spaces of a Carbon Aerogel. *Adsorpt. Sci. Technol.* **2003**, *21* (2), 199–203. https://doi.org/10.1260/026361703769013925.

(126) Machoke, A. G.; Beltrán, A. M.; Inayat, A.; Winter, B.; Weissenberger, T.; Kruse, N.; Güttel, R.; Spiecker, E.; Schwieger, W. Micro/Macroporous System: MFI-Type Zeolite Crystals with Embedded Macropores. *Adv. Mater.* **2015**, *27* (6), 1066–1070. https://doi.org/10.1002/adma.201404493.

(127) Zhu, H.; Liu, Z.; Wang, Y.; Kong, D.; Yuan, X.; Xie, Z. Nanosized CaCO 3 as Hard Template for

Creation of Intracrystal Pores within Silicalite-1 Crystal. *Chem. Mater.* **2008**, *20* (3), 1134–1139. https://doi.org/10.1021/cm071385o.

(128) Zhang, B.; Davis, S. A.; Mann, S. Starch Gel Templating of Spongelike Macroporous Silicalite Monoliths and Mesoporous Films. *Chem. Mater.* **2002**, *14* (3), 1369–1375. https://doi.org/10.1021/cm011251p.

(129) Naydenov, V.; Tosheva, L.; Antzutkin, O. N.; Sterte, J. Meso/Macroporous AlPO-5 Spherical Macrostructures Tailored by Resin Templating. *Microporous Mesoporous Mater.* **2005**, *78* (2–3), 181–188. https://doi.org/10.1016/j.micromeso.2004.10.008.

(130) Huo, Q.; Margolese, D. I.; Ciesla, U.; Feng, P.; Gier, T. E.; Sieger, P.; Leon, R.; Petroff, P. M.; Schüth, F.; Stucky, G. D. Generalized Synthesis of Periodic Surfactant/Inorganic Composite Materials. *Nature* **1994**, *368* (6469), 317–321. https://doi.org/10.1038/368317a0.

(131) Choi, M.; Cho, H. S.; Srivastava, R.; Venkatesan, C.; Choi, D. H.; Ryoo, R. Amphiphilic Organosilane-Directed Synthesis of Crystalline Zeolite with Tunable Mesoporosity. *Nat. Mater.* **2006**, *5* (9), 718–723. https://doi.org/10.1038/nmat1705.

(132) Xue, Z.; Ma, J.; Hao, W.; Bai, X.; Kang, Y.; Liu, J.; Li, R. Synthesis and Characterization of Ordered Mesoporous Zeolite LTA with High Ion Exchange Ability. *J. Mater. Chem.* **2012**, *22* (6), 2532–2538. https://doi.org/10.1039/c1jm14740d.

(133) Choi, M.; Srivastava, R.; Ryoo, R. Organosilane Surfactant-Directed Synthesis of Mesoporous Aluminophosphates Constructed with Crystalline Microporous Frameworks. *Chem. Commun.* **2006**, No. 42, 4380. https://doi.org/10.1039/b612265e.

(134) Inayat, A.; Knoke, I.; Spiecker, E.; Schwieger, W. Assemblies of Mesoporous FAU-Type Zeolite Nanosheets. *Angew. Chemie - Int. Ed.* **2012**, *51* (8), 1962–1965. https://doi.org/10.1002/anie.201105738.

(135) Choi, M.; Na, K.; Kim, J.; Sakamoto, Y.; Terasaki, O.; Ryoo, R. Stable Single-Unit-Cell Nanosheets of Zeolite MFI as Active and Long-Lived Catalysts. *Nature* **2009**, *461* (7261), 246–249. https://doi.org/10.1038/nature08288.

(136) Na, K.; Jo, C.; Kim, J.; Cho, K.; Jung, J.; Seo, Y.; Messinger, R. J.; Chmelka, B. F.; Ryoo, R. Directing Zeolite Structures into Hierarchically Nanoporous Architectures. *Science (80-.).* **2011**, *333* (6040), 328–332. https://doi.org/10.1126/science.1204452.

(137) Kamal, M. S. A Review of Gemini Surfactants: Potential Application in Enhanced Oil Recovery. *J. Surfactants Deterg.* **2016**, *19* (2), 223–236. https://doi.org/10.1007/s11743-015-1776-5.

(138) Xu, D.; Che, S.; Terasaki, O. A Design Concept of Amphiphilic Molecules for Directing Hierarchical Porous Zeolite. *New J. Chem.* **2016**, *40* (5), 3982–3992. https://doi.org/10.1039/c5nj02949j.

(139) Zhu, H.; Abou-Hamad, E.; Chen, Y.; Saih, Y.; Liu, W.; Kumar Samal, A.; Basset, J. M. Organosilane with Gemini-Type Structure as the Mesoporogen for the Synthesis of the Hierarchical Porous ZSM-5 Zeolite. *Langmuir* **2016**, *32* (8), 2085–2092. https://doi.org/10.1021/acs.langmuir.5b04383.

(140) Dong, X.; Shaikh, S.; Vittenet, J. R.; Wang, J.; Liu, Z.; Bhatte, K. D.; Ali, O.; Xu, W.; Osorio, I.;

Saih, Y.; Basset, J. M.; Ali, S. A.; Han, Y. Fine Tuning the Diffusion Length in Hierarchical ZSM-5 to Maximize the Yield of Propylene in Catalytic Cracking of Hydrocarbons. *ACS Sustain. Chem. Eng.* **2018**, *6* (11), 15832–15840. https://doi.org/10.1021/acssuschemeng.8b04441.

(141) Tian, Q.; Liu, Z.; Zhu, Y.; Dong, X.; Saih, Y.; Basset, J. M.; Sun, M.; Xu, W.; Zhu, L.; Zhang, D.; Huang, J.; Meng, X.; Xiao, F. S.; Han, Y. Beyond Creation of Mesoporosity: The Advantages of Polymer-Based Dual-Function Templates for Fabricating Hierarchical Zeolites. *Adv. Funct. Mater.* **2016**, *26* (12), 1881–1891. https://doi.org/10.1002/adfm.201504888.

(142) Wei, Y.; Parmentier, T. E.; De Jong, K. P.; Zečević, J. Tailoring and Visualizing the Pore Architecture of Hierarchical Zeolites. *Chem. Soc. Rev.* **2015**, *44* (20), 7234–7261. https://doi.org/10.1039/c5cs00155b.

(143) Aramburo, L. R.; Karwacki, L.; Cubillas, P.; Asahina, S.; De Winter, D. A. M.; Drury, M. R.; Buurmans, I. L. C.; Stavitski, E.; Mores, D.; Daturi, M.; Bazin, P.; Dumas, P.; Thibault-Starzyk, F.; Post, J. A.; Anderson, M. W.; Terasaki, O.; Weckhuysen, B. M. The Porosity, Acidity, and Reactivity of Dealuminated Zeolite ZSM-5 at the Single Particle Level: The Influence of the Zeolite Architecture. *Chem. - A Eur. J.* **2011**, *17* (49), 13773–13781. https://doi.org/10.1002/chem.201101361.

(144) Landers, J.; Gor, G. Y.; Neimark, A. V. Density Functional Theory Methods for Characterization of Porous Materials. *Colloids Surfaces A Physicochem. Eng. Asp.* **2013**, *437*, 3–32. https://doi.org/10.1016/j.colsurfa.2013.01.007.

(145) Cychosz, K. A.; Guillet-Nicolas, R.; García-Martínez, J.; Thommes, M. Recent Advances in the Textural Characterization of Hierarchically Structured Nanoporous Materials. *Chem. Soc. Rev.* **2017**, *46* (2), 389–414. https://doi.org/10.1039/c6cs00391e.

(146) Thommes, M.; Kaneko, K.; Neimark, A. V.; Olivier, J. P.; Rodriguez-Reinoso, F.; Rouquerol, J.; Sing, K. S. W. Physisorption of Gases, with Special Reference to the Evaluation of Surface Area and Pore Size Distribution (IUPAC Technical Report). *Pure Appl. Chem.* **2015**, *87* (9–10), 1051–1069. https://doi.org/10.1515/pac-2014-1117.

(147) Kenvin, J.; Mitchell, S.; Sterling, M.; Warringham, R.; Keller, T. C.; Crivelli, P.; Jagiello, J.; Pérez-Ramírez, J. Quantifying the Complex Pore Architecture of Hierarchical Faujasite Zeolites and the Impact on Diffusion. *Adv. Funct. Mater.* **2016**, *26* (31), 5621–5630. https://doi.org/10.1002/adfm.201601748.

(148) Garcia-Martinez, J.; Xiao, C.; Cychosz, K. A.; Li, K.; Wan, W.; Zou, X.; Thommes, M. Evidence of Intracrystalline Mesostructured Porosity in Zeolites by Advanced Gas Sorption, Electron Tomography and Rotation Electron Diffraction. *ChemCatChem* **2014**, *6* (11), 3110–3115. https://doi.org/10.1002/cctc.201402499.

(149) Cimino, R.; Cychosz, K. A.; Thommes, M.; Neimark, A. V. Experimental and Theoretical Studies of Scanning Adsorption-Desorption Isotherms. *Colloids Surfaces A Physicochem. Eng. Asp.* **2013**, *437*, 76–89. https://doi.org/10.1016/j.colsurfa.2013.03.025.

(150) Lønstad Bleken, B. T.; Mino, L.; Giordanino, F.; Beato, P.; Svelle, S.; Lillerud, K. P.; Bordiga, S. Probing the Surface of Nanosheet H-ZSM-5 with FTIR Spectroscopy. *Phys. Chem. Chem. Phys.* **2013**, *15* (32), 13363–13370. https://doi.org/10.1039/c3cp51280k.

(151) Corma, A.; Fornés, V.; Forni, L.; Márquez, F.; Martínez-Triguero, J.; Moscotti, D. 2,6-Di-Tert-Butyl-Pyridine as a Probe Molecule to Measure External Acidity of Zeolites. *J. Catal.* **1998**, *179* (2), 451–458. https://doi.org/10.1006/jcat.1998.2233.

(152) Holm, M. S.; Svelle, S.; Joensen, F.; Beato, P.; Christensen, C. H.; Bordiga, S.; Bjørgen, M. Assessing the Acid Properties of Desilicated ZSM-5 by FTIR Using CO and 2,4,6-Trimethylpyridine (Collidine) as Molecular Probes. *Appl. Catal. A Gen.* **2009**, *356* (1), 23–30. https://doi.org/10.1016/j.apcata.2008.11.033.

(153) Thibault-starzyk, F.; Stan, I.; Abelló, S.; Bonilla, A.; Thomas, K.; Fernandez, C.; Gilson, J.; Pérez-ramírez, J. Quantification of Enhanced Acid Site Accessibility in Hierarchical Zeolites – The Accessibility Index. *J. Catal.* **2009**, *264* (1), 11–14. https://doi.org/10.1016/j.jcat.2009.03.006.

(154) Holm, M. S.; Svelle, S.; Joensen, F.; Beato, P.; Christensen, C. H.; Bordiga, S.; Bjørgen, M. Assessing the Acid Properties of Desilicated ZSM-5 by FTIR Using CO and 2,4,6-Trimethylpyridine (Collidine) as Molecular Probes. *Appl. Catal. A Gen.* **2009**, *356* (1), 23–30. https://doi.org/10.1016/j.apcata.2008.11.033.

(155) Bleken, B.-T. L.; Wragg, D. S.; Arstad, B.; Gunnæs, A. E.; Mouzon, J.; Helveg, S.; Lundegaard, L. F.; Beato, P.; Bordiga, S.; Olsbye, U.; Svelle, S.; Lillerud, K. P. Unit Cell Thick Nanosheets of Zeolite H-ZSM-5: Structure and Activity. *Top. Catal.* **2013**, *56* (9–10), 558–566. https://doi.org/10.1007/s11244-013-0010-9.

(156) Skorpa, R.; Bordiga, S.; Bleken, F.; Olsbye, U.; Arstad, B.; Tolchard, J.; Mathisen, K.; Svelle, S.; Bjørgen, M. Assessing the Surface Sites of the Large Pore 3-Dimensional Microporous Material H-ITQ-7 Using FT-IR Spectroscopy and Molecular Probes. *Microporous Mesoporous Mater.* **2011**, *141* (1–3), 146–156. https://doi.org/10.1016/j.micromeso.2010.10.050.

(157) Airi, A.; Signorile, M.; Bonino, F.; Quagliotto, P.; Bordiga, S.; Martens, J. A.; Crocellà, V. Insights on a Hierarchical MFI Zeolite: A Combined Spectroscopic and Catalytic Approach for Exploring the Multilevel Porous System down to the Active Sites. *ACS Appl. Mater. Interfaces* **2021**, *13* (41), 49114–49127. https://doi.org/10.1021/acsami.1c11614.

(158) Vuong, G.-T.; Do, T.-O. Nanozeolites and Nanoporous Zeolitic Composites: Synthesis and Applications. In *Mesoporous Zeolites*; Wiley-VCH Verlag GmbH & Co. KGaA: Weinheim, Germany, 2015; pp 79–114. https://doi.org/10.1002/9783527673957.ch3.

(159) Thommes, M.; Cychosz, K. A. Physical Adsorption Characterization of Nanoporous Materials: Progress and Challenges. *Adsorption* **2014**, *20* (2–3), 233–250. https://doi.org/10.1007/s10450-014-9606-z.

(160) Signorile, M.; Bonino, F.; Damin, A.; Bordiga, S. A Novel Raman Setup Based on Magnetic-Driven Rotation of Sample. *Top. Catal.* **2018**, *61* (14), 1491–1498. https://doi.org/10.1007/s11244-018-1033-z.

(161) Marchese, L.; Chen, J.; Thomas, J. M.; Coluccia, S.; Zecchina, A. Bronsted, Lewis, and Redox Centers on CoAPO-18 Catalysts. 1. Vibrational Modes of Adsorbed Water. *J. Phys. Chem.* **1994**, *98* (50), 13350–13356. https://doi.org/10.1021/j100101a040.

(162) Xie, J.; Firth, D. S.; Cordero-lanzac, T.; Airi, A.; Negri, C.; Øien-ødegaard, S.; Lillerud, K. P.;

Bordiga, S.; Olsbye, U. MAPO-18 Catalysts for the Methanol to Ole Fi Ns Process: In Fl Uence of Catalyst Acidity in a High-Pressure Syngas (CO and H 2) Environment. **2022**. https://doi.org/10.1021/acscatal.1c04694.

(163) Marchese, L.; Martra, G.; Damilano, N.; Coluccia, S.; Thomas, J. M. Elucidating the Nature of the Cobalt Centres in CoAPO-18 Acid Catalysts. *Stud. Surf. Sci. Catal.* **1996**, *101 B*, 861–870. https://doi.org/10.1016/s0167-2991(96)80297-7.

(164) Bordiga, S.; Lamberti, C.; Bonino, F.; Travert, A.; Thibault-Starzyk, F. Probing Zeolites by Vibrational Spectroscopies. *Chem. Soc. Rev.* **2015**, *44* (20), 7262–7341. https://doi.org/10.1039/c5cs00396b.

(165) Lercher, J. A.; Veefkind, V.; Fajerwerg, K. In Situ IR Spectroscopy for Developing Catalysts and Catalytic Processes. *Vib. Spectrosc.* **1999**, *19* (1), 107–121. https://doi.org/10.1016/s0924-2031(98)00094-0.

(166) Busca, G. Acidity and Basicity of Zeolites: A Fundamental Approach. *Microporous Mesoporous Mater.* **2017**, *254* (June 2016), 3–16. https://doi.org/10.1016/j.micromeso.2017.04.007.

(167) Pazé, C.; Bordiga, S.; Lamberti, C.; Salvalaggio, M.; Zecchina, A.; Bellussi, G. Acidic Properties of H−β Zeolite As Probed by Bases with Proton Affinity in the 118−204 Kcal Mol -1 Range: A FTIR Investigation. *J. Phys. Chem. B* **1997**, *101* (24), 4740–4751. https://doi.org/10.1021/jp970649z.

(168) Wakabayashi, F.; Kondo, J.; Domen, K.; Hirose, C. Dinitrogen as a Probe of Acid Sites of Zeolites. *Catal. Letters* **1993**, *21* (3–4), 257–264. https://doi.org/10.1007/BF00769477.

(169) Giordanino, F.; Vennestrøm, P. N. R.; Lundegaard, L. F.; Stappen, F. N.; Mossin, S.; Beato, P.; Bordiga, S.; Lamberti, C. Characterization of Cu-Exchanged SSZ-13: A Comparative FTIR, UV-Vis, and EPR Study with Cu-ZSM-5 and Cu-β with Similar Si/Al and Cu/Al Ratios. *Dalt. Trans.* **2013**, *42* (35), 12741. https://doi.org/10.1039/c3dt50732g.

(170) Huybrechts, W.; Mijoin, J. érôme; Jacobs, P. A.; Martens, J. A. Development of a Fixed-Bed Continuous-Flow High-Throughput Reactor for Long-Chain n-Alkane Hydroconversion. *Appl. Catal. A Gen.* **2003**, *243* (1), 1–13. https://doi.org/10.1016/S0926-860X(02)00536-7.

(171) Meng, L.; Vanbutsele, G.; Pestman, R.; Godin, A.; Romero, D. E.; van Hoof, A. J. F.; Gao, L.; Kimpel, T. F.; Chai, J.; Martens, J. A.; Hensen, E. J. M. Mechanistic Aspects of N-Paraffins Hydrocracking: Influence of Zeolite Morphology and Acidity of Pd(Pt)/ZSM-5 Catalysts. *J. Catal.* **2020**, *389*, 544–555. https://doi.org/10.1016/j.jcat.2020.06.031.

(172) Jacobs, P. A.; Martens, J. A.; Weitkamp, J.; Beyer, H. K. Shape-Selectivity Changes in High-Silica Zeolites. *Faraday Discuss. Chem. Soc.* **1981**, *72*, 353. https://doi.org/10.1039/dc9817200353.

(173) MARTENS, J. Evidence for Branching of Long-Chain n-Alkanes via Protonated Cycloalkanes Larger than Cyclopropane. *J. Catal.* **1990**, *124* (2), 357–366. https://doi.org/10.1016/0021-9517(90)90184-L.

(174) Corma, A.; Miguel, P. J.; Orchille´s, A. V. Influence of Hydrocarbon Chain Length and Zeolite Structure on the Catalyst Activity and Deactivation for N-Alkanes Cracking. *Appl. Catal. A*

Gen. **1994**, *117* (1), 29–40. https://doi.org/10.1016/0926-860X(94)80156-8.

(175) Martens, J. A.; Tielen, M.; Jacobs, P. A.; Weitkamp, J. Estimation of the Void Structure and Pore Dimensions of Molecular Sieve Zeolites Using the Hydroconversion of N-Decane. *Zeolites* **1984**, *4* (2), 98–107. https://doi.org/10.1016/0144-2449(84)90044-7.

(176) Jacobs, P. A.; Martens, J. A. Exploration of the Void Size and Structure of Zeolites and Molecular Sieves Using Chemical Reactions. *Pure Appl. Chem.* **1986**, *58* (10), 1329–1338. https://doi.org/10.1351/pac198658101329.

(177) Martens, J. A.; Jacobs, P. A. The Potential and Limitations of the N-Decane Hydroconversion as a Test Reaction for Characterization of the Void Space of Molecular Sieve Zeolites. *Zeolites* **1986**, *6* (5), 334–348. https://doi.org/10.1016/0144-2449(86)90061-8.

(178) AABSPEC 2000_a.Pdf. CAHNERS-DENVER PUBLISHING CO8773 S RIDGELINE BLVD, HIGHLANDS RANCH, CO 80126-2329.

(179) Vaschetto, E. G.; Monti, G. A.; Herrero, E. R.; Casuscelli, S. G.; Eimer, G. A. Influence of the Synthesis Conditions on the Physicochemical Properties and Acidity of Al-MCM-41 as Catalysts for the Cyclohexanone Oxime Rearrangement. *Appl. Catal. A Gen.* **2013**, *453*, 391–402. https://doi.org/10.1016/j.apcata.2012.12.016.

(180) Lønstad Bleken, B.-T.; Mino, L.; Giordanino, F.; Beato, P.; Svelle, S.; Lillerud, K. P.; Bordiga, S. Probing the Surface of Nanosheet H-ZSM-5 with FTIR Spectroscopy. *Phys. Chem. Chem. Phys.* **2013**, *15* (32), 13363. https://doi.org/10.1039/c3cp51280k.

(181) Tzoulaki, D.; Jentys, A.; Pérez-Ramírez, J.; Egeblad, K.; Lercher, J. A. On the Location, Strength and Accessibility of Bronsted Acid Sites in Hierarchical ZSM-5 Particles. *Catal. Today* **2012**, *198* (1), 3–11. https://doi.org/10.1016/j.cattod.2012.03.078.

(182) Aerts, A.; Van Isacker, A.; Huybrechts, W.; Kremer, S. P. B.; Kirschhock, C. E. A.; Collignon, F.; Houthoofd, K.; Denayer, J. F. M.; Baron, G. V.; Marin, G. B.; Jacobs, P. A.; Martens, J. A. Decane Hydroconversion on Bifunctional Zeogrid and Nano-Zeolite Assembled from Aluminosilicate Nanoslabs of MFI Framework Type. *Appl. Catal. A Gen.* **2004**, *257* (1), 7–17. https://doi.org/10.1016/S0926-860X(03)00592-1.

(183) Verheyen, E.; Jo, C.; Kurttepeli, M.; Vanbutsele, G.; Gobechiya, E.; Korányi, T. I.; Bals, S.; Van Tendeloo, G.; Ryoo, R.; Kirschhock, C. E. A.; Martens, J. A. Molecular Shape-Selectivity of MFI Zeolite Nanosheets in n-Decane Isomerization and Hydrocracking. *J. Catal.* **2013**, *300* (2013), 70–80. https://doi.org/10.1016/j.jcat.2012.12.017.

(184) Kremer, S. P. B.; Kirschhock, C. E. A.; Aerts, A.; Aerts, C. A.; Houthoofd, K. J.; Grobet, P. J.; Jacobs, P. A.; Lebedev, O. I.; Van Tendeloo, G.; Martens, J. A. Zeotile-2: A Microporous Analogue of MCM-48. *Solid State Sci.* **2005**, *7* (7), 861–867. https://doi.org/10.1016/j.solidstatesciences.2005.01.021.

(185) Patel, V.; Ray, D.; Aswal, V. K.; Bahadur, P. Triton X-100 Micelles Modulated by Solubilized Cinnamic Acid Analogues: The PH Dependant Micellar Growth. *Colloids Surfaces A Physicochem. Eng. Asp.* **2014**, *450* (1), 106–114. https://doi.org/10.1016/j.colsurfa.2014.03.015.

(186) Treacy, M. M. J.; J.B., H. *Collection of Simulated XRD Powder Patterns for Zeolites*, Fourth Rev.; Association, P. on behalf of the S. C. of the I. Z., Ed.; Elsevier, 2007. https://doi.org/10.1016/B978-0-444-53067-7.X5470-7.

(187) Bardestani, R.; Patience, G. S.; Kaliaguine, S. Experimental Methods in Chemical Engineering: Specific Surface Area and Pore Size Distribution Measurements—BET, BJH, and DFT. *Can. J. Chem. Eng.* **2019**, *97* (11), 2781–2791. https://doi.org/10.1002/cjce.23632.

(188) Fan, W.; Duan, R. G.; Yokoi, T.; Wu, P.; Kubota, Y.; Tatsumi, T. Synthesis, Crystallization Mechanism, and Catalytic Properties of Titanium-Rich TS-1 Free of Extraframework Titanium Species. *J. Am. Chem. Soc.* **2008**, *130* (31), 10150–10164. https://doi.org/10.1021/ja7100399.

(189) Zecchina, A.; Bordiga, S.; Spoto, G.; Damin, A.; Berlier, G.; Bonino, F.; Prestipino, C.; Lamberti, C. In Situ Characterization of Catalysts Active in Partial Oxidations: TS-1 and Fe-MFI Case Studies. *Top. Catal.* **2002**, *21* (1–3), 67–78. https://doi.org/10.1023/A:1020504115146.

(190) Signorile, M.; Crocellà, V.; Damin, A.; Rossi, B.; Lamberti, C.; Bonino, F.; Bordiga, S. Effect of Ti Speciation on Catalytic Performance of TS-1 in the Hydrogen Peroxide to Propylene Oxide Reaction. *J. Phys. Chem. C* **2018**, *122* (16), 9021–9034. https://doi.org/10.1021/acs.jpcc.8b01401.

(191) Bordiga, S.; Damin, A.; Bonino, F.; Ricchiardi, G.; Lamberti, C.; Zecchina, A. The Structure of the Peroxo Species in the TS-1 Catalyst as Investigated by Resonant Raman Spectroscopy. *Angew. Chemie - Int. Ed.* **2002**, *41* (24), 4734–4737. https://doi.org/10.1002/anie.200290032.

(192) Bordiga, S.; Damin, A.; Bonino, F.; Ricchiardi, G.; Zecchina, A.; Tagliapietra, R.; Lamberti, C. Resonance Raman Effects in TS-1: The Structure of Ti(Iv) Species and Reactivity towards H2O, NH3 and H2O 2: An in Situ Study. *Phys. Chem. Chem. Phys.* **2003**, *5* (20), 4390–4393. https://doi.org/10.1039/b306041c.

(193) Ricchiardi, G.; Damin, A.; Bordiga, S.; Lamberti, C.; Spanò, G.; Rivetti, F.; Zecchina, A. Vibrational Structure of Titanium Silicate Catalysts. A Spectroscopic and Theoretical Study. *J. Am. Chem. Soc.* **2001**, *123* (46), 11409–11419. https://doi.org/10.1021/ja010607v.

(194) Ge, T.; Hua, Z.; Lv, J.; Zhou, J.; Guo, H.; Zhou, J.; Shi, J. Hydrophilicity/Hydrophobicity Modulated Synthesis of Nano-Crystalline and Hierarchically Structured TS-1 Zeolites. *CrystEngComm* **2017**, *19* (10), 1370–1376. https://doi.org/10.1039/c6ce02435a.

(195) Cundy, C. S.; Forrest, J. O.; Plaisted, R. J. Some Observations on the Preparation and Properties of Colloidal Silicalites. Part I: Synthesis of Colloidal Silicalite-1 and Titanosilicalite-1 (TS-1). *Microporous Mesoporous Mater.* **2003**, *66* (2–3), 143–156. https://doi.org/10.1016/j.micromeso.2003.08.021.

(196) Vasile, A.; Busuioc-Tomoiaga, A. M. A New Route for the Synthesis of Titanium Silicalite-1. *Mater. Res. Bull.* **2012**, *47* (1), 35–41. https://doi.org/10.1016/j.materresbull.2011.10.008.

(197) Caremans, T. P.; Loppinet, B.; Follens, L. R. A.; van Erp, T. S.; Vermant, J.; Goderis, B.; Kirschhock, C. E. A.; Martens, J. A.; Aerts, A. Investigation of Nanoparticles Occurring in the Colloidal Silicalite-1 Zeolite Crystallization Process Using Dissolution Experiments. *Chem.*

Mater. **2010**, *22* (12), 3619–3629. https://doi.org/10.1021/cm9023343.

(198) Lehman, S. E.; Larsen, S. C. Zeolite and Mesoporous Silica Nanomaterials: Greener Syntheses, Environmental Applications and Biological Toxicity. *Environ. Sci. Nano* **2014**, *1* (3), 200–213. https://doi.org/10.1039/C4EN00031E.

(199) Emdadi, L.; Wu, Y.; Zhu, G.; Chang, C. C.; Fan, W.; Pham, T.; Lobo, R. F.; Liu, D. Dual Template Synthesis of Meso- and Microporous MFI Zeolite Nanosheet Assemblies with Tailored Activity in Catalytic Reactions. *Chem. Mater.* **2014**, *26* (3), 1345–1355. https://doi.org/10.1021/cm401119d.

(200) Wang, Q.; Xu, S.; Chen, J.; Wei, Y.; Li, J.; Fan, D.; Yu, Z.; Qi, Y.; He, Y.; Xu, S.; Yuan, C.; Zhou, Y.; Wang, J.; Zhang, M.; Su, B.; Liu, Z. Synthesis of Mesoporous ZSM-5 Catalysts Using Different Mesogenous Templates and Their Application in Methanol Conversion for Enhanced Catalyst Lifespan. *RSC Adv.* **2014**, *4* (41), 21479–21491. https://doi.org/10.1039/C4RA02695K.

(201) Kumar, D.; Schumacher, K.; du Fresne von Hohenesche, C.; Grün, M.; Unger, K. . MCM-41, MCM-48 and Related Mesoporous Adsorbents: Their Synthesis and Characterisation. *Colloids Surfaces A Physicochem. Eng. Asp.* **2001**, *187–188*, 109–116. https://doi.org/10.1016/S0927-7757(01)00638-0.

(202) Astorino, E.; Peri, J. B.; Willey, R. J.; Busca, G. Spectroscopic Characterization of Silicalite-1 and Titanium Silicalite-1. *J. Catal.* **1995**, *157* (2), 482–500. https://doi.org/10.1006/jcat.1995.1313.

(203) Armaroli, T.; Simon, L. J.; Digne, M.; Montanari, T.; Bevilacqua, M.; Valtchev, V.; Patarin, J.; Busca, G. Effects of Crystal Size and Si/Al Ratio on the Surface Properties of H-ZSM-5 Zeolites. *Appl. Catal. A Gen.* **2006**, *306*, 78–84. https://doi.org/10.1016/j.apcata.2006.03.030.

(204) Armaroli, T.; Trombetta, M.; Gutièrrez Alejandre, A.; Ramirez Solis, J.; Busca, G. FTIR Study of the Interaction of Some Branched Aliphatic Molecules with the External and Internal Sites of H-ZSM5 Zeolite. *Phys. Chem. Chem. Phys.* **2000**, *2* (14), 3341–3348. https://doi.org/10.1039/b001807o.

(205) Coudurier, G.; Naccache, C.; Vedrine, J. C. Uses of i.r. Spectroscopy in Identifying ZSM Zeolite Structure. *J. Chem. Soc. Chem. Commun.* **1982**, No. 24, 1413. https://doi.org/10.1039/c39820001413.

(206) Lesthaeghe, D.; Vansteenkiste, P.; Verstraelen, T.; Ghysels, A.; Kirschhock, C. E. A.; Martens, J. A.; Speybroeck, V. Van; Waroquier, M. MFI Fingerprint: How Pentasil-Induced IR Bands Shift during Zeolite Nanogrowth. *J. Phys. Chem. C* **2008**, *112* (25), 9186–9191. https://doi.org/10.1021/jp711550s.

(207) Zecchina, A.; Spoto, G.; Bordiga, S. Vibrational Spectroscopy of Zeolites.

(208) Tabacchi, G.; Gianotti, E.; Fois, E.; Martra, G.; Marchese, L. Understanding the Vibrational and Electronic Features of Ti (IV) Sites in Mesoporous Silicas by Integrated Ab Initio and Spectroscopic Investigations. *J. Phys. Chem. C* **2007**, *111* (13), 4946–4955. https://doi.org/10.1021/jp0665168.

(209) Zuo, Y.; Zhang, T.; Liu, M.; Ji, Y.; Song, C.; Guo, X. Mesoporous/Microporous Titanium Silicalite with Controllable Pore Diameter for Cyclohexene Epoxidation. *Ind. Eng. Chem. Res.* **2018**, *57* (2), 512–520. https://doi.org/10.1021/acs.iecr.7b03719.

(210) Vos, D. E. De; Feijen, E. J. P.; Jacobs, P. A. Raman Spectroscopy on Zeolites ’. *Microporous Mater.* **1997**, *8*, 3–17. https://doi.org/10.1016/S0927-6513(96)00088-0.

(211) Scarano, D.; Zecchina, A.; Bordiga, S.; Geobaldo, F.; Spoto, G.; Anic, E.; Ricerche, C.; Pietro, S. Fourier-Transform Infrared and Raman Spectra of Pure and Al- , B- , Ti- and Fe-Substituted Silicalites : Stretching-Mode Region. *J. Chem. Soc. Faraday Trans.* **1993**, *89* (22), 4123–4130. https://doi.org/10.1039/FT9938904123.

(212) Li, Y. G.; Lee, M.; Porter, J. F. The Synthesis and Characterization of Titanium Silicalite-1. *J. Mater. Sci.* **2002**, *37* (10), 1959–1965. https://doi.org/10.1023/A:1015234812360.

(213) Rutherford, E. The Infrared Spectra of Propylene and Propylene-D6*. *J. Opt. Soc. Am.* **1952**, *79*. https://doi.org/10.1364/JOSA.43.001079.

(214) Tobin, M. C. The Infrared Spectrum of Propylene Oxide. *Spectrochim. Acta* **1960**, *16* (9), 1108–1110. https://doi.org/10.1016/0371-1951(60)80153-1.

(215) Bordiga, S.; Ugliengo, P.; Damin, A.; Lamberti, C.; Spoto, G.; Zecchina, A.; Spanò, G.; Buzzoni, R.; Dalloro, L.; Rivetti, F. Hydroxyls Nests in Defective Silicalites and Strained Structures Derived upon Dehydroxylation: Vibrational Properties and Theoretical Modelling. *Top. Catal.* **2001**, *15* (1), 43–52. https://doi.org/10.1023/A:1009019829376.

(216) Bolis, V.; Fubini, B.; Marchese, L.; Martra, G.; Costa, D. Hydrophilic and Hydrophobic Sites on Dehydrated Crystalline and Amorphous Silicas. *J. Chem. Soc. Faraday Trans.* **1991**, *87* (3), 497. https://doi.org/10.1039/ft9918700497.

(217) Buzzoni, R.; Bordiga, S.; Ricchiardi, G.; Lamberti, C.; Zecchina, A.; Bellussi, G. Interaction of Pyridine with Acidic (H-ZSM5, H-β, H-MORD Zeolites) and Superacidic (H-Nafion Membrane) Systems: An IR Investigation. *Langmuir* **1996**, *12* (4), 930–940. https://doi.org/10.1021/la950571i.

(218) Bordiga, S.; Lamberti, C.; Bonino, F.; Travert, A.; Thibault-Starzyk, F. Probing Zeolites by Vibrational Spectroscopies. *Chem. Soc. Rev.* **2015**, *44* (20), 7262–7341. https://doi.org/10.1039/c5cs00396b.

(219) Grahn, M.; Faisal, A.; Öhrman, O. G. W.; Zhou, M.; Signorile, M.; Crocellà, V.; Nabavi, M. S.; Hedlund, J. Small ZSM-5 Crystals with Low Defect Density as an Effective Catalyst for Conversion of Methanol to Hydrocarbons. *Catal. Today* **2020**, *345* (July 2019), 136–146. https://doi.org/10.1016/j.cattod.2019.09.023.

(220) Busca, G. Acidity and Basicity of Zeolites: A Fundamental Approach. *Microporous Mesoporous Mater.* **2017**, *254* (June 2016), 3–16. https://doi.org/10.1016/j.micromeso.2017.04.007.

(221) Bordiga, S.; Roggero, I.; Ugliengo, P.; Zecchina, A.; Bolis, V.; Artioli, G.; Buzzoni, R.; Marra, G.; Rivetti, F.; Spanò, G.; Lamberti, C. Characterisation of Defective Silicalites †. *J. Chem. Soc. Dalt. Trans.* **2000**, No. 21, 3921–3929. https://doi.org/10.1039/b004794p.

(222) Busca, G. Acid Catalysts in Industrial Hydrocarbon Chemistry. *Chem. Rev.* **2007**, *107* (11),

5366–5410. https://doi.org/10.1021/cr068042e.

(223) DATKA, J. Acidic Properties of Supported Niobium Oxide Catalysts: An Infrared Spectroscopy Investigation. *J. Catal.* **1992**, *135* (1), 186–199. https://doi.org/10.1016/0021-9517(92)90279-Q.

(224) Zecchina, A.; Geobaldo, F.; Spoto, G.; Bordiga, S.; Ricchiardi, G.; Buzzoni, R.; Petrini, G. FTIR Investigation of the Formation of Neutral and Ionic Hydrogen-Bonded Complexes by Interaction of H-ZSM-5 and H-Mordenite with CH 3 CN and H 2 O: Comparison with the H-NAFION Superacidic System. *J. Phys. Chem.* **1996**, *100* (41), 16584–16599. https://doi.org/10.1021/jp960433h.

(225) Heard, C. J.; Grajciar, L.; Uhlík, F.; Shamzhy, M.; Opanasenko, M.; Čejka, J.; Nachtigall, P. Zeolite (In)Stability under Aqueous or Steaming Conditions. *Adv. Mater.* **2020**, *32* (44), 1–29. https://doi.org/10.1002/adma.202003264.

(226) Signorile, M.; Bonino, F.; Damin, A.; Bordiga, S. A Novel Raman Setup Based on Magnetic-Driven Rotation of Sample. *Top. Catal.* **2018**, *61* (14), 1491–1498. https://doi.org/10.1007/s11244-018-1033-z.

(227) Dutta, P. K.; Rao, K. M.; Park, J. Y. Correlation of Raman Spectra of Zeolites with Framework Architecture. *J. Phys. Chem.* **1991**, *95* (17), 6654–6656. https://doi.org/10.1021/j100170a050.

(228) Chen, J.; Thomas, J. M.; Sankar, G. IR Spectroscopic Study of CD3CN Adsorbed on ALPO-18 Molecular Sieve and the Solid Acid Catalysts SAPO-18 and MeAPO-18. *J. Chem. Soc. Faraday Trans.* **1994**, *90* (22), 3455. https://doi.org/10.1039/ft9949003455.

(229) Sankar, G.; Thomas, J. M.; Chen, J.; Wright, P. A.; Barrett, P. A.; Greaves, G. N.; Catlow, C. R. A. EXAFS Investigation of Divalent Metal Ion Substituted AlPOs. *Nucl. Instruments Methods Phys. Res. Sect. B Beam Interact. with Mater. Atoms* **1995**, *97* (1–4), 37–40. https://doi.org/10.1016/0168-583X(94)00356-4.

(230) Verberckmoes, A. A.; Weckhuysen, B. M.; Schoonheydt, R. A. Spectroscopy and Coordination Chemistry of Cobalt in Molecular Sieves. *Microporous Mesoporous Mater.* **1998**, *22* (1–3), 165–178. https://doi.org/10.1016/S1387-1811(98)00091-2.

(231) Barrett, P. A.; Sankar, G.; Catlow, C. R. A.; Thomas, J. M. X-Ray Absorption Spectroscopic Study of Brønsted, Lewis, and Redox Centers in Cobalt-Substituted Aluminum Phosphate Catalysts. *J. Phys. Chem.* **1996**, *100* (21), 8977–8985. https://doi.org/10.1021/jp953034f.

(232) Martis, V.; Martis, M.; Lipp, J.; Detollenaere, D.; Rayment, T.; Sankar, G.; Bras, W. Energy-Resolved Electron-Yield XAS Studies of Nanoporous CoAlPO-18 and CoAlPO-34 Catalysts. *J. Synchrotron Radiat.* **2014**, *21* (4), 744–750. https://doi.org/10.1107/S1600577514008108.

(233) Muncaster, G.; Sankar, G.; Catlow, C. R. A.; Thomas, J. M.; Coles, S. J.; Hursthouse, M. The Local Structure of Tetrahedral Co(III): A Detailed Crystal Structure Investigation of K 5 Co III W 12 O 40 ·20H 2 O. *Chem. Mater.* **2000**, *12* (1), 16–18. https://doi.org/10.1021/cm990500v.

(234) Iton, L. E.; Choi, I.; Desjardins, J. A.; Maroni, V. A. Stabilization of Co (III) in Aluminophosphate Molecular Sieve Frameworks. *Zeolites* **1989**, *9* (6), 535–538.

https://doi.org/10.1016/0144-2449(89)90051-1.

(235) Modén, B.; Oliviero, L.; Dakka, J.; Santiesteban, J. G.; Iglesia, E. Structural and Functional Characterization of Redox Mn and Co Sites in ALPO Materials and Their Role in Alkane Oxidation Catalysis. *J. Phys. Chem. B* **2004**, *108* (18), 5552–5563. https://doi.org/10.1021/jp037257e.

(236) Nakashiro, K.; Ono, Y. Coordination Environment and Redox Property of Co(II) in the Framework of CoAPO-36 Molecular Sieve. *Bull. Chem. Soc. Jpn.* **1993**, *66* (1), 9–17. https://doi.org/10.1246/bcsj.66.9.

(237) Thomson, S.; Luca, V.; Howe, R. Framework Co(II) in CoAPO-5. *Phys. Chem. Chem. Phys.* **1999**, *1* (4), 615–619. https://doi.org/10.1039/a807709f.

(238) Frache, A.; Gianotti, E.; Marchese, L. Spectroscopic Characterisation of Microporous Aluminophosphate Materials with Potential Application in Environmental Catalysis. *Catal. Today* **2003**, *77* (4), 371–384. https://doi.org/10.1016/S0920-5861(02)00381-4.

(239) Marchese, L.; Gianotti, E.; Damilano, N.; Coluccia, S.; Thomas, J. M. Assessing the Br�nsted Acidity of CoAPO-18 Catalysts by Using N2 as Molecular Probe. *Catal. Letters* **1996**, *37* (1–2), 107–111. https://doi.org/10.1007/BF00813527.

(240) Bordiga, S.; Turnes Palomino, G.; Pazè, C.; Zecchina, A. Vibrational Spectroscopy of H2, N2, CO and NO Adsorbed on H, Li, Na, K-Exchanged Ferrierite. *Microporous Mesoporous Mater.* **2000**, *34* (1), 67–80. https://doi.org/10.1016/S1387-1811(99)00160-2.

(241) Knözinger, H.; Huber, S. IR Spectroscopy of Small and Weakly Interacting Molecular Probes for Acidic and Basic Zeolites. *J. Chem. Soc. - Faraday Trans.* **1998**, *94* (15), 2047–2059. https://doi.org/10.1039/a802189i.

(242) Gianotti, E.; Vishnuvarthan, M.; Berlier, G.; Marchese, L.; Coluccia, S. FTIR Study of Cobalt Containing Aluminophosphates with Chabasite like Structure by Using Co and No as Molecular Probes. *Catal. Letters* **2009**, *133* (1–2), 27–32. https://doi.org/10.1007/s10562-009-0053-5.

(243) Geobaldo, F.; Onida, B.; Rivolo, P.; Di Renzo, F.; Fajula, F.; Garrone, E. Nature and Reactivity of Co Species in a Cobalt-Containing Beta Zeolite: An FTIR Study. *Catal. Today* **2001**, *70* (1–3), 107–119. https://doi.org/10.1016/S0920-5861(01)00411-4.

(244) Góra-Marek, K.; Gil, B.; Śliwa, M.; Datka, J. An IR Spectroscopy Study of Co Sites in Zeolites CoZSM-5. *Appl. Catal. A Gen.* **2007**, *330* (1–2), 33–42. https://doi.org/10.1016/j.apcata.2007.06.033.

(245) Wulfers, M. J.; Jentoft, F. C. The Role of Cyclopentadienium Ions in Methanol-to-Hydrocarbons Chemistry. *ACS Catal.* **2014**, *4* (10), 3521–3532. https://doi.org/10.1021/cs500722m.

(246) Hernandez, E. D.; Jentoft, F. C. Spectroscopic Signatures Reveal Cyclopentenyl Cation Contributions in Methanol-to-Olefins Catalysis. *ACS Catal.* **2020**, *10* (10), 5764–5782. https://doi.org/10.1021/acscatal.0c00721.

(247) Qian, Q.; Ruiz-Martínez, J.; Mokhtar, M.; Asiri, A. M.; Al-Thabaiti, S. A.; Basahel, S. N.; Weckhuysen, B. M. Single-Catalyst Particle Spectroscopy of Alcohol-to-Olefins Conversions:

Comparison between SAPO-34 and SSZ-13. *Catal. Today* **2014**, *226*, 14–24. https://doi.org/10.1016/j.cattod.2013.09.056.

(248) Qian, Q.; Ruiz-Martínez, J.; Mokhtar, M.; Asiri, A. M.; Al-Thabaiti, S. A.; Basahel, S. N.; van der Bij, H. E.; Kornatowski, J.; Weckhuysen, B. M. Single-Particle Spectroscopy on Large SAPO-34 Crystals at Work: Methanol-to-Olefin versus Ethanol-to-Olefin Processes. *Chem. - A Eur. J.* **2013**, *19* (34), 11204–11215. https://doi.org/10.1002/chem.201300540.

(249) Qian, Q.; Ruiz-Martínez, J.; Mokhtar, M.; Asiri, A. M.; Al-Thabaiti, S. A.; Basahel, S. N.; Weckhuysen, B. M. Single-Particle Spectroscopy of Alcohol-to-Olefins over SAPO-34 at Different Reaction Stages: Crystal Accessibility and Hydrocarbons Reactivity. *ChemCatChem* **2014**, *6* (3), 772–783. https://doi.org/10.1002/cctc.201300962.

(250) Madeira, F. F.; Gnep, N. S.; Magnoux, P.; Maury, S.; Cadran, N. Ethanol Transformation over HFAU, HBEA and HMFI Zeolites Presenting Similar Brønsted Acidity. *Appl. Catal. A Gen.* **2009**, *367* (1–2), 39–46. https://doi.org/10.1016/j.apcata.2009.07.033.

(251) Colthup, N. B.; Daly, L. H.; Wiberley, S. E. *Introduction to Infrared and Raman Spectroscopy*, 2nd Editio.; Academic Press, Ed.; Elsevier, 1975. https://doi.org/10.1016/B978-0-12-182552-2.X5001-3.

(252) Ono, Y.; Mori, T. Mechanism of Methanol Conversion into Hydrocarbons over ZSM-5 Zeolite. *J. Chem. Soc. Faraday Trans. 1 Phys. Chem. Condens. Phases* **1981**, *77* (9), 2209–2221. https://doi.org/10.1039/F19817702209.

(253) Yamazaki, H.; Shima, H.; Imai, H.; Yokoi, T.; Tatsumi, T.; Kondo, J. N. Evidence for a “Carbene-like” Intermediate during the Reaction of Methoxy Species with Light Alkenes on H-ZSM-5. *Angew. Chemie Int. Ed.* **2011**, *50* (8), 1853–1856. https://doi.org/10.1002/anie.201007178.

Appendix I: related publications

ACS APPLIED MATERIALS & INTERFACES

October 20, 2021
Volume 13
Number 41
pubs.acs.org/acsami

ACS Publications
Most Trusted. Most Cited. Most Read.

www.acs.org

ACS APPLIED MATERIALS & INTERFACES

www.acsami.org

Research Article

Insights on a Hierarchical MFI Zeolite: A Combined Spectroscopic and Catalytic Approach for Exploring the Multilevel Porous System Down to the Active Sites

Alessia Airi, Matteo Signorile, Francesca Bonino, Pierluigi Quagliotto, Silvia Bordiga, Johan A. Martens, and Valentina Crocellà*

Cite This: *ACS Appl. Mater. Interfaces* 2021, 13, 49114−49127

Read Online

ACCESS | Metrics & More | Article Recommendations | Supporting Information

ABSTRACT: The hierarchization of zeolites to overcome the major drawbacks related to molecular diffusion limitation in micropores is a popular concept in heterogeneous catalysis. Despite the constant increase of new synthesis strategies to produce such hierarchical systems, the deep knowledge of their structural arrangement and how the zeolitic lattice is organized in a multilevel porous system is often missing. This information is essential to design a structure, tuning the porosity and the distribution of easily accessible active sites, and successively controlling the catalytic properties. In the present work, the synthesis of one of the most sophisticated forms of the hierarchical ZSM-5 zeolite has been reproduced, obtaining two multilevel porous materials with different crystallinity degrees, with the final aim of investigating and clarifying the finest features of their active sites. For this purpose, an extended characterization step by means of a unique multitechnique approach has been performed, thus revealing the active site nature, abundance, and distribution. IR spectroscopy with different molecular probes and a targeted catalytic test based on the hydroconversion reaction of *n*-decane were the toolbox for disclosing how the MFI lattice takes part in the hierarchical structure and how it, working in synergy with the mesoporous system, confers to this material a totally new shape−size selectivity. Merging the information obtained for the synthesized hierarchical zeolite with the characterization results of two reference materials (a mesoporous aluminum-containing MCM-41 and a microporous commercial ZSM-5), it was possible to define an internal and external map of the pore network of this complex and unique molecular sieve, where strong Brønsted acidic sites are located at the mouth of the MFI micropores and, at the same time, exposed at the surface of the mesoporous channels. Hence, the possibility of easily releasing bulky products is ensured and the application possibilities of the MFI lattice are expanded beyond cracking reactions.

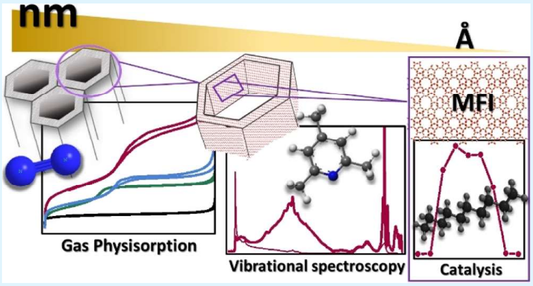

KEYWORDS: *hierarchical MFI, multilevel porosity, textural properties, IR and Raman spectroscopies, acidic active sites, n-decane hydroconversion*

1. INTRODUCTION

The rigidity and the precise shape of the inner space of zeolites, organized in a microporous channel system, combined with the distribution of the active sites, allow them to be classified as molecular sieves and are responsible for their shape-selectivity in catalysis.[1,2] These characteristics, indeed, allow the control and prediction of the access of reactants to the active sites and drive the formation of selected products through the imposition of the shape of intermediates and transition states. At the same time, the zeolites' active sites confinement in a narrowed space represents the major drawback of these materials. Indeed, the zeolite microchannels (diameter < 1 nm) cause strong limitations in the accessibility and in the diffusion rate of the reacting species and force the molecular transport, giving rise to the catalyst deactivation by obstruction. For this reason, mesoporous silicate materials obtained from synthetic design inspired by zeolites, such as MCM-41[3] and SBA-15,[4] attract considerable interest because they offer increased surface areas and a reduced deactivation rate. On the other hand, the amorphous nature of such materials does not allow them to compete with zeolitic microcrystalline systems in terms of stability during the reactions, shape selectivity, and controllability of the active

Received: June 21, 2021
Published: September 20, 2021

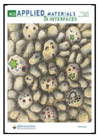

https://doi.org/10.1021/acsami.1c11614

sites.[5] Therefore, the most promising and innovative route is the production of systems that would preserve the crystalline arrangement and the bulk properties of a zeolite, while being a part of a multilevel structured system of pores with different diameters, the so-called hierarchical zeolites.[6,7] Indeed, the existence of a mesoporous network allows increasing the accessible surface area and the mass transport, limiting possible deactivation phenomena, whereas the ordered microporous domains offer a shorter path for reagent diffusion, maintaining the well-known shape selectivity of the zeolitic systems. Such a conformation paves the way for a wide range of possible substrates and specific products determined using a multilevel molecular sieve.[8]

The routes for introducing additional porous levels into an ordered material are substantially distinguishable in two main approaches: "top-down" and "bottom-up". The "top-down" strategies refer essentially to postsynthetic treatments over crystalline zeolites, in order to promote the formation of mesopores, such as partial desilication or dealumination.[9,10] Contrarily, "bottom-up" approaches imply the growing of a hierarchical system directly during synthesis, through the application of proper structure-directing agents (SDA), which drive the atomic assembly of the framework.[11−14] As a result of this new fruitful line of synthetic research, a large amount of new materials presenting both micro and meso (or macro) pores are documented, but, when they can actually be considered "hierarchical zeolites" remains a matter of discussion. The latter point is related to the term "hierarchical" itself, often used in a broad sense. Hierarchy in a porous system, in fact, implies a continuum between the different pore levels, passing through a subdivision of the inner space by distinct, but complementary, structural units: the channels must be connected without an interruption, like the organization of the vascular system of the human body.[15] This complex structure affects and defines the catalyst performances in a shape-size-driven reaction pathway. Materials presenting segregated regions with different porosities or non-connected pores of various dimensions cannot actually be considered hierarchical, even if they present multiple levels of pore diameters; this type of structures can be usually obtained through desilication by alkaline hydroxides, a not well-controllable process.[16,17] The discrimination of an actual hierarchical system by means of common characterization techniques is not always straightforward. For example, the structure resolution by powder X-ray diffraction (PXRD) is often not possible due to the reduced extension of the crystalline domains in micro−mesoporous systems.[18,19] Therefore, the identification of a "truly" hierarchical zeolite requires a tailor-made protocol for characterization.

Successful attempts with the creation of mesoporous zeolites have been achieved in 2006 by applying the quaternary ammonium surfactant in combination with cationic polymers,[22] and then afterward by developing hard templating techniques.[21] In 2011,[20] Ryoo and co-workers supplied a revolutionary synthetic approach for the soft templated formation of mesoporous zeolites, based on the bifunctional action of a single-molecular SDA. The bifunctional templating agent drives the assembly of the silicate framework over the surface of the micelles formed in aqueous medium, producing, at the same time, both micro- (by means of quaternary ammonium functionalities) and mesopores (by means of long alkylic tails). They proposed a synthesis templated by the dual surfactant $C_{18}-N_3-C_{18}$ (C_{18} refers to the length of the alkylic chains and N_3 to the number of ammonium functionalities) of an aluminum silicate organized in hexagonal mesoporous channels (similar to the MCM-41), encompassed by zeolitic structures (i.e., thin crystalline zeolitic walls with a MFI topology). In the same paper,[20] Ryoo and co-workers reported this new molecular sieve to be highly active as a catalyst for various acid-catalyzed reactions of bulky molecular substrates, compared with conventional zeolites and ordered mesoporous amorphous materials. In this scenario, it is evident how the considerably improved catalytic activity of this hierarchically structured zeolite deserves a further specialized investigation to clarify the finest features of its active sites.

For this reason, in the present work, we decided to replicate the synthesis procedure proposed by Ryoo to develop a tailor-made advanced characterization procedure for disclosing the nature, abundance, and distribution of the catalyst active sites, highlighting how the peculiar hierarchical organization affects the shape-size selectivity of the MFI framework. After the synthesis of the catalyst in its acidic form, we retraced the structural characterization of the material by means of PXRD and transmission electron microscopy (TEM), and then we investigated the active sites' intimate nature and location within the multilevel porous system, by combining a unique spectroscopic approach and targeted catalytic experiments. For this purpose, after a careful analysis of the size and volume of the different pore families by applying the non-localized density functional theory (NLDFT) model to nitrogen physisorption isotherms, different molecules with various steric hindrance and basic characters have been selected as probes.[23−26] Such information has been merged with the results obtained by employing the material as the catalyst in *n*-decane hydroconversion. The so-called "decane test" represents a powerful "characterization" technique for disclosing the inner space of a zeolitic material,[27] through the evaluation of isomerization and cracking products during the conversion pathways. For comparison, the same multitechnique characterization approach has been carried out on two reference materials (an aluminum containing MCM-41 as a mesoporous model and a commercial ZSM-5 as a microporous reference) finally allowing the indirect evaluation of the internal and external map of the porous network of this complex and unique molecular sieve.

2. EXPERIMENTAL SECTION

2.1. Commercial Reference ZSM-5 CBV3024E (Si/Al = 15). The zeolite in the ammonic form was provided by Zeolyst and converted into the protonic form by thermal treatment at high temperature (500 °C in vacuum) when needed. The protonic acid zeolite is hereafter referred to as H-ZSM-5.

2.2. Synthesis. *2.2.1. Synthesis of Reference Al-MCM-41 (Nominal Si/Al = 20).* The mesoporous silicate Al-MCM-41 was synthetized by hydrothermal treatment, according to the procedure published by Vaschetto et al. in 2013.[28] Tetraethyl orthosilicate (TEOS, Sigma-Aldrich, ≥99.0%) was used as a silicon source, sodium aluminate ($NaAlO_2$ Sigma-Aldrich, technical, anhydrous) as an aluminum precursor, and hexadecyltrimethylammonium bromide (CTA-Br, Sigma-Aldrich, 95%) as an organic template. The gel composition was chosen following the molar ratios

$$1SiO_2:\ 0.025Al_2O_3:\ 0.50NaOH:\ 0.12CTA\text{-}Br:\ 132H_2O$$

First, 0.589 g NaOH (Sigma-Aldrich, ≥98%, pellets, anhydrous) is solubilized in 70 mL H_2O within a two-neck round-bottom flask, under stirring at 40 °C, then 1.288 g CTA-Br is added, followed by dropwise addition of 6.58 mL TEOS. The aqueous solution is kept under stirring for 30 min at constant temperature. After this time, 0.1207 g $NaAlO_2$ is added and the mixture is stirred for 4 h at room temperature, to promote the formation of the gel. At the end, the solution is kept in a teflon-coated stainless-steel autoclave for the hydrothermal treatment at a constant temperature of 100 °C for 2 days. The material is then separated by filtration, washed with deionized water, and then calcined in a tubular oven within an alumina crucible, heating up to 550 °C (with a ramp of 2 °C/min) under N_2 flow and then O_2 flow at the same temperature for 7 h.

2.2.2. Synthesis of Non-Commercial Surfactant C_{18}—N_3—C_{18}. The molecule has been synthetized following the procedure of Na et al.[20] The first intermediate is obtained by mixing 5 g *N*,*N*-dimethyloctadecan-1-amine (TCI Chemicals, >90.0%) and 25.8 mL 1,6-dibromohexane (TCI Chemicals, >97.0%) (1:10 ratio) then solubilized dropwise (through a drip funnel) within a 1:1 mixture of 250 mL acetonitrile (Sigma-Aldrich, ≥99.9%) and 250 mL toluene (Sigma-Aldrich, ≥99.5%). The reaction is carried forward for 24 h under stirring at 65 °C. At the end of the reaction, the solvents are removed by evaporation under vacuum, obtaining an oily raw product. The product is then crystallized and washed from reactant residues by ethyl ether baths (400 mL), under stirring for 2 h and repeating the procedure three times. A white precipitate was obtained, isolated by in vacuum filtration. For the second intermediate, 10 g 1-bromooctadecane (TCI Chemicals, >97.0%) and 64.1 mL *N*1,*N*1,*N*6,*N*6-tetramethyl hexane-1,6-diamine (TCI Chemicals >98.0%) (1:10 ratio) were reacted following the same procedure described for the intermediate 1. The final product is obtained by the coupling of intermediates 1 and 2 in a ratio of 1:1 and solubilized dropwise in 500 mL acetonitrile at 65 °C. The reaction is conducted under stirring and monitored by frequent sampling and analysis by mass spectrometry. All the products have been analyzed by ^{1}H NMR spectroscopy, confirming the success of the synthesis.

2.2.3. Synthesis of Hierarchical mM-Z (Nominal Si/Al = 20). The hierarchical aluminum silicate material, hereafter referred to as mM-Z (microMeso Zeolite), has been synthesized by hydrothermal treatment, using the non-commercial surfactant C_{18}—N_3—C_{18} as the templating agent, following the procedure of Na et al.[20]

The gel composition is as follows

$$6.62Na_2O: 0.75Al_2O_3: 30SiO_2: 1.5C_{18}{-}N_3{-}C_{18}: 240EtOH: 2132H_2O$$

Two different samples have been obtained and described here, evaluating the influence of different temperature control during the gel-aging process.

The sample hereafter termed mM-Z1 has been obtained as follows: first C_{18}—N_3—C_{18} is solubilized in 4.639 mL ethanol (Sigma-Aldrich, ≥99.5%) and 6.14 mL deionized water and kept under stirring at 65 °C until obtaining a clear liquid, with the formation of surfactant micelles. Then, 0.0478 g $NaAlO_2$ and 0.1480 g NaOH are solubilized in 6 mL of water, where subsequently, 2.218 g TEOS has been added. This second solution is added dropwise to the first one and then kept for 6 h under stirring at a liquor temperature of 65 °C for the gel aging. During this phase, the temperature has been monitored by immersing a traditional mercury thermometer directly into the reaction liquid. This ensures that the temperature remains constant throughout this stage prior to hydrothermal treatment.

The sample hereafter labeled mM-Z2 has been obtained with the same procedure, but with a different temperature control. During surfactant micellization and gel aging, the temperature has been kept at 60 °C by electronic control of the heating bath through the thermocouple integrated in the heating system. It is assumed that there is a deviation of about 10 °C less from the temperature of the reaction liquid. In both cases, the white gels were then kept in a teflon-lined steal autoclave for the hydrothermal treatment, in an oven at 140 °C for 8 days under tumbling conditions. At the end, the obtained powders were filtered under vacuum and repeatedly washed with deionized water, then calcined within an alumina crucible, and kept in a tubular oven at 550 °C (a heating ramp of 2 °C/min) for 7 h under dry air flow.

2.2.4. Cation Exchange. mM-Z1, mM-Z2, and Al-MCM-41 have been synthesized in the sodic form. The Na^+ cations were exchanged with NH_4^+ ions to generate the acidic catalyst. The procedure adopted is as follows: the powder is immersed for 6 h in a 1 M solution of NH_4NO_3 (Sigma-Aldrich, ≥99.0%) (20 mL solution/g sample) at 80 °C then the ion-exchanged material is separated by centrifugation and the same procedure is repeated three times. NH_4^+ substitutes Na^+ in the aluminum silicate structure, and finally NH_3 is released, when needed, by thermal activation (refer to this in the further sections), at high temperature (400−500 °C), leaving only H^+ for charge balancing, giving the final material with acidic character. The samples in the protonic form are labeled as: H-mM-Z1, H-mM-Z2, and H-Al-MCM-41.

2.3. Characterization Techniques. *2.3.1. Transmission Electron Microscopy.* The TEM analysis has been conducted using a TEM JEOL JEM 3010 UHR microscope (a theoretical resolution of 0.17 nm) equipped with a LaB_6 electron source working at 300 kV of accelerating potential and an EDS OXFORD X-STREAM energy dispersion detector. The images have been collected using a CCD camera Gatan, model 894 US1000 (2k × 2k). The sample has been prepared depositing a small amount of powder over a 200-mesh lacey carbon copper grid.

2.3.2. X-ray Powder Diffraction (PXRD). The XRD measurements have been carried out using the Bragg−Brentano geometry with a PANalytical PW3050/60 X'Pert PRO MPD diffractometer with a Cu anode ($K\alpha$ = 1.5418 Å) and an X'Celerator detector.

2.3.3. N_2 Physisorption. Isothermal N_2 physisorption measurements at liquid nitrogen temperature were performed on a Micromeritics ASAP 2020. Prior to the measurement, the powders were degassed overnight at 100 °C and 4 h at 350 °C. Specific surface areas were determined by using both the Brunauer−Emmett−Teller and the Langmuir models. Pore size distributions were obtained by applying the NL-DFT method.

2.3.4. Infrared Spectroscopy. 2.3.4.1. Transmission IR Experiments. The samples were analyzed in the form of self-supporting pellets kept in a home-made quartz cell with KBr or CaF_2 windows (depending on the molecular probe used), designed for thermal outgassing before each experiment. The thermal activation consisted of the controlled heating at 5 °C/min until 500 °C, with the contemporary removal of gaseous species through a glass-line equipped with vacuum pumps, until reaching 5×10^{-4} mbar of internal pressure of the quartz cell. Then, in order to oxidize all the adsorbed species on the porous sample surface, 100 mbar of pure O_2 was introduced in the cell and kept in contact for 1 h. Finally, O_2 was outgassed, and the sample was cooled to RT, under vacuum. The infrared (IR) spectra were acquired in transmission mode with a Bruker Vertex 70 spectrophotometer equipped with a MCT cryodetector, collecting 32 scans for each spectrum with a resolution of 2 cm^{-1}. Under acquisition, the samples were kept connected to the vacuum glass-line, which allowed the dosage of gaseous probe molecules for in situ measurements, recording the spectral changes during adsorption/desorption. Every probe molecule—carbon monoxide (CO);[29] pyridine (Py);[30] and 2,4,6-trimethyl pyridine (collidine)—[31] requires a specific experimental setting, according to the specific literature reported.[32,33]

2.3.4.2. ATR-IR Experiments. The spectra were collected on the same instrument, opportunely equipped with a Bruker Platinum ATR accessory with a diamond single-reflection internal refraction element and a DTGS detector. The samples have been analyzed without any previous treatment.

2.3.5. Raman Spectroscopy. The 244 nm Raman spectra were collected on a Renishaw inVia Raman microscope spectrometer, equipped with a Coherent Innova 300C motoFreD frequency-doubled Ar^+ laser as the excitation source, a 3600 line/mm grating, and a UV-enhanced CCD detector. The light was focused on samples through a 15× objective. In order to prevent degradation phenomena induced by the intense, highly energetic excitation light, samples were kept under continuous rotation by using a home-made sample holder.[34] Three spectra were collected for each sample and averaged to yield a better signal-to-noise ratio.

2.4. Catalytic Hydroconversion of *n*-Decane. The samples were first loaded with 0.3% (w/w) of Pt, by wet impregnation with an aqueous solution of $Pt(NH_3)_4Cl_2$ (Sigma-Aldrich, 98%). Once dried, the powders were pelletized and kept in a high-throughput reactor, a home-made design of KU Leuven University.[35] In each experiment, 50 mg of bifunctional catalyst pellets was loaded in quartz reactor tubes with an internal diameter of 2 mm. The materials have been pretreated in situ by heating to 400 °C at 5 °C/min under O_2 flow for 1 h, then flushed with N_2 for 25 min, and finally reduced in a pure H_2 atmosphere at 400 °C for 1 h. Before starting the feed *n*-decane injection, the reactor has been cooled down to 100 °C. The H_2/*n*-decane molar ratio in the catalytic experiments was 214, and the space time (W/F_o) was 1400 kg s/mol. The reaction temperature was increased stepwise at constant space time. The reaction products were sampled for in-line gas chromatographic (GC) analysis 1 h after reaching a temperature set point with a rising slope of 5 °C for every step until complete conversion of the feed *n*-decane was reached.

3. RESULTS AND DISCUSSION

Herein, we report the complete, tailor-made characterization protocol of the two hierarchical mM-Z materials, with the aim of disclosing their intimate and finest features. The two materials exhibit non-negligible differences, which will be described in detail in the following. This fact shows that slight variations in the synthesis procedure, and in particular during the aging phase prior to hydrothermal treatment, have a strong influence on the final material.

From ICP measurements, compared also with EDX elemental analysis, the average silicon to aluminum (SAR) ratio of the mM-Z samples is equal to 15. The two reference materials (the mesoporous MCM-41 and the commercial microporous ZSM-5) have the same SAR of the hierarchical structures.

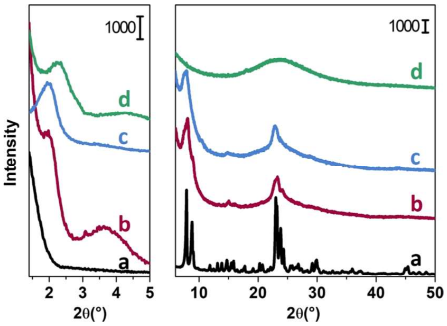

Figure 1. Left panel: small angles. Right panel: wide-angle powder XRD patterns of calcined samples: reference ZSM-5 (a), mM-Z1 (b), mM-Z2 (c), and Al-MCM-41 (d).

3.1. Morphological and Structural Properties. Figure 1 shows the PXRD patterns of mM-Z1 (b) and mM-Z2 (c), compared with the bulk commercial ZSM-5 (a) and the Al-MCM-41 sample (d), both in the low-angle (below 5°2θ) and wide-angle regions. The mM-Z1 sample displays two resolved Bragg reflections at around 2 and 3.5° (see the Figure 1 left panel). These peaks are totally absent in the MFI pattern and they have been indicized by Na et al.[20] as (*hk*) reflections, corresponding to a long distance *d* of a mesoscale lattice with 2D hexagonal symmetry, similar to MCM-41.[36] The reflections (11) and (10) are well visible for mM-Z1, whereas only the (10) peak is present in the mM-Z2 diffractogram. In Figure 1 right panel (wide angles), both mM-Z samples exhibit only the principal diffraction peaks corresponding to the reflections of the MFI lattice along the [*a**] crystallographic direction. As explained by Ryoo et al.,[20] determining the microporous framework structure of such materials accurately by XRD is challenging because the mesopore walls are composed of only a single layer of zeolitic micropores, which can be less than a single-unit-cell dimension of a bulk zeolite. Moreover, the zeolite-like mesopore walls extend over a very narrow diffractive domain in width. The broader peaks of both mM-Z samples indicate the less extension of the crystalline domains compared to the bulk reference H-ZSM-5 zeolite. The mM-Z1 sample presents more resolved peaks with respect to mM-Z2, suggesting the presence of more structural elements of the MFI lattice in its mesoporous framework. Observing the profile of both mM-Z diffractograms, which present a limited number of rather wide reflections, it is possible to exclude the presence of a segregated MFI phase, but at the same time, the baseline trend does not suggest the presence of a significant amorphous phase. The hierarchical samples, therefore, have their own level of order, characterized by thin crystalline domains. The second level of order is detectable by the XRD reflections at small angles, the trace of a larger structure, comparable to the 2D hexagonal openings of MCM-41 (d).

The TEM micrographs shown in Figure 2 confirm the presence of a hexagonal array of mesopores of around 4 nm for mM-Z1 (Figure 2a,b). These images are in line with those reported by Ryoo and co-workers,[20] confirming that the material is organized in elongated tubular structures of hollow hexagonal section with 1 nm thick walls. For the mM-Z2 sample (Figure 2c,d), the hexagonal array of mesopores is not so evident (Figure 2d). At this level of resolution, however, it is not possible to distinguish, for both samples, the micropores of the MFI zeolitic system on the mesoporous walls. More detailed information about the presence of microchannels will be obtained from the textural analysis reported in the next section.

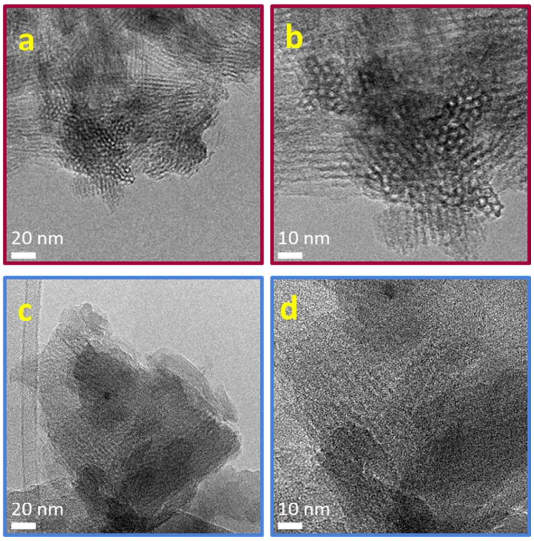

Figure 2. TEM micrographs of calcined mM-Z1 (a,b) and calcined mM-Z2 (c,d) at increasing magnifications.

As reported by Ryoo et al.,[20] the peculiar XRD pattern is not sufficient for the precise determination of the microporous

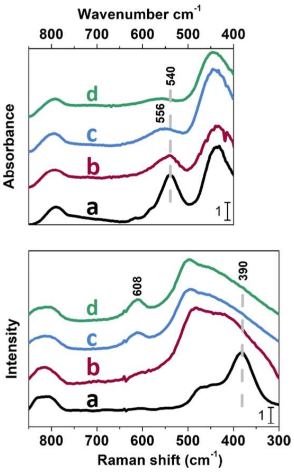

Figure 3. Top panel: ATR-IR spectra. Bottom panel: Raman spectra of reference ZSM-5 (a), mM-Z1 (b), mM-Z2 (c), and Al-MCM-41 (d) in the spectral region corresponding to the framework Si−O vibrational modes. Spectra have been normalized to the Si−O stretching overtone modes and shifted on the *Y* axis for the safety of clarity.

framework structure. For this reason, IR and Raman spectra have been employed to really identify the structural fingerprints of the MFI lattice of mM-Z samples. Figure 3 shows the framework vibrational mode region of ATR-IR (Figure 3 top panel) and Raman (Figure 3 bottom panel) spectra. As far as regarding the IR spectrum, three maxima are visible in the 800−400 cm^{-1} spectral region of Figure 3 for the reference ZSM-5 (a). The bands located at 790 and 435 cm^{-1} correspond to the symmetric stretching and out of plane rocking vibrations of Si−O−Si units, respectively. The signal at 540 cm^{-1} is considered the spectroscopic signature of zeolites with MFI topology, being the collective vibrational mode of condensed five-membered units of Si atoms (pentasil units).[37−41] The band associated with pentasil framework vibrations (highlighted by the vertical dashed line) falls at 540 cm^{-1} in the mM-Z1 spectrum (b) and at 556 cm^{-1} in the mM-Z2 spectrum (c), whereas it is almost absent in Al-MCM-41 (d). Theoretical molecular dynamics simulations demonstrated that, upon decreasing the number of pentasil units, which participate in this framework mode, the band undergoes a hypsochromic shift until reaching a frequency of 650 cm^{-1}, the vibration of the isolated pentasil unit.[41] The shift to a higher frequency of this band attested in the mM-Z sample spectra suggests the materials contain a decreased number of pentasil units compared to the standard MFI framework. This strongly supports the hypothesis that the mesopore walls of the mM-Z samples are composed of a thin layer of zeolitic micropores, less than a single-unit-cell dimension of a standard MFI zeolite. The spectral behavior of mM-Z1 is closer to that of the bulk ZSM-5 (maximum at 540 cm^{-1}), testifying its higher degree of crystallinity. Concerning the Raman spectra, the ZSM-5 reference exhibits a maximum at 800 cm^{-1} (symmetric Si−O−Si stretching, active in both IR and Raman), and a broad signal below 500 cm^{-1} corresponding to the Si−O−Al stretching modes. The intense component at 380 cm^{-1} (highlighted by the dotted line in Figure 3, bottom panel) is attributed to the stretching Raman active mode of pentasil-units typical of the MFI framework.[37] A component related to pentasil stretching vibrations at 390 cm^{-1} is recognizable in the spectrum of the mMZ-1 sample (b), confirming the presence of a MFI structural organization. In contrast, the mM-Z2 spectrum is similar to the one of the amorphous Al-MCM-41 silica. The mM-Z2 spectrum presents also a signal at 608 cm^{-1}, attributed to the amorphous silica.[37,42,43] This spectral behavior does not exclude the existence of a MFI microporous framework in the mMZ-2 sample, as already proved by the XRD pattern and by the presence of the IR band at 540 cm^{-1} (even if less resolved compared to mMZ-1) due to pentasil units. The differences observed in the mMZ-2 sample simply point out that the crystalline MFI domains of its mesoporous walls are less extended.

3.2. Textural Properties. Figure 4 (top panel) shows the N_2 physisorption isotherms at liquid nitrogen temperature. The pore size distribution and the cumulative pore volume, calculated by modern pore modeling techniques based on NL-DFT, are reported in Figures 4 (bottom panel) and S1. Textural properties of all samples are summarized in detail in Table 1.[44] According to IUPAC classification,[45] the two reference ZSM-5 and Al-MCM-41 materials possess a type I (black curve) and a type IV(b) (green curve) isotherm,

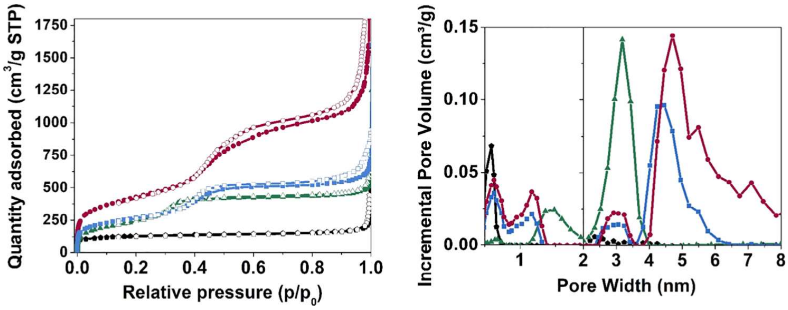

Figure 4. Top panel: N_2 adsorption−desorption isotherms collected at liquid nitrogen temperature of: reference ZSM-5 (black ⬟), mM-Z1 (red ●), mM-Z2 (blue ■), and Al-MCM-41 (green ▲), filled symbols refer to adsorption and empty symbols to desorption. Bottom panel: compared pore size distribution calculated using the NL-DFT model of: reference ZSM-5 (black ⬟), mM-Z1 (red ●), mM-Z2 (blue ■), and Al-MCM-41 (green ▲).

Table 1. Textural Properties of Hierarchical mM-Z Samples Compared with Reference Mesoporous Al-MCM-41 and Microporous ZSM-5 Materials

sample name	BET SSA (m^2/g)	Langmuir SSA (m^2/g)	total pore volume[a] (cm^3/g)	micropore volume[a] (cm^3/g)	mesopore volume[b] (cm^3/g)	ultra-micropore size[c] (nm)	supermicropore size[c] (nm)	main mesopore size[c] (nm)
reference ZSM-5	381	507	0.19	0.19	0	0.6		
mM-Z1	1544	2128	2.04	0.4	1.64	0.6	1.1	3.0−4.7
mM-Z2	962	1323	0.94	0.27	0.67	0.6	1.1	3.0−4.5
Al-MCM-41	890	1243	0.76	0.13	0.63		1.5	3.2

[a] Calculated using the cumulative pore volume graph (Figure S1) obtained from NL-DFT analysis of the adsorption isotherm. [b] Obtained using the difference between the total pore volume and micropore volume values. [c] Calculated using the pore size distribution graph (Figure 4, bottom panel) obtained from NL-DFT analysis of the adsorption isotherm.

respectively. The reference isotherm profile agrees with what extensively reported in the literature for pure microporous and mesoporous amorphous (like MCM-41) systems.[46−48] On the other side, both mM-Z1 and mM-Z2 samples (red and blue curves, respectively) exhibit composite isotherms, generated by the combination of type I and type IV(a) models. Both mM-Z1 and mM-Z2 isotherms present a type H4 hysteresis loop (according to IUPAC classification)[45,49] typical of materials containing micro- and mesoporosity such as hierarchical zeolites. The symmetrical shape of the hysteresis loops suggests a gradual process of filling/evacuation of the porous system and, at the same time, it allows excluding some pore blocking or cavitation phenomena.[50] A certain degree of order of the mesoporous structure can be, therefore, supposed for both mM-Z materials. It is worth noting that, even if the isotherms of the two hierarchical materials present the same profile, the quantity of N_2 adsorbed on mM-Z1 is about twice in comparison with mM-Z2, being so responsible for a significantly higher specific surface area (see Table 1) in agreement with the results obtained in the paper reported by Na et al.[20] Concerning the pore size distribution (Figure 4b), the classical ZSM-5 exhibits only a family of ultramicropores (diameter < 1 nm) with an average size of 0.6 nm in accordance with the microchannels of the MFI lattice. In contrast, the mesoporous Al-MCM-41 presents, as a major contribution to the pore volume, a family of mesopores centered at 3.2 nm and, as a minor contribution, a family of supermicropores of 1.5 nm width, with no presence of ultramicropores. The size of the mesopores of the reference Al-MCM-41 system is also responsible for the absence of any hysteresis loop in the isotherm (green curve in Figure 4, top). Indeed, for N_2 adsorption in cylindrical pores at liquid nitrogen temperature, hysteresis occurs for pores wider than 4 nm and, hence, for adsorbents having mesopores of smaller width, completely reversible type IV(b) isotherms are observed. Interestingly, the mM-Z samples replicate at the same time the textural features of the two reference materials. The pore size distribution of mM-Z materials (Figure 4, bottom) displays a family of ultramicropores (0.6 nm), compatible with the MFI microchannels and a family of supermicropores (1.1 nm), already attested for MCM-41.[51] The population of mesopores in the two samples is more heterogenous if compared to the reference mesoporous sample: a contribution of around 3.0 nm (the size of the MCM-41 mesopores) is always present, in the two hierarchical materials together with a maximum between 4 and 5 nm. These cavities are compatible with the hexagonal openings recognizable in the TEM micrographs, more evident for mM-Z1 (Figure 2b) and only slightly visible in mM-Z2 (Figure 2d). The mM-Z1 sample presents a consistent increase of the total pore volume if compared to the ZSM-5 and MCM-41 references, reaching 2.04 cm^3/g. A relevant contribution to the total pore volume is ascribable to the microporous cavities (0.4 cm^3/g), significantly exceeding the value assessed for the bulk zeolite (0.19 cm^3/g), whereas the difference arises from its widely extended mesoporous system (1.64 cm^3/g). The mesopore volume of mM-Z2 (0.67 cm^3/g) is lower compared to that of mM-Z1 and more similar to the value of the reference mesoporous Al-MCM-41 material. The mM-Z2 total pore volume overcomes the one of the mesoporous references thanks to the contribution of 0.27 cm^3/g deriving from a family of ultramicropores, exactly of the MFI size (0.6 nm), totally absent in the amorphous Al-MCM-41. These results are particularly helpful in describing the interconnected porous structure of the mM-Z materials, showing what was not completely confirmed by the structural characterization: the dual $C_{18}-N_3-C_{18}$ templating agent selectively acts producing the microporous system, organizing the general layout in an ordered mesostructure. In summary, it is undeniable that the textural data can be traced back to a hierarchical framework (according to the previous work reported in the literature),[49,50] also for the less-crystalline mM-Z2.

3.3. Nature, Abundance, and Location of Active Sites Probed by In Situ IR Spectroscopy. Among the large arsenal of characterization techniques, transmission IR spectroscopy is certainly one of the more powerful experimental tools to obtain a detailed description of the surface properties of a porous material, specifically due to the possibility to use different probe molecules in combination with an investigative technique able to monitor, with an extremely high sensitivity, the probe-surface interaction. Ideally, molecular probes for IR studies should have a small size, to monitor surfaces in all details. However, the parallel use of various probe molecules of increasing size results in a surface site speciation able to discriminate the different active sites based on their accessibility. This advanced characterization tool is particularly useful in the presence of hierarchical structures.[25] Indeed, following the adsorption and desorption by in situ IR spectroscopy of basic molecular probes with different proton affinity (or Lewis character) and steric hindrance allows us to obtain information regarding the acidic sites strength, amount, and different locations within the porous framework.[23,52,53]

The full spectra of all dehydrated samples are reported in Figure S2 of Supporting Information, whereas the spectral region of OH stretching vibrations (ν_{OH}), between 3800 and 3500 cm^{-1}, is displayed in insets a, b, c, and d of Figure 5. The commercial H-ZSM-5 (Figure 5 inset a, light gray curve) spectrum is dominated by two main bands located at 3747 and 3610 cm^{-1} ascribed to isolated SiOH groups located on the external surface of the zeolite and to bridged Si(OH)Al hydroxyl groups with Brønsted acidic character, respectively.[32]

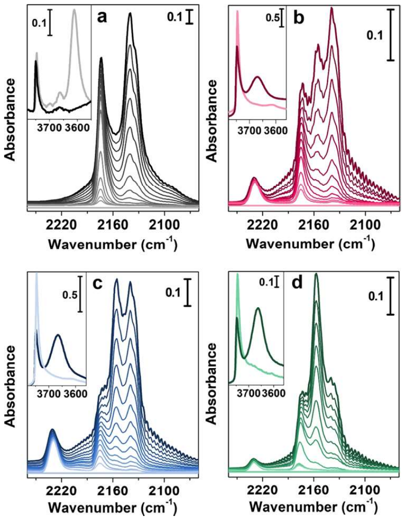

Figure 5. Main panels: differential IR spectra of CO adsorption at liquid nitrogen temperature in the CO stretching region (2300−2000 cm^{-1}) on (a) commercial standard H-ZSM-5, (b) H-mM-Z1, (c) H-mM-Z2, and (d) H-Al-MCM-41. Strongest colors represent the highest CO coverage (80 mbar). Lighter colors indicate decreasing pressure steps. Insets: IR spectra in the O−H stretching region (3700−3500 cm^{-1}) after activation in vacuum (5×10^{-4} mbar) at 500 °C (light curves) and after CO saturation (dark curves).

The spectra of activated H-mM-Z1, H-mM-Z2, and H-Al-MCM-41 (Figure 5 insets b, c, and d, light red, light blue, and light green curves) substantially differ from the spectrum of reference H-ZSM-5. Indeed, the OH stretching region is mainly characterized by the intense signal of virtually isolated SiOH groups at 3747 cm^{-1}. For all materials, a weak band at 3610 cm^{-1} is also evident, partially overlapped to the long tail of the 3747 cm^{-1} signal, extended to lower wavenumbers, generated by terminal OH groups in hydrogen-bonded silanol chains located inside the zeolite structure (i.e., inside defective nanovoids generated by silicon vacancies).[33] It is worth noting that the band ascribable to Brønsted bridged hydroxyl species at 3610 cm^{-1}, whose intensity is proportional to the crystallization degree of the sample, is more intense in the mM-Z1 sample.

The acidic properties of the materials were first probed using CO at liquid nitrogen temperature. CO is a weak basic probe, able to detect and discriminate among acidic sites of different nature (also in the presence of rather small differences in acid strength), and, thanks to the absence of steric limitation, it can diffuse inside the zeolitic micropores. The CO adsorption/desorption spectra collected at liquid nitrogen temperature after activation at 500 °C are reported in Figure 5. As reported in the extended Figure S3, upon CO exposure, a new envelope of bands appears in the 2260−2060 cm^{-1} range and, in parallel, a clear perturbation of the OH stretching modes between 3800 and 3500 cm^{-1} occurs. Concerning the latter spectral region, a detailed explanation of the various components and of their spectral behavior is reported in the infrared spectroscopy section of the Supporting Information. The main panels of Figure 5 present the C≡O stretching region between 2260 and 2060 cm^{-1}. In each figure, the spectra acquired at the highest CO coverage (the darkest curve) and upon decreasing the pressure by dynamic outgassing (lighter curves) until complete CO removal are reported. The evaluation of spectral changes at different CO coverages is extremely useful to evaluate the stability (and consequently the acid strength) of different adsorbing sites. The attribution of each band, originated by the interaction between the probe molecule and the catalyst sites, can be easily operated thanks to the extensive literature on the subject.[23,54] In the H-ZSM-5 spectra (Figure 5a), a very intense band at 2174 cm^{-1} is visible, corresponding to the interaction of CO with the Si(OH)Al Brønsted sites. This band is very persistent also at very low CO coverages (light gray curves), indicating the strong character of these acidic sites. The signal, centered at 2140−2138 cm^{-1}, is due to the liquid-like CO phase, which forms inside the zeolite micropores. The spectra of the mM-Z1, mM-Z2, and H−Al-MCM-41 samples (Figure 5b−d) exhibit the band generated by Brønsted acidity at 2175 cm^{-1}, persisting until low CO coverages. The spectral behavior of this component is similar to that of the reference microporous H-ZSM-5, proving that the Brønsted Si(OH)Al acid sites of all mesoporous samples, both hierarchical (H-mM-Z1 and H-mM-Z2) and reference (H-Al-MCM-41), have possibly the same nature and the same acidic strength. Moreover, in the spectra of all mesoporous materials, a very stable band, totally absent in the reference zeolite, is visible at 2230 cm^{-1}, corresponding to the interaction of CO with the polarized electronic density of Al^{3+} in the trigonal coordination, which lies in a partial framework position and possesses strong Lewis acidity.[24,32,55,56] The Lewis acidity is basically absent in the commercial H-ZSM-5, whereas in micro−meso H-mM-Z1 and H-mM-Z2 materials, it is directly associated with an intrinsic defectivity that moves them closer to the properties of the amorphous H-Al-MCM-41. Other two components are visible in the spectra of all mesoporous materials located at 2155 cm^{-1} and at 2138 cm^{-1}, ascribable to CO interacting with SiOH groups and to the liquid-like phase, respectively.

After the qualitative assessment of the acidic species present in hierarchical samples by means of CO adsorption, a careful quantification of both Brønsted (BAS) and Lewis (LAS) acid sites was performed by employing pyridine (Py) as the molecular probe.[32,57] This molecule interacts with strong Lewis acid centers and, thanks to its high proton affinity (930 kJ/mol), undergoes protonation in the presence of sites with Brønsted acid character; moreover, its kinetic diameter of 0.57 nm allows it to diffuse within the microchannels of the MFI framework (∼0.6 nm), allowing the detection of all BAS and LAS located in both micropores or mesopores. The acid site titration was performed integrating the area of the analytical 19b Py vibrational modes generated by its irreversible interaction with the acidic sites (i.e., after Py adsorption and thermal removal under vacuum at 200 °C for 1 h). IR spectra collected after sample activation and after Py contact and following outgassing at 200 °C for 2 h are reported in Figure S4 in an extended IR spectral range. The spectral region of Py ring vibrational modes is instead reported in Figure 6, left panel. The band associated with the formation of a pyridinium ion (Py adsorbed on Brønsted acid sites, Py^+-BAS) is located at 1550 cm^{-1}, whereas the band at 1450 cm^{-1} is related to the Py interaction with strong Lewis acid sites (Py-LAS). The quantitative evaluation of BAS and LAS is achievable, according to the Lambert−Beer law, by using one of the sets of experimental molar extinction coefficients available in the

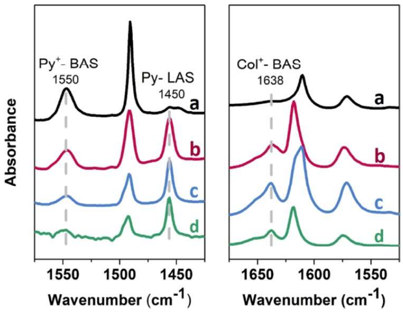

Figure 6. Left panel: IR spectra of pyridine adsorption on activated ZSM-5 (a), mM-Z1 (b), mM-Z2 (c), and Al-MCM-41 (d) after contact with the probe vapors at room temperature and following evacuation at 200 °C for 1 h. Right panel: IR spectra of collidine adsorption on activated ZSM-5 (a), mM-Z1 (b), mM-Z2 (c), and Al-MCM-41 (d) after contact with the probe vapor at room temperature. Spectra have been normalized to the Si−O stretching overtone modes and shifted on the *Y* axis for the safety of clarity.

literature[31] and employing the procedure reported in detail in ref 32. The results of the quantification procedure are summarized in Table 2. It should be kept in mind that this quantification method, closely related to empirical conditions, is liable to an intrinsic experimental error. This does not detract from the validity of the evaluation, if we consider it more than simply an absolute value, but a method of comparison between different samples, useful to evaluate the total acidity more in qualitative terms.

Table 2. Concentrations of BAS and LAS in mol/kg Calculated by In Situ IR Spectroscopy of Adsorbed Pyridine after 2 h of Outgassing at 200 °C[a]

sample name	BAS (mol/kg)	LAS (mol/kg)	total acid sites (mol/kg)
H-ZSM-5	1.099	0.149	1.248
H-mM-Z1	0.410	0.468	0.878
H-mM-Z2	0.142	0.495	0.637
H-Al-MCM-41	0.019	0.073	0.092

[a] The quantification has been carried out following the experimental procedure reported in ref 32 and the integrated molar extinction coefficients of ref 31.

The amount of BAS of the reference H-ZSM-5 significantly overcomes the one of the other materials, even if it contains the same concentration of aluminum atoms. The two H-mM-Z samples have a reasonable amount of BAS and at the same time, a not negligible concentration of LAS, comparable to that of H-Al-MCM-41 and ascribable to the presence of Al atoms in the trigonal coordination. The H-mM-Z1 sample, with a higher crystallinity degree, exhibits a relevant concentration of BAS, higher than that of LAS, as for the bulk H-ZSM-5. Contrarily, the less-crystalline H-mM-Z2 presents a higher concentration of LAS, almost twice the amount of BAS, with a similar trend to the reference H-Al-MCM-41.

It is worth noting the total amount of acidic sites follows the trend H-ZSM-5 > H-mM-Z1 > H-mM-Z2 > H-Al-MCM-41, exactly coincident with the crystallinity degree of the materials.

Dotted gray lines underline the vibrational band identifying the formation of the pyridinium ion (Py$^+$-BAS), pyridine interaction with acidic Lewis centers (Py-LAS), and collidinium ion formation (Col$^+$-BAS).

A step forward in the study of acid site speciation has been made using the sterically hindered 2,4,6-trimethyl pyridine (2,4,6-collidine, Col) as a molecular probe. The high proton affinity of this molecule (980 kJ/mol) allows the formation of collidinium ion in the presence of sites with Brønsted acid character (Col$^+$-BAS) but, due to the three substituents on the pyridine ring, its kinetic diameter (0.74 nm) exceeds the size of the narrow microchannels of the MFI zeolite.[58,59] It is thus possible to make a distinction between the acidic sites located on the outer surface of the material (which can interact with Col) and on the inner surface of the micropores, which is inaccessible to this sterically hindered probe molecule. The full spectrum of the three samples before and after contact with collidine vapors is shown in Figure S5. The interaction with Col causes a clear perturbation of the OH-stretching region (3800−3200 cm^{-1}) and the appearance of new absorption bands in the ring vibrational mode range (1700−1500 cm^{-1}). For what concerns H-ZSM-5, the band at 3747 cm^{-1}, ascribed to the isolated SiOH group, is completely consumed, whereas the component at 3610 cm^{-1}, due to bridged Si(OH)Al species, is substantially unperturbed. This is a clear indication of the location of the different OH groups. Indeed, if a silanol stretching band is affected by the adsorption of Col, it means that the species are located outside the microchannels. In parallel to the consumption of the band at 3747 cm^{-1}, a very broad envelope appears below 3650 cm^{-1}, produced by the H-bonding interactions of external SiOH and AlOH species with the probe molecule. In contrast, the band at 3610 cm^{-1} is still visible after Col contact (even if perturbed due to the superimposition with the broad bands produced by OH groups interacting by H-bonding with Col), indicating that the BAS are not accessible to the hindered molecule, because they are essentially located inside the MFI micropores. The region of Col ring vibrational modes is reported in Figure 6, right panel (curve a). The spectrum of Col vapors contacts with the H-ZSM-5 exhibits two main components, at 1619 and 1575 cm^{-1}, ascribable to Col interacting with isolated external OH species. Another weak signal is also present at 1638 cm^{-1}, suggesting that the collidinium ion forms to a very limited extent, due to the presence of a small fraction of Brønsted acid sites approachable by Col. This spectral behavior suggests these BAS are located at the micropore mouth, and so exposed to the external surface. Concerning the H-mM-Z samples (Figure 6 right panel, b and c curves), the component at 1638 cm^{-1} is more intense, suggesting that a significant amount of Col has been protonated by interaction with BAS. It means that a non-negligible amount of BAS is accessible to Col and, therefore, reasonably located at the micropore mouth. The interaction of Col with SiOH groups is well visible in both Figures S5 and 6 (right panel). The band at 3747 cm^{-1} is only partially eroded in the H-mM-Z samples, suggesting that a fraction of the silanols is not accessible to the bulky molecule. The not accessible SiOH species are associated with hydrogen-bonded silanol chains present in the defects (nanovoids generated by silicon vacancies) of the zeolitic framework and are absent in the reference H-ZSM-5. The presence of defectivity in both H-mM-Z samples reflects the difficulty of crystallization of these micro−mesostructures, with an evident perturbation of the long-range structural ordering of the zeolitic framework along the walls of the mesoporous channels. The use of size-selective probe molecules is particularly informative in the study of a hierarchical material, especially if coupled the use of a molecular probe with suitable dimensions to spread inside the micropores (namely CO at liquid nitrogen temperature).[60,61] Indeed, the consecutive adsorption of Col and CO helps to discriminate the fraction of sites not accessible to collidine, but available to interact with a probe that can easily enter the microchannels. For this reason, adsorption of Col vapors was preliminary carried out on the activated H-mM-Z2 sample, saturating all the accessible sites, then the adsorption/desorption of CO at liquid nitrogen temperature was performed according to the above-reported procedure (Figure S6). A comparison with Figure 6 (right panel) clearly highlights that the band at 2230 cm^{-1} (CO interacting with trigonal Al^{3+} species) is no more present, while the component at 2157 cm^{-1} (CO interacting with Si–OH groups) persists. The band ascribable to Si(OH)Al Brønsted acidic species at 2177 cm^{-1} is instead very weak and distinguishable at very low CO coverages. Summarizing, in hierarchical H-mM-Z materials, trigonal Al^{3+} species with Lewis acid character are not located inside the micropores, whereas just a small fraction of BAS is unavailable for collidine adsorption, indicating that these sites are almost completely concentrated in close proximity to the micropore mouths. This arrangement of the Brønsted acidic species further confirms the walls of the mesoporous channels are made of thin layers of the MFI framework, in which the periodicity of the zeolite is retained in one dimension.

3.4. Catalytic Hydroconversion of *n*-Decane. The analysis of the products of the hydroconversion reaction of a model long-chain *n*-alkane gives precious information about the location of active sites and about the inner space architecture of a zeolitic structure. To this purpose, the acidic zeolite was loaded with Pt particles (as reported in the Experimental Section) constituting a bifunctional catalyst. The catalytic hydroconversion involves two different types of active sites, the noble metal particles and the Brønsted acid. The reaction is initiated by the dehydrogenation of the alkane by the action of the noble metal functionality to form an alkene. The acidic Brønsted site can protonate the alkene forming an alkylcarbenium ion. The rearrangement of this cationic intermediate drives the generation of structural isomers passing by a cyclic iso-alkylcarbenium ion intermediate and then the cracked products can be generated by β-scission.[27] The shape selectivity of a zeolite drives the location of the positive charge along the linear chain and thus the positional selectivity of chain branching or breaking.[62] The steric limitations imposed by a zeolitic lattice, combined with the distribution of the active sites, stabilizes specific conformation of the alkylcarbenium ion intermediates, thus reflecting in the selectivity for specific isomers and cracked products. A list of specific criteria and the tabulation according to the opening diameter of the channels of the most common zeolite frameworks makes the "*n*-decane test" an easy-to-read tool for disclosing new structures and their modifications.[63−65] It was applied here to investigate the activity as well as the spatial constraints around the active sites contributing to the catalytic activity.

The *n*-decane conversion curves, as a function of the reaction temperature, are reported in Figure 7 (top panel) for all the samples. The *n*-decane conversion is complete at 170 °C over the reference H-ZSM-5 catalyst (curve a), whereas the hierarchical H-mM-Z samples need 230 °C (curves b and c). In contrast, the amorphous H-Al-MCM-41, even above 300 °C, is still not able to completely convert the feed hydrocarbon (curve d). The apparent activation energy values, computed from Arrhenius plots reported in Figure S7, exactly reflect the large differences between the samples in terms of activity (Table 3). The significantly higher activity of the commercial H-ZSM-5 sample must be attributed to the much higher concentration of active acid sites (as already discussed in the section dedicated to the IR study of pyridine adsorption) guaranteed by the bulk zeolitic structure, where the Brønsted acidic sites are located inside the extended microporous lattice. On the contrary, the hierarchical H-mM-Z samples present a lower concentration of BAS, compensating by a high amount of LAS and a high concentration of isolated and terminal silanols. The lower activity of these two samples is also related to the short extension of the crystalline MFI domains. The adsorption/diffusion processes, being part of the total catalytic process, are strongly influenced by the rigidity of the framework and by its extension. The more flexible (i.e., amorphous) a structure is, the less active it appears, because the adsorption/diffusion of the feed molecule is hindered. The same happens when the dimension of the crystals decreases. This consideration gains importance as the amorphous degree increases, as for the H-mM-Z2 sample compared to H-mM-Z1 and mostly to the bulk H-ZSM-5.

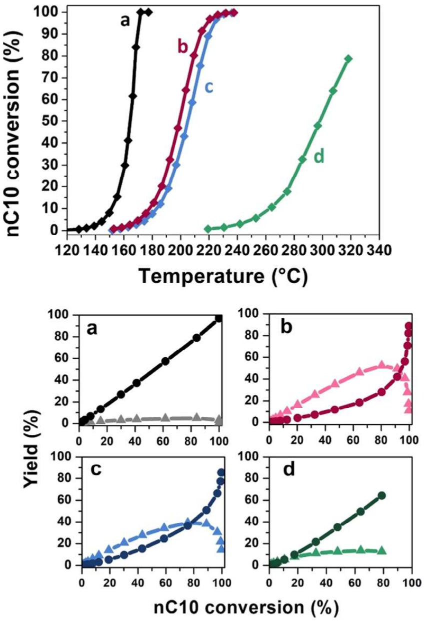

Figure 7. Top panel: Conversion curves of *n*-decane over commercial H-ZSM-5 (a), H-mM-Z1 (b), H-mM-Z2 (c), and H-Al-MCM-41 (d): the percentage of *n*-decane converted moles is reported as a function of increasing reaction temperature. Bottom panel: yields of skeletal isomers (light lines) and cracked products (dark lines) as a function of *n*-decane converted by commercial H-ZSM-5 (a), H-mM-Z1 (b), H-mM-Z2 (c), and H-Al-MCM-41 (d).

Figure 7 (bottom panel) shows the yield of products of *n*-decane hydroconversion over the different catalysts, divided over skeletal isomers and cracked products. The 10 membered ring (10MR) H-ZSM-5, with a limited internal space, prevents the formation of structural isomers and promotes the formation of shorter cracked products. This catalytic behavior

Table 3. List of the Main Products and Principal Parameters of the *n*-Decane Test

	H-ZSM-5	H-mM-Z1	H-mM-Z2	H-Al-MCM-41
apparent activation energy (kJ/mol)[a]	179	150	144	128
refined constraint index (CI°)[b]	4.66	3.25	4.03	1.66
ethyloctane (%) in monobranched isomers at 5% isomerization yield	3.16	0.21	0.18	9.57
propylheptane (%) in monobranched isomers at 5% isomerization yield	0.0	0.0	0.0	0.0
dibranched isomers (%) at maximum isomerization yield	21.05	14.58	17.58	12.48
amount of 2,7-DMC8 (%) in dibranched isodecanes at 5% of dibranching yield	21.21	15.50	18.90	5.77
C3−C7 (mol/100 mol C10 cracked) at 35% cracking yield	12.21	7.56	5.68	11.86
C4−C6 (mol/100 mol C10 cracked) at 35% cracking yield	6.11	3.70	2.50	4.44
C5 isomers (mol/100 mol cracked) at 35% cracking yield	11.82	21.33	21.51	1.36
dimensionality index (DI°)[c]	18.32	11.26	8.18	16.30

[a] Calculated using the Arrhenius equation $\ln k = -E_a/RT + \ln A$ from the plots reported in Figure S7. [b] Ratio of the yield of 2-methylnonane to 5-methylnonane at 5% isomerization yield. [c] Sum of the fractions (|C3−C7| + |C4−C6|) at 35% of cracking yield.

is visible in Figure 7 (bottom panel, section a), where the cracking yield (dark line) grows linearly starting from low conversion values, while the isomerization yield (light curve) is basically close to zero. In contrast, the H-mM-Z samples exhibit an opposite trend as reported in Figure 7 (bottom panel, sections b and c): the isomerization yields (light red and light blue curves) override the darkest curves due to cracking from the very early stages of the reaction and only when the conversion overcomes 75%, an inverse trend is observed. If the isomerization yield of reference H-ZSM-5 does not exceed 10%, it reaches 50 and 40% for H-mM-Z1 and H-mM-Z2, respectively. This behavior can be explained by the presence of mesopores, which allows the stabilization of cyclic transition states that lead to the isomerization of the chains. At the same time, thanks to mesoporous cavities, the branched chains can be easily expelled from the hierarchical framework as structural isomers, having a higher steric hindrance than linear substrate chains or cracked fractions. At high conversions, cracking products (a mixture of linear and branched molecules) prevail. The reference H-Al-MCM-41 sample has a totally different catalytic trend compared to the hierarchical materials, with a prevalence of linear cracked products. The occurrence of hydrogenolysis instead of hydrocracking, driven by the lower amount of Brønsted acid sites of the purely mesoporous samples, could explain the different product distribution of this material.

In 10-membered ring zeolites such as MFI, shape selectivity influences the composition of skeletal isomers from *n*-decane.[66,67] The distribution of main products is summarized in Table 3 and Figure S8 and described in detail in the Supporting Information. The selectivity of the catalysts is directly expressed by the calculated constraint index[65] CI° values, which are 3.25 for H-mM-Z1, 4.03 for H-mM-Z2, 4.66 for the commercial H-ZSM-5, and only 1.66 for H-Al-MCM-41. A CI° value close to 1 suggests the absence of shape selectivity (usually for the MFI, the CI° exceeds a value of 2.7). In contrast, the prevalence of isomerization to form 2-methylnonane proves the existence of a 10MR structure in the H-mM-Z samples and the PCP transition-state shape selectivity typical of the MFI topology. Another proof testifying the existence of the MFI framework in the H-mM-Z samples is the prevalence of the 2,7-methyloctane di-branched product. The branching occurring at the extremities of the chain is always induced by an acidic site located at the pore mouth, the only point within the MFI lattice, where there is enough space for hosting the cyclopropane intermediate. In this specific case, the isomerization is induced by the action of two sites lying in the mouth of very close pore openings, where the substrate chain can be positioned only in a key-lock configuration. The percentage of 2,7-dimethyloctane produced is reported in Table 3. From these results, it is possible to conclude that the H-mM-Z samples are shape selective and active thanks to acidic sites mainly located at the mouth of the MFI microchannels (as already proved by the in situ IR study of adsorbed collidine), working as the acidic sites of a bulk H-ZSM-5.

The analysis of individual cracked product fractions (grouped by the carbon atom number) offers other relevant information about the microporosity of the materials (Figure 8). The bifunctional mechanism of hydrocracking of *n*-alkanes involves a preferential *β*-scission of the alkylcarbenium ion intermediate, consecutively to branching steps. Short chains are preferentially produced by the narrow MFI framework, while if no geometrical restrictions exist (the zeolite Y case), the splitting occurs in the central position, giving rise mainly to the C5 chains. For ZSM-5, the distribution of cracked products

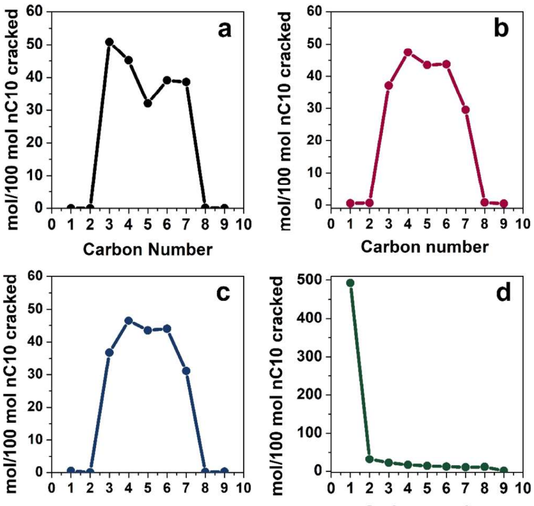

Figure 8. Distribution of *n*-decane cracked products per carbon number chain length, in the presence of commercial H-ZSM-5 (a), H-mM-Z1 (b), H-mM-Z2 (c), and H-AlMCM-41 (d). Products obtained at ca. 35% *n*-decane hydrocracking conversion.

displays a typical "M-shape", with a minimum for C5 products and two maxima positioned at C3−C7 or C4−C6 (depending on the specific sample), due to the preferential branching and cracking at the extremities of the C10 chains. A symmetrical "M shape" testifies the prevalence of primary cracking. Secondary cracking usually occurs in systems with narrow channels as MFI, whence the fragments escape after a long residence time. The sum of |C3−C7| + |C4−C6| molar yields defines the dimensionality index (DI°). The lower this index, the more symmetrical the "M curve" and the more primary cracking is favored. As reported in Figure 8, the reference H-ZSM-5 and both H-mM-Z samples exhibit a "M"-shaped curve, the fingerprint of the MFI topology. The cracked product distribution of H-ZSM-5 (Figure 8a) presents an absolute maximum for the C3 fragments, the shortest molecules that can be obtained via β-scission. Indeed, its high DI° value of 18.32 reveals the cracking is occurring in a constrained molecular environment.

On the other hand, H-mM-Z samples (Figure 8b,c) have a more symmetrical "M curve" (and lower DI° index), with a content of the C5 fraction higher than 40% and two maxima in correspondence of C4−C6 fractions. This trend suggests that cracking of the C10 chains occurs with less geometrical restrictions, due to the increased product diffusion favored by the mesoporous channels. This fact limits the secondary cracking and allows C10 skeletal isomers to be released before cracking. In contrast, H-Al-MCM-41 reference does not display any shape selectivity, with a complete conversion of the decane to methane (Figure 8d), reasonably produced by hydrogenolysis on Pt particles. If only primary cracking occurs, the total sum of the molar yields of each fraction of cracked products out of 100 mol of feed *n*-decane should sum up to 200 mol per 100 mol *n*-decane cracked. A deviation from this marker number stands for secondary cracking reactions. Figure S9 shows the trends for the different catalysts. Again, the results prove how the micropores exposing the acid sites and the large space offered by the mesoporous channels in H-mM-Z materials work together to achieve performances resembling a standard H-ZSM-5, but at the same time differing in terms of diffusivity and mass transport.

4. CONCLUSIONS

Two hierarchical structures were synthesized following the procedure reported by Ryoo and co-workers,[20] employing the dual-porogenic surfactant $C_{18}-N_3-C_{18}$ as the templating agent. After the replication and optimization of the synthetic strategy, an advanced and unique characterization approach was carried out, combining spectroscopic tools and targeted catalytic tests. These characterization techniques were the toolbox for disclosing the amount, location, and distribution of the active sites, in order to really understand how the multilevel porosity affects the catalytic activity and the shape-size selectivity.

By reproducing the synthesis procedure reported in the literature, it was found that the gel temperature during the aging phase considerably affects the final characteristics of the materials and, mainly, the level of crystallinity. Both materials possess an ordered mesostructure containing an ultramicroporous network exactly comparable in size to the microcavities of a standard ZSM-5; however, the extent of the microporous MFI domains is lower for the mM-Z2 sample. The acid sites were investigated by means of in situ IR spectroscopy with different molecular probes. The adsorption of CO proved the nature and the acid strength of the Brønsted sites were equivalent to those of a standard H-ZSM-5, whereas their concentration (quantified by pyridine adsorption) was significantly lower. In contrast to the standard zeolite, acidic sites with Lewis character were also detected in both hierarchical materials due to their intrinsic defectivity (the presence of Al^{3+} in partial framework positions), comparable to the reference Al-MCM-41. The final proof of the existence of a microporous MFI framework, really integrated with the ordered mesostructure, was obtained by the *n*-decane test.[68] The catalytic results proved the hierarchical samples exhibited a shape selectivity of a 10-membered ring lattice and the distribution of *n*-decane conversion products typical of a H-ZSM-5, operated by the action of Brønsted acid sites located at the mouth of the micropores. In addition, the transport and diffusion properties of products of micro−/meso- materials were superior to those of a standard bulk zeolite, due to the presence of the mesoporous network, which limits the secondary cracking and, at the same time, allows an easy release of the structural isomers. The evaluation of intermediates and products of the *n*-decane test unveiled the totally new shape-size selectivity determined by the interconnectivity of micropores and mesopores.

Surprisingly, these catalytic features were even more pronounced in the H-mM-Z2 sample than in H-mM-Z1, which instead possesses more extended MFI crystal domains. However, even if H-mM-Z2 is more similar to a standard ordered mesoporous silica, its catalytic behavior cannot be questioned, as highlighted by the total absence of activity and selectivity of the mesoporous H-Al-MCM-41 reference.

By merging the data of this advanced multitechnique characterization approach and comparing the results of the catalytic *n*-decane hydroconversion, performed on other hierarchical structures (such as two-dimensional MFI nanosheets),[69] we proved the hierarchical mM-Z samples are constituted by mesoporous channels with a hexagonal array, whose walls are made up of a thin layer of MFI domains, displaying almost all acidic sites at the micropore mouths, along the mesochannels' internal surface (totally accessible to bulky substrates, as testified by the easy adsorption of collidine).

For all these reasons, the structure of mM-Z can be effectively categorized in the definition of "reverse hierarchy" (a porous system, where a collection of small pores flows together into a larger pore to gain a faster outlet).[49] Finally, it is worth noting that the presence of more extended crystalline MFI domains in the mesopores' walls does not improve the catalytic performances in *n*-decane hydroconversion, but the synergy between the two different levels of porosity is responsible for the peculiar catalytic activity and shape selectivity of these hierarchical zeolites.

■ ASSOCIATED CONTENT

Supporting Information

The Supporting Information is available free of charge at https://pubs.acs.org/doi/10.1021/acsami.1c11614.

N_2 physisorption at liquid nitrogen temperature (cumulative pore volume distribution calculated using the NL-DFT model); transmission IR spectroscopy (IR spectra of the activated samples, IR spectra of the activated samples upon contact with CO, IR spectra of the activated samples upon contact with pyridine, IR spectra of the activated samples upon contact with collidine, and IR spectra of the activated samples upon contact with collidine and then with CO); *n*-decane hydroconversion (Arrhenius plots, *n*-decane monobranched isomers, and total amount of *n*-decane fractions per 100 mol of *n*-decane cracked) (PDF)

AUTHOR INFORMATION

Corresponding Author

Valentina Crocellà − *Department of Chemistry, NIS and INSTM Reference Centre, University of Turin, 10125 Turin, Italy*; orcid.org/0000-0002-3606-8424;
Email: velentina.crocella@unito.it

Authors

Alessia Airi − *Department of Chemistry, NIS and INSTM Reference Centre, University of Turin, 10125 Turin, Italy*; orcid.org/0000-0003-0206-4887

Matteo Signorile − *Department of Chemistry, NIS and INSTM Reference Centre, University of Turin, 10125 Turin, Italy*; orcid.org/0000-0003-0521-3702

Francesca Bonino − *Department of Chemistry, NIS and INSTM Reference Centre, University of Turin, 10125 Turin, Italy*; orcid.org/0000-0002-6822-6685

Pierluigi Quagliotto − *Department of Chemistry, NIS and INSTM Reference Centre, University of Turin, 10125 Turin, Italy*; orcid.org/0000-0002-7984-6839

Silvia Bordiga − *Department of Chemistry, NIS and INSTM Reference Centre, University of Turin, 10125 Turin, Italy*; orcid.org/0000-0003-2371-4156

Johan A. Martens − *Centre for Surface Chemistry and Catalysis, KU Leuven, B-3001 Leuven, Belgium*

Complete contact information is available at:
https://pubs.acs.org/10.1021/acsami.1c11614

Notes

The authors declare no competing financial interest.

ACKNOWLEDGMENTS

A.A. acknowledges the KU Leuven University for the financial support during her visiting period. Gina Vanbutsele is acknowledged for performing the catalytic testing. Prof. Guido Viscardi is acknowledged for his support in synthesizing the organic template and Dr. Maria Carmen Valsania for the TEM experiments.

REFERENCES

(1) Čejka, J.; Corma, A.; Zones, S. *Zeolites and Catalysis*; Wiley, 2010; Vol. *1*−*2*.

(2) Kulprathipanja, S. *Zeolites in Industrial Separation and Catalysis*; Wiley, 2010.

(3) Kresge, C. T.; Leonowicz, M. E.; Roth, W. J.; Vartuli, J. C.; Beck, J. S. Ordered Mesoporous Molecular Sieves Synthesized by a Liquid-Crystal Template Mechanism. *Nature* **1992**, *359*, 710−712.

(4) Zhao, D. Triblock Copolymer Syntheses of Mesoporous Silica with Periodic 50&Nbsp;to 300&Nbsp;Angstrom Pores. *Science* **1998**, *279*, 548−552.

(5) Kremer, S. P. B.; Kirschhock, C. E. A.; Aerts, A.; Aerts, C. A.; Houthoofd, K. J.; Grobet, P. J.; Jacobs, P. A.; Lebedev, O. I.; Van Tendeloo, G.; Martens, J. A. Zeotile-2: A Microporous Analogue of MCM-48. *Solid State Sci.* **2005**, *7*, 861−867.

(6) Vernimmen, J.; Meynen, V.; Cool, P. Synthesis and Catalytic Applications of Combined Zeolitic/Mesoporous Materials. *Beilstein J. Nanotechnol.* **2011**, *2*, 785−801.

(7) Möller, K.; Bein, T. Pores Within Pores—How to Craft Ordered Hierarchical Zeolites. *Science* **2011**, *333*, 297−298.

(8) Möller, K.; Bein, T. Mesoporosity − a New Dimension for Zeolites. *Chem. Soc. Rev.* **2013**, *42*, 3689−3707.

(9) Verboekend, D.; Pérez-Ramírez, J. Design of Hierarchical Zeolite Catalysts by Desilication. *Catal. Sci. Technol.* **2011**, *1*, 879−890.

(10) Milina, M.; Mitchell, S.; Crivelli, P.; Cooke, D.; Pérez-Ramírez, J. Mesopore Quality Determines the Lifetime of Hierarchically Structured Zeolite Catalysts. *Nat. Commun.* **2014**, *5*, 3922.

(11) Srivastava, R. Synthesis and Applications of Ordered and Disordered Mesoporous Zeolites: Present and Future Prospective. *Catal. Today* **2018**, *309*, 172−188.

(12) Wang, L.; Zhang, Z.; Yin, C.; Shan, Z.; Xiao, F.-S. Hierarchical Mesoporous Zeolites with Controllable Mesoporosity Templated from Cationic Polymers. *Microporous Mesoporous Mater.* **2010**, *131*, 58−67.

(13) Zhang, D.; Jin, C.; Zou, M.; Huang, S. Mesopore Engineering for Well-Defined Mesoporosity in Al-Rich Aluminosilicate Zeolites. *Chem.—Eur. J.* **2019**, *25*, 2675.

(14) Emdadi, L.; Wu, Y.; Zhu, G.; Chang, C.-C.; Fan, W.; Pham, T.; Lobo, R. F.; Liu, D. Dual Template Synthesis of Meso- and Microporous MFI Zeolite Nanosheet Assemblies with Tailored Activity in Catalytic Reactions. *Chem. Mater.* **2014**, *26*, 1345−1355.

(15) Schwieger, W.; Machoke, A. G.; Weissenberger, T.; Inayat, A.; Selvam, T.; Klumpp, M.; Inayat, A. Hierarchy Concepts: Classification and Preparation Strategies for Zeolite Containing Materials with Hierarchical Porosity. *Chem. Soc. Rev.* **2016**, *45*, 3353−3376.

(16) Sachse, A.; Grau-Atienza, A.; Jardim, E. O.; Linares, N.; Thommes, M.; García-Martínez, J. Development of Intracrystalline Mesoporosity in Zeolites through Surfactant-Templating. *Cryst. Growth Des.* **2017**, *17*, 4289−4305.

(17) Li, K.; Valla, J.; Garcia-Martinez, J. Realizing the Commercial Potential of Hierarchical Zeolites: New Opportunities in Catalytic Cracking. *ChemCatChem* **2014**, *6*, 46−66.

(18) Kenvin, J.; Mitchell, S.; Sterling, M.; Warringham, R.; Keller, T. C.; Crivelli, P.; Jagiello, J.; Pérez-Ramírez, J. Quantifying the Complex Pore Architecture of Hierarchical Faujasite Zeolites and the Impact on Diffusion. *Adv. Funct. Mater.* **2016**, *26*, 5621−5630.

(19) Mitchell, S.; Pinar, A. B.; Kenvin, J.; Crivelli, P.; Kärger, J.; Pérez-Ramírez, J. Structural Analysis of Hierarchically Organized Zeolites. *Nat. Commun.* **2015**, *6*, 8633.

(20) Na, K.; Jo, C.; Kim, J.; Cho, K.; Jung, J.; Seo, Y.; Messinger, R. J.; Chmelka, B. F.; Ryoo, R. Directing Zeolite Structures into Hierarchically Nanoporous Architectures. *Science* **2011**, *333*, 328−332.

(21) Fan, W.; Snyder, M. A.; Kumar, S.; Lee, P.-S.; Yoo, W. C.; McCormick, A. V.; Lee Penn, R.; Stein, A.; Tsapatsis, M. Hierarchical Nanofabrication of Microporous Crystals with Ordered Mesoporosity. *Nat. Mater.* **2008**, *7*, 984−991.

(22) Xiao, F.-S.; Wang, L.; Yin, C.; Lin, K.; Di, Y.; Li, J.; Xu, R.; Su, D. S.; Schlögl, R.; Yokoi, T.; Tatsumi, T. Catalytic Properties of Hierarchical Mesoporous Zeolites Templated with a Mixture of Small Organic Ammonium Salts and Mesoscale Cationic Polymers. *Angew. Chem.* **2006**, *118*, 3162−3165.

(23) Bordiga, S.; Lamberti, C.; Bonino, F.; Travert, A.; Thibault-Starzyk, F. Probing Zeolites by Vibrational Spectroscopies. *Chem. Soc. Rev.* **2015**, *44*, 7262−7341.

(24) Holm, M. S.; Svelle, S.; Joensen, F.; Beato, P.; Christensen, C. H.; Bordiga, S.; Bjørgen, M. Assessing the Acid Properties of Desilicated ZSM-5 by FTIR Using CO and 2,4,6-Trimethylpyridine (Collidine) as Molecular Probes. *Appl. Catal., A* **2009**, *356*, 23−30.

(25) Lønstad Bleken, B.-T.; Mino, L.; Giordanino, F.; Beato, P.; Svelle, S.; Lillerud, K. P.; Bordiga, S. Probing the Surface of Nanosheet H-ZSM-5 with FTIR Spectroscopy. *Phys. Chem. Chem. Phys.* **2013**, *15*, 13363.

(26) Tzoulaki, D.; Jentys, A.; Pérez-Ramírez, J.; Egeblad, K.; Lercher, J. A. On the Location, Strength and Accessibility of Bronsted Acid Sites in Hierarchical ZSM-5 Particles. *Catal. Today* **2012**, *198*, 3−11.

(27) Meng, L.; Vanbutsele, G.; Pestman, R.; Godin, A.; Romero, D. E.; van Hoof, A. J. F.; Gao, L.; Kimpel, T. F.; Chai, J.; Martens, J. A.; Hensen, E. J. M. Mechanistic Aspects of N-Paraffins Hydrocracking: Influence of Zeolite Morphology and Acidity of Pd(Pt)/ZSM-5 Catalysts. *J. Catal.* **2020**, *389*, 544−555.

(28) Vaschetto, E. G.; Monti, G. A.; Herrero, E. R.; Casuscelli, S. G.; Eimer, G. A. Influence of the Synthesis Conditions on the Physicochemical Properties and Acidity of Al-MCM-41 as Catalysts for the Cyclohexanone Oxime Rearrangement. *Appl. Catal., A* **2013**, *453*, 391−402.

(29) Zecchina, A.; Spoto, G.; Bordiga, S.; Padovan, M.; Leofanti, G.; Petrini, G. IR Spectra of CO Adsorbed at Low Temperature (77 K) on Titaniumsilicalite; H-ZSM5 and Silicalite. *Stud. Surf. Sci. Catal.* **1991**, *65*, 671−680.

(30) Datka, J. Acidic Properties of Supported Niobium Oxide Catalysts: An Infrared Spectroscopy Investigation. *J. Catal.* **1992**, *135*, 186−199.

(31) Nesterenko, N. S.; Thibault-Starzyk, F.; Montouilliout, V.; Yushchenko, V. V.; Fernandez, C.; Gilson, J.-P.; Fajula, F.; Ivanova, I. I. The Use of the Consecutive Adsorption of Pyridine Bases and Carbon Monoxide in the IR Spectroscopic Study of the Accessibility of Acid Sites in Microporous/Mesoporous Materials. *Kinet. Catal.* **2006**, *47*, 40−48.

(32) Grahn, M.; Faisal, A.; Öhrman, O. G. W.; Zhou, M.; Signorile, M.; Crocellà, V.; Nabavi, M. S.; Hedlund, J. Small ZSM-5 Crystals with Low Defect Density as an Effective Catalyst for Conversion of Methanol to Hydrocarbons. *Catal. Today* **2020**, *345*, 136−146.

(33) Signorile, M.; Crocellà, V.; Damin, A.; Rossi, B.; Lamberti, C.; Bonino, F.; Bordiga, S. Effect of Ti Speciation on Catalytic Performance of TS-1 in the Hydrogen Peroxide to Propylene Oxide Reaction. *J. Phys. Chem. C* **2018**, *122*, 9021−9034.

(34) Signorile, M.; Bonino, F.; Damin, A.; Bordiga, S. A Novel Raman Setup Based on Magnetic-Driven Rotation of Sample. *Top. Catal.* **2018**, *61*, 1491−1498.

(35) Huybrechts, W.; Mijoin, J.; Jacobs, P. A.; Martens, J. A. Development of a Fixed-Bed Continuous-Flow High-Throughput Reactor for Long-Chain n-Alkane Hydroconversion. *Appl. Catal., A* **2003**, *243*, 1−13.

(36) Anunziata, O. A.; Beltramone, A. R.; Cussa, J. Synthesis at Atmospheric Pressure and Characterization of Highly Ordered Al, V, and Ti-MCM-41 Mesostructured Catalysts. *Catal. Today* **2008**, *133–135*, 891−896.

(37) Astorino, E.; Peri, J. B.; Willey, R. J.; Busca, G. Spectroscopic Characterization of Silicalite-1 and Titanium Silicalite-1. *J. Catal.* **1995**, *157*, 482−500.

(38) Armaroli, T.; Simon, L. J.; Digne, M.; Montanari, T.; Bevilacqua, M.; Valtchev, V.; Patarin, J.; Busca, G. Effects of Crystal Size and Si/Al Ratio on the Surface Properties of H-ZSM-5 Zeolites. *Appl. Catal., A* **2006**, *306*, 78−84.

(39) Armaroli, T.; Trombetta, M.; Gutièrrez Alejandre, A.; Ramirez Solis, J.; Busca, G. FTIR Study of the Interaction of Some Branched Aliphatic Molecules with the External and Internal Sites of H-ZSM5 Zeolite. *Phys. Chem. Chem. Phys.* **2000**, *2*, 3341−3348.

(40) Coudurier, G. l.; Naccache, C.; Vedrine, J. C. Uses of i.r. Spectroscopy in Identifying ZSM Zeolite Structure. *J. Chem. Soc., Chem. Commun.* **1982**, *24*, 1413.

(41) Lesthaeghe, D.; Vansteenkiste, P.; Verstraelen, T.; Ghysels, A.; Kirschhock, C. E. A.; Martens, J. A.; Speybroeck, V. V.; Waroquier, M. MFI Fingerprint: How Pentasil-Induced IR Bands Shift during Zeolite Nanogrowth. *J. Phys. Chem. C* **2008**, *112*, 9186−9191.

(42) Dutta, P. K.; Rao, K. M.; Park, J. Y. Correlation of Raman Spectra of Zeolites with Framework Architecture. *J. Phys. Chem.* **1991**, *95*, 6654−6656.

(43) Scarano, D.; Zecchina, A.; Bordiga, S.; Geobaldo, F.; Spoto, G.; Petrini, G.; Leofanti, G.; Padovan, M.; Tozzola, G. Fourier-Transform Infrared and Raman Spectra of Pure and Al-, B-, Ti- and Fe-Substituted Silicalites: Stretching-Mode Region. *J. Chem. Soc., Faraday Trans.* **1993**, *89*, 4123.

(44) Landers, J.; Gor, G. Y.; Neimark, A. V. Density Functional Theory Methods for Characterization of Porous Materials. *Colloids Surf., A* **2013**, *437*, 3−32.

(45) Thommes, M.; Kaneko, K.; Neimark, A. V.; Olivier, J. P.; Rodriguez-Reinoso, F.; Rouquerol, J.; Sing, K. S. W. Physisorption of Gases, with Special Reference to the Evaluation of Surface Area and Pore Size Distribution (IUPAC Technical Report). *Pure Appl. Chem.* **2015**, *87*, 1051−1069.

(46) Corma, A.; Kan, Q.; Navarro, M. T.; Pérez-Pariente, J.; Rey, F. Synthesis of MCM-41 with Different Pore Diameters without Addition of Auxiliary Organics. *Chem. Mater.* **1997**, *9*, 2123−2126.

(47) Adjdir, M.; Ali-Dahmane, T.; Weidler, P. G. The Structural Comparison between Al-MCM-41 and B-MCM-41. *C. R. Chim.* **2009**, *12*, 793−800.

(48) La-Salvia, N.; Lovón-Quintana, J. J.; Lovón, A. S. P.; Valença, G. P. Influence of Aluminum Addition in the Framework of MCM-41 Mesoporous Molecular Sieve Synthesized by Non-Hydrothermal Method in an Alkali-Free System. *Mater. Res.* **2017**, *20*, 1461−1469.

(49) Cychosz, K. A.; Guillet-Nicolas, R.; García-Martínez, J.; Thommes, M. Recent Advances in the Textural Characterization of Hierarchically Structured Nanoporous Materials. *Chem. Soc. Rev.* **2017**, *46*, 389−414.

(50) Coasne, B. Multiscale Adsorption and Transport in Hierarchical Porous Materials. *New J. Chem.* **2016**, *40*, 4078−4094.

(51) Matsumoto, A.; Chen, H.; Tsutsumi, K.; Grün, M.; Unger, K. Novel Route in the Synthesis of MCM-41 Containing Framework Aluminum and Its Characterization. *Microporous Mesoporous Mater.* **1999**, *32*, 55−62.

(52) Thibault-Starzyk, F.; Stan, I.; Abelló, S.; Bonilla, A.; Thomas, K.; Fernandez, C.; Gilson, J.-P.; Pérez-Ramírez, J. Quantification of Enhanced Acid Site Accessibility in Hierarchical Zeolites − The Accessibility Index. *J. Catal.* **2009**, *264*, 11−14.

(53) Busca, G. Acidity and Basicity of Zeolites: A Fundamental Approach. *Microporous Mesoporous Mater.* **2017**, *254*, 3−16.

(54) Zecchina, A.; Spoto, G.; Bordiga, S. Probing the Acid Sites in Confined Spaces of Microporous Materials by Vibrational Spectroscopy. *Phys. Chem. Chem. Phys.* **2005**, *7*, 1627.

(55) Busco, C.; Barbaglia, A.; Broyer, M.; Bolis, V.; Foddanu, G. M.; Ugliengo, P. Characterisation of Lewis and Brønsted Acidic Sites in H-MFI and H-BEA Zeolites: A Thermodynamic and Ab Initio Study. *Thermochim. Acta* **2004**, *418*, 3−9.

(56) Busco, C.; Bolis, V.; Ugliengo, P. Masked Lewis Sites in Proton-Exchanged Zeolites: A Computational and Microcalorimetric Investigation. *J. Phys. Chem. C* **2007**, *111*, 5561−5567.

(57) Buzzoni, R.; Bordiga, S.; Ricchiardi, G.; Lamberti, C.; Zecchina, A.; Bellussi, G. Interaction of Pyridine with Acidic (H-ZSM5, H-β, H-MORD Zeolites) and Superacidic (H-Nafion Membrane) Systems: An IR Investigation. *Langmuir* **1996**, *12*, 930−940.

(58) Erigoni, A.; Newland, S. H.; Paul, G.; Marchese, L.; Raja, R.; Gianotti, E. Creating Accessible Active Sites in Hierarchical MFI Zeolites for Low-Temperature Acid Catalysis. *ChemCatChem* **2016**, *8*, 3161−3169.

(59) Mlekodaj, K.; Tarach, K.; Datka, J.; Góra-Marek, K.; Makowski, W. Porosity and Accessibility of Acid Sites in Desilicated ZSM-5 Zeolites Studied Using Adsorption of Probe Molecules. *Microporous Mesoporous Mater.* **2014**, *183*, 54−61.

(60) Bleken, B.-T. L.; Wragg, D. S.; Arstad, B.; Gunnæs, A. E.; Mouzon, J.; Helveg, S.; Lundegaard, L. F.; Beato, P.; Bordiga, S.; Olsbye, U.; Svelle, S.; Lillerud, K. P. Unit Cell Thick Nanosheets of Zeolite H-ZSM-5: Structure and Activity. *Top. Catal.* **2013**, *56*, 558−566.

(61) Skorpa, R.; Bordiga, S.; Bleken, F.; Olsbye, U.; Arstad, B.; Tolchard, J.; Mathisen, K.; Svelle, S.; Bjørgen, M. Assessing the Surface Sites of the Large Pore 3-Dimensional Microporous Material H-ITQ-7 Using FT-IR Spectroscopy and Molecular Probes. *Microporous Mesoporous Mater.* **2011**, *141*, 146−156.

(62) Corma, A.; Miguel, P. J.; Orchille's, A. V. Influence of Hydrocarbon Chain Length and Zeolite Structure on the Catalyst

Activity and Deactivation for N-Alkanes Cracking. *Appl. Catal., A* **1994**, *117*, 29−40.

(63) Martens, J. A.; Tielen, M.; Jacobs, P. A.; Weitkamp, J. Estimation of the Void Structure and Pore Dimensions of Molecular Sieve Zeolites Using the Hydroconversion of N-Decane. *Zeolites* **1984**, *4*, 98−107.

(64) Jacobs, P. A.; Martens, J. A. Exploration of the Void Size and Structure of Zeolites and Molecular Sieves Using Chemical Reactions. *Pure Appl. Chem.* **1986**, *58*, 1329−1338.

(65) Martens, J. A.; Jacobs, P. A. The Potential and Limitations of the N-Decane Hydroconversion as a Test Reaction for Characterization of the Void Space of Molecular Sieve Zeolites. *Zeolites* **1986**, *6*, 334−348.

(66) Martens, J. A.; Parton, R.; Uytterhoeven, L.; Jacobs, P. A.; Froment, G. F. Selective Conversion of Decane into Branched Isomers. *Appl. Catal.* **1991**, *76*, 95−116.

(67) Souverijns, W.; Verrelst, W.; Vanbutsele, G.; Martens, J. A.; Jacobs, P. A. Micropore Structure of Zeolite MCM-22 as Determined by the Decane Catalytic Test Reaction. *J. Chem. Soc., Chem. Commun.* **1994**, *14*, 1671.

(68) Reichinger, M.; Schmidt, W.; Berg, M. W. E. v. d.; Aerts, A.; Martens, J. A.; Kirschhock, C. E. A.; Gies, H.; Grünert, W. Alkene Epoxidation with Mesoporous Materials Assembled from TS-1 Seeds − Is There a Hierarchical Pore System ? *J. Catal.* **2010**, *269*, 367−375.

(69) Verheyen, E.; Jo, C.; Kurttepeli, M.; Vanbutsele, G.; Gobechiya, E.; Korányi, T. I.; Bals, S.; Van Tendeloo, G.; Ryoo, R.; Kirschhock, C. E. A.; Martens, J. A. Molecular Shape-Selectivity of MFI Zeolite Nanosheets in n-Decane Isomerization and Hydrocracking. *J. Catal.* **2013**, *300*, 70−80.

ACS Catalysis

pubs.acs.org/acscatalysis

Research Article

MAPO-18 Catalysts for the Methanol to Olefins Process: Influence of Catalyst Acidity in a High-Pressure Syngas (CO and H_2) Environment

Jingxiu Xie, Daniel S. Firth, Tomás Cordero-Lanzac, Alessia Airi, Chiara Negri, Sigurd Øien-Ødegaard, Karl Petter Lillerud, Silvia Bordiga, and Unni Olsbye*

Cite This: ACS Catal. 2022, 12, 1520−1531

Read Online

ACCESS | Metrics & More | Article Recommendations | Supporting Information

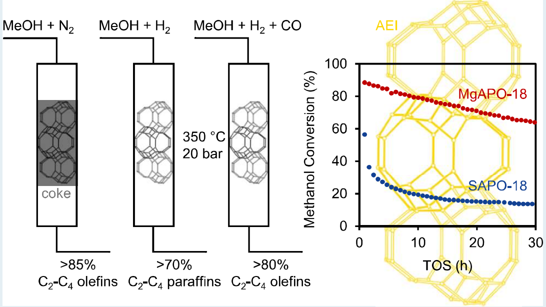

ABSTRACT: The transition from integrated petrochemical complexes toward decentralized chemical plants utilizing distributed feedstocks calls for simpler downstream unit operations. Less separation steps are attractive for future scenarios and provide an opportunity to design the next-generation catalysts, which function efficiently with effluent reactant mixtures. The methanol to olefins (MTO) reaction constitutes the second step in the conversion of CO_2, CO, and H_2 to light olefins. We present a series of isomorphically substituted zeotype catalysts with the AEI topology (MAPO-18s, M = Si, Mg, Co, or Zn) and demonstrate the superior performance of the M(II)-substituted MAPO-18s in the conversion of MTO when tested at 350 °C and 20 bar with reactive feed mixtures consisting of $CH_3OH/CO/CO_2/H_2$. Co-feeding high pressure H_2 with methanol improved the catalyst activity over time, but simultaneously led to the hydrogenation of olefins (olefin/paraffin ratio < 0.5). Co-feeding $H_2/CO/CO_2/N_2$ mixtures with methanol revealed an important, hitherto undisclosed effect of CO in hindering the hydrogenation of olefins over the Brønsted acid sites (BAS). This effect was confirmed by dedicated ethene hydrogenation studies in the absence and presence of CO co-feed. Assisted by spectroscopic investigations, we ascribe the favorable performance of M(II)APO-18 under co-feed conditions to the importance of the M(II) heteroatom in altering the polarity of the M−O bond, leading to stronger BAS. Comparing SAPO-18 and MgAPO-18 with BAS concentrations ranging between 0.2 and 0.4 mmol/g_{cat}, the strength of the acidic site and not the density was found to be the main activity descriptor. MgAPO-18 yielded the highest activity and stability upon syngas co-feeding with methanol, demonstrating its potential to be a next-generation MTO catalyst.

KEYWORDS: *methanol-to-hydrocarbons, methanol to olefins, zeolites, SAPO, synthesis gas, alkene hydrogenation, lifetime*

INTRODUCTION

The conversion of methanol to olefins (MTO) using zeolite/zeotype catalysts provides a viable key step to the production of chemicals from alternative carbon raw materials, including natural gas, CO_2, biomass, and municipal waste.[1,2] The industrial process typically operates at 350−500 °C and 1 bar, using SAPO-34 (12-/8-ring CHA topology) and ZSM-5 (10-ring MFI topology) catalysts.[3−5] High selectivity toward C_2−C_4 olefins achieved with SAPO-34 is due to its topology which limits product effusion to molecules smaller than 3.8 Å.[6] On the other hand, high selectivity toward propene is attained with ZSM-5 by the recycling of products and operation at higher temperatures (>500 °C) to facilitate the cracking of the hydrocarbon products.[3] On the molecular scale, MTO product distribution is governed by a delicate balance between relative diffusivities, competitive adsorption, and reaction on the internal surface of the microporous catalysts.[7] The reaction path is dominated by the dual-cycle mechanism (Figure S1), in which alkenes and arenes [the hydrocarbon (HC) pool species] are methylated and subsequently cracked or dealkylated to form light olefins.[3,8−10] The cycles are connected through hydrogen transfer reactions, that are also core to HC pool initiation by first C−C bond formation, as well as deactivation by coke formation.[1,11−13] In addition to the zeolite/zeotype topology,[14−17] the number/strength/distribution of acidic sites,[18−21] lattice defects, and crystal size/morphology influence MTO catalyst performance.[22−24] Reaction conditions such as temperature, methanol partial pressure, and contact time[25,26] are also paramount to optimal catalyst performance.

Received: October 12, 2021
Revised: December 12, 2021

https://doi.org/10.1021/acscatal.1c04694
ACS Catal. 2022, 12, 1520−1531

Recent breakthroughs on the MTO process focuses on high reaction pressures, for example >20 bar with H_2 co-feeding, due to the development of tandem processes to directly convert $CO/CO_2/H_2$ feed to lower olefins *via* methanol.[27−31] Bhan and co-workers demonstrated that co-feeding H_2 at high pressures (400 °C, 4−30 bar P_{H2}, and 0.13 bar P_{MeOH}) over SAPO-34 mitigated catalyst deactivation without significantly decreasing selectivity toward lower olefins.[32] They extended this strategy to other zeolites with CHA, AEI, FER, and BEA topology and isostructural SAPO-34 and SSZ-13.[33,34] Upon H_2 co-feeding, the more acidic SSZ-13 not only had a longer lifetime than SAPO-34 but also higher selectivities toward methane and paraffins. The hydrogenation of coke precursors including formaldehyde and 1,3-butadiene was concluded to suppress the production of deactivation-inducing polycyclics thereby improving the catalyst lifetime. Independently, the group of Liu arrived at a similar strategy to prolong the lifetime of SAPO-34 (425 °C, 40 bar, and $H_2/MeOH/H_2O$ = 6/1/5.33) and highlighted the synergistic effect of co-feeding H_2 and H_2O at high pressures.[35] They showed that co-feeding H_2 with methanol led to a longer lifetime but an obvious decrease in selectivity toward lower olefins. Hence, co-feeding H_2 and H_2O was required to improve the stability and maintain olefins selectivity. Unfortunately, high pressure steam addition simultaneously led to SAPO-34 structural damage.[35] Clearly, challenges remain in bridging the gaps between the current and future MTO process conditions.

In this contribution, we study zeotype acidity in the presence of high $CO/CO_2/H_2/N_2$ co-feed partial pressures, for a next-generation MTO process. We focus on the AEI topology due to its high propene selectivity[17] and vary acidity by heteroatom M substitution of Si, Mg, Co, and Zn and by M/Al elemental ratio.[36−38] SAPO-18 expectedly outperformed the M(II)APO-18s under typical MTO conditions of 350 °C and 1 bar, methanol in N_2 feed, but the M(II)APO-18s achieved 2−3 times higher propene yield than SAPO-18 at 350 °C, 20 bar, and methanol in syngas feed. The superior catalytic stability of the more acidic MgAPO-18s [Brønsted acid sites, (BAS) = 0.2 to 0.4 mmol/g_{cat}] originated from the acid site strength and not density, thus revealing their potential as next-generation MTO catalysts. We also emphasize the role of CO co-feeding. Beyond prior studies, which showed the role of CO in direct C−C bond formation in MTO,[39−44] CO is here proven to prevent the hydrogenation of lower olefins.

EXPERIMENTAL METHODS

Synthesis of MAPO-18 Catalysts. All catalysts were prepared *via* hydrothermal synthesis using the same organic structure-directing agent, *N*,*N*-diisopropylethylamine (DIPEA, ≥99%, Sigma-Aldrich).[45] The other chemicals were alumina [AlO(OH), Pural, Sasol], orthophosphoric acid (85 % wt. H_3PO_4 in H_2O, Sigma-Aldrich), colloidal silica (40 % wt. SiO_2 suspension in H_2O, Ludox AS-40, Sigma-Aldrich), magnesium acetate tetrahydrate [$(CH_3COO)_2Mg\cdot 4H_2O$, ≥98%, Sigma-Aldrich], cobalt(II) acetate tetrahydrate [$(CH_3COO)_2Co\cdot 4H_2O$, ≥98%, Sigma-Aldrich], zinc acetate dihydrate [$(CH_3COO)_2Zn\cdot 2H_2O$, ≥98%, Sigma-Aldrich] and deionized water. SAPO-18 was synthesized with a gel composition of $AlO(OH)/SiO_2/H_3PO_4/DIPEA/H_2O$ = 1/0.1/0.9/0.95/9.5 as described previously and is referred to as SAPO-18.[23] SAPO-18a-d was synthesized by varying Si/T atomic composition in the synthesis gels. The P source, H_2O, and DIPEA were first mixed together. Pural was subsequently added slowly with stirring for 5 min, and Ludox was finally added. The synthesis gel was left to stir for 20 min to ensure homogeneity. The gel was transferred to a Teflon-lined stainless-steel autoclave and heated at 190 °C under rotation for 12 h. MAPO-18 (where M refers to Mg, Co, or Zn) catalysts were synthesized with identical gel compositions of $AlO(OH)/(CH_3COO)_2M/H_3PO_4/DIPEA/H_2O$ = 1/0.1/0.9/0.95/19. MgAPO-18a-c catalysts were prepared with the same M/T atomic composition in the synthesis gels as SAPO-18a-c. The metal acetate precursor was first dissolved in minimal amount of H_2O. The P source, H_2O, and DIPEA were then mixed together. Pural was subsequently added slowly with stirring for 5 min, and M acetate precursor solution was finally added. The synthesis gel was left to stir for 20 min to ensure homogeneity. The gel was transferred to a Teflon-lined stainless-steel autoclave (∼50% filled) and heated at 160 °C under rotation for 8 days. All products were washed and centrifuged three times with deionized water and dried at 100 °C for 18 h. Calcination was performed at 550 °C (3 °C/min) under static air condition for 4 h.

Catalyst Characterization. The powder X-ray diffraction (PXRD) patterns of the as-synthesized and calcined catalysts were measured using a Siemens Bruker D8 Discover instrument with Bragg−Brentano geometry by using Cu K_α radiation (λ = 1.5406 Å). Samples were mounted on flat sample holders and measured in the reflectance mode with Bragg−Brentano geometry. All patterns were fitted using TOPAS6. Rietveld fittings were performed using previously published crystal structures of AlPO-18, both containing OSDA and calcined catalysts.[46] Peaks belonging to CHA impurities, both CHA intergrowths and separate phases, were fitted qualitatively by the Pawley method. Due to the high degree of disorder in the materials, quantification of these intergrowths was not attempted. The size and morphology of the calcined zeotype particles were analyzed by scanning electron microscopy (SEM), recorded with a Hitachi SU 8230 field emission scanning electron microscope. The elemental composition was determined utilizing energy-dispersive X-ray spectroscopy (EDS) attached to the same instrument. N_2 physisorption was carried out at 77 K by using a BELSORP-mini II equipment to determine the Brunauer−Emmett−Teller (BET) surface areas and pore volumes. Calcined catalysts were outgassed under vacuum for 4 h, 0.5 h at 80 °C, followed by a period of 3 h at 300 °C. The BET surface areas were determined on the basis of a linear fit of the data in the relative pressure (p/p_0) range of 0.005−0.05. Temperature-programmed desorption of *n*-propylamine was performed at atmospheric pressure in a fixed-bed glass reactor (inner diameter, 11 mm), similar to the procedure described previously.[47] Calcined catalysts (250−420 μm) were pretreated at 550 °C under flowing air condition. The catalyst was then cooled to 130 °C, after which 80 mL/min N_2 bubbled through a saturator containing *n*-propylamine at room temperature was then fed to the catalyst for 30 min. The excess amount of *n*-propylamine was removed by flowing 80 mL/min N_2 for 4 h at 130 °C. The temperature was then increased to 550 °C (20 °C/min) and the amount of propene desorbed was quantified by using an online Pfeiffer Omnistar quadrupole mass spectrometer. Fourier-transform infrared (FTIR) spectroscopy was performed in the transmission mode using a Bruker Vertex 70 spectrophotometer (resolution: 2 cm^{-1}; cryodetector: MCT) collecting 32 scans for each spectrum. An aliquot of each MAPO-18 catalyst was pressed in

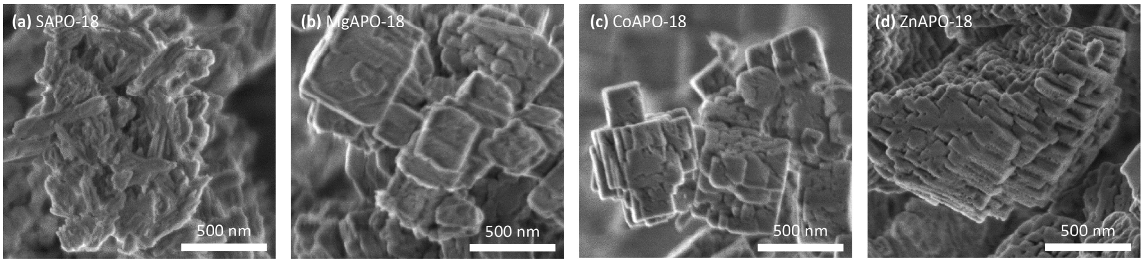

Figure 1. SEM images of calcined MAPO-18s. (a) SAPO-18, (b) MgAPO-18, (c) CoAPO-18, and (d) ZnAPO-18.

a self-supporting pellet enveloped in a pure gold cover and placed in a home-made quartz cell equipped with KBr windows designed to carry out spectroscopic measurements at *ca.* 77 K. The cell was connected to a vacuum line (residual pressure: 1×10^{-4} mbar) allowing for the thermal treatment and adsorption experiments to be carried out *in situ*. All the investigated samples were activated under dynamic vacuum at 400 °C for 90 min before each experiment. CO was dosed *in situ* and then adsorbed by cooling the system to 77 K using liquid N_2.

Catalytic Tests at 1 bar. The ambient pressure MTH test rig was described previously.[36] The quantity of calcined catalyst loaded (250−420 μm) was varied depending on the reaction temperature. 100 mg of MAPO-18 was loaded in a fixed-bed U-shaped quartz reactor and heated to 550 °C (5 °C/min) in synthetic air feed (N_2/O_2 = 80/20 %v and 25 mL/min). At 550 °C, the synthetic air feed was switched to 100 % v O_2 feed for 1 h, after which the temperature was decreased to the reaction temperature of 350 °C (2 °C/min) in 100 % v N_2 feed. During the reaction, methanol was fed to the reactor by bubbling He through a saturator at 20 °C, resulting in a methanol partial pressure of 0.13 bar and WHSV of 4 g_{MeOH} g_{cat}^{-1} h^{-1}. The total feed flow was 40 mL/min. The effluent from the reactor was analyzed using an online gas chromatography−mass spectrometry (GC−MS) instrument (Agilent 7890 with flame ionization detector and 5975C MS detector) equipped with two Restek Rtx-DHA-150 columns. Hydrogen (Praxair, purity 6.0) was used as the carrier gas. Both methanol and dimethyl ether were considered to be reactants when calculating the conversion for activity. Product selectivity was determined based on carbon atoms measured by the FID detector.

Catalytic Tests at 20 bar. Methanol conversion over the MAPO-18s at 20 bar in various reactive feeds was investigated using a commercial Microactivity Effi test rig from PID Eng & Tech. Blank reactor tests were also performed and they showed no reactivity of methanol or CO/CO_2. 400 mg of calcined MAPO-18 (250−420 μm) was loaded in a silicon-coated (Silcolloy coating from SilcoTek) stainless-steel reactor with an inner diameter of 6 mm. The catalyst bed (isothermal zone of 5 cm) was supported by glass wool placed above 5 mm glass beads, and a thermocouple (Type K) was inserted in the catalyst bed. The catalyst was heated to the reaction temperature of 350 °C (5 °C/min) at 1 bar in 100 % v inert feed (N_2 and Ar) for 1 h. No significant differences in performance at typical MTO conditions were observed with the two activation protocols (350 °C in inert atmosphere *vs* 550 °C in air). The feed flow was then switched to bypass the reactor for 4 h so as to obtain a stable methanol feed flow. N_2 was used to pressurize the methanol liquid feed tank and line, and methanol liquid feed flow was controlled with a CORI-FLOW controller (Bronkhorst). Methanol was evaporated in the hot box at 140 °C and swept by the flowing gas stream. Methanol feed flow was 1 g/h, and internal standard Ar feed flow was 7 mLn/min. Individual gas mass flow controllers (Bronkhorst) were used to set the flow rate for each gas, namely CO_2, CO, H_2, N_2, and Ar, and the gases were mixed before the methanol feed line. Total feed flow was 220 to 230 mLn/min, resulting in a GHSV of 16 000 h^{-1}. The reaction pressure of 20 bar within the reactor was controlled by a back pressure regulator and this is a PID Eng & Tech patented system based on a high-speed precision servo-controlled valve (VMM01) with eight turns of rotational movement. The product stream was connected to the vent and the online gas chromatograph (Scion 456-GC). The gas chromatograph was equipped with 1 TCD and 2 FID detectors and six columns (MolSieve 13X, HayeSep Q, HayeSep N, Rt-Stabilwax, Rt-Alumina/MAPD, and Rtx-1). Helium was used as the carrier gas.

The same equipment was used for ethene hydrogenation control experiments performed at 10 bar under N_2 and CO flows. Blank tests were also carried out and, in these cases, small conversions of *ca.* 4.5 and 2.3%, respectively, were observed. This was caused by the thermal reaction over steel tubing, reactor, and inner lines of the gas chromatograph. These values were subtracted from the shown results that only represent hydrogenation due to the acidic sites of the zeotype. 320 mg of SAPO-18 was loaded in the same reactor and subjected to the same pretreatment at 350 °C in inert atmosphere for 1 h. The reactor was then pressurized whereas the reactants mix (now 205 mLn/min, aiming at 0.25 bar C_2 and H_2/N_2, or CO ratio of 3) was flowed through the bypass line for stabilization. The experiments were performed at low C_2 partial pressure and GHSV of 18 500 h^{-1} to avoid oligomerization reactions. The carbon balance was closed at 99.5% with ethene and ethane, suggesting that the only reaction taking place was hydrogenation.

Computational Details. Structures were optimized and properties calculated with the program Dmol3 as implemented in BIOVIA Materials Studio 2020. The calculations were done on periodic models based on one unit cell of the AlPO-18 structure with either one phosphorous replaced by a silicon or one aluminum replaced by magnesium. The unit cell composition is $MgAl_{23}P_{24}O_{96}H$ or $SiAl_{24}P_{23}O_{96}H$ and the adsorbed molecule C_2H_4 comes in addition. The optimizations were first calculated with the simple LDA-PWC functional with coarse convergence criteria. The optimized geometries were then optimized further with the m-GGA-M06-L functional with medium convergence criteria.[48,49] Electron density and electrostatics were calculated and are the basis for the electron

Table 1. Textural and Acidic Properties of the MAPO-18 Catalysts

	crystal shape[a]	crystal size (μm)[a]	S_{BET} (m^2/g)[b]	V_{micr} (cm^3/g)[b]	S_{ext} (m^2/g)	elemental composition[c]			density of M (mmol/g_{cat})[c]	Brønsted acidity (mmol/g_{cat})[d]
						P/Al	M/Al	M/(Al + P)		
SAPO-18	rods	~0.5	750	0.26	86	1.0	0.12	0.06	0.61	0.29
MgAPO-18	cubes	~0.5	730	0.25	92	1.1	0.12	0.05	0.55	0.17
CoAPO-18	cubes	≤0.5	639	0.22	90	1.0	0.16	0.08	0.78	0.27
ZnAPO-18	irregular	~1.0	96	0.01	68	1.1	0.14	0.07	0.66	0.04

[a] Properties determined using SEM. [b] N_2 physisorption using the BET method. [c] SEM−EDS. [d] Propylamine-TPD.

isosurface with charge distribution visualized by spectral colors, blue negative and red positive. The isosurface value used for Figure 5c,d is 0.2. Coordinates for the optimized geometries in Figure 3 are reported in Supporting Information, Section 4.

RESULTS AND DISCUSSION

Catalysts. The MAPO-18s were prepared *via* hydrothermal synthesis using DIPEA as the structure-directing agent.[45] Crystal sizes and morphologies of the calcined zeotypes were determined using SEM (Figure 1, Table 1). The crystals of MgAPO-18 and CoAPO-18 were cubic with rough surfaces, suggesting they are agglomerates of smaller crystals. ZnAPO-18 crystals also showed rough surfaces, but the crystals were significantly larger and not cubic. SAPO-18 was formed as rods, in agreement with the prior literature.[23] The homogeneity of the crystals was reflected in the SEM images with lower magnification (Figure S2), with the elemental composition checked using SEM−EDS at different locations (Table S1). PXRD patterns of the as-synthesized and calcined zeotypes were complicated by the intentionally small domain size, yet confirmed the AEI topology of the calcined samples (Figure S3). One sample, ZnAPO-18, partially collapsed and contained dense phases in addition to the AEI phase after calcination. More details are reported in Supporting Information, Section S2. N_2 adsorption−desorption isotherms are reported in Figure S4 and specific surface areas and micropore volumes are reported in Table 1. The porosity of the samples were in accordance with the XRD data, indicating highly crystalline AEI for Mg-, Co-, and Si-APO-18, whereas ZnAPO-18 contained mainly dense phases.

The elemental ratio of the synthesis gels was identical (M/(Al + P) = 0.05), and the measured elemental compositions from SEM−EDS of MAPO-18s were close to the expected values (Table 1). Propylamine TPD results, which selectively quantifies BAS, showed that only a fraction (<1/2) of the heteroatoms led to BAS formation (Table 1). Although the reason for the discrepancy remains indistinct, the influence of heteroatom and BAS density was investigated for a series of SAPO-18 and MgAPO-18 samples with M/(Al + P) ratios in the 0.03−0.06 range (Table S2, Section S2) and found to have minor influence on catalytic properties (vide infra). Hence, in the following, emphasis will be set on heteroatom characteristics and not on the density of BAS. Inspection of the desorption temperature of propylamine cracking products (propene and NH_3, Figure S5) suggested that the acid strength of the highly crystalline samples increased in the order: SAPO-18 < CoAlPO-18 < MgAPO-18.

FTIR spectroscopy was used to provide further insights into the acidity of the MAPO-18 catalysts.[38,45] IR spectra illustrating the ν(OH) frequency region of the activated powders (treated in high vacuum at 400 °C) are reported in Figure 2. All catalysts showed a band at 3680 cm^{-1} assigned to the stretching modes of P−(OH) terminal groups. Their abundance correlated well with the small crystal size observed by SEM (Figure 1). Except for ZnAPO-18, the vibrational bands of Al−OH terminal groups were visible at 3795 and 3770 cm^{-1}. An additional band at 3745 cm^{-1}, due to terminal Si−OH, was observed for SAPO-18 (Figure 2 line a). Moreover, SAPO-18 showed two bands at 3627 and 3600 cm^{-1} attributed to ν Si−(OH)−Al, corresponding to BAS located in two different crystallographic positions.[38] Coming to the MgAPO-18 (Figure 2 line b) and CoAPO-18 (Figure 2 line c) samples, IR spectra are characterized by quite broad absorption at much lower frequency, centered at 3582 and at 3570 cm^{-1}, respectively.[50] The progressive downward shifts of these bands in the series SAPO-18, MgAPO-18, and CoAPO-18, can be explained in terms of an increased BAS acidity strength in relation with the heteroatom, that follows the order Si ≪ Mg < Co.

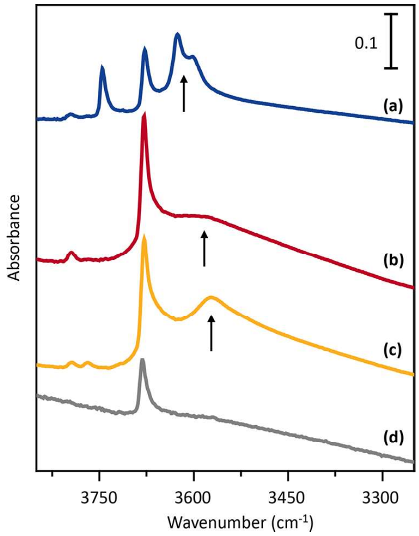

Figure 2. OH stretching region of IR spectra of the activated MAPO-18s. (a) SAPO-18, (b) MgAPO-18, (c) CoAPO-18, and (d) ZnAPO-18. The spectra are normalized to the pellets'thicknesses. The vertical arrows underline the downward shift of the BAS ν (OH) vibrational band.

Finally, in the case of ZnAPO-18 (Figure 2 line d), the lack of strong Brønsted sites can be explained with the formation of dense phases (Figure S3). Further insights on the acidity in the series were obtained by IR measurements coupled with CO adsorption at 77 K. Upon CO interaction, the IR spectra evolved in the ν (OH) stretching region showing BAS band

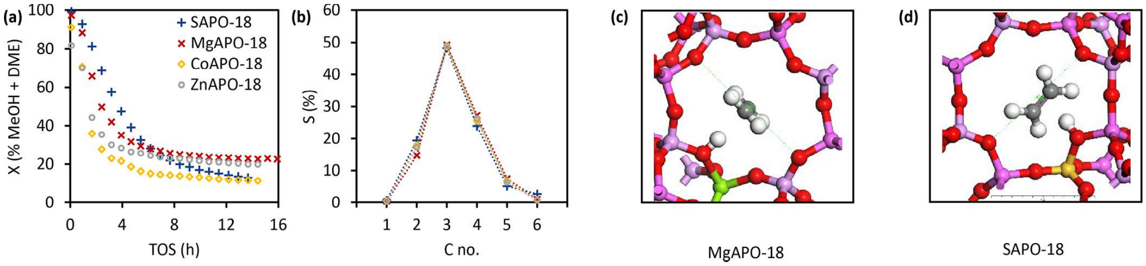

Figure 3. Catalytic performance of MAPO-18s at MTO reaction conditions. Reaction conditions: 350 °C, 1 bar, 0.13 bar MeOH (WHSV = 4 $g_{MeOH}\ g_{cat}^{-1}\ h^{-1}$), and 0.87 bar He. (a) Activity in terms of % sum of MeOH and dimethyl ether (DME) conversion over TOS and (b) hydrocarbon product distribution in terms of C no. compared at 35–40% conversion. Paraffin selectivity in all cases was less than 1%. From the reproducibility tests, the data sets were reproducible at more than 95% confidence interval and the error bars are included in Figure S15. Structure optimized 8-ring window of (c) MgAPO-18 ($MgAl_{23}P_{24}O_{96}H$) and (d) SAPO-18 ($SiAl_{24}P_{23}O_{96}H$) with adsorbed ethene. Ethene is perfectly centered through the 8-ring of MgAPO-18, but pushed out of the 8-ring of SAPO-18.

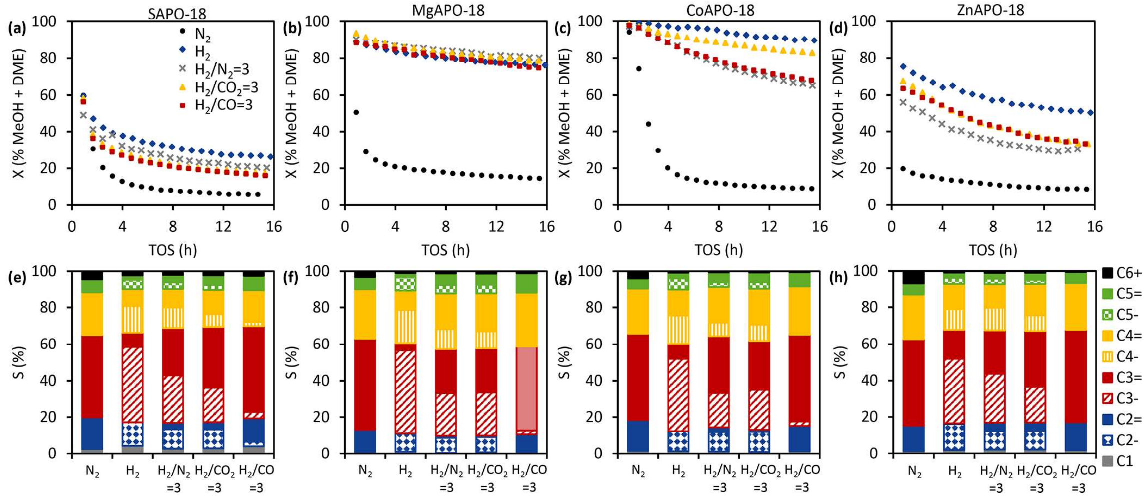

Figure 4. Catalytic performance of MAPO-18s at 350 °C, 20 bar, 1 bar MeOH (WHSV = 2.5 $g_{MeOH}\ g_{cat}^{-1}\ h^{-1}$), 0.6 bar Ar internal standard, 18.4 bar N_2 or H_2, or $H_2/X = 3$ (in which X = N_2, CO_2, or CO), and GHSV ≈ 16 000 $mL_{total\ flow}\ mL_{cat}^{-1}.\ H^{-1}$. (a–d) Activity in terms of % sum of MeOH and DME conversion over TOS for (a) SAPO-18, (b) MgAPO-18, (c) CoAPO-18, and (d) ZnAPO-18. (e–h) Product selectivity at TOS = 10 h for (e) SAPO-18, (f) MgAPO-18, (g) CoAPO-18, and (h) ZnAPO-18. From the reproducibility tests, the data sets were reproducible at more than 95% confidence interval and the error bars are included in Figure S16.

downward shifts as evidenced in Figure S6. More details are reported in Supporting Information, Section S2.

Catalytic Performance at 1 bar and 350 °C MTO Reaction Conditions. The influence of acid strength created by various heteroatom substitution was first evaluated under typical MTO conditions at 350 °C, 1 bar and 0.13 bar MeOH in N_2. These conditions were selected to illustrate the “true” deactivation profile of these catalysts, meaning 100% conversion was not sustained over time-on-stream (TOS). From Figure 3a, SAPO-18 deactivated the slowest in the first 5 h of TOS, followed by MgAPO-18, ZnAPO-18, and CoAPO-18. The slower deactivation of SAPO-18 may be due to its higher number of BAS. Moreover, the possible redox activity of CoAPO-18 and ZnAPO-18 may lead to more rapid coking and faster deactivation, as in the case of CoAPO-5 and ZnAPO-5 described earlier.[36] The superior lifetime of SAPO-18 over other MAPO-18 catalysts was also reported by other groups.[17,51] After 5 h of TOS, the activity of the MAPO-18s appeared to stabilize at 10–25% conversion. The methanol conversion capacities of the MAPO-18s were compared with a commercial SAPO-34 (from ACS Materials) as shown in Figure S13 and the selectivity *versus* conversion plots are included in Figure S14.

Referring to Figure 3b, all MAPO-18s were selective toward propene, attaining 49% propene selectivity. On the other hand, ethene selectivity varied depending on the heteroatom and was 5% higher for SAPO-18 than for MgAPO-18. Correspondingly, butenes and pentenes selectivities were lower for SAPO-18. This difference could be assigned to a change in the steady-state HC pool composition, yielding more arenes and ethene in SAPO-18 *versus* the more strongly acidic M(II)APO-18 catalysts (Figure 2). Such an effect was previously observed for the AFI topology (a 1D, 12-ring straight channel topology with less diffusion restrictions).[36] It was concluded that the stronger Brønsted acids [M(II)APO-5s] produce more propene and butenes, typical alkene cycle products, whereas M(IV)APO-5 (*i.e.*, SAPO-5) produces more ethene, aromatics, and alkanes, typical arene cycle products.[36] This conclusion was recently

Table 2. MeOH Conversion Capacity and Olefins-to-Paraffins Ratios at 350 °C, 20 bar, 1 bar MeOH (WHSV = 2.5 g_{MeOH} g_{cat}^{-1} h^{-1}), 0.6 bar Ar Internal Standard, 18.4 bar N_2 or H_2, or $H_2/X = 3$ (in which X = N_2, CO_2, or CO[a])

	(MeOH + DME) conv. capacity after 16 h (g_{MeOH} g_{cat}^{-1})					olefins/paraffins ($C_{2-4}^{=/-}$) at 10 h TOS				
	N_2	H_2	$H_2/N_2 = 3$	$H_2/CO_2 = 3$	$H_2/CO = 3$	N_2	H_2	$H_2/N_2 = 3$	$H_2/CO_2 = 3$	$H_2/CO = 3$
SAPO-18	5.1	13.1	10.6	9.6	9.1	40.2	0.3	0.8	1.4	9.6
MgAPO-18	7.6	30.2	30.2	30.3	29.1	101	0.2	1.1	1.1	22.8
CoAPO-18	8.4	34.1	28.5	32.4	28.7	81.5	0.3	1.5	1.2	22.7
ZnAPO-18	4.6	22.0	13.7	17.0	16.4	95.8	0.5	0.8	1.3	91.2

[a] Please note that the conversion levels differ between the catalysts (*cf.* Figure 4).

supported by propene and benzene methylation experiments performed over Mg-, Si-, and Zr-APO-5. They revealed a higher selectivity toward propene methylation (relative to benzene methylation) over the more strongly acidic MgAPO-5 material.[52] Finally, in the case of the AEI materials studied here, we cannot exclude the possibility that the slightly distorted 8-ring windows in M(II)APO-18 compared to Si(IV)APO-18 impacts product selectivity, by facilitating $C_{3+}^{=}$ product diffusion (Figure 3c,d).[53,54]

Reactive Feeds at 20 bar and 350 °C. The influence of various heteroatom substitutions was next evaluated at higher reaction pressure of 20 bar and relevant reactants N_2, H_2, CO, and CO_2 were co-fed with methanol. The results are presented in Figure 4 and Table 2 and revealed important reaction atmosphere effects. Detailed catalytic performance and reproducibility checks are presented in Figures S15 and S16, respectively. The increase in pressure from 1 bar to 20 bar (0.13 *vs* 1 bar MeOH in inert N_2 feed) had negligible influence on the deactivation profiles. All MAPO-18s deactivated strongly in the first 5 h of TOS and their activities subsequently stabilized at 10−20% conversion. The commercial SAPO-34 was also tested at 350 °C, 20 bar, MeOH in N_2 feed, and it deactivated completely after 3 h of TOS (Figure S17). Propene selectivity over MgAPO-18 was the highest at 49%, followed by CoAPO-18 and ZnAPO-18 at 47%, and SAPO-18 at 44%. SAPO-18 showed higher ethene and C_{6+} selectivities in comparison to the M(II)APO-18s.

Next, the general strategy of co-feeding H_2 with methanol at high pressures to improve the catalyst lifetime was proven to be effective, in accordance with the earlier literature.[32−35] This improvement in lifetime was usually obtained at the expense of lower conversion levels or steep initial deactivation, due to the higher production of paraffins as terminal products.[33,34] Remarkably, beyond prior studies, a comparison between the four materials showed that less H_2 is needed to acquire high, semistable activity over MgAPO-18 than over the other three materials (Figure 4a−d). All three M(II)APO-18 catalysts showed higher conversion levels in H_2 than those in N_2 environment, despite the increased production of paraffins. Furthermore, the M(IV) heteroatom substituted SAPO-18 was the only catalyst which showed a steep initial deactivation. This steep initial deactivation was reported recently by Shi *et al.* for both SAPO-34 and SSZ-13 under high pressure H_2 co-feeding, although the activity of the more acidic SSZ-13 later stabilized at ∼15% conversion.[34] This result may be linked to the parameters discussed above, such as the potential preference of M(II)APO materials for the alkene cycle mechanism,[52] or facilitated product diffusion with distorted windows (Figure 3c,d). In both cases, less hydrogen addition may be needed to balance the steady-state HC pool composition in a favorable direction for the non-transition metal catalyst with stronger acid sites, MgAPO-18, followed by Co- and Zn-APO-18. The increase in turnover numbers upon hydrogen addition to the MTO feed, due to the hydrogenation of the coke precursors formaldehyde and dienes, were previously concluded experimentally and theoretically.[32−34,55] Their hydrogenation rates is strongly favored over alkene (and particularly arene) hydrogenation, and all hydrogenation rates are favored by a higher BAS strength.

H_2 does not only hydrogenate coke precursors, but it also hydrogenates the olefinic products hence decreasing the olefins-to-paraffins ratio (Table 2).[33,35,56] Applicable to all MAPO-18 catalysts, the olefins-to-paraffins ratio was lowest for C_2, followed by C_3 and then C_4 (Figure 4e−h, Table S3). This is in contrast to the mechanistic studies performed on zeolites with CHA, AEI, FER, and BEA topology.[33] Arora *et al.* observed the lowest hydrogenation rate for ethene in all zeolites and higher formation of propane especially for SSZ-39, which is the zeolite version of MAPO-18s.[33] For the isostructural CHA catalysts, propane selectivity was notably higher than ethane and butanes, and SSZ-13 with stronger acidic strength resulted in higher hydrogenation rate constants than SAPO-34.[34] According to DeLuca *et al.*, the reaction barrier to alkene hydrogenation decreases with an increasing chain length and stabilization of the intermediate carbocation-like species.[55] Comparison of the SSZ-13 zeolite to the isostructural SAPO-34 material further showed a positive relation between the acid strength and hydrogenation rates, and this acid strength effect is more significant than topology (ZSM-5 *vs* SAPO-34).[55] In the current case, the preferred hydrogenation of ethene suggests that the heteroatoms are preferably located in the 8-ring windows of the AEI topology: strong confinement effects for small-molecule conversion have recently been demonstrated for $C_2^{=}$−$C_4^{=}$ methylation in 1D 10-ring ZSM-22 (TON)[57] and for methanol carbonylation reactions in the 8-ring pockets of MOR.[58,59]

The simultaneous hydrogenation of olefinic products due to H_2 co-feeding calls for an improvement to this strategy for enlarging lifetimes. A possible solution suggested by the Liu group is the co-feeding of H_2O with H_2 and methanol.[35] As H_2O may lead to material degradation and was calculated to compete for BAS adsorption with methanol, potentially yielding lower conversion rates,[60] we suggest co-feeding CO with H_2 and methanol instead. Although this approach resulted in a negative effect on the semistable conversion level for most materials (Figure 4a−d), it also led to a dramatic, positive effect on the olefins-to-paraffins ratios for all MAPO-18 catalysts (Figure 4e−h). Strikingly, MgAlPO-18, the non-transition metal material with the highest acid strength, showed similar, enhanced conversion level as with H_2 co-feed, with olefins-to-paraffins ratios higher than 22 for the C_2−C_4 products (Table 2). This result points to a distinct role of CO in the MTO reaction, as reflected in the ongoing debate on whether CO is a co-catalyst or a stoichiometric reactant in

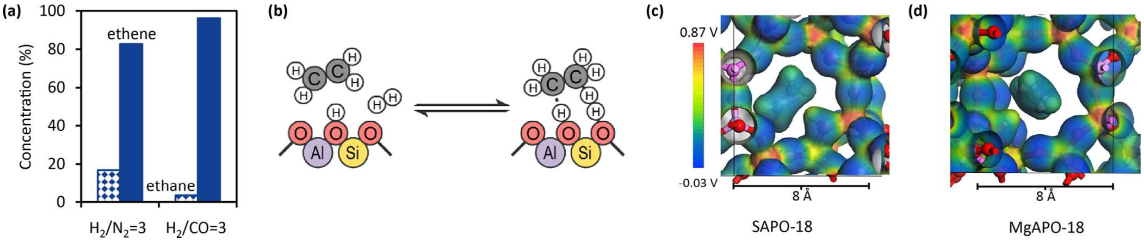

Figure 5. Mechanistic insights of the interaction between ethene and CO. (a) Ethene hydrogenation over SAPO-18 with N_2 or CO co-feeding at 350 °C, 10 bar, 0.25 bar ethene, and WHSV = 1.0 h^{-1}. (b) Illustration of ethene hydrogenation precursor states in SAPO-18, adapted from Hibbitts *et al.*[55] Optimized electron cloud distribution in (c) SAPO-18 and (d) MgAPO-18 with ethene, showing the more polar character of the Mg−O bond compared to the Si−O one. The atom positions are the same as in Figure 3.

the initiation of the dual-cycle MTO mechanism,[39−44] and in recent CH_3OH and CO co-feed studies that demonstrated C insertion from CO in HC products over ZSM-5.[61] Complementary tests in which CO was co-fed with methanol over the Si-, Mg-, and Co-APO-18 catalysts, without H_2 co-feed, showed negligible impact on the activity and product distribution (Figures S18−S20). These results suggest either that CO does not take part in the reaction under the conditions studied here or that the cavity-window structure of the AEI topology leads to a diffusivity-dominated steady-state HC pool composition that masks its contribution in the absence of H_2 co-feed.

Identical experiments of co-feeding CO_2 with H_2 and methanol were performed over the MAPO-18s as well. Although there were more olefins produced with CO_2/H_2 co-feed than pure H_2 co-feed (Figure 4e−h), this was likely due to the lower H_2 partial pressure. This hypothesis was confirmed with reference experiments carried out in N_2/H_2 co-feed environment in which the H_2 partial pressure was kept constant, as similar olefins-to-paraffins ratios were attained (Table 2, Figure S15). These results underline the unique role of CO in the MTO process, which will be covered in detail in the following section.

Role of CO in the MTO Process. The limited deactivation coupled with high selectivity toward olefins suggests that CO suppressed the hydrogenation of the olefinic products but not the coke precursors. In the recent literature, the hydrogenation rate constants of coke precursors such as formaldehyde and butadiene were measured to be at least 2 orders of magnitude higher than that of propene and ethene in high pressure H_2 studies, and this was proposed to be the origin of the lifetime improvement with limited increase (2−3 times) in paraffin selectivity.[33,34] This is not the case for the reaction conditions used here because paraffin selectivity increased dramatically for all catalysts (Table 2). A wider range of reaction conditions, including different CO/CO_x feed ratios and lower methanol partial pressure, were then explored with SAPO-18 (Figure S21). At those conditions, the ratio between H_2 and hydrocarbon products was higher and almost 100% paraffin selectivity was obtained in the presence of CO_2 exclusively (CO/CO_x = 0 in Figure S21). A clear decrease in paraffin selectivity was observed when the CO/CO_x ratio was increased. With lower MeOH partial pressure, that is, higher H_2/MeOH ratio, paraffin selectivity was also close to 100% in the presence of CO_2, yet less than 20% in the presence of CO. This affirmed the inhibition of olefin hydrogenation due to the presence of CO.

To further substantiate this conclusion, ethene and H_2 were co-fed over SAPO-18 with CO or N_2 at 350 °C, 10 bar, and 0.25 bar ethene (WHSV = 1.0 h^{-1}). From Figure 5a, the ethane concentration decreased ∼5 times upon switching from N_2 to CO co-feeding with H_2, and this reduction coincided with the drop in ethane selectivity from 11 to 2% during the MTO experiments (Figure 4). Thus, in addition to the discussed roles of CO in the initiation of the dual-cycle MTO mechanism or insertion into the aromatic products, these results demonstrate that CO also plays a role in inhibiting olefin hydrogenation, which is illustrated in Figure 5b. Returning to MTO conditions, catalytic stability was largely preserved when CO was added to the H_2 co-feed (Figure S21). Hence, CO appeared not to affect the hydrogenation of diene or aromatic precursors.

Notably, CO is a weak base, which scarcely competes with methanol or DME for adsorption on BAS. Hence, initial conversion levels are maintained in the presence of the syngas co-feed, as observed in Figure 4. However, in terms of its much higher concentration (>5 times CO/alkene ratio) during co-feed experiments, CO may compete favorably with alkenes for adsorption on BAS, thereby distorting the precursor state for alkene hydrogenation reactions, leading to the observed improvements in olefins-to-paraffins ratios (Figures 4, 5). The seemingly contradictory effect of CO on alkene hydrogenation *versus* diene or aromatic hydrogenation could have multiple reasons. Van Speybroeck and co-workers performed density functional theory (DFT) calculations and derived protonation enthalpies for alkenes, cyclopentadiene, and benzene derivatives in ZSM-5 at 500 °C.[21] They revealed that the protonation enthalpy is positive for alkenes and generally negative for cyclopentenes and benzene derivatives. Longer alkyl chains and enhanced branching generally led to higher proton affinities, hence promoting the interaction with BAS compared to light olefins and CO. Another contributing factor is the narrow window size of MAPO-18, which will lead to accumulation of the larger products in the cavities, hence increasing their local concentration, whereas light olefins will diffuse out. Support for the competitive adsorption of CO *versus* light alkenes is found in Figure S21, which demonstrates the CO concentration effect on alkene hydrogenation reactions. In line with this observation, Liu and co-workers recently reported that CO addition to the methanol feed over H-ZSM-5 constituted a carbonylation route to aromatics, whereas the hydrogen transfer path to aromatics was instead suppressed by CO.[61]

Role of Acidity (SAPO-18 *vs* MgAPO-18) in the MTO Process with Syngas Co-feeding. Although the data

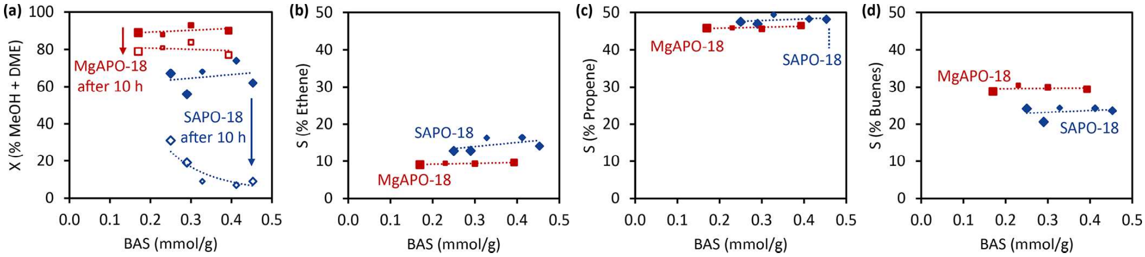

Figure 6. Catalytic performance of SAPO-18 and MgAPO-18 with varying BAS densities. Reaction conditions: 350 °C, 20 bar, 1 bar MeOH (WHSV = 2.5 g_{MeOH} g_{cat}^{-1} h^{-1}), 0.6 bar Ar internal standard, 18.4 bar H_2/CO = 3, and GHSV ≈ 16 000 $mL_{total\ flow}$ mL_{cat}^{-1} h^{-1}. (a) Activity in terms of % sum of MeOH and DME conversion and (b−d) C_2−C_4 olefin selectivity as a function of BAS density. The symbol size correlates to heteroatom loading (from M/T = 0.02 to 0.05) and lines are added to guide the eye.

presented in this study demonstrate strong performance improvements of MgAPO-18 compared to SAPO-18 under H_2/CH_3OH/CO co-feed conditions, the reason is not obvious. MTO product selectivity relies on a delicate balance between product diffusivity and kinetics of individual reactions in the dual-cycle scheme. Overall, alkene selectivity and methanol conversion capacity require high alkene methylation and cracking rates, compared to hydrogen transfer rates. In the syngas co-feed reaction scheme, the hydrogenation of formaldehyde and dienes, as well as olefins, further complicate the picture.

This research was started on the hypothesis that M(II) heteroatom substitution in zeotypes generates M−O bonds with higher polarity leading to stronger acidic sites than M(IV), that is Si, which would in turn amplify the positive influences of the reactive feeds at high reaction pressure. Theoretical predictions, based on dispersion-corrected DFT calculations, indicate a linear correlation between the BAS strength and alkene methylation activity for MAPO-X materials (M = Mg, Zn, Si, Ge, or Ti; X = 5, 18, or 34), with different slope for each topology.[62] A similar correlation for benzene methylation activity as well as the promotion of propene *versus* benzene methylation rates over MgAPO-5 *versus* SAPO-5 was recently confirmed experimentally.[52] Experimental studies further suggest that cracking reactions are promoted by high acid strength[63−65] and so are formaldehyde, diene, and alkene hydrogenation reactions.[55] The above results provide confidence that this is indeed the case, but absolute conclusions could not be made due to the differences in heteroatom uptake despite identical synthesis gel composition and the lack of control in specific heteroatom location. Therefore, a series of SAPO-18 and MgAPO-18 with varying heteroatom loadings were prepared to elucidate the acidity−performance relations.

From Figure 6a, the higher activity and stability of the stronger acidic MgAPO-18 over SAPO-18 catalysts were upheld over a range of BAS density and heteroatom content (see Supporting Information for extra IR characterization details, Figure S11). This indicates the stronger influence of acidic strength on performance in comparison to density of acidic sites, thus justifying our motivation to use M(II) heteroatom substitution. Product selectivities appeared to be independent of BAS density and heteroatom loading (Figure 6b−d), but with clear distinctions between SAPO-18 and MgAPO-18. Notably, MgAPO-18 enhanced the production of butenes whereas SAPO-18 produced more ethene. Furthermore, all MgAPO-18 samples maintained high activity after 10 h of TOS whereas the SAPO-18 samples deactivated strongly, hence supporting the conclusions made in earlier sections. Catalytic performance over TOS for all samples is included in Figure S22. The role of acidic strength in high pressure H_2 co-feeding MTO process was recently studied by the Bhan group with isostructural SAPO-34 zeotype and SSZ-13 zeolite with BAS density of 0.92 and 0.44 mmol/g, respectively.[34] There is agreement that the stronger acidic sites deactivated slower in high pressure H_2 co-feeds, and we further established acidic strength rather than density to be a key performance descriptor.

Although the positive influence of syngas co-feeding was amplified with the M(II)APO-18s, pointing to the influence of acid strength, the reason remains elusive. As cited above, prior studies indicate that alkene and benzene methylation reactions, alkene cracking, as well as alkene, diene, and arene hydrogenation reactions are promoted by higher acid strength, albeit to a different extent. To the best of our knowledge, no predictive model has yet been presented for acid strength influence on two other relevant reaction classes, carbonylation and hydrogen transfer reactions. However, the recent literature suggests that a LAS adjacent to a BAS promotes hydrogen transfer reactions. Employing ZSM-5 catalysts with varied BAS and LAS contents, Lercher and co-workers found that the methanol conversion rate correlated with BAS concentration only whereas the rate of hydrogen transfer reactions from methanol to an alkene correlated with LAS concentration.[13] The Olsbye group studied methanol−butene co-reactions over ZSM-5 and found that LAS alone had negligible activity for hydrogen transfer reactions, compared to BAS-containing materials.[66] Together, these studies strongly suggest that a LAS adjacent to a BAS promotes hydrogen transfer reactions. Of particular relevance to our contribution is a recent study in which Gascon and co-workers studied the effect of adding Lewis acidic alkaline metal ions (Ca^{2+} and Mg^{2+}) to ZSM-5. They found a strong, positive influence of Ca^{2+} and Mg^{2+} counterions on its alkene selectivity and conversion capacity for the MTO reaction. Extensive experimental and theoretical studies suggested that the counterion reduced the alkene and arene methylation rates over ZSM-5 by more than an order of magnitude, and moreover, arene methylation rates were more strongly reduced than alkene methylation rates, thereby leading to the observed propene selectivity and conversion capacity improvements.[21,63] Interestingly, propene and benzene methylation studies of the same system suggested that the rate of hydrogen transfer reactions, relative to the methylation rates, is higher in the LAS-containing materials.[21] This result is in line with the studies cited above for pristine ZSM-5.[13,66]

Returning to the MAPO-18 materials studied here, two types of Lewis acid sites were detected by FTIR spectroscopy: *M^{2+}ion exchanged onto BAS.* M^{2+} counterions were observed in the CoAlPO-18 sample and in the MgAlPO-18 sample with highest Mg^{2+} content (*cf.* Figure S6), yet not in the MgAlPO-18 samples with lower Mg contents (Figure S12). Overall, the substantially lower turnover rates reported for ion-exchanged ZSM-5 compared to pristine ZSM-5 in the literature,[21] together with the similar conversion-selectivity performance observed in this contribution for MgAlPO-18 with different Mg content (*cf.* Figure 6), may suggest that Lewis sites corresponding to M^{2+} counterions have minor influence on the observed catalyst performance in our contribution. *Extra-Framework M(II) or M(III) Cations.* Extra-framework cations were observed in the CoAlPO-18 sample (Figure S6).

An additional source of Lewis acidity, known from the prior literature, is the Lewis acid character of the M(II)−O lattice bonds (*cf.* electron distribution plots in Figure 5c,d). Such Lewis acid sites have previously been observed by Thomas and co-workers and by Catlow and co-workers, using acetonitrile as the probe molecule. The authors concluded that interaction of the MAPO-18 materials with this strongly basic probe molecules led to breaking of the M(II)−(OH)−P bond and hence to the loss of the BAS.[37,38,67,68] Overall, LAS could influence the catalytic properties of BAS by the presence of two next-neighboring M(II) sites (−M−O−P−O−M−), where one M(II) would constitute the BAS and the other M(II) would form a (partial) extra-framework LAS site. High M(II) concentrations would increase the probability of two adjacent BAS sites being transformed to a BAS−LAS pair. In the current case, the similar performance of MgAlPO-18 catalysts with different acid site concentration (Figure 6) may suggest that even such LAS have little effect on product selectivity. However, the impact of the cavity-window structure of the AEI topology in tuning HC pool composition and effluent concentrations by restricting product diffusivities should not be underestimated (Figure 3).[6,54,69,70]

Returning finally to the effect of BAS strength, the selectivity of the more strongly acidic MgAPO-5 material toward alkene (*vs* arene) methylation,[36,52] combined with the slightly larger window size of MgAPO-18 compared to SAPO-18 (Figure 3) are in line with and could explain the favorable performance observed for MgAPO-18 under high pressure MTO conditions with reactive co-feeds.

CONCLUSIONS

We introduced M(II)APO-18s, in particular MgAPO-18, as favorable methanol to olefins catalysts for high pressure methanol conversion in the presence of reactive gases. All M(II)APO-18 (M = Mg, Co, or Zn) outperformed Si(IV)-APO-18 at 350 °C, 20 bar, and 1 bar methanol partial pressure (WHSV = 2.5 h^{-1}) with H_2/CO or CO_2 co-feeds. Product selectivity, specifically hydrocarbon and paraffin/olefin distributions, were regulated by zeotype composition and CO co-feeding, respectively. Furthermore, CO was proven to inhibit the hydrogenation of olefins without altering the stability of MgAPO-18. Acidity, in particular, acidic site strength and not density, was the main descriptor for the catalytic activity and stability. CO co-feeding with H_2 and methanol is thus an effective strategy to suppress the hydrogenation of olefinic products in the MTO process.

ASSOCIATED CONTENT

Supporting Information

The Supporting Information is available free of charge at https://pubs.acs.org/doi/10.1021/acscatal.1c04694.

Catalyst characterization (XRD, SEM−EDS, N_2 physisorption, IR spectroscopy, and propylamine-TPD), catalyst performance, and DFT calculations (PDF)

AUTHOR INFORMATION

Corresponding Author

Unni Olsbye − *Centre for Materials Science and Nanotechnology, Department of Chemistry, University of Oslo, Oslo N-0315, Norway;* orcid.org/0000-0003-3693-2857; Email: unni.olsbye@kjemi.uio.no

Authors

Jingxiu Xie − *Centre for Materials Science and Nanotechnology, Department of Chemistry, University of Oslo, Oslo N-0315, Norway*
Daniel S. Firth − *Centre for Materials Science and Nanotechnology, Department of Chemistry, University of Oslo, Oslo N-0315, Norway*
Tomás Cordero-Lanzac − *Centre for Materials Science and Nanotechnology, Department of Chemistry, University of Oslo, Oslo N-0315, Norway;* orcid.org/0000-0002-1365-931X
Alessia Airi − *Department of Chemistry, NIS and INSTM Reference Centre, Università di Torino, Torino 10125, Italy;* orcid.org/0000-0003-0206-4887
Chiara Negri − *Centre for Materials Science and Nanotechnology, Department of Chemistry, University of Oslo, Oslo N-0315, Norway*
Sigurd Øien-Ødegaard − *Centre for Materials Science and Nanotechnology, Department of Chemistry, University of Oslo, Oslo N-0315, Norway*
Karl Petter Lillerud − *Centre for Materials Science and Nanotechnology, Department of Chemistry, University of Oslo, Oslo N-0315, Norway*
Silvia Bordiga − *Department of Chemistry, NIS and INSTM Reference Centre, Università di Torino, Torino 10125, Italy;* orcid.org/0000-0003-2371-4156

Complete contact information is available at:
https://pubs.acs.org/10.1021/acscatal.1c04694

Author Contributions

U.O. and J.X. conceived research and designed experiments. J.X. synthesized most catalysts and evaluated catalyst performance. D.F. was consulted for zeolite/zeotype preparation, synthesized some catalyst samples, and measured structural properties of the catalysts. T.C.-L. performed some co-feed and all ethene hydrogenation tests as well as N_2 and propyl amine sorption measurements and analysis. A.A., C.N., and S.B. performed the FTIR measurements and analysis. S.Ø.-Ø. performed the XRD analysis. K.P.L. performed the computational studies. J.X. and U.O. wrote the manuscript with input from all authors.

Notes

The authors declare no competing financial interest.

ACKNOWLEDGMENTS

This project has received funding from the European Union's Horizon 2020 research and innovation program under grant agreement no. 837733 (COZMOS). DF acknowledges the European Union's Horizon 2020 research and innovation program for support under grant agreement no. 814671 (Bizeolcat). Dr. Evgeniy Redekop and Prof. Stian Svelle are acknowledged for technical discussions and assistance related to the upgrading of the high-pressure test rig.

■ REFERENCES

(1) Yarulina, I.; Chowdhury, A. D.; Meirer, F.; Weckhuysen, B. M.; Gascon, J. Recent Trends and Fundamental Insights in the Methanol-to-Hydrocarbons Process. *Nat. Catal.* **2018**, *1*, 398−411.

(2) Ye, R.-P.; Ding, J.; Gong, W.; Argyle, M. D.; Zhong, Q.; Wang, Y.; Russell, C. K.; Xu, Z.; Russell, A. G.; Li, Q.; Fan, M.; Yao, Y. G. CO2 Hydrogenation to High-Value Products via Heterogeneous Catalysis. *Nat. Commun.* **2019**, *10*, 5698.

(3) Olsbye, U.; Svelle, S.; Bjørgen, M.; Beato, P.; Janssens, T. V. W.; Joensen, F.; Bordiga, S.; Lillerud, K. P. Conversion of Methanol to Hydrocarbons: How Zeolite Cavity and Pore Size Controls Product Selectivity. *Angew. Chem. Int. Ed.* **2012**, *51*, 5810−5831.

(4) Tian, P.; Wei, Y.; Ye, M.; Liu, Z. Methanol to Olefins (MTO): From Fundamentals to Commercialization. *ACS Catal.* **2015**, *5*, 1922−1938.

(5) Yang, M.; Fan, D.; Wei, Y.; Tian, P.; Liu, Z. Recent Progress in Methanol-to-Olefins (MTO) Catalysts. *Adv. Mater.* **2019**, *31*, 1902181−1902196.

(6) Hereijgers, B. P. C.; Bleken, F.; Nilsen, M. H.; Svelle, S.; Lillerud, K.-P.; Bjørgen, M.; Weckhuysen, B. M.; Olsbye, U. Product Shape Selectivity Dominates the Methanol-to-Olefins (MTO) Reaction over H-SAPO-34 Catalysts. *J. Catal.* **2009**, *264*, 77−87.

(7) Gao, M.; Li, H.; Liu, W.; Xu, Z.; Peng, S.; Yang, M.; Ye, M.; Liu, Z. Imaging Spatiotemporal Evolution of Molecules and Active Sites in Zeolite Catalyst during Methanol-to-Olefins Reaction. *Nat. Commun.* **2020**, *11*, 3641.

(8) Svelle, S.; Joensen, F.; Nerlov, J.; Olsbye, U.; Lillerud, K.-P.; Kolboe, S.; Bjørgen, M. Conversion of Methanol into Hydrocarbons over Zeolite H-ZSM-5: Ethene Formation Is Mechanistically Separated from the Formation of Higher Alkenes. *J. Am. Chem. Soc.* **2006**, *128*, 14770−14771.

(9) Ilias, S.; Bhan, A. Mechanism of the Catalytic Conversion of Methanol to Hydrocarbons. *ACS Catal.* **2013**, *3*, 18−31.

(10) Lezcano-Gonzalez, I.; Campbell, E.; Hoffman, A. E. J.; Bocus, M.; Sazanovich, I. V.; Towrie, M.; Agote-Aran, M.; Gibson, E. K.; Greenaway, A.; De Wispelaere, K.; Van Speybroeck, V.; Beale, A. M. Insight into the Effects of Confined Hydrocarbon Species on the Lifetime of Methanol Conversion Catalysts. *Nat. Mater.* **2020**, *19*, 1081−1087.

(11) Stöcker, M. Methanol-to-Hydrocarbons: Catalytic Materials and Their Behavior. *Microporous Mesoporous Mater.* **1999**, *29*, 3−48.

(12) Olsbye, U.; Svelle, S.; Lillerud, K. P.; Wei, Z. H.; Chen, Y. Y.; Li, J. F.; Wang, J. G.; Fan, W. B. The Formation and Degradation of Active Species during Methanol Conversion over Protonated Zeotype Catalysts. *Chem. Soc. Rev.* **2015**, *44*, 7155−7176.

(13) Müller, S.; Liu, Y.; Kirchberger, F. M.; Tonigold, M.; Sanchez-Sanchez, M.; Lercher, J. A. Hydrogen Transfer Pathways during Zeolite Catalyzed Methanol Conversion to Hydrocarbons. *J. Am. Chem. Soc.* **2016**, *138*, 15994−16003.

(14) Teketel, S.; Lundegaard, L. F.; Skistad, W.; Chavan, S. M.; Olsbye, U.; Lillerud, K. P.; Beato, P.; Svelle, S. Morphology-Induced Shape Selectivity in Zeolite Catalysis. *J. Catal.* **2015**, *327*, 22−32.

(15) Goetze, J.; Meirer, F.; Yarulina, I.; Gascon, J.; Kapteijn, F.; Ruiz-Martínez, J.; Weckhuysen, B. M. Insights into the Activity and Deactivation of the Methanol-to-Olefins Process over Different Small-Pore Zeolites As Studied with Operando UV-Vis Spectroscopy. *ACS Catal.* **2017**, *7*, 4033−4046.

(16) Li, C.; Paris, C.; Martínez-Triguero, J.; Boronat, M.; Moliner, M.; Corma, A. Synthesis of reaction-adapted zeolites as methanol-to-olefins catalysts with mimics of reaction intermediates as organic structure-directing agents. *Nat. Catal.* **2018**, *1*, 547−554.

(17) Kang, J. H.; Alshafei, F. H.; Zones, S. I.; Davis, M. E. Cage-Defining Ring: A Molecular Sieve Structural Indicator for Light Olefin Product Distribution from the Methanol-to-Olefins Reaction. *ACS Catal.* **2019**, *9*, 6012−6019.

(18) Dahl, I. M.; Mostad, H.; Akporiaye, D.; Wendelbo, R. Structural and Chemical Influences on the MTO Reaction: A Comparison of Chabazite and SAPO-34 as MTO Catalysts. *Microporous Mesoporous Mater.* **1999**, *29*, 185−190.

(19) Zhu, Q.; Kondo, J. N.; Ohnuma, R.; Kubota, Y.; Yamaguchi, M.; Tatsumi, T. The Study of Methanol-to-Olefin over Proton Type Aluminosilicate CHA Zeolites. *Microporous Mesoporous Mater.* **2008**, *112*, 153−161.

(20) Mores, D.; Kornatowski, J.; Olsbye, U.; Weckhuysen, B. M. Coke Formation during the Methanol-to-Olefin Conversion: In Situ Microspectroscopy on Individual H-ZSM-5 Crystals with Different Brønsted Acidity. *Chem.—Eur. J.* **2011**, *17*, 2874−2884.

(21) Yarulina, I.; De Wispelaere, K.; Bailleul, S.; Goetze, J.; Radersma, M.; Abou-Hamad, E.; Vollmer, I.; Goesten, M.; Mezari, B.; Hensen, E. J. M.; Martínez-Espín, J. S.; Morten, M.; Mitchell, S.; Perez-Ramirez, J.; Olsbye, U.; Weckhuysen, B. M.; Van Speybroeck, V.; Kapteijn, F.; Gascon, J. Structure-performance descriptors and the role of Lewis acidity in the methanol-to-propylene process. *Nat. Chem.* **2018**, *10*, 804−812.

(22) Chen, D.; Moljord, K.; Fuglerud, T.; Holmen, A. The Effect of Crystal Size of SAPO-34 on the Selectivity and Deactivation of the MTO Reaction. *Microporous Mesoporous Mater.* **1999**, *29*, 191−203.

(23) Martínez-Franco, R.; Li, Z.; Martínez-Triguero, J.; Moliner, M.; Corma, A. Improving the Catalytic Performance of SAPO-18 for the Methanol-to-Olefins (MTO) Reaction by Controlling the Si Distribution and Crystal Size. *Catal. Sci. Technol.* **2016**, *6*, 2796−2806.

(24) Dai, H.; Shen, Y.; Yang, T.; Lee, C.; Fu, D.; Agarwal, A.; Le, T. T.; Tsapatsis, M.; Palmer, J. C.; Weckhuysen, B. M.; Dauenhauer, P. J.; Zou, X.; Rimer, J. D. Finned Zeolite Catalysts. *Nat. Mater.* **2020**, *19*, 1074−1080.

(25) Wilson, S.; Barger, P. The Characteristics of SAPO-34 Which Influence the Conversion of Methanol to Light Olefins. *Microporous Mesoporous Mater.* **1999**, *29*, 117−126.

(26) Arora, S. S.; Bhan, A. The Critical Role of Methanol Pressure in Controlling Its Transfer Dehydrogenation and the Corresponding Effect on Propylene-to-Ethylene Ratio during Methanol-to-Hydrocarbons Catalysis on H-ZSM-5. *J. Catal.* **2017**, *356*, 300−306.

(27) Bansode, A.; Urakawa, A. Towards Full One-Pass Conversion of Carbon Dioxide to Methanol and Methanol-Derived Products. *J. Catal.* **2014**, *309*, 66−70.

(28) Jiao, F.; Li, J.; Pan, X.; Xiao, J.; Li, H.; Ma, H.; Wei, M.; Pan, Y.; Zhou, Z.; Li, M.; Miao, S.; Li, J.; Zhu, Y.; Xiao, D.; He, T.; Yang, J.; Qi, F.; Fu, Q.; Bao, X. Selective Conversion of Syngas to Light Olefins. *Science* **2016**, *351*, 1065−1068.

(29) Cheng, K.; Gu, B.; Liu, X.; Kang, J.; Zhang, Q.; Wang, Y. Direct and Highly Selective Conversion of Synthesis Gas into Lower Olefins: Design of a Bifunctional Catalyst Combining Methanol Synthesis and Carbon-Carbon Coupling. *Angew. Chem. Int. Ed.* **2016**, *128*, 4803−4806.

(30) Bao, J.; Yang, G.; Yoneyama, Y.; Tsubaki, N. Significant Advances in C1 Catalysis: Highly Efficient Catalysts and Catalytic Reactions. *ACS Catal.* **2019**, *9*, 3026−3053.

(31) Zhou, W.; Cheng, K.; Kang, J.; Zhou, C.; Subramanian, V.; Zhang, Q.; Wang, Y. New Horizon in C1 Chemistry: Breaking the Selectivity Limitation in Transformation of Syngas and Hydrogenation of CO2 into Hydrocarbon Chemicals and Fuels. *Chem. Soc. Rev.* **2019**, *48*, 3193−3228.

(32) Arora, S. S.; Nieskens, D. L. S.; Malek, A.; Bhan, A. Lifetime Improvement in Methanol-to-Olefins Catalysis over Chabazite Materials by High-Pressure H2 Co-Feeds. *Nat. Catal.* **2018**, *1*, 666−672.

(33) Arora, S. S.; Shi, Z.; Bhan, A. Mechanistic Basis for Effects of High-Pressure H2 Cofeeds on Methanol-to-Hydrocarbons Catalysis over Zeolites. *ACS Catal.* **2019**, *9*, 6407−6414.

(34) Shi, Z.; Neurock, M.; Bhan, A. Methanol-to-Olefins Catalysis on HSSZ-13 and HSAPO-34 and Its Relationship to Acid Strength. *ACS Catal.* **2021**, *11*, 1222−1232.

(35) Zhao, X.; Li, J.; Tian, P.; Wang, L.; Li, X.; Lin, S.; Guo, X.; Liu, Z. Achieving a Superlong Lifetime in the Zeolite-Catalyzed MTO Reaction under High Pressure: Synergistic Effect of Hydrogen and Water. *ACS Catal.* **2019**, *9*, 3017−3025.

(36) Mortén, M.; Mentel, Ł.; Lazzarini, A.; Pankin, I. A.; Lamberti, C.; Bordiga, S.; Crocellà, V.; Svelle, S.; Lillerud, K. P.; Olsbye, U. A Systematic Study of Isomorphically Substituted H-MAlPO-5 Materials for the Methanol-to-Hydrocarbons Reaction. *ChemPhysChem* **2018**, *19*, 484−495.

(37) Corà, F.; Alfredsson, M.; Barker, C. M.; Bell, R. G.; Foster, M. D.; Saadoune, I.; Simperler, A.; Catlow, C. R. A. Modeling the Framework Stability and Catalytic Activity of Pure and Transition Metal-Doped Zeotypes. *J. Solid State Chem.* **2003**, *176*, 496−529.

(38) Chen, J.; Thomas, J. M.; Sankar, G. IR Spectroscopic Study of CD3CN Adsorbed on ALPO-18 Molecular Sieve and the Solid Acid Catalysts SAPO-18 and MeAPO-18. *J. Chem. Soc., Faraday Trans.* **1994**, *90*, 3455−3459.

(39) Liu, Y.; Müller, S.; Berger, D.; Jelic, J.; Reuter, K.; Tonigold, M.; Sanchez-Sanchez, M.; Lercher, J. A. Formation Mechanism of the First Carbon-Carbon Bond and the First Olefin in the Methanol Conversion into Hydrocarbons. *Angew. Chem. Int. Ed.* **2016**, *128*, 5817−5820.

(40) Chowdhury, A. D.; Paioni, A. L.; Houben, K.; Whiting, G. T.; Baldus, M.; Weckhuysen, B. M. Bridging the Gap between the Direct and Hydrocarbon Pool Mechanisms of the Methanol-to-Hydrocarbons Process. *Angew. Chem. Int. Ed.* **2018**, *130*, 8227−8231.

(41) Plessow, P. N.; Studt, F. Unraveling the Mechanism of the Initiation Reaction of the Methanol to Olefins Process Using Ab Initio and DFT Calculations. *ACS Catal.* **2017**, *7*, 7987−7994.

(42) Plessow, P. N.; Studt, F. Theoretical Insights into the Effect of the Framework on the Initiation Mechanism of the MTO Process. *Catal. Lett.* **2018**, *148*, 1246−1253.

(43) Plessow, P. N.; Smith, A.; Tischer, S.; Studt, F. Identification of the Reaction Sequence of the MTO Initiation Mechanism Using Ab Initio-Based Kinetics. *J. Am. Chem. Soc.* **2019**, *141*, 5908−5915.

(44) Yang, L.; Yan, T.; Wang, C.; Dai, W.; Wu, G.; Hunger, M.; Fan, W.; Xie, Z.; Guan, N.; Li, L. Role of Acetaldehyde in the Roadmap from Initial Carbon-Carbon Bonds to Hydrocarbons during Methanol Conversion. *ACS Catal.* **2019**, *9*, 6491−6501.

(45) Chen, J.; Thomas, J. M. MAPO-18 (M = Mg, Zn, Co): A New Family of Catalysts for the Conversion of Methanol to Light Olefins. *J. Chem. Soc., Chem. Commun.* **1994**, 603−604.

(46) Simmen, A.; McCusker, L. B.; Baerlocher, C.; Meier, W. M. The Structure Determination and Rietveld Refinement of the Aluminophosphate AlPO4-18. *Zeolites* **1991**, *11*, 654−661.

(47) Kresnawahjuesa, O.; Gorte, R. J.; De Oliveira, D.; Lau, L. Y. A Simple, Inexpensive, and Reliable Method for Measuring Brønsted-Acid Site Densities in Solid Acids. *Catal. Lett.* **2002**, *82*, 155−160.

(48) Zhao, Y.; Truhlar, D. G. A new local density functional for main-group thermochemistry, transition metal bonding, thermochemical kinetics, and noncovalent interactions. *J. Chem. Phys.* **2006**, *125*, 194101.

(49) Zhao, Y.; Truhlar, D. G. Density Functional for Spectroscopy: No Long-Range Self-Interaction Error, Good Performance for Rydberg and Charge-Transfer States, and Better Performance on Average than B3LYP for Ground States. *J. Phys. Chem. A* **2006**, *110*, 13126−13130.

(50) Marchese, L.; Chen, J.; Thomas, J. M.; Coluccia, S.; Zecchina, A. Bronsted, Lewis, and Redox Centers on CoAPO-18 Catalysts. 1. Vibrational Modes of Adsorbed Water. *J. Phys. Chem.* **1994**, *98*, 13350−13356.

(51) Wendelbo, R.; Akporiaye, D.; Andersen, A.; Dahl, I. M.; Mostad, H. B. Synthesis, Characterization and Catalytic Testing of SAPO-18, MgAPO-18, and ZnAPO-18 in the MTO Reaction. *Appl. Catal., A* **1996**, *142*, L197−L207.

(52) Mortén, M.; Cordero-Lanzac, T.; Cnudde, P.; Redekop, E. A.; Svelle, S.; van Speybroeck, V.; Olsbye, U. Acidity Effect on Benzene Methylation Kinetics over Substituted H-MeAlPO-5 Catalysts. *J. Catal.* **2021**, *404*, 594.

(53) Pinilla-Herrero, I.; Olsbye, U.; Márquez-Álvarez, C.; Sastre, E. Effect of Framework Topology of SAPO Catalysts on Selectivity and Deactivation Profile in the Methanol-to-Olefins Reaction. *J. Catal.* **2017**, *352*, 191−207.

(54) Ferri, P.; Li, C.; Millán, R.; Martínez-Triguero, J.; Moliner, M.; Boronat, M.; Corma, A. Impact of Zeolite Framework Composition and Flexibility on Methanol-To-Olefins Selectivity: Confinement or Diffusion? *Angew. Chem. Int. Ed.* **2020**, *59*, 19708−19715.

(55) DeLuca, M.; Janes, C.; Hibbitts, D. Contrasting Arene, Alkene, Diene, and Formaldehyde Hydrogenation in H-ZSM-5, H-SSZ-13, and H-SAPO-34 Frameworks during MTO. *ACS Catal.* **2020**, *10*, 4593−4607.

(56) Nieskens, D. L. S.; Lunn, J. D.; Malek, A. Understanding the Enhanced Lifetime of SAPO-34 in a Direct Syngas-to-Hydrocarbons Process. *ACS Catal.* **2019**, *9*, 691−700.

(57) Redekop, E. A.; Lazzarini, A.; Bordiga, S.; Olsbye, U. A Temporal Analysis of Products (TAP) Study of C2-C4 Alkene Reactions with a Well-Defined Pool of Methylating Species on ZSM-22 Zeolite. *J. Catal.* **2020**, *385*, 300−312.

(58) Cheung, P.; Bhan, A.; Sunley, G.; Law, D.; Iglesia, E. Site Requirements and Elementary Steps in Dimethyl Ether Carbonylation Catalyzed by Acidic Zeolites. *J. Catal.* **2007**, *245*, 110−123.

(59) Gounder, R.; Iglesia, E. The Roles of Entropy and Enthalpy in Stabilizing Ion-Pairs at Transition States in Zeolite Acid Catalysis. *Acc. Chem. Res.* **2012**, *45*, 229−238.

(60) De Wispelaere, K.; Wondergem, C. S.; Ensing, B.; Hemelsoet, K.; Meijer, E. J.; Weckhuysen, B. M.; Van Speybroeck, V.; Ruiz-Martínez, J. Insight into the Effect of Water on the Methanol-to-Olefins Conversion in H-SAPO-34 from Molecular Simulations and in Situ Microspectroscopy. *ACS Catal.* **2016**, *6*, 1991−2002.

(61) Chen, Z.; Ni, Y.; Zhi, Y.; Wen, F.; Zhou, Z.; Wei, Y.; Zhu, W.; Liu, Z. Coupling of Methanol and Carbon Monoxide over H-ZSM-5 to Form Aromatics. *Angew. Chem. Int. Ed.* **2018**, *130*, 12729−12733.

(62) Wang, C.-M.; Brogaard, R. Y.; Xie, Z.-K.; Studt, F. Transition-State Scaling Relations in Zeolite Catalysis: Influence of Framework Topology and Acid-Site Reactivity. *Catal. Sci. Technol.* **2015**, *5*, 2814−2820.

(63) Lin, L.; Qiu, C.; Zhuo, Z.; Zhang, D.; Zhao, S.; Wu, H.; Liu, Y.; He, M. Acid Strength Controlled Reaction Pathways for the Catalytic Cracking of 1-Butene to Propene over ZSM-5. *J. Catal.* **2014**, *309*, 136−145.

(64) Lin, L. F.; Zhao, S. F.; Zhang, D. W.; Fan, H.; Liu, Y. M.; He, M. Y. Acid Strength Controlled Reaction Pathways for the Catalytic Cracking of 1-Pentene to Propene over ZSM-5. *ACS Catal.* **2015**, *5*, 4048−4059.

(65) Meusinger, J.; Vinek, H.; Lercher, J. A. Cracking of n-hexane and n-butane over SAPO5, MgAPO5 and CoAPO5. *J. Mol. Catal.* **1994**, *87*, 263−273.

(66) Martínez-Espín, J. S.; De Wispelaere, K.; Janssens, T. V. W.; Svelle, S.; Lillerud, K. P.; Beato, P.; Van Speybroeck, V.; Olsbye, U. Hydrogen Transfer versus Methylation: On the Genesis of Aromatics Formation in the Methanol-To-Hydrocarbons Reaction over H-ZSM-5. *ACS Catal.* **2017**, *7*, 5773−5780.

(67) Barrett, P. A.; Sankar, G.; Jones, R. H.; Catlow, C. R. A.; Thomas, J. M. Interaction of Acetonitrile with Cobalt-Containing Aluminophosphates: An X-Ray Absorption Investigation. *J. Phys. Chem. B* **1997**, *101*, 9555−9562.

(68) Saadoune, I.; Corà, F.; Catlow, C. R. A. Computational Study of the Structural and Electronic Properties of Dopant Ions in Microporous AlPOs. 1. Acid Catalytic Activity of Divalent Metal Ions. *J. Phys. Chem. B* **2003**, *107*, 3003−3011.

(69) Chen, J.; Li, J.; Yuan, C.; Xu, S.; Wei, Y.; Wang, Q.; Zhou, Y.; Wang, J.; Zhang, M.; He, Y.; Xu, S.; Liu, Z. Elucidating the Olefin Formation Mechanism in the Methanol to Olefin Reaction over AlPO-18 and SAPO-18. *Catal. Sci. Technol.* **2014**, *4*, 3268−3277.

(70) Zhong, J.; Han, J.; Wei, Y.; Xu, S.; He, Y.; Zheng, Y.; Ye, M.; Guo, X.; Song, C.; Liu, Z. Increasing the Selectivity to Ethylene in the MTO Reaction by Enhancing Diffusion Limitation in the Shell Layer of SAPO-34 Catalyst. *Chem. Commun.* **2018**, *54*, 3146–3149.

Appendix II: off topic publication

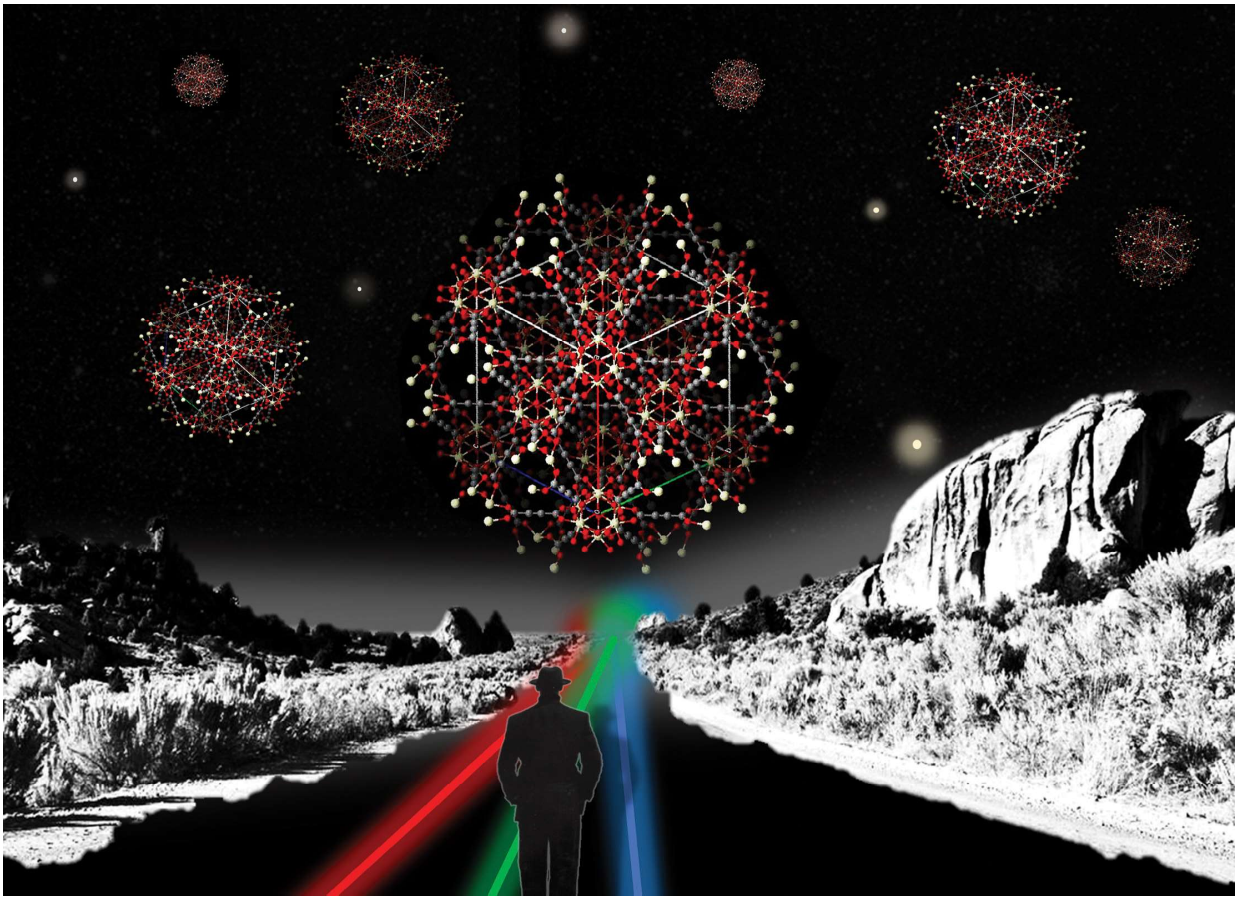

Showcasing research from Professor Bordiga's laboratory, Department of Chemistry, University of Turin, Italy.

A spectroscopic and computational study of a tough MOF with a fragile linker: Ce-UiO-66-ADC

A spectroscopic and computational insight in the nature of an acetylene dicarboxylic acid based Ce-MOF, having UiO-66 topology and denoted as Ce-UiO-66-ADC MOF.

As featured in:

See Cesare Atzori, Silvia Bordiga *et al.*, *Dalton Trans.*, 2020, **49**, 12.

rsc.li/dalton

Dalton
Transactions

COMMUNICATION

View Article Online
View Journal | View Issue

Check for updates

Cite this: *Dalton Trans.*, 2020, **49**, 12

Received 21st October 2019,
Accepted 25th November 2019

DOI: 10.1039/c9dt04112e

rsc.li/dalton

A spectroscopic and computational study of a tough MOF with a fragile linker: Ce-UiO-66-ADC†

Alessia Airi,[a] Cesare Atzori, *[a] Francesca Bonino, [a] Alessandro Damin,[a] Sigurd Øien-Ødegaard,[b] Erlend Aunan[b] and Silvia Bordiga *[a,b]

The thermolabile acetylene dicarboxylic acid has been introduced as linker in UiO-66 topology, synthetizing the compound with formula [$Ce_6O_4(OH)_4(ADC)_6$] and denoted as Ce-UiO-66-ADC MOF. The characterization by multi-technique approach coupled with computational modelling revealed a peculiar intrinsic defective nature related to the nature of the linker.

Metal–organic frameworks (MOFs) represent a rather new class of synthetic crystalline materials, constituted by discrete inorganic (metal–oxide clusters) and organic (multitopic organic linkers) units, connected together by coordination bonds.[1,2] The units represent the building blocks for the formation, through their opportune choice and combination,[3] of a large variety of different structures, in which the metal–oxide clusters occupy the nodes and are connected to each other by the ligands, which act as spacers, originating an ideal porous system.[4–7] Thanks to the possibility to predict and to tailor their lattices and composition, over the last two decades, MOFs have been the object of increasing interest. Moreover, these materials may be characterized by high specific surface areas, tuneable pore size and chemical functionalities, opening a wide landscape on potential applications in various fields, among which catalysis[8,9] and gas adsorption and storage are emerging.[10,11]

Since its discovery in 2008,[12] the MOF denoted as UiO-66 [$Zr_6O_4(OH)_4(BDC)_6$], has attracted considerable attention by the scientific community, mainly because of its exceptional toughness: it resists at temperature around 400 °C, it shows considerable resistance to hydrolysis and also high tolerance for defects.[13] Moreover, the formation of the cubic lattice by self-assembling of the Zr(IV) clusters (in presence of linear dicarboxylic linkers) is so favoured that the formation of secondary phases, in the same synthetic conditions, is avoided;[14] this encouraged the fruitful research of UiO-66 isostructural derivatives obtained by changing the linker or the metal cation.[15–18] In this scenario, the present work aimed to introduce the acetylene dicarboxylate (ADC), as linker in the UiO-66 framework and fully characterize its peculiar features. The thermal lability and quite reactive nature of the precursor molecule (the acetylene dicarboxylic acid H_2ADC undergoes very easily to decarboxylation), made it an almost forgotten linker in the history of MOFs,[19,20] even if a consistent literature on ADC-based coordination polymers is known.[21–29] On the other hand, recently, it was demonstrated that it is possible to obtain the structure of UiO-66, using cerium(IV) as metal centre.[30] It was attested that Ce(IV) admits the same coordination of Zr(IV) and the same topology of the MOF, while it offers much shorter times and milder conditions for the synthesis, opening a new fruitful research concerning Ce-UiO-66 derivatives[31–36] and for the introduction of ADC.[37]

With the aim to observe the behaviour of the thermolabile molecule within the UiO-66 lattice, we synthetized the MOF hereafter called Ce-UiO-66-ADC, which contains Ce(IV) as metal cation and ADC as organic linker, following the sub-solvothermal method developed for Ce(IV) UiO-66 derivatives by Lammert *et al.* in 2015.[30]

More in detail, the acetylene dicarboxylic acid (H_2ADC) was solubilized in dimethylformamide (DMF), then a 0.53 M aqueous solution of [$(NH_4)_2[Ce(NO_3)_6]$] (CAN) was added to the first one. The quantities were calculated to obtain a 1 : 1 molar ratio between the metal precursor and the organic linker. The closed vial was then inserted in oven at 90 °C for 15 minutes (see ESI, section 1.1†). The procedure described above produced a yellowish powder with a yield of about 5%. Powder X-Ray diffraction (PXRD) proved that the product is composed by a single crystalline phase showing the principal reflexes of UiO-66 pattern, thus confirming the success of the synthesis. On the other hand, the transmission IR spectroscopy (see ESI, Fig. S1†), performed on outgassed sample, revealed intense

---

[a] *Department of Chemistry, NIS and INSTM Reference Centre, University of Torino, Via G. Quarello 15, 10135 Torino, Italy. E-mail: cesare.atzori@unito.it, silvia.bordiga@unito.it*

[b] *Catalysis Section, Department of Chemistry, University of Oslo, P.O. Box 1033, N-0315 Oslo, Norway*

† Electronic supplementary information (ESI) available. See DOI: 10.1039/c9dt04112e

signals of an unexpected species. The bands at 3260 cm^{-1} (m) due to ν C$\equiv$(C–H) and at 2107 cm^{-1} (s) due to ν R–(C$\equiv$C)–H, are compatible with the presence of a terminal alkyne.[38] This first analysis suggested that the linker undergoes a decarboxylation reaction caused by the heating, justifying a so low yield. In fact, a systematic study concerning decarboxylation of H_2ADC, conducted by Li *et al.* in 2002,[39] reports that the presence of H_2O favours the decarboxylation and allows it to occur at lower temperatures (already at 60 °C). Water accelerates the process stabilizing a transition state in which it mediates the transfer of acid protons from the carboxylic acid to the α-carbon, forming a stable terminal alkyne. H_2ADC and HADC$^-$ possess acid protons thus they can easily undergo the water mediated decarboxylation at the synthetic temperature (90 °C–100 °C). The reaction products are the terminal alkynes, propiolic acid and propiolate anion (Scheme 1). On the basis of this hypothesis, the reason of a so low yield, is ascribable to a loss of the pristine linker that, if reacted, is not available anymore to build the framework.

The decarboxylation reaction is, in fact, in competition with the reaction of self-assembling that induces the linker to react with the metal ion, to give rise to the three-dimensional structure of the MOF. For this reason, the synthesis was improved introducing a Brønsted base (triethylamine) in the reaction mixture in ratio 1 : 1 respect to the reagents, in order to stabilize the double deprotonated form (ADC^{2-}) that is much less converted into propiolate. Therefore, in basic solution a higher amount of linker would be preserved from decarboxylation and would be available to interact directly with cerium to form the MOF lattice. The synthesis in basic conditions was performed following the same procedure already described: after mixing the reactants, the solution was treated in oven at 100 °C for 15 minutes (see ESI, section 1.1a†). This strategy resulted to be successful: the expected crystal phase was obtained as evidenced by PXRD (see ESI, Fig. S2†) and the yield raised to about 40%. Obtaining a relevant amount of sample, a deep multitechnique characterization was performed, first collecting information about the bulk structure and its stability, then studying the finest features by means of vibrational spectroscopies and computational modelling. The morphology of the MOF crystals has been explored by SEM and TEM microscopy, showing spherical particles that do not exceed the nanometric size (ESI, Fig. S3–4†). The crystal structure was refined by Rietveld method, using the UiO-66 lattice as starting guess (space group $Fm\bar{3}m$) for refining the diffractogram of the sample obtained by Micro Wave irradiation (following the aforementioned synthetic strategy, see ESI section 1.1b,† for further details), considerable as reference compound, because of the better quality of the pattern. Fig. 1 shows the isostructurality with UiO-66, indicating an FCC packed structure with stoichiometry $Ce_6O_4(OH)_4(ADC)_6$ (the structural details are reported in ESI in section 3.4 and Fig. S5†). In order to obtain a first clue concerning the main electronic and vibrational features of the ideal material, the refined structure has been the subject of periodic DFT(B3LYP) based calculations (see ESI section 4 and Table S1,† for further details) by exploiting the whole capabilities offered by the CRYSTAL17 code. The fully optimized cell (F-43m) resulted to have a = 19.18 Å and V = 7058.4 Å^3. No negative frequencies are obtained on such structure, confirming its relative stability. As far as the electronic features are concerned, a E_g = 3.04 eV is obtained (see ESI, Fig. S6† for density of states). The DRS-UV-Vis spectrum of the Ce-UiO-66-ADC (see ESI, Fig. S7†) is characterized by an edge at around 400 nm, that finds a correspondence in the computed band gap. The close inspection of the computed DOSs shows that the major contributions to the highest occupied states below the Fermi level (E_0), become from Oxygen and Carbon atoms of the linker, with a minor contribution due to cluster Oxygen atoms; while the lower unoccupied state above E_0 corresponds to cerium orbitals. This suggests that the lowest observed energy absorption corresponds to a ligand to metal charge transfer (LMCT) that explain the yellow colour of the material. Studies concerning thermal stability started with variable temperature X-Ray diffraction (VTXRD), showing that the diffraction pattern remains almost unvaried until 90 °C, marking the thermal limit for crystal structure (see ESI, Fig. S8†). Over 90 °C the crystallinity loss is visible from a gradual disappearance of the principal reflex, positioned at 2θ = 7.9°. At the same time, the TGA curves (see ESI, Fig. S9†) show a rapid weight loss, starting below 100 °C with a first

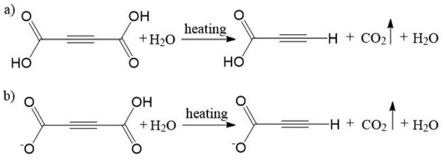

Scheme 1 (a) Water mediated decarboxylation of ADC, producing propiolic acid. (b) Water mediated decarboxylation of ADC$^-$, producing propiolate anion.

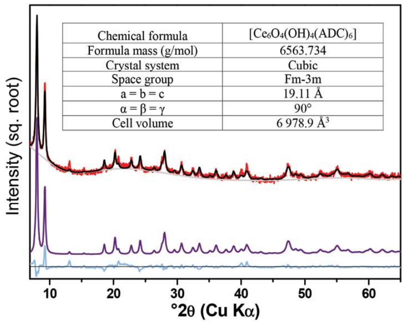

Chemical formula	$[Ce_6O_4(OH)_4(ADC)_6]$
Formula mass (g/mol)	6563.734
Crystal system	Cubic
Space group	Fm-3m
a = b = c	19.11 Å
α = β = γ	90°
Cell volume	6 978.9 Å^3

Fig. 1 Rietveld refinement of PXRD pattern of Ce-UiO-66-ADC (black). The Rietveld fitted curve is shown in black, the deconvoluted pattern in violet, the background in grey and the residuals in blue. The position of Ce atoms was allowed to refine freely, whereas the other atoms (O, C) were fixed to force field-optimized positions. Inset: table containing the most relevant structural details.

onset point around 150 °C, while the DMF loss is indistinguishable. The latter is an important information if combined with VTXRD results. It is clear that the crystalline structure collapses before the degradation occurs (weight loss in TGA), suggesting that, as long as the MOF shows a crystalline structure (until 90 °C), the solvent is still trapped into the cavities. Also reasonably, DMF has a role in stabilizing the porous system, as confirmed by 77 K N_2 adsorption results, collected in order to point out the specific surface area and the porosity of the MOF. Adsorption measurements were carried out on sample aliquots previously thermally outgassed in vacuum at rising temperature (RT, 60 °C, 90 °C, 120 °C). The obtained isotherms are describable as type I (see ESI, Fig. S10†) indicating a microporous system. The surface area has been calculated by B.E.T. (taking into account the Rouquerol rules)[40] and Langmuir models, obtaining the values reported in ESI, Table S2.† The material reveals an accessible surface area that can be related to the microporous system, since it grows by increasing the temperature from RT to 60 °C (partial removal of the trapped solvent) and it decreases with the collapse of the structure (over 90 °C). The very mild outgassing temperature allows to obtain a considerable value of Langmuir surface area of about 400 m^2 g^{-1}, but it corresponds to 1/3 of the calculated one (1131 m^2 g^{-1} see ESI, section 7†), because the temperature is too low to completely remove the DMF from the pores. *In situ* FT-IR and Raman measurements were collected along thermal activation under high vacuum, from RT (black curves) to 90 °C (violet curves), as shown in Fig. 2. In the high frequency region (3800–2800 cm^{-1}), the infrared spectrum is dominated by intense broad bands that goes out of scale due to presence of the adsorbates interacting by H-bonds (water and DMF). A prolonged in vacuum activation allows to reveal other signals ascribable[38] to both the MOF and the adsorbed solvent (90 °C is not enough to completely remove DMF): 3620 cm^{-1} (w) ν(O–H); 3260 cm^{-1} (m) ν(C–H) of terminal alkyne; 2935 cm^{-1} (m) 2810 cm^{-1} (w) respectively $\nu(\text{C–H})_{sym}$ and $\nu(\text{C–H})_{asym}$ stretching of N,N amide aliphatic groups; 2107 cm^{-1} (s) ν(C≡C) of asymmetrically substituted alkyne; 1690–1280 cm^{-1} $\nu(\text{COO}^-)$ saturated zone containing symmetric and asymmetric modes of framework carboxylate groups (region omitted in Fig. 2). Signals related to amides (*N*-aliphatic CH of methyl groups) indicate the unequivocally presence of reaction solvent (DMF). The bands at 3260 and 2107 cm^{-1} (marked with asterisks in Fig. 2) are very informative, indicating also in this case, the presence of propiolates produced by ligand decarboxylation during synthesis. Meanwhile the presence of acetylene dicarboxylate was ascertained by a parallel experiment performed by micro-Raman using an incident laser wavelength of 785 nm. The results are illustrated in the inset of Fig. 2. In this case, it is observed the appearance of two components at 2235 cm^{-1} and at 2107 cm^{-1}, due to ν(R–C≡C–R) and ν(R–C≡C–H), respectively hashtag and asterisk in Fig. 3. The assignments of the two bands are confirmed by the comparison of the Raman spectrum of the MOF with those collected on two reference compounds: acetylene dicarboxylate (dark green) and propiolate (light green) in basic aqueous solutions (Fig. 3). The first band is ascribable to the MOF linker ADC (symmetric alkyne), while the second one to the propiolate (terminal alkyne). Note that signals related to propiolate do not change in intensity during heating (Fig. 2), suggesting that such species is most probably connected to the framework and its incorporation is independent to the synthetic procedure, so it is considerable as a feature of the material. As the monocarboxylic propiolate can chelate only on one side the cluster, while the terminal alkyne remains free, the expected material would be characterized by point defects. It is compatible with the very high tolerance for defectivity reported for UiO-66 structure by many different experimental and computational studies, that opened the way for systematic studies about defect engineering of this kind of MOFs, expanding their properties and functionalities.[41–43] As introduced before, Ce-UiO-66-ADC is characterized by a strong absorption around 400 nm associated to a LMCT transition (Fig. S6†). This opens the possibility to observe the enhancement of some bands by means of the Raman Resonance effect when the sample is probed by an exciting laser line of the correct wavelength. Fig. 4 shows the Raman spectra of Ce-UiO-66-ADC collected with three lasers having different wavelengths (785 nm, 514 nm and 442 nm).

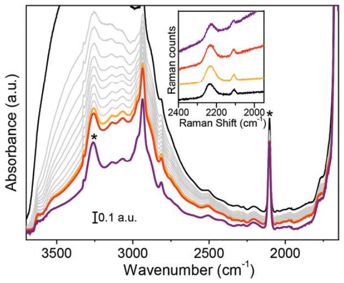

Fig. 2 FT-IR spectra collected during Ce-UiO-66-ADC thermal activation. Inset: Raman spectra reported in the 2400–1900 cm^{-1} (triple bonds stretching region) range collected with λ_{inc} = 785 nm. Black: as synthetized RT; grey: in vacuum RT outgassing; yellow: 30 °C; orange: 60 °C; violet: 90 °C.

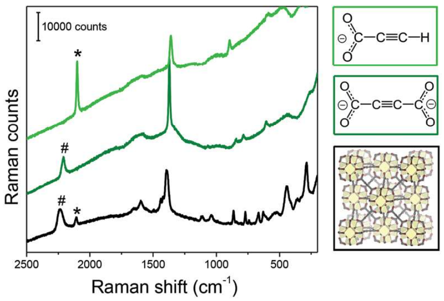

Fig. 3 Raman spectra (λ_{inc} = 785 nm) of: Ce-UiO-66-ADC (black), acetylene dicarboxylate solution (dark green), propiolate solution (light green).

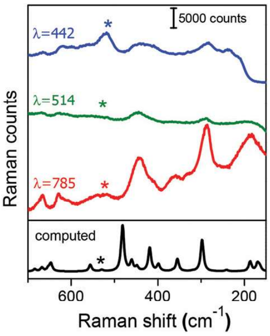

Fig. 4 Ce–O cluster vibrational modes region of Raman spectra of Ce-UiO-66-ADC acquired with different λ_{inc}. Black line: computed spectrum.

The most relevant observation is that λ_{inc} = 442 nm causes an increase in relative intensity of the band observed at 521 cm^{-1}, highlighted by the asterisks. The analogous band in the simulated spectrum is found, as expected, at higher frequencies (556 cm^{-1}) and is due to a complex vibrational mode of the cluster where the major contribution is given by the Ce–O bond stretching of the cluster. The complete assignment is reported in ESI† as comparison between experimental and computed frequencies of the principal vibrational modes (see ESI, Fig. S11 and Table S3†).

In conclusion, it has been demonstrated the possibility to obtain an UiO-66 derivative containing the acetylene dicarboxylate as linker, in presence of Ce(IV) as metal centre. This work highlighted that the reactive and extremely thermolabile nature of the linker implies the necessity of protecting it from decarboxylation reaction in aqueous medium, by Brønsted base addition, which is then removed by washing. This strategy allows to improve the yield from about 5% to about 40%. The combined use of vibrational spectroscopies and DFT calculations revealed an intrinsic defective structure of the material: the product of linker decarboxylation takes part in the framework, implying the loss of connectivity with metal centres, and constituting a local defect. The presence of the terminal alkyne can be used profitably in further studies, as it could represent an expansion of specific surface area; in addition, the functional group could be used as an anchor point for the functionalization of the MOF. For this reason, it is strictly necessary an effective removal of the solvent and the study is already underway.

Conflicts of interest

There are no conflicts to declare

Notes and references

1 S. Kaskel, *The Chemistry of Metal-Organic Frameworks: Synthesis, Characterization, and Applications*, Wiley-VCH Verlag GmbH & Co. KGaA, Weinheim, Germany, 2016.

2 J. L. C. Rowsell and O. M. Yaghi, *Microporous Mesoporous Mater.*, 2004, **73**, 3–14.

3 N. Stock and S. Biswas, *Chem. Rev.*, 2012, **112**, 933–969.

4 O. M. Yaghi, M. O'Keeffe and M. Kanatzidis, *J. Solid State Chem.*, 2000, **152**, 1–2.

5 J. Kim, B. Chen, T. M. Reineke, H. Li, M. Eddaoudi, D. B. Moler, M. O'Keeffe and O. M. Yaghi, *J. Am. Chem. Soc.*, 2001, **123**, 8239–8247.

6 O. M. Yaghi, M. O'Keeffe, N. W. Ockwig, H. K. Chae, M. Eddaoudi and J. Kim, *Nature*, 2003, **423**, 705–714.

7 M. Eddaoudi, D. B. Moler, H. Li, B. Chen, T. M. Reineke, M. O'Keeffe and O. M. Yaghi, *Acc. Chem. Res.*, 2001, **34**, 319–330.

8 A. Corma, H. García and F. X. Llabrés i Xamena, *Chem. Rev.*, 2010, **110**, 4606–4655.

9 J. Gascon, A. Corma, F. Kapteijn and F. X. Llabrés i Xamena, *ACS Catal.*, 2014, **4**, 361–378.

10 K. Sumida, D. L. Rogow, J. A. Mason, T. M. McDonald, E. D. Bloch, Z. R. Herm, T.-H. Bae and J. R. Long, *Chem. Rev.*, 2012, **112**, 724–781.

11 J. Yang, Q. Zhao, H. Xu, L. Li, J. Dong and J. Li, *J. Chem. Eng. Data*, 2012, **57**, 3701–3709.

12 J. H. Cavka, S. Jakobsen, U. Olsbye, N. Guillou, C. Lamberti, S. Bordiga and K. P. Lillerud, *J. Am. Chem. Soc.*, 2008, **6**, 13850–13851.

13 L. Valenzano, B. Civalleri, S. Chavan, S. Bordiga, M. H. Nilsen, S. Jakobsen, K. P. Lillerud and C. Lamberti, *Chem. Mater.*, 2011, **23**, 1700–1718.

14 S. Øien-Ødegaard, G. C. Shearer, K. P. Lillerud and S. Bordiga, in *Nanosponges*, ed. F. Trotta and A. Mele, Wiley-VCH Verlag GmbH & Co. KGaA, Weinheim, Germany, First edn, 2019, pp. 59–121.

15 D. Zhao, D. J. Timmons, D. Yuan and H.-C. Zhou, *Acc. Chem. Res.*, 2011, **44**, 123–133.

16 S. J. Garibay and S. M. Cohen, *Chem. Commun.*, 2010, **46**, 7700.

17 V. Bon, I. Senkovska, M. S. Weiss and S. Kaskel, *CrystEngComm*, 2013, **15**, 9572.

18 M. J. Katz, Z. J. Brown, Y. J. Colón, P. W. Siu, K. A. Scheidt, R. Q. Snurr, J. T. Hupp and O. K. Farha, *Chem. Commun.*, 2013, **49**, 9449.

19 D. J. Tranchemontagne, J. R. Hunt and O. M. Yaghi, *Tetrahedron*, 2008, **64**, 8553–8557.

20 C. Serre, J. Marrot and G. Férey, *Inorg. Chem.*, 2005, **44**, 654–657.

21 C. Robl and S. Hentschel, *Z. Anorg. Allg. Chem.*, 1990, **591**, 188–194.

22 C. Robl and S. Hentschel, *Z. Anorg. Allg. Chem.*, 1991, **596**, 149–155.

23 A. Michaelides and S. Skoulika, *Cryst. Growth Des.*, 2005, **5**, 529–533.

24 I. Stein and U. Ruschewitz, *Z. Anorg. Allg. Chem.*, 2010, **636**, 400–404.

25 A. Schuy, I. Stein and U. Ruschewitz, *Z. Anorg. Allg. Chem.*, 2010, **636**, 1026–1031.

26 S. Khullar and S. K. Mandal, *RSC Adv.*, 2014, **4**, 39204–39213.

27 D. Hermann, C. Näther and U. Ruschewitz, *Solid State Sci.*, 2011, **13**, 1096–1101.

28 S. Busch, I. Stein and U. Ruschewitz, *Z. Anorg. Allg. Chem.*, 2012, **638**, 2098–2101.

29 V. K. Gramm, A. Schuy, M. Suta, C. Wickleder, C. Sternemann and U. Ruschewitz, *Z. Anorg. Allg. Chem.*, 2018, **644**, 127–135.

30 M. Lammert, M. T. Wharmby, S. Smolders, B. Bueken, A. Lieb, K. A. Lomachenko, D. De Vos and N. Stock, *Chem. Commun.*, 2015, **51**, 12578–12581.

31 M. Lammert, C. Glißmann and N. Stock, *Dalton Trans.*, 2017, **46**, 2425–2429.

32 R. Dalapati, B. Sakthivel, A. Dhakshinamoorthy, A. Buragohain, A. Bhunia, C. Janiak and S. Biswas, *CrystEngComm*, 2016, **18**, 7855–7864.

33 S. Smolders, K. A. Lomachenko, B. Bueken, A. Struyf, A. L. Bugaev, C. Atzori, N. Stock, C. Lamberti, M. B. J. Roeffaers and D. E. De Vos, *ChemPhysChem*, 2018, **19**, 373–378.

34 S. Smolders, A. Struyf, H. Reinsch, B. Bueken, T. Rhauderwiek, L. Mintrop, P. Kurz, N. Stock and D. E. De Vos, *Chem. Commun.*, 2018, **54**, 876–879.

35 X.-P. Wu, L. Gagliardi and D. G. Truhlar, *J. Am. Chem. Soc.*, 2018, **140**, 7904–7912.

36 T. Islamoglu, D. Ray, P. Li, M. B. Majewski, I. Akpinar, X. Zhang, C. J. Cramer, L. Gagliardi and O. K. Farha, *Inorg. Chem.*, 2018, **57**, 13246–13251.

37 T. J. Matemb Ma Ntep, H. Reinsch, J. Liang and C. Janiak, *Dalton Trans.*, 2019, **48**, 15849–15855.

38 N. B. Colthup, L. H. Daly and S. E. Wiberley, *Introduction to Infrared and Raman Spectroscopy*, Academic Press, 2nd edn, 1975.

39 J. Li and T. B. Brill, *J. Phys. Chem. A*, 2002, **106**, 9491–9498.

40 M. Thommes, K. Kaneko, A. V. Neimark, J. P. Olivier, F. Rodriguez-Reinoso, J. Rouquerol and K. S. W. Sing, *Pure Appl. Chem.*, 2015, **87**, 1051–1069.

41 C. Atzori, G. C. Shearer, L. Maschio, B. Civalleri, F. Bonino, C. Lamberti, S. Svelle, K. P. Lillerud and S. Bordiga, *J. Phys. Chem. C*, 2017, **121**, 9312–9324.

42 G. C. Shearer, S. Chavan, J. Ethiraj, J. G. Vitillo, S. Svelle, U. Olsbye, C. Lamberti, S. Bordiga and K. P. Lillerud, *Chem. Mater.*, 2014, **26**, 4068–4071.

43 G. C. Shearer, S. Chavan, S. Bordiga, S. Svelle, U. Olsbye and K. P. Lillerud, *Chem. Mater.*, 2016, **28**, 3749–3761.

Electronic Supplementary Material (ESI) for Dalton Transactions.

Supporting information

A spectroscopic and computational study of a tough MOF with a fragile linker: Ce-UiO-66-ADC.

Alessia Airi[a], Cesare Atzori[a*], Francesca Bonino[a], Alessandro Damin[a],
Sigurd Øien-Ødegaard[b], Erlend Aunan[b] and Silvia Bordiga*[a,b]

List of content:

---

[a] *Department of Chemistry, NIS and INSTM Reference Centre, University of Torino, Via G. Quarello 15, 10135 Torino, Italy*

[b] Catalysis Section, Department of Chemistry, University of Oslo, P.O. Box 1033, N-0315 Oslo, Norway

1. Materials and methods

1.1. Synthesis procedure

Cerium ammonium nitrate $(NH_4)_2Ce(NO_3)_6$ (98.5%, Sigma-Aldrich) and acetylene dicarboxylic acid H_2ADC (>90.0%, TCI chemicals) were used as purchased.
0.065 g H_2ADC were solubilized in 3.2 mL of dimethylformamide (DMF, Sigma-Aldrich) within a thick-walled glass vial, obtaining a clear solution. Then 1.06 ml of an 0.53M aqueous solution of $[(NH_4)_2[Ce(NO_3)_6]$ (previously prepared with 7.305 g in 25 mL of water) was added to the first one. After mixing, the closed vial (with a screw cap) was inserted in a preheated oven at the constant temperature of 90°C and kept in for 15 minutes. After the thermal treatment, the obtained precipitate was separated from liquid phase by centrifuge at 10 000 rpm for 5 minutes then washed with fresh DMF. The solid was washed with acetone and centrifuged for 3 times, then air dried. Same variation to the synthesis have been applied:

a. **Basic conditions**: triethylammine Et_3N (≥99%, Sigma-Aldrich) was used in order to increase the yield, the base was added to the DMF H_2ADC solution (1:1 respect to H_2ADC moles), before mixing with $(NH_4)_2Ce(NO_3)_6$ solution, obtaining a very rapid precipitation. Then the reaction mixture has been inserted in oven at 100°C for 15 minutes. The precipitate product has been isolated by centrifuge and washed as previously described.
b. **Micro-Waves assisted synthesis**: the same procedure was applied also for testing different sources of heating, introducing the same synthetic mixture in a Biotage Initiator microwave furnace for 15 minutes at 90°C under stirring the best crystalline pattern was obtained (see Figure 1 in the main text).

1.2 ^{1}H-NMR spectroscopy

Digestion NMR analysis was performed on Ce-UiO-66-ADC in order to characterize any residual solvents in the pores. The MOF (200 mg) was digested in 1M NaOD in D_2O for 10 minutes under shaking before centrifuged to separate the insoluble Ce(OD)4 from the mother liquor containing the soluble organic species. The mother liquor was analyzed using NMR spectroscopy (Bruker AVII 400, 128 scans, d1=5 sec). The NMR analysis confirmed the presence of DMF (both from DMF itself, and from its decomposition products: formate and dimethylamine). No linker was observed, as expected as it contains no protons.

1.3. Electron Microscopies

SEM: the micrographs were collected using a Zeiss Evo 50 xvp microscope equipped with a LaB_6 crystal electron source working at 20 kV of accelerating potential. The sample had been previously coated in gold by sputter deposition.

TEM: the micrographs were collected using a TEM JEOL JEM 3010 UHR microscope equipped with a LaB_6 electron source working at 300 kV of accelerating potential and a EDS OXFORD energy dispersion detector (0,17 nm of theoretical resolution). The images have been collected by a CCD camera Gatan, Model 894 US1000 (2k x 2k). The sample has been prepared depositing a small amount of powder over a 200 mesh lacey carbon copper screen.

1.4. PXRD

The sample was placed in a 0.7 mm Ø glass capillary, and PXRD patterns in the range of 2θ = 4°-70° were acquired over 24 hours on a Bruker D8 Advance diffractometer with Cu K-α radiation.
VTXRD: Diffraction patterns have been collected with a PW3050/60 X'Pert PRO MPD diffractometer, working in Bragg-Brentano geometry, using Cu anode.
Non-ambient chamber Anton Paar XRK900 with Be windows was used to collect the PXRD data in dynamic vacuum, with ramp rate of 2°C/min. Each 2θ scan was collected every 10° C, rising in temperature from RT to 190°C.

1.5. DR-UV-vis spectroscopy

Ce-UiO-66-ADC spectra have been collected with a Varian Cary 5000 UV-vis-NIR spectrophotometer working in diffuse reflectance mode in the 200-2500 nm, with resolution of 1 nm.
H2ADC and [(NH4)2[Ce(NO3)6] aqueous solutions spectra have been collected in transmission mode in spectral range of 200-800 nm with a resolution of 1 nm.

1.6. Thermo Gravimetric Analysis

The thermo-gravimetric analysis (TGA) has been conducted using a TA Instruments Q600 programmed for rising 3°C/min from RT to 700°C in both air and N_2 atmosphere (100 mL/min flows), on about 10 mg of each sample in an alumina crucible.

1.7. 77K N_2 adsorption

Adsorption measurements were performed on a Micromeritics ASAP 2020 apparatus working at 77K with about 40 mg of sample.

1.8. FT-IR spectroscopy

Infra-red spectra have been collected by Thermo Scientific Nicolet 6700 FTIR spectrometer equipped with a HgCdTe detector in transmission mode using a self-supporting pellet in the range 400-4000 cm-1 with a resolution of 2 cm^{-1}.

1.9. Raman Spectroscopy

Raman spectra of a self-supporting pellet of sample activated at different temperatures, were collected with a Renishaw InVia Raman microscope working with a 785 nm laser diode and a 20X objective, accumulating for 20 seconds with 1 mW laser power in the 3200-100 cm^{-1} Raman shift range. Spectra of powdered material were collected using 785 nm, 514 nm (Ar^+ laser) and 442 nm (He-Cd lasers) exciting laser lines: spectra result from 10 acquisitions each one of 20 seconds. Power at the sample was maintained below 1 mW. In order to reduce the risk of thermal degradation, a special setup providing the sample rotation under the laser beam has been adopted.[1]

2. Detection of terminal alkyne

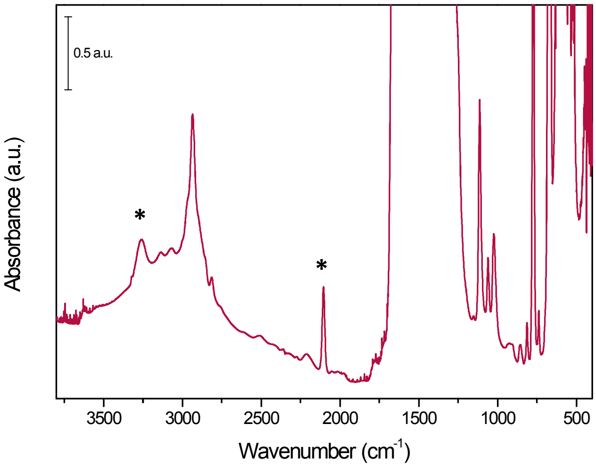

Figure S1 FT-IR spectrum of 90°C in vacuum outgassed material.

The IR spectrum was collected on the activated sample (high vacuum overnight at 90°C) in order to minimize interferences due to adsorbed molecules. The spectrum is characterized by the presence of a signal at 3260 cm^{-1} and a strong sharp band at 2107 cm^{-1} which can be easily attributed to a terminal alkyne, compatible with the decarboxylation product of the linker, see Scheme 1 in main text.

3. Structure and morphology description

3.1. Influence of Et_3N. PXRD

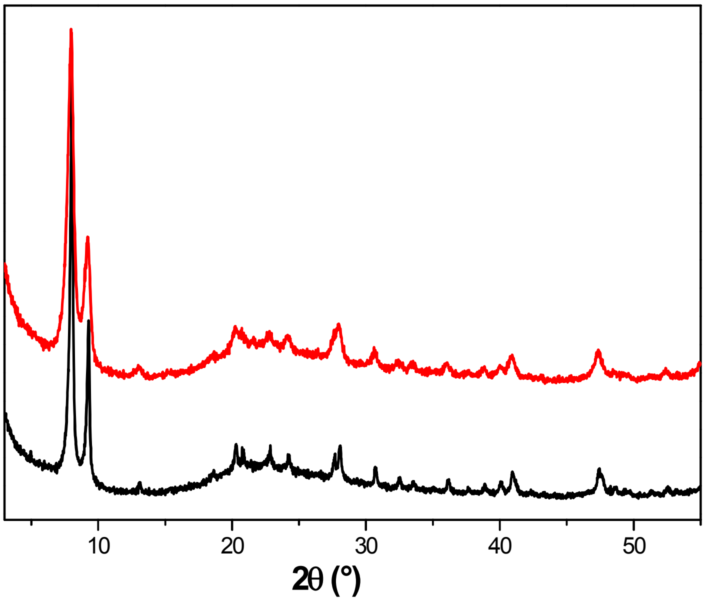

Figure S2. PXRD patterns of Ce-UiO-66-ADC. Sample obtained without the use of Et_3N (black line); sample obtained in presence of Et_3N (red line).

The two materials present the same pattern. None significant differences are visible except for the width of reflexes, due to the faster precipitation in presence of Et_3N, which produce smaller crystal domains.

By the comparison of the PXRD patterns it is possible to affirm that the different synthetic procedures applied result to produce the same crystal phase, denoted as Ce-UiO-66-ADC.

3.2. SEM microscopy

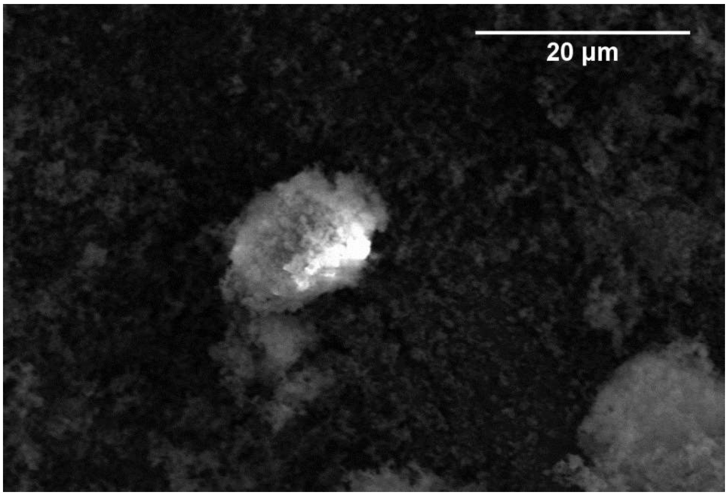

Figure S3. SEM images of Ce-UiO-66-ADC (synthetized in basic conditions).

3.3. TEM microscopy

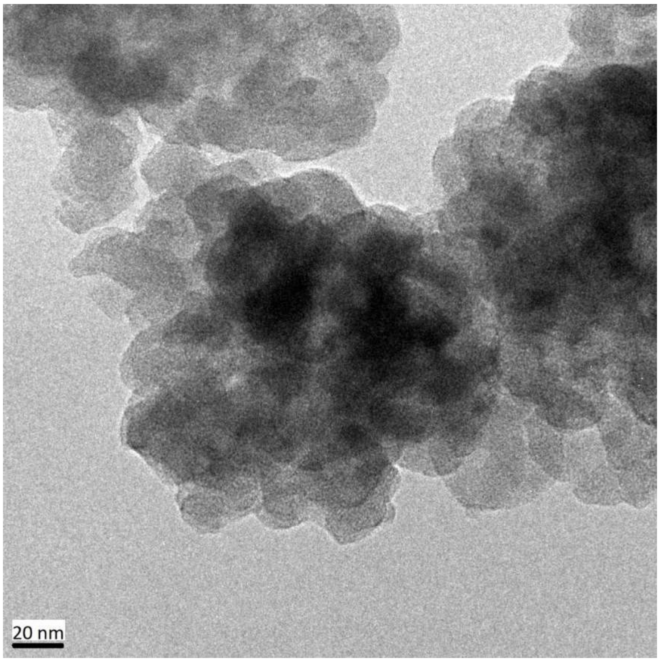

Figure S4. TEM images of Ce-UiO-66-ADC (synthetized in basic conditions).

3.4. Structure

Using cell parameters obtained from a Pawley fit (FM-3m, a = 19.11 Å), a model based on 12-connected clusters, containing 6 Ce atoms, was constructed in Materials Studio v8 (Biovia, 2019), and geometrically optimized with the Forcite program. This model was used in a Riedveld refinement (using 2θ 4°-65°) where the Ce position was allowed to refine, leading to the structure reported herein.

This is the output file of the refinement:

Chemical formula: $[Ce_6O_4(OH)_4(ADC)_6]$

```
R-Values

Rexp : 6.78     Rwp : 9.67      Rp  : 7.38   GOF : 1.43
Rexp`: 16.65    Rwp`: 23.75     Rp` : 24.03  DW  : 1.03

Quantitative Analysis - Rietveld
   Phase 1  : ""                                100.000 %

Background
   Chebychev polynomial, Coefficient  0      188.3758
                                      1      -140.7667
                                      2      100.135
                                      3      -54.67057
                                      4      40.87468
                                      5      -37.97169
                                      6      30.43907
                                      7      -4.02601
                                      8      -11.60408
                                      9      10.07483
                                      10     -9.637173

Instrument
   Primary radius (mm)                       166
   Secondary radius (mm)                     209
   Simple axial model (mm)                   7.688171

Corrections
   Zero error                                0.01658058
   LP Factor                                 27.3

Structure 1
   Phase name
   R-Bragg                                   3.525
   Spacegroup                                FM-3M
   Scale                                       3.03507e-007
   Cell Mass                                 6563.734
   Cell Volume (Å^3)                         6978.94642
   Wt% - Rietveld                            100.000
   Double-Voigt|Approach
      Cry size Lorentzian                    108.1
      k:  1  LVol-IB (nm)                    68.847
      k:  0.89  LVol-FWHM (nm)               96.248
```

```
   Strain
      Strain L                                     1.188662
      Strain G                                     0.0001
      e0                                           0.00259
   Crystal Linear Absorption Coeff. (1/cm)         300.588
   Crystal Density (g/cm^3)                        1.562
   Lattice parameters
      a (Å)                                        19.1101144

Site  Np    x           y           z           Atom Occ        Beq
Ce1    24  0.13662     0.00000     0.00000     Ce   1          0
O2     32  0.06392     0.06392     0.06392     O    1          0
C3     48  0.16710     0.16710     0.00000     C    1          0
C4     48  0.22598     0.22598     0.00000     C    1          0
O5     96  0.18582     0.10019     0.00000     O    1          0
```

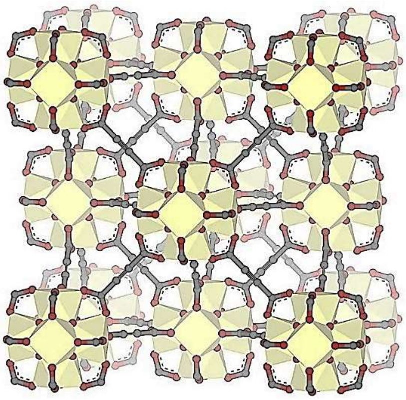

Figure S5. Elementary cell of Ce-UiO-66-ADC

4. DFT calculations

Periodic DFT[2] based calculations were performed by exploiting the hybrid B3LYP[3,4] functional and the empirical D3(BJ)[5–7] scheme for the description of dispersive interactions and including the Axilrod-Teller-Muto type three-body term. In the whole set of calculations, the CRYSTAL software[8,9] package was employed: this allows a complete treatment of periodic systems through the use of atom-centred linear combinations of Gaussian type functions for the description of atomic orbitals (basis set). Basis set adopted in present calculations is below described:

a) Ce inner electrons (28) were replaced by an effective core potential (ECP), the remaining 30 electrons being explicitly treated through a (10sp7d8f)/[4sp2d3f] basis set. The same scheme was already employed in Ref[10] for Ce description in CeO_2 and Ce_2O_3 systems. See also http://www.crystal.unito.it/basis-sets.php.

b) O and C atoms were described through a (8s6sp2d)/[1s3sp2d] and (6s5sp2d)/[1s3sp2d] all-electron basis sets respectively. They were obtained by ones employed in Ref[11], simply by splitting the original d shell through an even tempered recipe. For their full description see also Table S2.

c) For H atoms the adopted all electron basis set was a (7s1p)/[3s1p]] one already adopted in Ref[12]. See also http://www.crystal.unito.it/basis-sets.php.

Numerical accuracy in energy calculation were determined by setting thresholds for mono- and bi-electronic integral to {1188836} through the keyword (TOLINTEG). Shrinking factor parameter (keyword SHRINK), determining the k-points sampling in the reciprocal space, was set to 3 (corresponding to 4 irreducible k points). The defaults values for all the unreported computational parameters concerning the structure optimization, frequency and the associated Raman intensities calculation were used.

O (8s6sp2d)/[1s3sp2d] basis set	C (6s5sp2d)/[1s3sp2d] basis set
8 6	6 6
0 0 8 2 1.0	**0 0 6 2 1.0**
8020. 0.001080	4563.24000 0.00196665
1338. 0.008040	682.02400 0.01523060
255.4 0.053240	154.97300 0.07612690
69.22 0.168100	44.45530 0.26080100
23.90 0.358100	13.02900 0.61646200
9.264 0.385500	1.82773 0.22100000
3.851 0.146800	**0 1 3 4 1.0**
1.212 0.072800	20.96420 0.11466000 0.04024870
0 1 4 6 1.0	4.80331 0.91999900 0.23759400
49.43 -0.008830 0.009580	1.45933 -0.00303068 0.81585400
10.47 -0.091500 0.069600	**0 1 1 0 1.0**
3.235 -0.040200 0.206500	0.483456 1. 1.
1.217 0.379000 0.347000	**0 1 1 0 1.0**
0 1 1 0 1.0	0.145585 1. 1.
0.486 1. 1.	**0 3 1 0 1.0**
0 1 1 0 1.0	1.6 1.
0.1925 1. 1.	**0 3 1 0 1.**
0 3 1 0 1.	0.4 1.
1.6 1.	
0 3 1 0 1.	
0.4 1.	

Table S1: Gaussian basis sets (reported in the CRYSTAL code format) adopted in present calculations for the description of O and C atoms.

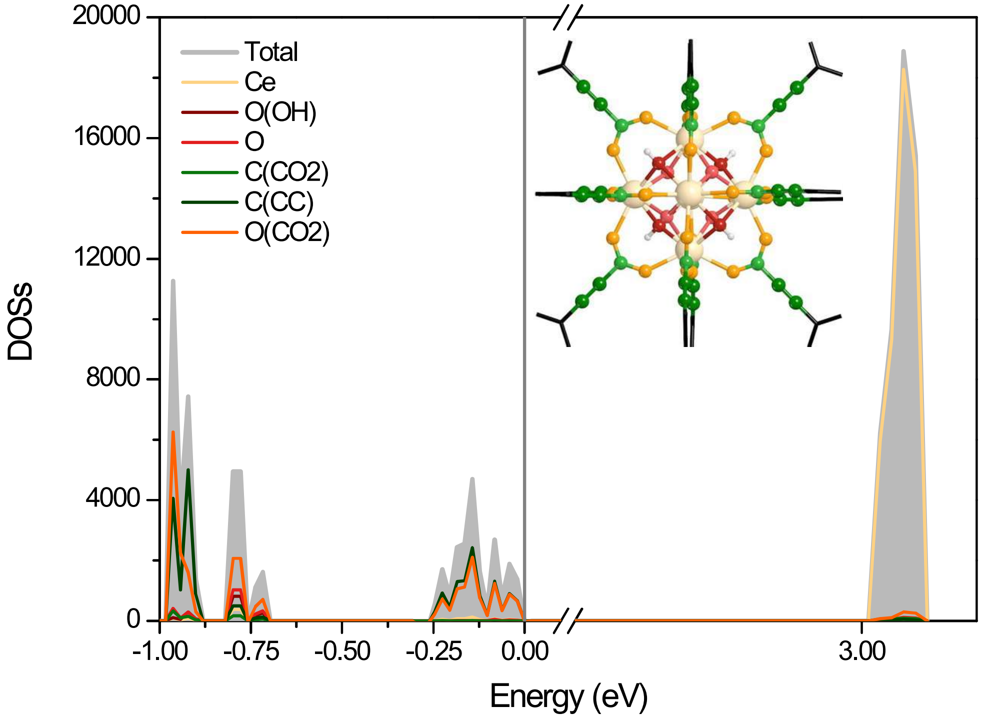

Figure S6. Total density of states (filled grey curve) computed on optimized Ce-UiO-66-ADC structure. Contributions from different atomic species (solid lines) constituting the repeating unit of Ce-UiO-66-ADC (see inset for a graphical representation) are also reported for the sake of comparison.

5. UV-vis spectroscopy

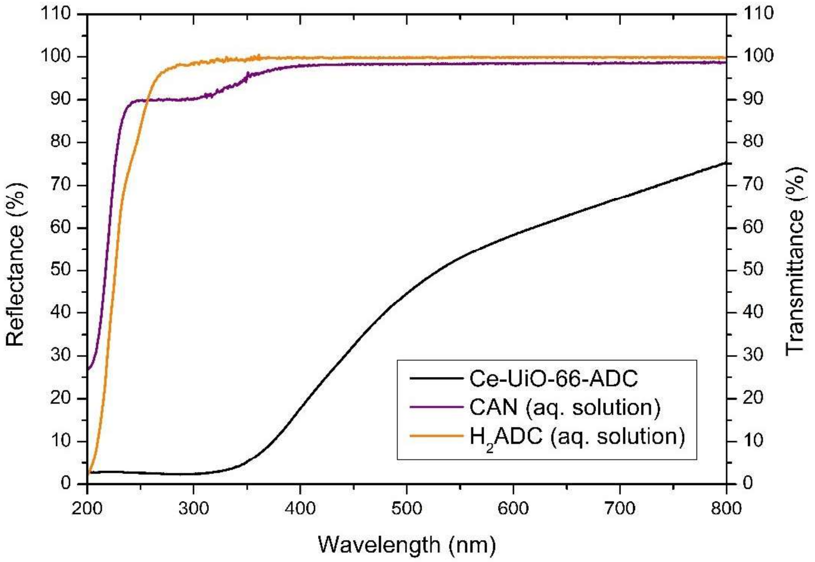

Figure S7. DR-UV-vis spectrum of Ce-UiO-66-ADC (black), compared with transmission UV-vis spectra of the solubilized precursors H_2ADC (orange) and Cerium ammonium nitrate CAN (violet).

As shown in Figure S7, the Ce-UiO-66-ADC UV-vis spectrum results to be more complex than the simply sum of the two spectra of its precursors, suggesting a deep change in the electronic structure with the formation of the solid.

6. Thermal stability

6.1. VTXRD

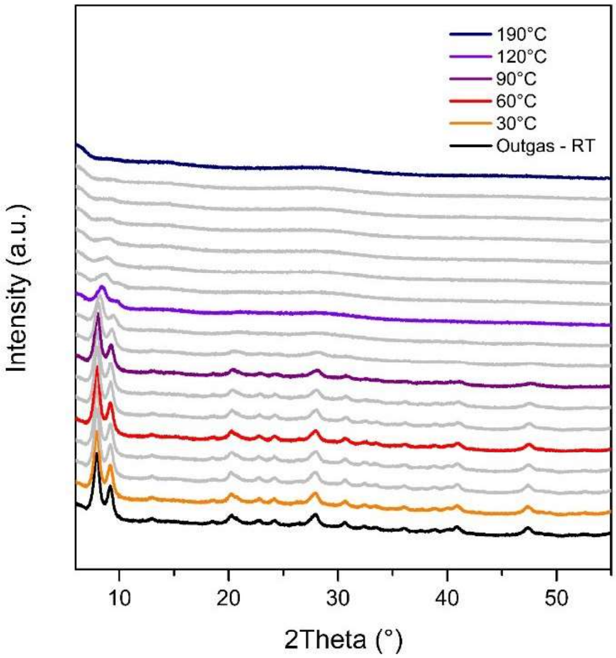

Figure S8. Ce-UiO-66-ADC PXRD patterns from RT (bottom) to 190°C (top) rising 10° per step. The colours underline the temperature selected for activation in following measurements (same colour code).

6.2. TGA

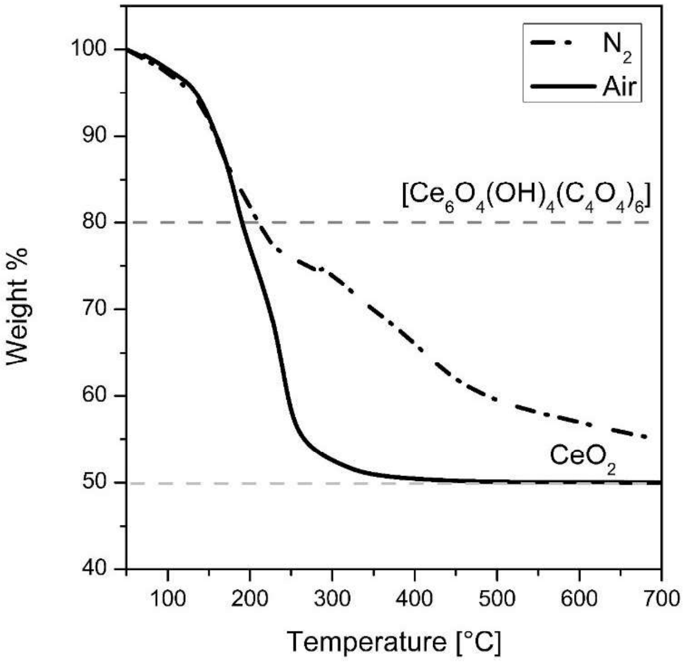

Figure S9. TGA curves of Ce-UiO-66-ADC, under dry air (solid line) and in N_2 (dot line) flux.

7. Specific surface area

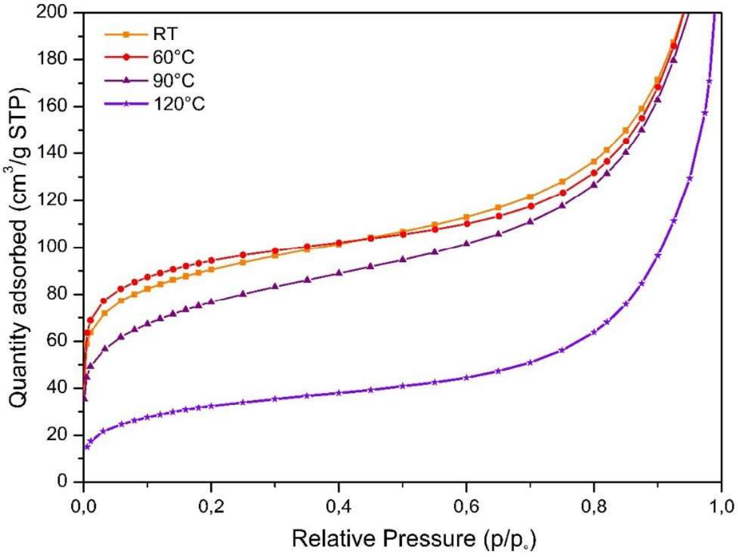

Figure S10. N$_2$ adsorption 77K isotherms for sample activated at different temperatures.

Outgassing Temperature (°C)	**Langmuir Surface area (m^2/g)**	**B.E.T. surface area (m^2/g)**
RT	425 ± 5	326 ± 2
60	437 ± 4	345 ± 2
90	371 ± 6	273 ± 2
120	163 ± 3	118 ± 1

Table S2. Specific surface area values after in vacuum thermal outgassing.

Theoretical Specific Surface Area:

N$_2$ accessible surface area was estimated using both a crude geometrical summation of the Connolly surface, and a simulated adsorption isotherm calculated using the Sorption module in Materials Studio. Surface calculation gave a result of 1131 m^2/g, whereas the simulated sorption isotherm gave a BET surface area of 889 m^2/g using the pressure range of $p/p_0 = 0.00031 – 0.01755$.

8. Raman spectrum analysis and bands assignment

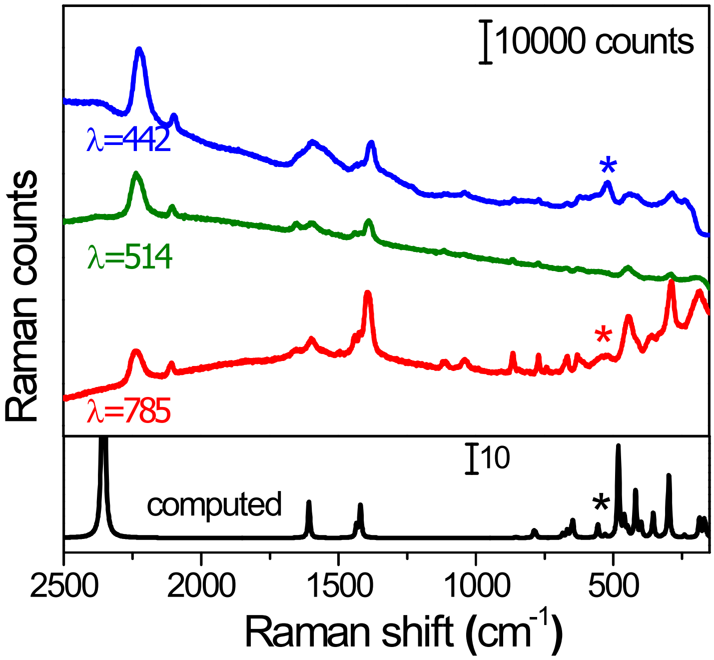

Figure S11. Raman spectra collected with different wavelength of irradiation (blue line: 442 nm, green: 514 nm, red: 785nm) in the Raman shift range between 2500 and 250 cm^{-1}, compared with the computed one (black line).

The Raman spectrum of Ce-UiO-66-ADC is characterized by three main regions, starting from higher wavenumbers: 2200-2100 cm^{-1} C≡C stretching region; 1600-1380 cm^{-1} carboxylate stretching region; below 1000 cm^{-1} are present the complex modes of the metal-oxide cluster. The Raman spectrum collected with the λ=785 nm laser shows also the fingerprints of DMF: maxima observed at 773, 864 ,1030, 1120 cm^{-1}.

The complete assignation of the Raman active modes of Ce-UiO-66-ADC is reported in Table S3.

Experimental (cm^{-1})	**Computed (cm^{-1})**	**Moiety**	**Description**
2235	2337	linker	R-(C≡C)-R stretching
2107	-	defective linker	R-(C≡C)-H stretching
1594	1592	linker	(COO$^-$) asymm stretching
1391	1416	linker	(COO$^-$) symm stretching
741	802	linker	COO$^-$ out of plane
665	656	cluster+ linker	O-H bending + C-(COO-) bending
622	644	cluster+ linker	O-H bending + COO- bending
521	556	cluster	Ce-O
440	482	cluster + linker	Ce-O(COO$^-$) symm stretching
418	412	cluster	Ce-O breathing symm
359	355	cluster + linker	Ce-O breathing asym + out of plane C-(COO)$^-$
285	302	cluster + linker	Ce-O(COO$^-$) asymm
205-150	184,162	cluster + linker	Coupled complex modes of Ce-O(COO$^-$)

Table S3. Frequencies of the principal Raman active vibrational modes of Ce-UiO-66-ADC.

REFERENCES:

1 M. Signorile, F. Bonino, A. Damin and S. Bordiga, *Top. Catal.*, 2018, **61**, 1491–1498.

2 P. Hohenberg and W. Kohn, *Phys. Rev.*, 1964, **136**, B864–B871.

3 A. D. Becke, *J. Chem. Phys.*, 1993, **98**, 1372–1377.

4 C. Lee, W. Yang and R. G. Parr, *Phys. Rev. B*, 1988, **37**, 785–789.

5 S. Grimme, J. Antony, S. Ehrlich and H. Krieg, *J. Chem. Phys.*, 2010, **132**, 154104.

6 S. Grimme, S. Ehrlich and L. Goerigk, *J. Comput. Chem.*, 2011, **32**, 1456–1465.

7 S. Grimme, A. Hansen, J. G. Brandenburg and C. Bannwarth, *Chem. Rev.*, 2016, **116**, 5105–5154.

8 R. Dovesi, A. Erba, R. Orlando, C. M. Zicovich-Wilson, B. Civalleri, L. Maschio, M. Rérat, S. Casassa, J. Baima, S. Salustro and B. Kirtman, *Wiley Interdiscip. Rev. Comput. Mol. Sci.*, 2018, **8**, 1–36.

9 R. Dovesi, V.R. Saunders, C. Roetti, R. Orlando, C. M. Zicovich-Wilson, F. Pascale, B. Civalleri, K. Doll, N.M. Harrison, I.J. Bush, Ph. D'Arco, M. Llunel, M. Causà, Y. Noel, L. Maschio, A. Erba, M. Rérat, S. Casassa, CRYSTAL17 User's Manual, 2018.

10 J. Graciani, A. M. Márquez, J. J. Plata, Y. Ortega, N. C. Hernández, A. Meyer, C. M. Zicovich-Wilson and J. F. Sanz, *J. Chem. Theory Comput.*, 2011, **7**, 56–65.

11 L. Valenzano, B. Civalleri, S. Chavan, S. Bordiga, M. H. Nilsen, S. Jakobsen, K. P. Lillerud and C. Lamberti, *Chem. Mater.*, 2011, **23**, 1700–1718.

12 R. Dovesi, C. Ermondi, E. Ferrero, C. Pisani and C. Roetti, *Phys. Rev. B*, 1984, **29**, 3591–3600.